



N-heterocyclic carbene ligands designed for improved stability and efficiency of ruthenium-based olefin metathesis catalysts

Pawel Krzesinski

► To cite this version:

Pawel Krzesinski. N-heterocyclic carbene ligands designed for improved stability and efficiency of ruthenium-based olefin metathesis catalysts. Coordination chemistry. Université de Toulouse, 2024. English. NNT : 2024TLSES006 . tel-04585049

HAL Id: tel-04585049

<https://theses.hal.science/tel-04585049>

Submitted on 23 May 2024

HAL is a multi-disciplinary open access archive for the deposit and dissemination of scientific research documents, whether they are published or not. The documents may come from teaching and research institutions in France or abroad, or from public or private research centers.

L'archive ouverte pluridisciplinaire **HAL**, est destinée au dépôt et à la diffusion de documents scientifiques de niveau recherche, publiés ou non, émanant des établissements d'enseignement et de recherche français ou étrangers, des laboratoires publics ou privés.

Doctorat de l'Université de Toulouse

préparé à l'Université Toulouse III - Paul Sabatier

Catalyseurs de métathèse des oléfines au ruthénium à stabilité et efficacité accrues par conception de nouveaux ligands carbènes N-hétérocycliques

Thèse présentée et soutenue, le 12 février 2024 par

Pawel KRZESINSKI

École doctorale

SDM - SCIENCES DE LA MATIERE - Toulouse

Spécialité

Chimie Organométallique et de Coordination

Unité de recherche

LCC - Laboratoire de Chimie de Coordination

Thèse dirigée par

Vincent CESAR et Karol Grela

Composition du jury

Mme Blanca MARTIN-VACA, Présidente, Université Toulouse III - Paul Sabatier

M. Hervé CLAVIER, Rapporteur, CNRS

Mme Joanna WENCZEL-DELORD, Rapporteure, Würzburg Universität

Mme Macarena POYATOS, Rapporteure, Universitat Jaume I

M. Jan ROMASKI, Examinateur, University of Warsaw

M. Grzegorz LITWINIENKO, Examinateur, University of Warsaw

M. Vincent CESAR, Directeur de thèse, CNRS Occitanie-Ouest

M. Karol GRELA, Co-directeur de thèse, University of Warsaw

Membres invités

Mme Stéphanie Bastin, CNRS Toulouse - LCC

Mme Anna Kajetanowicz, University of Warsaw



Paweł Krzesiński

426278

N-Heterocyclic Carbene Ligands Designed for Improved Stability and Efficiency of Ruthenium-Based Olefin Metathesis Catalysts

Doctoral dissertation
in the field of Natural Sciences
in the discipline of Chemical Sciences

Completed under the supervision of:
Karol Grela and Vincent César

University of Warsaw
Biological and Chemical Research Centre

Acknowledgments

I have carried out the work for this thesis in the two following research groups: the Organometallic Synthesis Laboratory (LSM) in Warsaw, Poland and the “Molecular Design of Transition Metal Pre-Catalysts” group (team A) of the Laboratory of Coordination Chemistry (LCC) in Toulouse, France. A part of the work was realized in Tecnalia Research & Innovation in Miñano, Spain. What’s more, the thesis was a part of the Coordination Chemistry Inspires Molecular Catalysis (CCIMC) project of Innovative Training Network (ITN). Suffice to say, it is impossible to list all the people that I interacted with during those years and that I’d like to acknowledge here. Nevertheless, I shall try...

First and foremost, I’d like to express my gratitude to my supervisors Vincent César (LCC) and Karol Grela (LSM) for the proposition of the topic of my thesis and their mentorship guiding me throughout it. Also, I’d like to thank my additional supervisors Stéphanie Bastin (LCC) and Anna Kajetanowicz (LSM) for the advice they gave me. At last, a special thanks to Pablo Ortiz from Tecnalia for the proposition of the research project I did there and for his guidance.

Next, I’d like to acknowledge the CCIMC project. I’d like to thank Rinaldo Poli, Anne-Marie Caminade and Alida Lefter for such a nice coordination of this ITN. Many thanks to all the members of the “Academic Board” for all the advice they gave me during our meetings. Last but definitely not least, for all the great time we’ve spent together I thank early stage researchers, Joris Langlois, Irina Bozhinovska, Zinnia Arora, Sara Bonfante, Wimonsiri Huadsai, Paven Kisten, Chantal Abou Fayssal, Joel Cejas, Deepthy Krishnan, Max Milewski, Massimo Petriccone, Aswin Chandran and Agustín Morales.

From LSM, for our scientific discussions and the advice they gave me, I’d like to thank Katarzyna Gajda, Adam Rajkiewicz, Mateusz Urban, Łukasz Grzesiński, Adrian Sytniczuk, Filip Struzik, Luis Mosigny and Sebastian Planer. For all the incredible moments we’ve spent together, many thanks to group members, Jakub Piątkowski, Łukasz Szczuciński, Anna Mączka, Maryana Nadirova, Maria Matveeva, Magdalena Walczak, Zofia Kowalik, Mariusz Milewski, Michał Patrzałek, and all the others.

From team A of LCC, a special thanks to permanent staff, Olivier Basle, Yves Canac, Dmitry Valyaev, Jean-Baptiste Sortais, and to Ekaterina Gulyaeva for the advice they gave me and scientific discussions we had. Also, I really enjoyed spending time with group members for which I’d like to thank Anna Bonfiglio, Jasmin Bioteau, Oussama Fayafrou, Alina Kravchenko, Cécile Barthes, Andrea Orellana Ben Amor, Romane Pointis, Paul Teixeira, Juliette Zanzi, Agnideep Das, Quentin Marchand, Riddi Tripathi and all others I didn’t mentioned.

Likewise, I will never forget the time I spent in the Basque Country in Tecnalia. For that, I thank the people I met there, Ander Centeno, Beñat Anda, Sergio Santos, Soraya Prieto, Olga Gomez, Iker Ayuso Marta Sagredo, Beatriz Aberasturi, Leire Lorenzo, and all others.

I’d also like to acknowledge collaborators, especially Chiara Dinoi and Iker del Rosal for carrying out the DFT calculations presented in the thesis. Many thanks to Damian Trzybiński (University of Warsaw) and Laure Vendier (LCC) for measuring and refining XRD crystal structures and also to Antoine Bonnet for his help with NMR measurements.

I’d also like to thank my friends and family for being there for me and the support they gave me.

This work has received funding from the European Union's Horizon 2020 research and innovation programme under the Marie Skłodowska-Curie grant agreement no. 860322 (CCIMC).

Abstract

No doubt catalysis is one of the most relevant tools used in the chemical industry, allowing to obtain a myriad of sometimes otherwise inaccessible molecules. Homogeneous catalysis has the advantage of more precise characterization of catalysts and intermediates which makes it more suitable for rational design. Catalyst's auxiliary ligands play a significant role in defining the activity, selectivity and stability of the resulting catalysts. In this respect, *N*-heterocyclic carbene (NHC) ligands have shown a broad utility as spectator ligands that can stabilize catalytic intermediates. The most important impact of NHCs is arguably in the field of olefin metathesis (OM), which is a carbon skeleton redistribution around an unsaturated carbon-carbon double bond. OM has already become a device of prominent importance thus earning an outstanding position in the organic synthesis toolbox. The work described here aimed at NHC ligand design to achieve more stable, durable and thus more efficient OM catalysts. Two strategies were investigated to enhance the stability of corresponding NHC OM catalysts.

The thesis is divided into six chapters. The first chapter of the thesis describes relevant state-of-the-art. In the second chapter, a strategy for a robust Z-selective OM catalyst was investigated, followed by chapter three reporting catalysts designed for an efficient tetrasubstituted carbon-carbon double bond formation. The last part of the work describes, in chapter four, a potential application of the obtained catalytic systems. The thesis concludes with an experimental section and references in chapters five and six respectively.

Within the first strategy for a more efficient catalyst, attempts to obtain a robust Z-selective catalyst bearing a chelating LX-type NHC ligand were explored by altering the X-type ligand to obtain a stable ruthenium-carbon(sp^3) bond. The research objectives were diversified into two axes, where a synthesis of OM catalysts bearing bidentate NHC ligands comprising either a barbituric heterocycle (axis A) or *N*-heterocyclic olefin (NHO) moiety (axis B) were attempted. Several ruthenium(II) complexes bearing the targeted NHC-barbiturate ligand were successfully synthetized. However, the planned subsequent installation of an alkylidene ligand proved particularly problematic and the corresponding OM catalyst could not be obtained. The reactivity with phenylacetylene was explored which resulted in the isolation of a ruthenium-NHC-barbiturate complex bearing a tetramerized phenylacetylene chelating ligand coordinated through an alkylidene and cyclopentadiene part. A mechanism was proposed for the formation of this unexpected complex, consisting of a formation of dicarbene intermediates rather than an expected vinylidene complex. In the next part, the synthesis of an NHC-NHO OM catalyst was attempted. A ligand precursor was obtained with the means of classical organic synthesis. However, the formation of the corresponding ruthenium-NHC complex was precluded due to an unexpected ring opening of the formed imidazolinylidene heterocycle. The reactivity of the novel class NHC-NHO ligand was explored in the coordination chemistry of rhodium(I) and palladium(II) metal centers, ultimately leading to the synthesis of the first NHC-NHO complex based on a palladium platform. Furthermore, the first rhodium-cyanomethyl complex supported by the NHC ligand was obtained.

The third chapter of the thesis is based on a second strategy for a more efficient catalyst. Presented here are advancements in the formation of tetrasubstituted carbon-carbon double bonds using OM. Considering that the anticipated, deleterious catalyst deactivation pathway requires the rotation of the *N*-aryl arm of the NHC ligand, a second decker of aromatic groups in benzimidazolylidene-based *N*-phenyl NHC ligands was introduced. This led to robust and highly efficient ruthenium OM catalysts in

challenging metathesis reactions of tri- and tetra-substituted olefins. The beneficial effect of these upper aromatic “wings” on the stability and activity of ruthenium complexes is rationalized through the experimental determination of the stereoelectronic properties of the NHC ligands, complemented by DFT calculations on the nature of the through-space interactions between the aromatics and on the decomposition pathway of precatalysts.

At last, the obtained catalytic systems were tested in the synthesis of bio-based polyesters and polyamides. To demonstrate the applicability of this study, a technical grade methyl oleate was used for the self-cross metathesis step. Such material derives from broadly available sunflower or rapeseed oil and contains a substantial amount (20 wt%) of methyl linoleate. The obtained dimethyl octadec-9-enedioate was used in a subsequent polycondensation with a co-monomer (diol or diamine), which resulted in the formation of polymeric materials.

The results presented in the doctoral dissertation led to the following publications: P. Krzesiński, V. César, K. Grela, S. Santos, P. Ortiz, Cross-metathesis of technical grade methyl oleate for the synthesis of bio-based polyesters and polyamides, *RSC Sustain.*, **2023**, Advance Article, DOI: 10.1039/d3su00305a and P. Krzesiński, C. Dinoi, I. D. Rosal, L. Vendier, S. Bastin, V. César, A. Kajetanowicz, K. Grela, Unhindered Biplane-Shaped N-Heterocyclic Carbene Ligands as a Remedy for Low Reactivity of Crowded Substrates in Ruthenium Catalyzed Olefin Metathesis, *ChemRxiv*, **2023**, Working Paper, DOI: 10.26434/chemrxiv-2023-b4btj (preprint).

Streszczenie

Bez wątpienia kataliza jest jednym z najistotniejszych narzędzi stosowanych w przemyśle chemicznym, pozwalającym uzyskać niezliczoną ilość czasami niedostępnych w inny sposób cząsteczek. Kataliza homogeniczna ma tę zaletę, że umożliwia bardziej precyzyjną charakteryzację katalizatorów i związków pośrednich, co czyni ją bardziej odpowiednią do racjonalnego projektowania. Ligandy pomocnicze odgrywają istotną rolę w określaniu aktywności, selektywności i stabilności otrzymanych katalizatorów. Pod tym względem ligandy NHC (karben *N*-heterocykliczny) wykazały szerokie zastosowanie jako ligandy, które mogą stabilizować katalityczne związki pośrednie. Prawdopodobnie największy wpływ ligandy NHC wywarły w dziedzinie metatezy olefin (MO), która to polega na redystrybucji szkieletu węglowego wokół nienasyconego wiązania podwójnego węgiel-węgiel. MO stała się narzędziem o wyjątkowym znaczeniu, zdobywając w ten sposób wysoką pozycję w zestawie narzędzi dostępnych w syntezie organicznej. Niniejsza rozprawa doktorska miała na celu zaprojektowanie ligandów NHC w celu uzyskania stabilniejszych i wydajniejszych katalizatorów MO. Dwie strategie zostały obrane mające na celu zwiększenie stabilności odpowiednich katalizatorów NHC MO.

Rozprawa jest podzielona na sześć rozdziałów. Pierwszy rozdział pracy opisuje aktualny stan wiedzy dotyczący badanego zagadnienia. W rozdziale drugim badano strategię na stabilny i wydajny katalizator Z-selektywny MO. Następnie w rozdziale trzecim opisano katalizatory zaprojektowane do wydajnego tworzenia czteropodstawionych wiązań podwójnych węgiel-węgiel. Ostatnia część pracy opisuje w rozdziale czwartym potencjalne zastosowanie otrzymanych układów katalitycznych. Pracę zamyka część eksperymentalna oraz bibliografia w rozdziałach piątym i szóstym.

W ramach pierwszej strategii na stabilniejszy katalizator podjęto próby otrzymania wydajnego Z-selektywnego katalizatora MO zawierającego chelatujący ligand NHC typu LX, poprzez zmianę liganda typu X w celu uzyskania stabilnego wiązania ruten-węgiel(sp^3). Cele badawcze podzielono na dwie osie, w których podjęto próby syntezy katalizatorów MO zawierających chelatujące ligandy NHC, zawierające jako ligand typu ugrupowanie barbituranowe (oś A) lub ugrupowanie *N*-heterocyklicznej olefiny (NHO) (oś B). Z powodzeniem zsyntetyzowano kilka kompleksów rutenu(II) zawierających docelowy ligand NHC-barbituranowy. Jednak planowana późniejsza instalacja ligandu alkilidenowego okazała się szczególnie problematyczna i nie udało się otrzymać odpowiedniego katalizatora MO. Zbadano reaktywność z fenyloacetylenem, co zaowocowało wyizolowaniem kompleksu rutenu z ligandem NHC-barbituran zawierającego także chelatujący ligand będący tetramerem fenyloacetylu skoordynowanym poprzez część alkilidenową i cyklopentadienową. Zaproponowano mechanizm powstawania tego nieoczekiwanej kompleksu uwzględniający powstawanie dikarbenowych produktów pośrednich w miejsce oczekiwanej kompleksu vinylidenowego. W kolejnej części podjęto próbę syntezy katalizatora NHC-NHO. Metodą klasycznej syntezy organicznej otrzymano prekursor liganda. Jednakże tworzenie odpowiedniego kompleksu NHC rutenu nie przebiegło pomyślnie ze względu na nieoczekiwane otwarcie pierścienia heterocyklicznego utworzonego imidazolinylidenu. Reaktywność nowej klasy ligandu NHC-NHO została zbadana w chemii koordynacyjnej centrów metalicznych rodu(I) i palladu(II), co ostatecznie doprowadziło do syntezy pierwszego kompleksu NHC-NHO na bazie palladu. Ponadto otrzymano pierwszy kompleks cyjanometylowy rodusza zawierający ligand NHC.

Trzeci rozdział pracy doktorskiej został oparty na innej strategii na bardziej stabilny i wydajny katalizator. Przedstawiono tutaj postępy w tworzeniu czteropodstawionych wiązań podwójnych węgiel-

węgiel przy użyciu OM. Biorąc pod uwagę, że przewidywana ścieżka rozpadu katalizatora wymaga rotacji podstawnika *N*-arylowego liganda NHC, wprowadzono drugą płaszczyznę grup aromatycznych w ligandach NHC opartych na *N*-fenylo benzimidazolylidenach. Zaowocowało to powstaniem wydajnych rutenowych katalizatorów w wymagających reakcjach metatezy trój- oraz czteropodstawionych olefin. Korzystny wpływ tych górnych „skrzydeł” aromatycznych na stabilność i aktywność kompleksów rutenu został wyjaśniony poprzez eksperymentalne określenie właściwości stereoelektronowych ligandów NHC, uzupełnione obliczeniami DFT na temat natury oddziaływań w między grupami aromatycznymi oraz na temat ścieżki rozkładu prekatalizatorów.

W ostatniej części pracy otrzymane układy katalityczne przetestowano w syntezie poliestrów i poliamidów biologicznego pochodzenia. Aby zademonstrować potencjał aplikacyjny tego badania, do etapu metatezy krzyżowej zastosowano techniczny oleinian metylu. Taki materiał pochodzi z powszechnie dostępnego oleju słonecznikowego lub rzepakowego i zawiera znaczną ilość (20% wagowych) linoleinianu metylu. Otrzymany oktadek-9-enodian dimetylu poddano późniejszej polikondensacji z komonumerem (diolem lub diaminą), w wyniku której powstały materiały polimerowe.

Wyniki przedstawione w rozprawie doktorskiej zaowocowały następującymi publikacjami: „P. Krzesiński, V. César, K. Grela, S. Santos, P. Ortiz, Cross-metathesis of technical grade methyl oleate for the synthesis of bio-based polyesters and polyamides, *RSC Sustain.*, **2023**, Advance Article, DOI: 10.1039/d3su00305a” oraz „P. Krzesiński, C. Dinoi, I. D. Rosal, L. Vendier, S. Bastin, V. César, A. Kajetanowicz, K. Grela, Unhindered Biplane-Shaped N-Heterocyclic Carbene Ligands as a Remedy for Low Reactivity of Crowded Substrates in Ruthenium Catalyzed Olefin Metathesis, *ChemRxiv*, **2023**, Working Paper, DOI: 10.26434/chemrxiv-2023-b4btj” (preprint).

Résumé

Introduction

La catalyse est sans aucun doute l'un des outils les plus pertinents utilisés dans l'industrie chimique, permettant d'obtenir une myriade de molécules parfois inaccessibles autrement. La catalyse homogène présente l'avantage d'une caractérisation plus précise des catalyseurs et des intermédiaires, ce qui la rend plus adaptée à une conception rationnelle. Les ligands auxiliaires du catalyseur jouent un rôle important dans la définition de l'activité, de la sélectivité et de la stabilité des catalyseurs résultants.

Presque toutes les réactions chimiques consistent en une série d'étapes élémentaires, définies comme une transformation directe de molécules réactives en produits via un seul état de transition. Une telle séquence d'étapes élémentaires est appelée mécanisme réactionnel et lorsqu'elle décrit des formes de catalyseur, elle est appelée cycle catalytique. Un pré-catalyseur est un composé stable utilisé pour générer le catalyseur actif *in situ* par un processus d'activation. Une espèce hors boucle est définie comme un complexe en équilibre avec un intermédiaire catalytique mais lui-même non impliqué dans le cycle catalytique. Enfin, lorsque la formation d'une espèce hors boucle est irréversible, la désactivation du catalyseur a lieu et le composé formé est appelé catalyseur mort ou désactivé.

Les carbènes *N*-hétérocycliques (NHC) sont des espèces de carbone divalent neutre ayant six électrons de valence compris dans un cycle contenant au moins un atome d'azote adjacent. Les atomes d'azote sont à la fois attracteurs inductifs et mésomères donneurs. En conséquence, les NHC sont des carbènes singulets. L'un des avantages les plus significatifs des NHC est leur modularité de synthèse relativement simple qui permet d'ajuster les propriétés stériques et électroniques du ligand. La capacité globale des ligands NHC à donner des électrons peut être quantifiée en enregistrant la fréquence moyenne des vibrations d'elongation des ligands carbonyle dans des complexes de nickel, de rhodium ou d'iridium. Les propriétés donneuses σ peuvent être évaluées en mesurant la constante de couplage $^1J(\text{C}-\text{H})$ entre les atomes de carbone et d'hydrogène en position pré-carbénique dans les précurseurs d'azolium. De plus, les propriétés π -acceptrices des NHC peuvent être déterminées indépendamment en enregistrant le déplacement chimique des noyaux de ^{77}Se dans les adduits sélénocorrespondants.

La métathèse des oléfines (MO) est une redistribution du squelette carboné autour d'une double liaison carbone-carbone insaturée via sa scission puis sa régénération. La réaction est catalysée par un complexe de métal de transition. En ce qui concerne les catalyseurs de MO à base de ruthénium, l'impact des ligands NHC dans ce domaine a été sans doute bien plus important par rapport à d'autres domaines de la catalyse de métaux de transition. En 2005, Chauvin, Grubbs et Schrock ont reçu le prix Nobel de chimie pour le développement de la méthode de métathèse en synthèse organique. Malgré les progrès incroyables réalisés dans la discipline, de nombreux obstacles restent encore à surmonter, comme *i*) la stéréosélectivité des réactions ou *ii*) la formation de doubles liaisons carbone-carbone tétrasubstituées. C'est à ces deux problématiques que nous nous sommes intéressés pendant la thèse.

Objectifs de la thèse

Les travaux décrits ici visaient à concevoir des ligands NHC afin d'obtenir des catalyseurs MO plus stables, durables et donc plus efficaces et répondre aux deux problématiques mentionnées précédemment. Deux stratégies ont été étudiées pour améliorer la stabilité des catalyseurs de MO à base de NHCs correspondants.

Le premier objectif vise à développer un catalyseur de MO à sélectivité Z portant un ligand NHC chélateur de type LX en s'appuyant sur la solution présentée par Grubbs et ses collègues (**Ru-21**, Schéma 1). La plus grande faiblesse de ces complexes provient de la présence d'une liaison ruthénium-alkyle qui les rend sujets à des voies de décomposition impliquant l'insertion d'un ligand alkylidène dans une liaison ruthénium-alkyle. Ce travail visait à obtenir un catalyseur MO porteur de NHCs chélatisant présentant une liaison ruthénium-carbone (sp^3) plus stable. Nous avons envisagé que le remplacement du groupe alkyle (adamantyle) par un ligand carboné de type X plus stable stabiliserait les complexes chélatisés. Avec ces objectifs à l'esprit, nous avons étudié la synthèse de ligands NHC bidentes comprenant soit un hétérocycle barbiturique (axe A), soit un fragment oléfine *N*-hétérocyclique (NHO) (axe B).

Le NHC imidazo[1,5-*a*]pyridin-3-ylidène contenant un hétérocycle barbiturique a été choisi car il s'est avéré être une plateforme polyvalente pour les centres métalliques d^6 [Ru(II), Mn(I)] et d^8 [Pd(II), Rh(I), Ir(I), Au(III)], donnant accès à des complexes stables. L'architecture du ligand NHC-NHO constitue quant à elle une approche totalement nouvelle et donc aussi intéressante du point de vue de la science fondamentale que de l'application. De plus, le domaine des ligands NHO est beaucoup moins exploré que celui des NHCs et les exemples de complexes métalliques NHO bien définis restent plutôt rares dans la littérature.

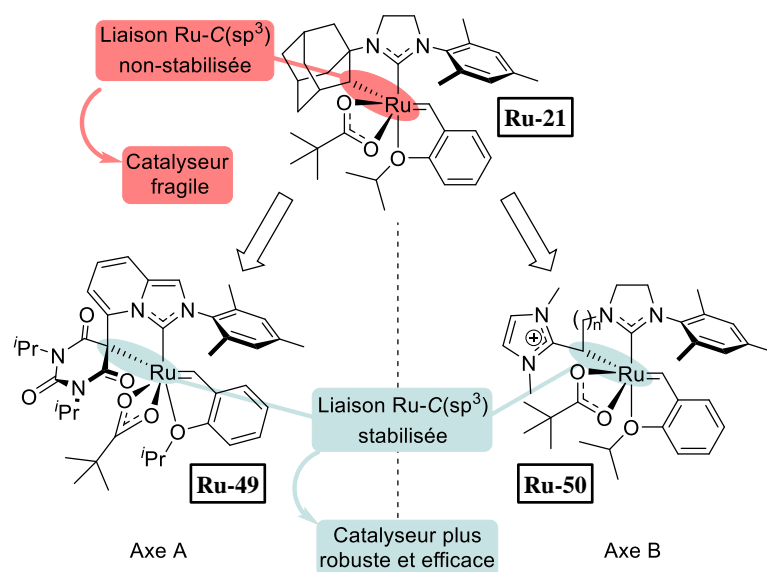


Schéma 1 Le concept d'un catalyseur OM robuste sélectif Z.

Le deuxième objectif visait des catalyseurs robustes et efficaces pour la formation de doubles liaisons carbone-carbone tétrasubstituées (**Ru-67**, Schéma 2). L'approche couramment utilisée est basée sur des catalyseurs spécialisés au ruthénium avec des ligands NHC faiblement encombrés, capables de s'adapter à des substrats oléfiniques plus encombrés pendant les étapes catalytiques. Pourtant, bien qu'étant très actifs, ces complexes sont plutôt instables, principalement en raison de l'activation intramoléculaire C–H en position *ortho* d'un groupe *N*-aryle du ligand NHC, conduisant à la désactivation du catalyseur. Considérant que le processus d'activation de C–H est délétère et nécessite la rotation du bras *N*-aryle du ligand NHC, nous avons estimé que l'introduction de substituants aromatiques supplémentaires sur le squelette arrière ie sur le groupe phényle des ligands benzimidazolylidène substitués par des groupements phényl sur les atomes d'azote améliorerait la stabilité et l'efficacité des catalyseurs correspondant, tout en maintenant leur activité en métathèse de liaisons stériquement encombrées. Nous voulions

également explorer si les interactions π - π contribueraient à bloquer la rotation. À ces fins, on a tenté d'installer des groupes phényles dans le squelette (**Ru-68**) puisque la synthèse devrait être réalisable, mais également des groupes pentafluorophényles (**Ru-69**) afin de générer des interactions π - π plus fortes.

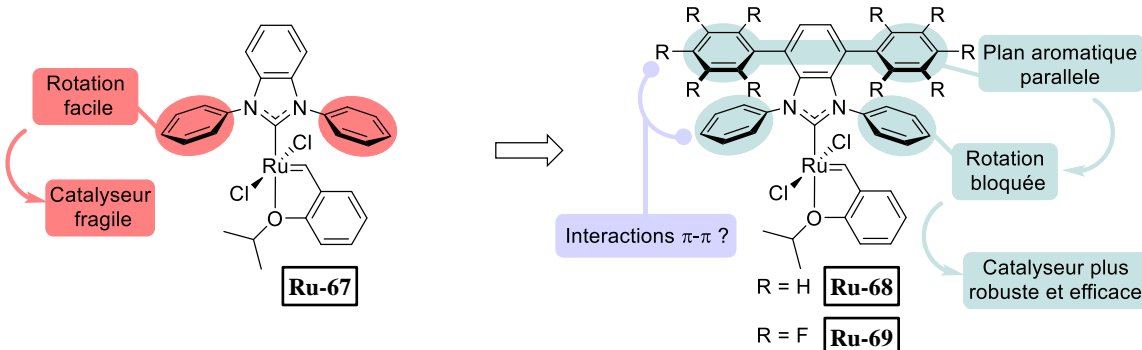


Schéma 2 Le concept d'un catalyseur OM robuste pour la formation de doubles liaisons carbone-carbone tétrasubstituées.

La dernière partie du travail décrit une application potentielle des systèmes catalytiques obtenus dans la synthèse de polyesters et polyamides biosourcés (Schéma 3). Pour démontrer l'applicabilité de cette étude, un oléate de méthyle (**29**) de qualité technique a été utilisé comme matière première pour l'étape de self-métathèse croisée. Ce substrat provient d'huile de tournesol ou de colza largement disponible et contient une quantité substantielle (20 % en poids) de linoléate de méthyle (**94**), qui est l'ester méthylique d'acide gras polyinsaturé (FAME) le plus abondant. Le produit de la réaction, l'octadéc-9-ènedioate de diméthyle (**29**), a été utilisé dans une réaction de polycondensation ultérieure pour obtenir des matériaux polymères. Dans cette recherche, nous avons utilisé des catalyseurs disponibles dans le commerce **Ru-10**, **Ru-18**, **Ru-17**, **Ru-71** et les catalyseurs **Ru-68**, **Ru-69** développés dans la partie précédente.

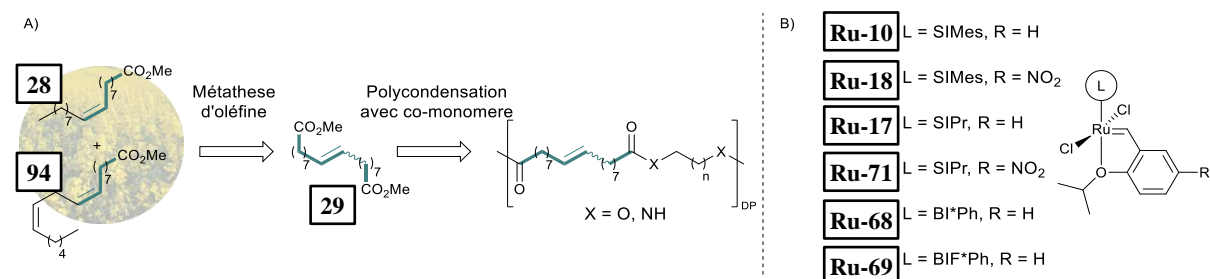


Schéma 3 A) Procédé proposé de synthèse de polyesters et de polyamides biosourcés par self-CM d'oléate de méthyle de qualité technique (**28**) et réaction de polycondensation ultérieure. B) Catalyseurs utilisés dans l'étude.

Complexes de ruthénium supportés par un ligand chélateur NHC comprenant un hétérocycle barbiturique

Dans ce projet, le complexe **Ru-54** a été étudié en tant que précurseur métallique puisque ses ligands méthallyle pouvaient servir de base interne pour déprotoner le précurseur de NHC imidazopyridinium **31** pour former un complexe ruthénium-NHC. La réaction du complexe **Ru-54** avec deux équivalents du précurseur **31** a conduit à la formation du complexe stable **Ru-56** avec un rendement isolé de 30 % (Schéma 4). En effet, le fragment méthallyle de **Ru-54** a servi de base interne pour déprotoner la position imidazopyridinium de **31** et former le complexe ruthénium-NHC souhaité. Cependant, la réaction ne s'est pas arrêtée après la première étape de protonolyse et le deuxième groupe méthallyle a été utilisé pour la cyclométallation du groupe méthyle en position *ortho* du substituant *N*-mésityle. Étonnamment,

le ligand cyclooctadiène (COD) a été remplacé par une deuxième molécule de précurseur d'imidazopyridinium **31** afin de compléter la sphère de coordination du centre métallique. Fait intéressant, on a observé une coordination η^3 de la partie carbone-carbone-oxygène du malonate pour donner le complexe à 18e⁻ **Ru-56**. Dans les publications précédentes de l'équipe, seul le mode de coordination η^1 du carbone malonate a été observé dans les sept complexes décrits.

Dans l'étape suivante, nous avons tenté de cliver la liaison ruthénium-mésityle à l'aide d'acide pivalique. En effet, la réaction a donné le complexe **Ru-57** avec un groupe *N*-mésityle libre, et s'est accompagnée d'un changement de mode de coordination de l'hétérocycle barbiturique qui est devenu η^1 . Il est intéressant de noter que lorsque l'acide pivalique a été ajouté en présence de PPh₃, cela a abouti à un complexe **Ru-58** avec un hétérocycle barbiturique coordonné selon un mode η^3 . De plus, on observe une coordination du ligand PPh₃ en *cis* par rapport au NHC du fait de l'encombrement stérique imposé par l'hétérocycle barbiturique.

Enfin, nous avons tenté l'installation du ligand pyridine dans l'espoir d'avoir une fonctionnalité labile adaptée à l'introduction d'un ligand alkylidène. En effet, la réaction de **Ru-57** avec la pyridine anhydre a donné le complexe **Ru-59** avec deux ligands pyridine coordonnés, cependant, la structure cristalline de **Ru-59** a également révélé une molécule d'eau coordonnée. Etant donné qu'un réactif anhydre a été utilisé pour cette réaction, il est très probable que l'eau ait été introduite pendant le traitement de la réaction. Les quatre nouveaux complexes ont été caractérisés par spectroscopie de résonance magnétique nucléaire (RMN) et diffraction des rayons X (DRX).

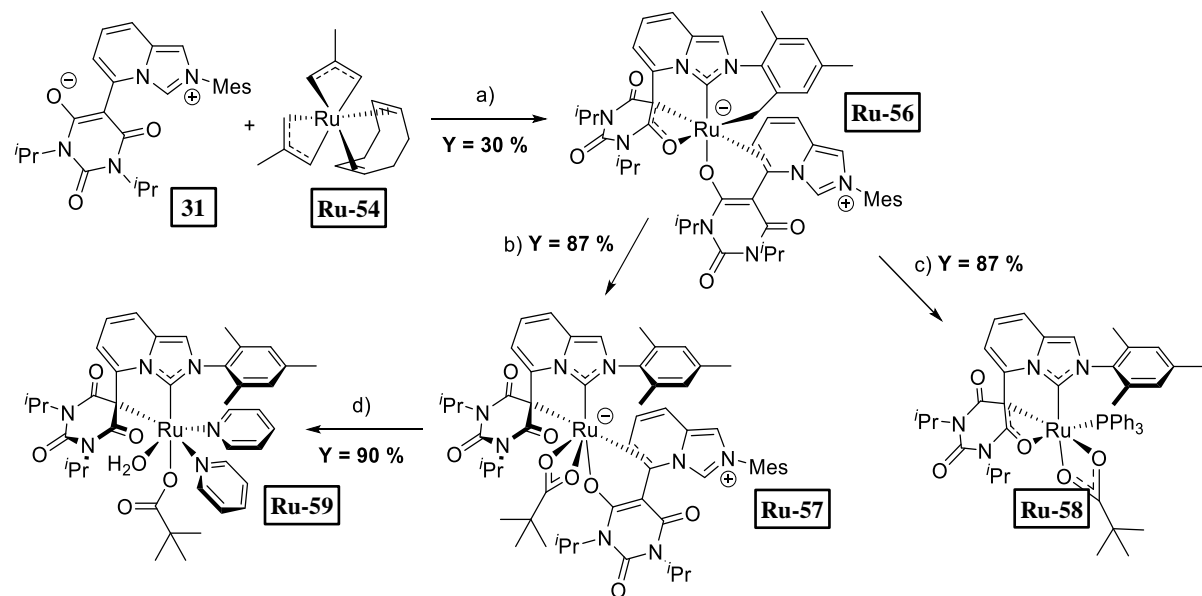


Schéma 4 Synthèse de complexes de ruthénium **Ru-56-Ru-59** portant le ligand chélateur NHC. Conditions de réaction : a) 2 équiv. de **31**, 1 équiv. de **Ru-54**, THF, 90 °C, 2 h ; b) 2,2 équiv. $^t\text{BuCO}_2\text{H}$, THF, 80 °C, 15 h ; c) 1,2 équiv. PPh₃, 1,2 équiv. $^t\text{BuCO}_2\text{H}$, DCE, 80 °C, 6 h ; d) pyridine sèche (excès), 80 °C, 2 h.

Avec la petite bibliothèque de complexes de ruthénium portant le ligand NHC ciblé, l'installation d'un ligand alkylidène a été tentée. Tout d'abord, la réaction des complexes **Ru-57-Ru-59** avec le dérivé diazométhane **34** a été tentée, cependant, aucune réactivité n'a été observée, les complexes de départ restant inchangés (Schéma 5A). Même le très prometteur dérivé de la pyridine **Ru-59** n'a présenté aucune réactivité avec **34**. Nous avons ensuite tenté une réaction avec l'alcool propargylique **18** à 80 °C. Cette fois, une réactivité des complexes de départ a été observée, cependant aucun produit n'a pu être

isolé et caractérisé car un mélange complexe d'espèces non identifiées est obtenu. Enfin, nous avons porté notre attention sur le phénylacétène (**19**) comme précurseur de l'alkylidène. Un schéma de réactivité assez similaire à celui de la réaction avec **18** a été observé dans le sens où un mélange de produits s'est formé. Cependant, cette fois, il a été possible d'isoler le produit majoritaire **Ru-60** issu de la réaction de **Ru-57** avec **19** (Schéma 5B). En effet, **Ru-60** contenait une fonctionnalité alkylidène dans sa structure, cependant, une tétramérisation inattendue du phénylacétène s'est produite pour former une unité cyclopentadiényle. Cette dernière s'est coordonnée selon un mode η^5 en remplacement de l'anion pivalate donnant le complexe de type tabouret de piano **Ru-60** dont la structure a été confirmée par DRX.

En résumé, plusieurs complexes de ruthénium portant le ligand chélateur NHC-barbiturique ont été synthétisés avec succès. En fonction de la nature des autres ligands présents dans la structure, il a été constaté que le NHC dérivé du barbiturique peut s'adapter de manière flexible entre le mode de coordination η^1 via le carbone malonate et η^3 via la partie carbone-carbone-oxygène du malonate afin de stabiliser la sphère de coordination. De plus, le ligand NHC-barbiturique peut même adopter un mode de coordination tétradenté lorsque la position benzylique du substituant *N*-mésityl est cyclométallée (structure **Ru-56**).

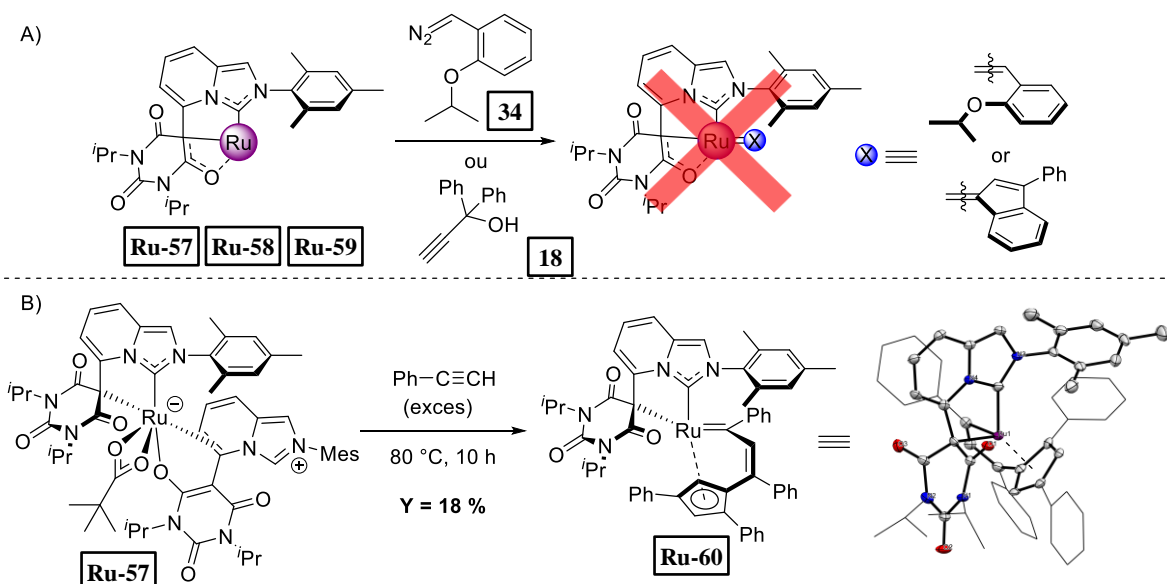


Schéma 5 Tentatives de réaction des complexes **Ru-57**-**Ru-59** avec soit le dérivé diazométhane **34**, soit le dérivé alcool propargylique **18**. B) Réaction du complexe **Ru-57** avec le phénylacétène.

Il a été possible d'installer un ligand alkylidène sur un complexe de ruthénium portant le ligand chélatant NHC-barbiturique, cependant, une tétramérisation inattendue du phénylacétène s'est produite conduisant à la formation d'un co-ligand cyclopentadiényle (complexe **Ru-60**). Il est possible que l'isolement du complexe **Ru-60** résulte de la formation préférentielle d'espèces dicarbène de ruthénium plutôt que du complexe vinylidène attendu.

Architecture du ligand NHC-NHO

Ce projet a débuté par la synthèse du précurseur du ligand NHC-NHO **48** porteur de pré-fonctionnalités NHC et NHO reliées via deux unités CH_2 (Schéma 6). À partir de l'iodure de diméthylimidazolium (**45**), le diméthylimidazolylidene IMe correspondant a été formé par déprotonation avec l'hexaméthyldisilazide de lithium (LiHMDS) qui, ensuite, dans une réaction de substitution nucléophile avec du 1,3-dibromopropane (**46**) suivie d'une réaction de Finkelstein, a donné le composé **47** attendu. Le pré-ligand

48 a été obtenu par une réaction de substitution nucléophile de la *N*-mésitylimidazoline sur le composé **47**. La structure de **48** a été confirmée par DXR (Schéma 6).

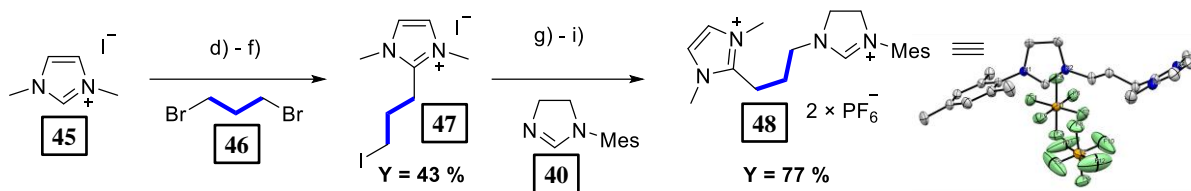


Schéma 6 La synthèse du précurseur **48** du ligand NHC-NHO et sa structure DXR (les ellipsoïdes sont dessinés avec une probabilité de 50 %, les hydrogènes ont été omis pour plus de clarté) ; conditions de réaction : d) 1,05 équiv. de LiHMDS, THF, ta, 80 min ; e) 20 équiv. de **46**, -80 °C à température ambiante, pendant la nuit. f) 5 équiv. de NaI, acétone, ta, pendant la nuit ; g) 1,3 équiv. de **40**, MeCN, 90 °C, pendant la nuit ; h) 3,4 équiv. de AgCl, eau, température ambiante, 30 min ; i) 5,6 équiv. de KPF₆, DCM, 40 °C, 7 jours.

Avec le précurseur **48** du ligand NHC-NHO en main, la synthèse du catalyseur de MO NHC-ruthénium correspondant (**Ru-66**, Schéma 7A) a été tentée. Dans cette approche, le remplacement couramment utilisé du ligand PCy₃ dans la structure de **Ru-9** par le ligand NHC a été étudié. Cependant, le complexe **Ru-66** n'a pas pu être obtenu de cette manière. Nous avons décidé à ce stade de délaisser les tentatives de synthèse des catalyseurs NHC au ruthénium et de nous concentrer sur une étude générale de la nouvelle architecture de type ligand NHC-NHO.

Pour mieux comprendre pourquoi le complexe **Ru-66** ne s'est pas formé, des études de réactivité du NHC-NHO ont été réalisées. Nous avons constaté qu'une fois la position imidazolinium de **48** déproto-née, le NHC **51** formé peut subir deux réactions concurrentes (Schéma 7B). **51** peut soit former le complexe souhaité avec l'électrophile (**52**), soit le cycle imidazolinylidène peut s'ouvrir, ce qui, après traitement réactionnel, donne le produit **50** *N*-formylé (produit observé par MS et RMN). Il est alors devenu clair pourquoi la synthèse du complexe ruthénium-NHC **Ru-66** avait échoué. La barrière énergétique du remplacement de PCy₃ par un NHC dans la structure de **Ru-9** est généralement relativement élevée car un chauffage est nécessaire. Par conséquent, la formation du produit secondaire **50** est plutôt préférée.

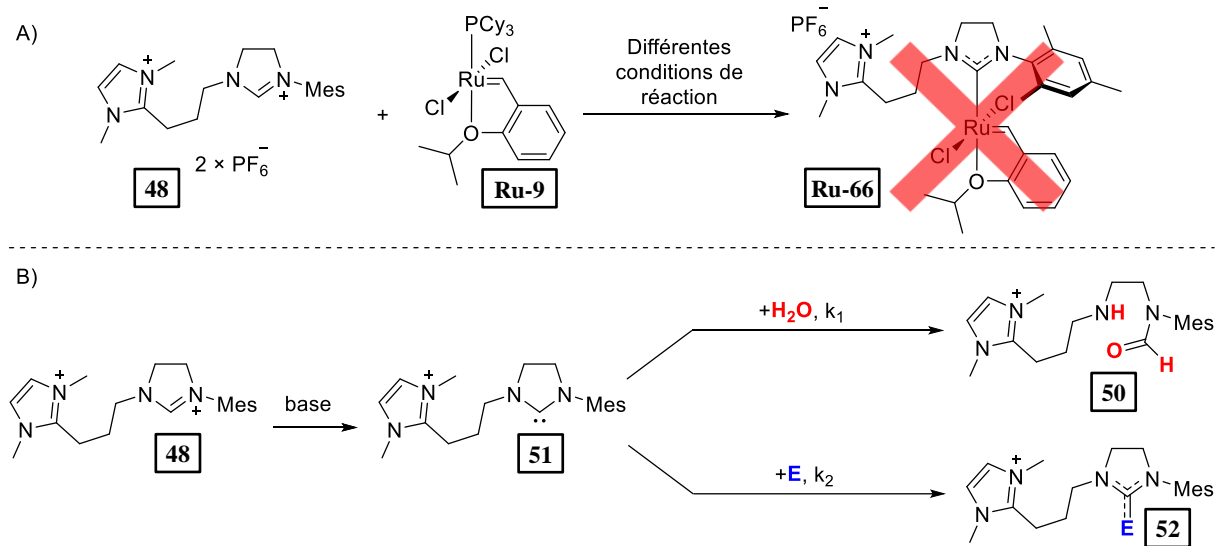


Schéma 7 A) Tentative de synthèse de **Ru-66**. B) Explication proposée pour la réactivité observée du carbène **51**.

Connaissant le modèle de réactivité de notre ligand, nous avons entrepris de synthétiser un complexe métallique portant le NHC cible et avons ensuite tenté la coordination du fragment NHO. Nous avons émis l'hypothèse qu'un précurseur métallique dimérique pourrait être suffisamment réactif pour donner un complexe métal-NHC avec un bon rendement. Le centre métallique rhodium (**I**) a été choisi car le complexe NHC correspondant serait a priori stable à l'air, isolable par chromatographie sur colonne (CC) et, après installation de ligands CO, permettrait de mesurer les propriétés électroniques du ligand (TEP). En effet, l'utilisation du dimère de rhodium **Rh-1** comme précurseur métallique s'est avérée être une bonne stratégie et a donné le complexe rhodium-NHC **Rh-2** isolé par CC avec un rendement de 73 % (Schéma 8A). La structure de **Rh-2** a été confirmée par DRX (Schéma 8B).

Dans l'étape suivante, la déprotonation de la position α -imidazolium a été tentée dans l'espoir de former le complexe NHO correspondant. Lorsque la réaction est réalisée dans le THF, quelle que soit la réactivité du complexe **Rh-2** observée, aucun complexe rhodium-NHC-NHO **Rh-3** n'a pu être isolé. Très probablement, un ligand alcoolate a remplacé le chlorure. Pour des raisons que nous n'avons pas pu expliquer, le complexe **Rh-3** souhaité ne s'est pas formé. Il est intéressant de noter que lorsque la même réaction a été tentée dans l'acetonitrile, un ligand cyanométhyle provenant de la déprotonation de l'acetonitrile a remplacé le chlorure pour donner le complexe **Rh-4**. Ce dernier est plutôt instable à l'air ou en solution, il a cependant pu être caractérisé par RMN et DRX (Schéma 8B). À notre connaissance, aucun complexe cyanométhylrhodium n'a été rapporté jusqu'à présent.

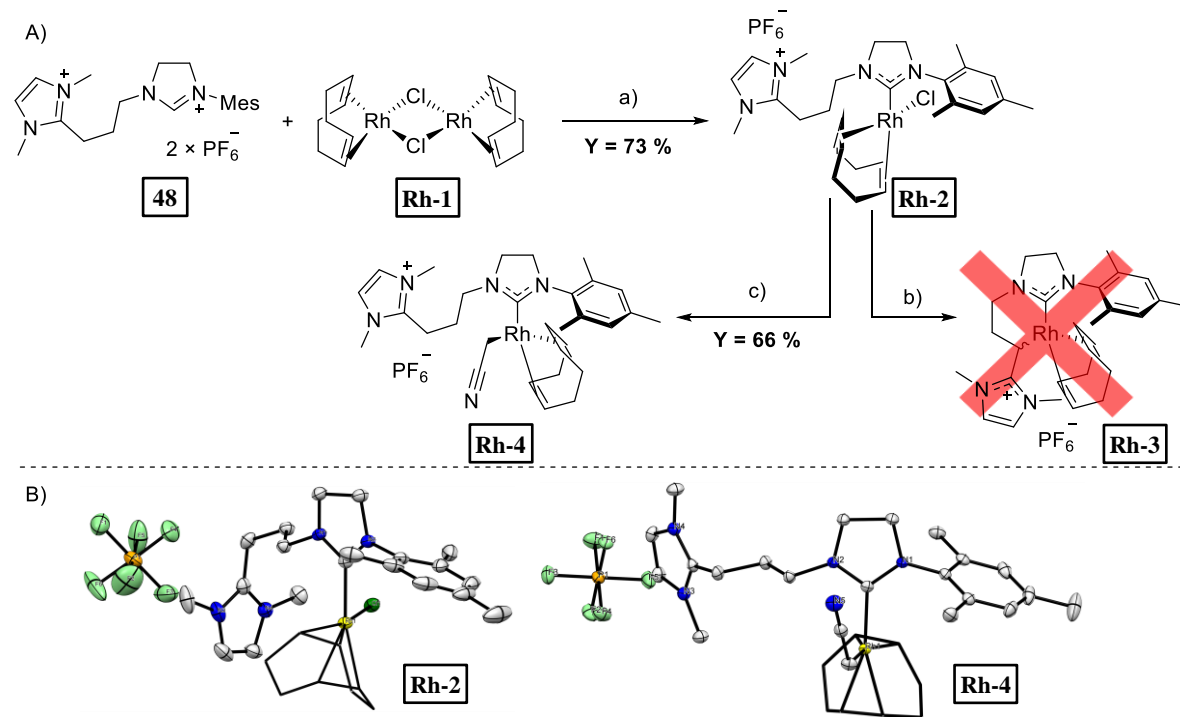


Schéma 8 A) Synthèse du complexe rhodium-NHC **Rh-2**, du complexe rhodium-NHC-cyanométhyle **Rh-4** et tentatives de synthèse du complexe rhodium-NHC-NHO **Rh-3**; conditions de réaction : a) 0,5 équiv. de **Rh-1**, 1,1 équiv. K_2CO_3 , acétone (HPLC), 60 °C, toute la nuit ; b) 1,1 équiv. KO^+Bu , THF, rt; c) 1,1 équiv. KO^+Bu , acetonitrile, rt, 4 h. B) Structures cristallines DRX de **Rh-2** et **Rh-4**, les ellipsoïdes sont dessinés avec une probabilité de 50 %, les hydrogènes ont été omis pour plus de clarté.

Face aux obstacles rencontrés lors de la réaction de cyclométallation du complexe de rhodium, nous nous sommes tournés ensuite vers le palladium dans l'espoir d'obtenir un complexe palladium-NHC-NHO. De la même manière que dans le cas de **Rh-1**, l'utilisation d'un précurseur dimère de palladium

Pd-1 a donné le complexe palladium-NHC **Pd-2** souhaité avec un bon rendement de 71 %. De plus, la déprotonation de la position α -imidazolium dans le complexe **Pd-2** **Pd-2** a donné le complexe palladium-NHC-NHO **Pd-3** cyclométallé attendu avec un rendement de 64% sous forme de deux diastéréomères dans un ratio de 60 :40. La structure de **Pd-3** a été confirmée par DRX (Schéma 9).

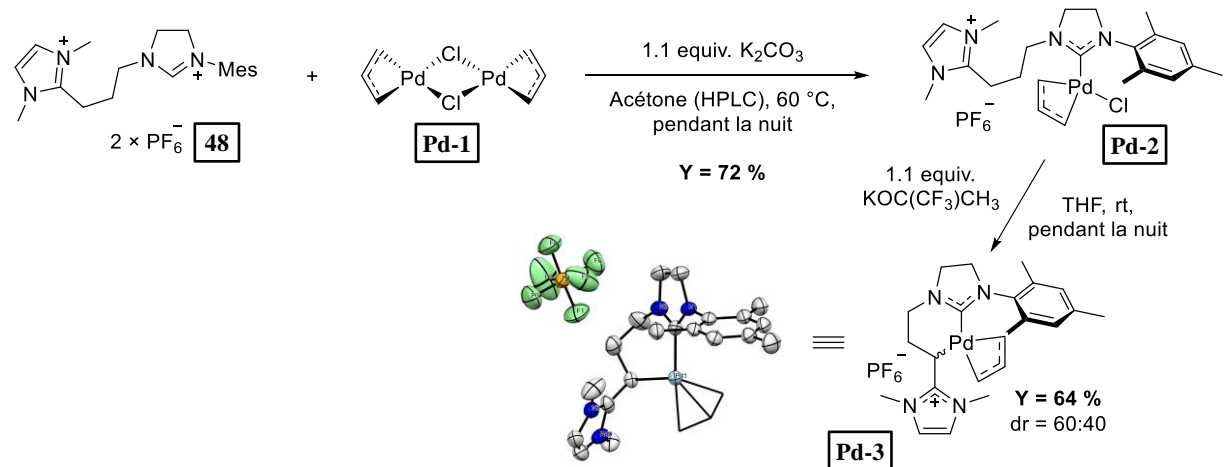


Schéma 9 Synthèse du complexe palladium-NHC-NHO **Pd-3** et de sa structure cristalline DRX (les ellipsoïdes sont dessinés avec une probabilité de 30 %, les hydrogènes ont été omis pour plus de clarté).

En résumé, un précurseur **48** du ligand NHC-NHO a été obtenu avec succès. Cependant, la formation du complexe ruthénium-NHC correspondant a été empêchée en raison d'une ouverture inattendue de l'hétérocycle imidazolinylidène formé. La réactivité du nouveau ligand NHC-NHO a été explorée dans en chimie de coordination des centres métalliques du rhodium (I) et du palladium (II), conduisant finalement à la synthèse du premier complexe NHC-NHO à base de palladium. De plus, le premier complexe rhodium-cyanométhyle supporté par le ligand NHC a été obtenu.

Ligands NHC de type biplan portant un double étage de cycles aromatiques pour des catalyseurs de MO efficaces pour la formation de doubles liaisons C-C tétrasubstituées

Le 4,7-dibromo-2,1,3-benzothiadiazole (**62**) disponible dans le commerce a été choisi comme précurseur des sels de benzimidazolium substitués par des groupes phényle et pentafluorophényle **67** et **71** (Schéma 10). Le couplage de type Suzuki a permis l'installation de groupes phényles pour donner le benzothiadiazole **63** fonctionnalisé avec un rendement de 73 % et une extrusion réductrice ultérieure du soufre a donné accès au dérivé o-phénylenediamine **64** avec un rendement de 99 %. Ensuite, le squelette bicyclique du benzimidazole a été obtenu en utilisant un protocole de cyclisation standard avec de l'orthoformiate de triéthyle, donnant **65** avec un rendement quantitatif. Les produits **63**, **64** et **65** ont été obtenus à l'échelle du gramme sans aucune étape de purification par CC. Dans l'étape finale, le sel de benzimidazolium **67** souhaité a été obtenu par arylation catalysée par le cuivre avec du tétrafluoroborate de diphenyliodonium. Bien que des exemples d'arylation d'imidazoles N-R pour donner les sels d'imidazolium correspondants puissent être trouvés dans la littérature, ainsi que des arylations d'imidazoles NH conduisant aux imidazoles N-aryl correspondants, il convient de souligner qu'une telle arylation directe de NH imidazole en sel d'imidazolium n'a jamais été rapportée dans la littérature. Ce protocole a donné un mélange du sel **67** de *N,N'*-diphenylbenzimidazolium souhaité (rendement isolé de 36 %) et du *N*-phénylbenzimidazole **66** neutre (rendement isolé de 58 %) qui ont été séparés par CC. L'arylation additionnelle réalisée sur le composé **66** précédemment isolé a donné le sel **67** avec un rendement de

77 %, donc les deux réactions d'arylation successives conduisent à un rendement global de 81 % en composé **67**.

La synthèse du dérivé **71** substitué par le pentafluorophényle présentait davantage de défis de synthèse. Un couplage de type Kumada-Corriu a été utilisé avec succès pour greffer les groupes pentafluorophényles sur le motif benzothiadiazole donnant **68** avec un rendement de 76 %. L'étape ultérieure d'extrusion réductrice de soufre a donné le dérivé d'*o*-phénylenediamine **69** avec un rendement de 72 %. Contrairement à la synthèse du sel **67**, les groupes *N*-phényle ont d'abord été installés par amination de Buchwald-Hartwig, donnant le composé **70** avec un rendement isolé de 21 %. Dans une étape finale, le sel de benzimidazolium **71** a été obtenu avec un rendement quantitatif en utilisant un protocole de cyclisation modifié utilisant de l'orthoformiate de triéthyle en présence de $\text{HBF}_4 \cdot \text{Et}_2\text{O}$.

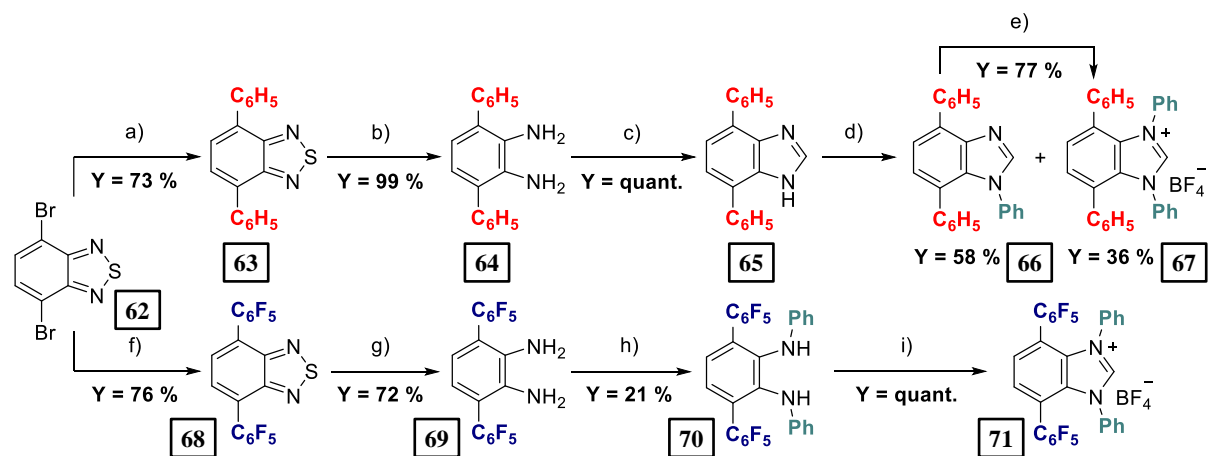


Schéma 10 Synthèse des sels de benzimidazolium **67** et **71** ; conditions de réaction : a) 2,1 équiv. de $\text{PhB}(\text{OH})_2$, 4 équiv. de K_2CO_3 , 0,8 mol% $\text{Pd}(\text{PPh}_3)_4$, toluène/eau 2,5 : 1 v/v, reflux, toute une nuit ; b) 9 équiv. de NaBH_4 , 6 mol% de $\text{CoCl}_2 \times 6\text{H}_2\text{O}$, EtOH/THF 3:1 v/v, reflux, 3 h ; c) $(\text{EtO})_3\text{CH}$ (excès), 6 équiv. de HCl_{aq} , reflux, pendant la nuit ; d) 2 x 2 équiv. de Ph_2IBF_4 , 2 × 5 mol% de $\text{Cu}(\text{OAc})_2 \times \text{H}_2\text{O}$, DMF, 100 °C, 24 h, puis 48 h ; e) 2 équiv. de Ph_2IBF_4 , 7,5 mol% de $\text{Cu}(\text{OAc})_2 \times \text{H}_2\text{O}$, DMF, 100 °C, pendant une nuit ; f) 3 équiv. de BrMgC_6F_5 , 10 mol% de $\text{Pd}(\text{PPh}_3)_3$, THF, 70 °C, pendant la nuit ; g) 3 équiv. de NaBH_4 , 7 mol% de $\text{CoCl}_2 \times 6\text{H}_2\text{O}$, EtOH/THF 3 : 1 v/v, 50 °C, 1 min. 30 secondes ; h) PhBr (excès), 2,5 mol% $\text{Pd}(\text{dba})_3$, 7,5 mol% $\text{P}'\text{Bu}_3$, 1,5 équiv. de KHMDS, 160 °C, 30 min. ; i) $(\text{EtO})_3\text{CH}$ (excès), 1 équiv. de $\text{HBF}_4 \cdot \text{Et}_2\text{O}$, 60 °C, 30 min.

Les complexes Hoveyda-Grubbs correspondants ont été obtenus par déplacement du ligand PCy_3 dans le précurseur de ruthénium **Ru-9** par les NHC libres générés en utilisant $\text{KOC}(\text{CF}_3)_2\text{CH}_3$ comme base (Schéma 11A). Le complexe **Ru-68** a été isolé par chromatographie sur colonne, tandis que le complexe **Ru-69** a été purifié par simple cristallisation à partir d'un mélange THF-pentane. Les deux complexes (solides brun-orange) sont stables pendant des mois lorsqu'ils sont stockés sous atmosphère protectrice. Il est à noter que lors de la synthèse du complexe **Ru-67** connu, nous avons remarqué sa fragilité lorsque la chromatographie sur colonne était réalisée avec des solvants ordinaires. Même avec des solvants secs soigneusement dégazés, le complexe **Ru-67** a été obtenu avec un rendement de 19 % seulement, ce qui est considérablement inférieur à celui de **Ru-68** et **Ru-69**, respectivement de 72 % et 43 %. Les structures moléculaires des complexes **Ru-68** et **Ru-69** ont été confirmées par des expériences DRX sur monocristaux obtenus par superposition de pentane sur des solutions de complexes **Ru-68** et **Ru-69** dans le DCM, respectivement (Schéma 11B).

Une caractérisation approfondie des propriétés électroniques des trois ligands a ensuite été réalisée (Schéma 11 et Tableau 1). Les abréviations des noms des nouveaux NHC répertoriés sur le Schéma 11A sont désormais utilisées. La propriété de donation d'électrons globale des ligands NHC a d'abord été quantifiée en enregistrant la fréquence d'elongation moyenne ($\nu_{\text{CO}}^{\text{av}}$) des ligands carbonyles dans les

complexes **Rh-10-Rh-12**, qui est corrélée à la valeur TEP du ligand par une corrélation linéaire. De plus, les capacités de donation σ et d'acceptation π des NHC ont été évaluées indépendamment en mesurant la constante de couplage $^1J(C-H)$ entre les atomes de carbone et d'hydrogène sur la position pré-carbénique dans les précurseurs d'azolium et en enregistrant le déplacement chimique des noyaux ^{77}Se dans les adduits séléno **Se-1-Se-3**, respectivement. De plus, les paramètres électroniques du congénère IMes à base d'imidazole ont été reproduits et comparés aux valeurs précédemment rapportées dans la littérature. Les données expérimentales ont montré que les trois NHC à base de benzimidazole sont moins donneurs que les IMes et donnent moins ou de la même manière que les SIMes lorsque l'on considère la donation électronique global. Au sein de la série des benzimidazolylidènes, la présence des deux groupes phényles distaux dans BI*Ph a légèrement augmenté sa donation σ mais également son acidité π par rapport au BIPh non substitué, conduisant à une donation électronique global légèrement plus fort avec une valeur TEP de $2052,2\text{ cm}^{-1}$. En revanche, la perfluoruration des cycles aryles du second pont a induit une diminution notable de la donation électronique avec une valeur de TEP allant de $2052,2\text{ cm}^{-1}$ pour BI*Ph à $2056,2\text{ cm}^{-1}$ pour BIF*Ph, comme on pouvait s'y attendre compte tenu du fort effet attracteur d'électrons des atomes de fluor. Globalement, à partir du BIPh non substitué, l'installation de la deuxième couche aryle à l'arrière du noyau benzimidazolyle génère le ligand BI*Ph le plus donneur d'électrons et le ligand BIF*Ph le moins donneur d'électrons.

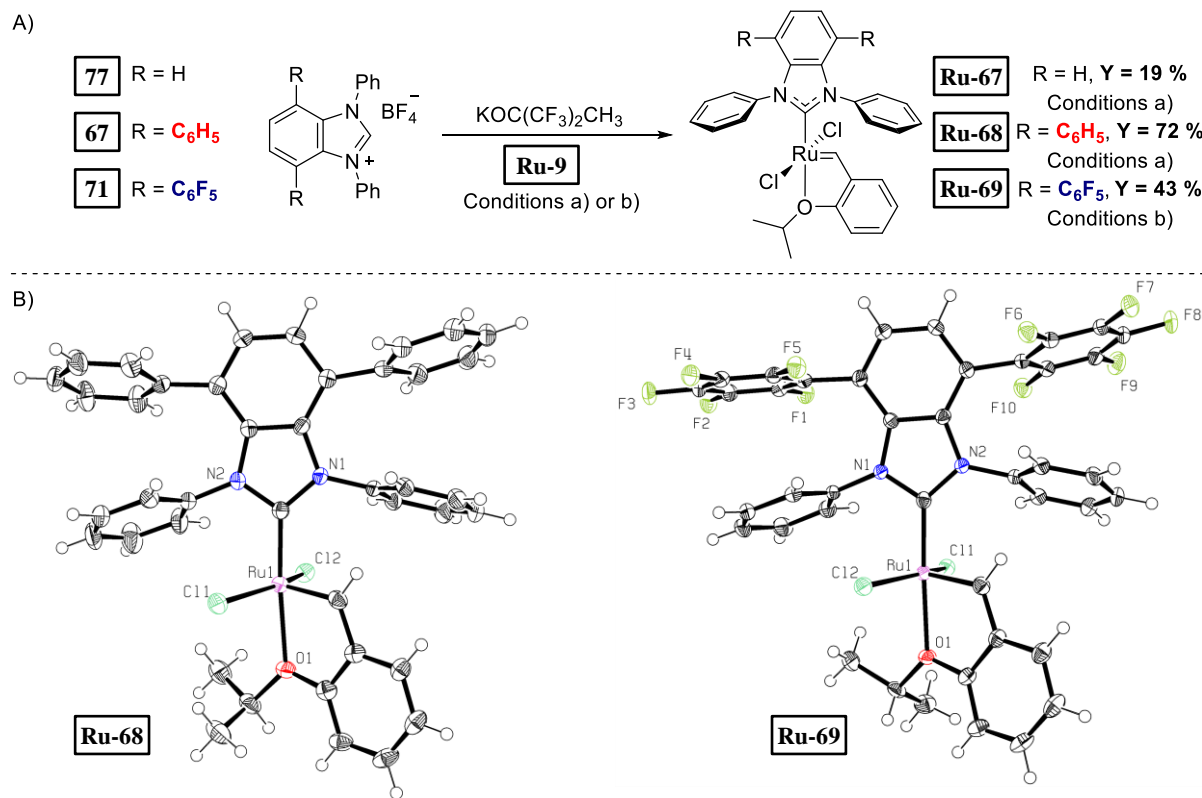


Schéma 11 A) Synthèse **Ru-67**, **Ru-68** et **Ru-69**; conditions de réaction : a) 1,75 équiv. de **77** ou **67**, 1,75 équiv. $KOC(CF_3)_2CH_3$, benzène, ta, 30 min. puis 1 équiv. **Ru-9**, 60 °C, 1 h ; b) 1,75 équiv. de **71**, 2 équiv. de $KOC(CF_3)_2CH_3$, benzène, ta, 15 min. puis 1 équiv. de **Ru-9**, 60 °C, 30 min. B) Structure DXR **Ru-68** et **Ru-69**, les ellipsoïdes sont dessinées avec une probabilité de 50 %.

Les longueurs de liaison et les angles sélectionnés des complexes **Ru-68** et **Ru-69** sont présentés dans le Tableau 2, ainsi que ceux correspondants pour le complexe **Ru-67** précédemment rapporté, qui peuvent servir de référence. Les paramètres géométriques décrivant les structures des complexes **Ru-68** et

Ru-69 sont bien corrélés à ceux du composé de référence **Ru-67**, comme l'illustre les structures superposées (Figure 1B). Les longueurs ruthénium-carbone(NHC) et ruthénium-carbone(alkylidène) (entrées 1 et 2, Tableau 2) dans les trois complexes ne diffèrent pas de plus de trois écarts-types estimés, il en est de même pour l'indice géométrique (τ_5), qui caractérise la distorsion de la géométrie pyramidale carrée [**Ru-67** : 0,35 ; **Ru-68** : 0,38 ; **Ru-69** : 0,40]. Cependant, les distances de liaison ruthénium-oxygène (entrée 3, Tableau 2) augmentent considérablement dans l'ordre **Ru-69**, **Ru-67**, **Ru-68**, respectivement, ce qui est parfaitement en corrélation avec les propriétés de donation électronique des NHC (globales et σ -donation) augmentant dans cet ordre $\text{BI}^*\text{FPh} < \text{BIPh} < \text{BI}^*\text{Ph}$, reflétant un effet *trans* croissant de BI^*FPh à BIPh et à BI^*Ph . Il est intéressant de noter qu'une telle observation diffère des catalyseurs de MO de deuxième génération dérivés des phosphines, dans lesquels l'augmentation de l'acidité π du ligand NHC explique un effet *trans* plus fort à mesure que la rétrodonation π métal-phosphine résultante s'affaiblit. Cela confirme la supposition précédente selon laquelle, puisque le ligand isopropoxy est un pur donneur σ , le NHC donneur σ le plus fort aura un effet *trans* plus fort. À notre connaissance, aucune hypothèse de ce type n'a été formulée jusqu'à présent.

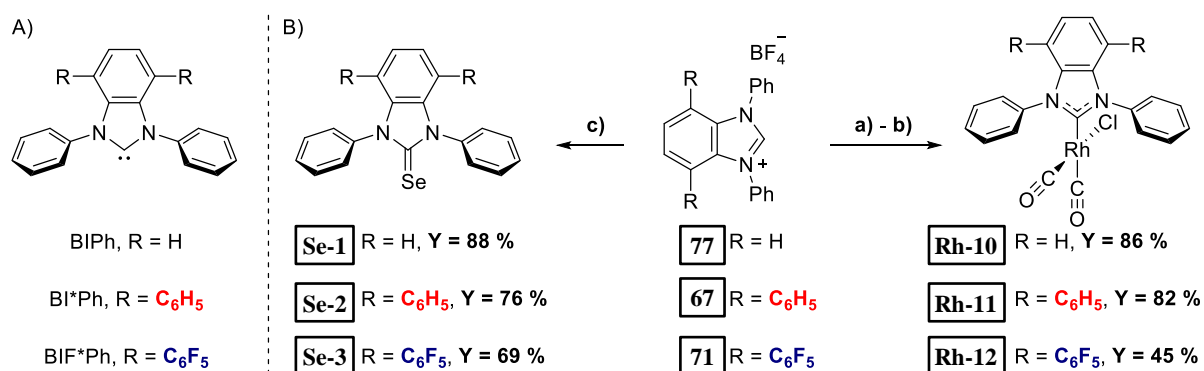


Schéma 11 A) Structures et abréviations des ligands NHC étudiés ici. B) Synthèse de complexes de rhodium carbonyle et de sélénourées ; conditions de réaction : a) 2,2 équiv. de **77** ou **67** ou **71**, 2,2 équiv. de KOC(CF₃)₂CH₃, THF, ta, 30 min. puis 1 équiv. de **Rh-1**, pendant la nuit ; b) CO (excès), DCM, ta, 30 min. ; c) 1 équiv. de **77** ou **67** ou **71**, 1 équiv. de KOC(CF₃)₂CH₃, THF, ta, 30 min. puis 2 équiv. de Se, pendant la nuit.

Tableau 1 Paramètres stéréoélectroniques des SIMes, IMes, BIPh, BI^{*}Ph et BIF^{*}Ph.

Ligand	v _{CO} ^{av} [cm ⁻¹] ^a	TEP [cm ⁻¹]	¹ J(C–H) ^c	$\delta(^{77}\text{Se})$ [ppm] ^d	%V _{bur} [%] ^e
SIMes	lit. 2040.5	2052.6	lit. 206	lit. 110	33.7
IMes	2037.5	2050.2	225	27	n.a. ^f
	(lit. 2037.6)	(2050.3)	(lit. 225)	(lit. 27)	
BIPh	2043.0	2054.6	224	127	32.9
BI [*] Ph	2040.0	2052.2	222	160	31.6
BIF [*] Ph	2045.0	2056.2	226	198	31.6

^a – Fréquence moyenne d'elongation du CO IR enregistrée dans les complexes Rh(NHC)(CO)₂Cl correspondants, mesurée dans le DCM. ^c – Constante de couplage ¹J (C–H) enregistrée des sels d'azolium correspondants provenant des satellites ¹³C du spectre RMN ¹H. ^d – Déplacement chimique ⁷⁷Se des sélénourées correspondantes mesuré dans CDCl₃. ^e – Calculé à partir des structures DRX des complexes Grubbs-Hoveyda correspondants. ^f – n.d. = non disponible.

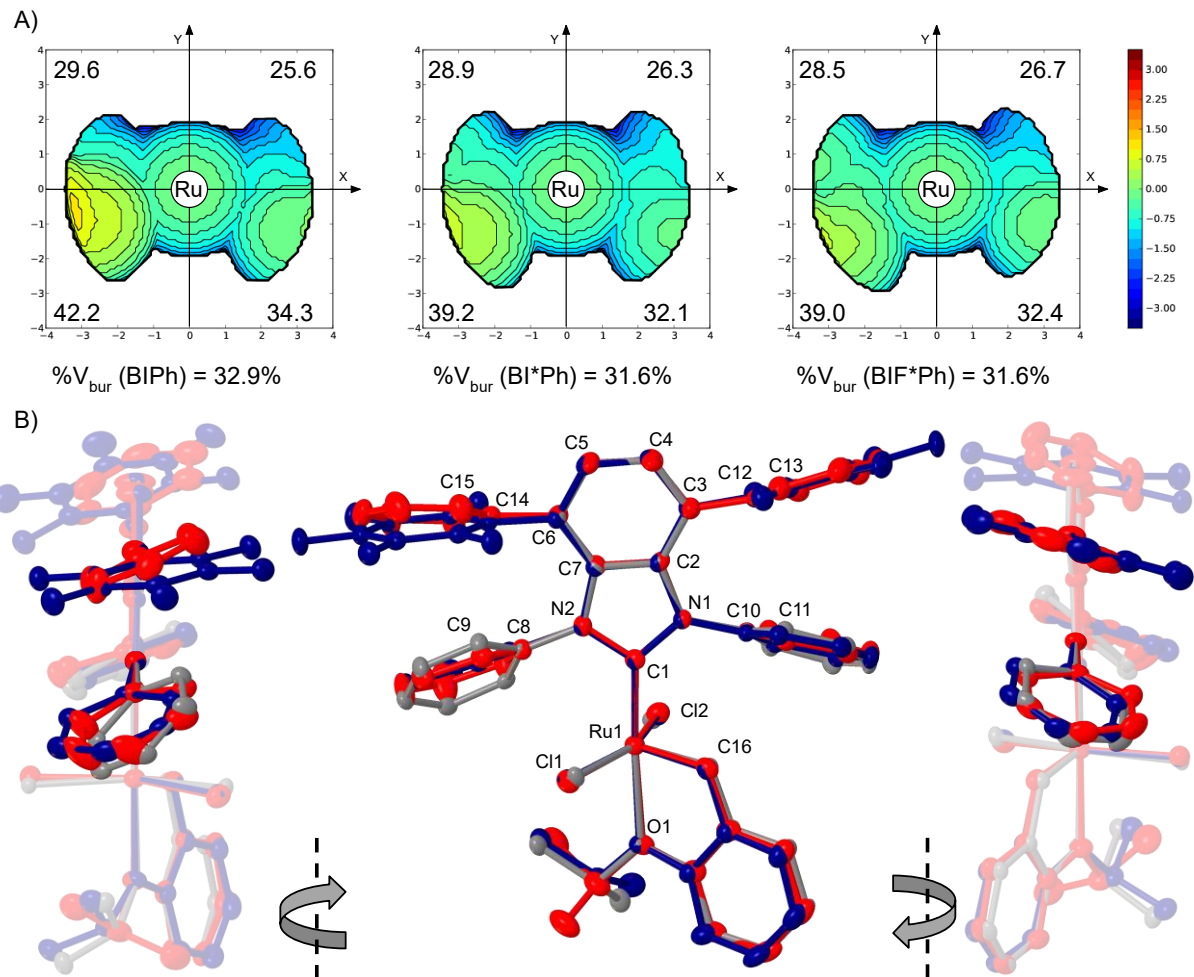


Figure 1 A) Cartes stériques des ligands NHC dans les complexes : gauche-**Ru-67**, centre-**Ru-68**, droite-**Ru-69**. Les valeurs aux quatre coins des cartes sont le %V_{bur} du ligand NHC dans le quadrant correspondant. B) Structures superposées de **Ru-67** (gris), **Ru-68** (rouge) et **Ru-69** (bleu).

Tableau 2 Longueurs de liaison (Å) et angles (deg) correspondants sélectionnés dans les structures cristallines aux rayons X des complexes **Ru-67**, **Ru-68** et **Ru-69**. L'étiquetage des atomes correspond à Figure 1B et non aux fichiers cif.

Entrée	Atomes	Ru-67	Ru-68	Ru-69
1	Ru1-C1	1.9618(10)	1.968(3)	1.9585(17)
2	Ru1-C16	1.8365(11)	1.830(3)	1.8326(17)
3	Ru1-O1	2.2692(7)	2.2807(19)	2.2539(12)
4	C1-Ru1-O1	176.19(4)	175.61(9)	177.09(5)
5	Cl1-Ru1-Cl2	155.303(10)	153.04(3)	153.163(14)
6	C7-N2-C8-C9	48.21	69.23	77.30
7	C2-N1-C10-C11	62.91	77.17	66.24
8	C5-C6-C14-C15	-	62.50	79.38
9	C4-C3-C12-C13	-	63.79	70.32

Les contraintes stériques relatives du BIPh parent non substitué et des deux nouveaux ligands BI*Ph et BIF*Ph à deux étages ont été quantifiées en établissant leurs cartes stériques topographiques dans les complexes **Ru-67**, **Ru-68** et **Ru-69** respectivement (Figure 1A et Tableau 1), en utilisant le programme SambVca2, et ont été comparés à l'encombrement stérique apporté par le ligand SIMes dans le catalyseur à usage général **Ru-10** (Tableau 1). De manière intéressante, il est apparu que la substitution du squelette benzimidazolyle a entraîné une légère diminution du %V_{bur} de 32,9 % pour BIPh dans **Ru-67** à 31,6 % pour BI*Ph et BIF*Ph dans **Ru-68** et **Ru-69**, ce qui résulte d'une orthogonalité plus élevée des groupes *N*-phényles par rapport à l'hétérocycle benzimidazolyle, caractérisés par l'augmentation des angles dièdres C7-N2-C8-C9 et C2-N1-C10-C11 (entrées 6 et 7, Tableau 2) de 48,21° et 62,91° en **Ru-67** à 69,23° et 77,17° dans **Ru-68** et 77,30° et 66,24° dans **Ru-69**. Cela peut être attribué à la substitution du squelette du cycle benzimidazolyle par des cycles phényles et pentafluorophényles dans **Ru-68** et **Ru-69** respectivement, ce qui entrave la rotation du *N*-phényle comme supposé. Cet effet de substitution du squelette dans l'espace est à l'opposé de l'effet de contrefort observé dans les catalyseurs NHC à décoration amino, dans lesquels les substituants amino volumineux sur le squelette forçaient les groupes *N*-aryles à tourner autour de la liaison N-C_{Ar}. Comme prévu, les trois ligands benzimidazolylidène fournissent une pression stérique inférieure à celle du ligand SIMes standard [% V_{bur} (SIMes) = 33,7 %], en raison de la présence de groupes *N*-phényle moins volumineux. De plus, lorsque **Ru-68** et **Ru-69** sont comparés, bien que les angles dièdres entre les groupes *N*-phényle et le cycle benzimidazolyle ne se distinguent pas clairement les uns des autres, les angles dièdres entre le noyau NHC et les substituants phényles ou pentafluorophényles de l'étage supérieur (C5-C6-C14- C15 et C4-C3-C12-C13, entrées 8 et 9, Tableau 2) augmentent explicitement de 62,50°, 63,79° à 70,32°, 79,38°, respectivement. Cette observation pourrait s'expliquer par des interactions π-π plus fortes entre les deux plans aromatiques dans la structure de **Ru-69**.

Afin de rationaliser l'effet de l'insertion d'un cycle phényle ou pentafluorophényle dans le squelette du groupe benzimidazolyle de **Ru-68** et **Ru-69** respectivement, une étude DFT a été réalisée au niveau théorique B3PW91-D3. En résumé, l'interaction entre le *N*-phényle et les seconds cycles phényle ou pentafluorophényle a été étudiée. Par conséquent, la comparaison des différentes *i*) distances de centroïde (3,607 et 3,427 Å pour **optRu-68** et **optRu-69** respectivement), *ii*) moments quadripolaires et *iii*) le chevauchement orbitalaire π, suggère que le cycle *N*-phényle interagit plus fortement avec le cycle squelette-pentafluorophényle dans **optRu-69** qu'avec le cycle squelette-phényle dans **optRu-68**.

La stabilité des deux complexes de ruthénium NHC de type biplan **Ru-68** et **Ru-69** nouvellement obtenus a ensuite été évaluée quantitativement et comparée à la référence **Ru-67**. Étant donné que le ligand NHC reste coordonné au centre métallique tout au long du cycle catalytique, les différences de stabilité des complexes devraient directement se traduisent par la stabilité des espèces qui se propagent réellement, traduisant ainsi leur efficacité en catalyse. Heureusement, **Ru-68** et **Ru-69** sont restés parfaitement inchangés pendant environ trois semaines en solution à température ambiante, tandis que **Ru-67** se dégradait lentement jusqu'à environ 50 % de la quantité initiale (Figure 2A, à gauche). Ce fait a confirmé notre observation précédente selon laquelle, lors de l'isolement, les complexes **Ru-68** et **Ru-69** sont considérablement plus stables que **Ru-67**. De plus, les différences de stabilité étaient encore plus prononcées à température plus élevée (Figure 2A, à droite), où **Ru-67** disparaissait complètement après environ 27 heures alors que **Ru-68** et **Ru-69** étaient encore détectables même après plus de 100 heures en solution à 80 °C. De plus, la température élevée a permis de distinguer **Ru-68** et **Ru-69** en termes de

stabilité et **Ru-69** s'est avéré être le précatalyseur le plus stable, ce que nous attribuons à l'impact bénéfique des interactions π - π entre les groupes *N*-phényle et les motifs du squelette pentafluorophényle.

Pour confirmer sans ambiguïté la nature de la voie de désactivation du catalyseur, nous avons tenté d'isoler le produit de dégradation de **Ru-67**. Une précédente publication présentant l'isolement et la caractérisation du produit de décomposition du catalyseur MO BiPh ruthénium décrit uniquement son dérivé PCy₃. L'évolution du complexe **Ru-67** a été suivie pendant une semaine dans le dichlorométhane à 22 °C, et le complexe **Ru-70** de ruthénium supporté par le ligand η^6 -arène-NHC attendu a été isolé (Figure 2B). La formation de ce complexe découle de l'activation d'une liaison C-H en position *ortho* d'un groupe N-phényle suivie d'une insertion dans l'alkylidène. La structure moléculaire du complexe **Ru-70** a été confirmée par des expériences DRX sur des monocristaux obtenus en déposant du pentane sur une solution du complexe **Ru-70** dans le dichlorométhane (Figure 2B).

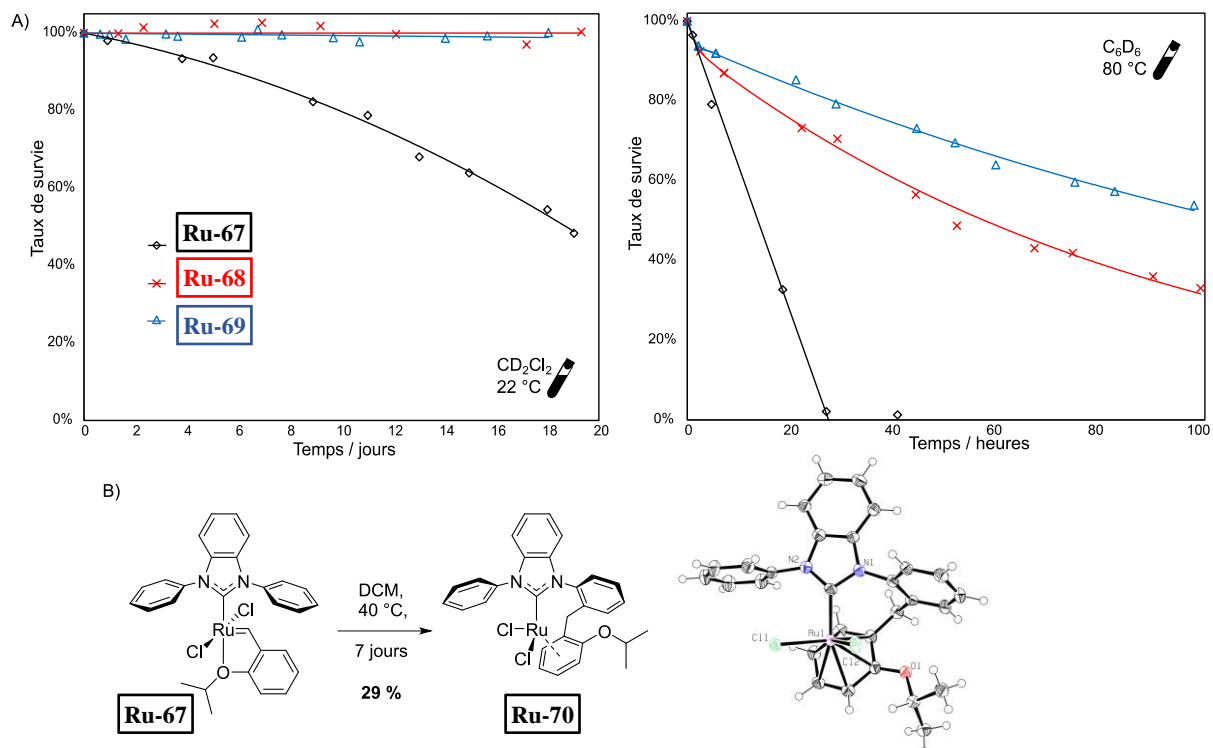


Figure 2 A) Tests de stabilité en solution à température ambiante et élevée. Mesuré par RMN (1,3,5-triméthoxybenzène ajouté comme référence). Les lignes sont uniquement une aide visuelle. Conditions : (à gauche) CD₂Cl₂ à 22 °C, sous argon ; (à droite) C₆D₆ à 80 °C, sous argon. B) étude de la décomposition du complexe Ru-67 en complexe Ru-70. C) Structure DRX du complexe Ru-70 (les ellipsoïdes sont dessinés avec une probabilité de 50%).

Afin d'expliquer la cinétique de décomposition plus lente des complexes **Ru-68** et **Ru-69** par rapport à celle de **Ru-67**, nous avons émis l'hypothèse que l'insertion d'un plan aromatique parallèle aux cycles *N*-aryle pourrait empêcher la rotation du groupe N-phényle diminuant ainsi la vitesse de l'activation du CH conduisant au produit de décomposition. Cependant, la désactivation des complexes ne peut pas être attribuée à ce processus simple de rotation du N-phényle, car les barrières d'énergie libre de Gibbs dans l'état de transition correspondant peuvent être facilement surmontées à température ambiante, contrairement à ce qui a été observé expérimentalement. Nous nous sommes donc demandé si la cinétique de décomposition observée expérimentalement pouvait plutôt être expliquée par une étape particulière du mécanisme de désactivation.

Inspiré par les rapports de Cavallo et de ses collègues expliquant la décomposition du dérivé PCy₃, le calcul de l'ensemble de la voie de décomposition des complexes **Ru-67**, **Ru-68** et **Ru-69** a été réalisé. En conclusion, le profil de décomposition calculé indique que la répulsion stérique entre les groupes *N*-phényles et phényles- et pentafluorophényles du squelette arrière affecte fortement l'étape cinétiquement déterminante de la réaction qui implique *i*) le transfert du proton agostique *N*-phényle vers l'atome de carbone α voisin du groupe benzylidène et *ii*) le transfert du proton benzylique au ruthénium couplé à la formation de liaisons carbone-carbone. La barrière cinétique correspondante est donc considérablement plus élevée pour les composés **Ru-68** et **Ru-69** que pour **Ru-67**, conformément à la cinétique de décomposition rapportée dans la Figure 2.

Les performances catalytiques des nouveaux complexes à double étage ont été comparées à celles du complexe **Ru-67** de référence connu à l'aide d'un ensemble de réactions modèles. Tout d'abord, nous avons vérifié leur activité dans les RCM avec formation de doubles liaisons carbone-carbone tétrasubstituées. À cette fin, le 2,2-di(2-méthylallyl)malonate de diéthyle (**78a**) a été choisi comme substrat modèle et les tracés de conversion en fonction du temps de sa réaction RCM ont été établis avec 0,2 mol% de chaque catalyseur dans du toluène à 80 °C (Figure 3). Tous les complexes ont présenté une activité élevée, permettant des conversions considérables au cours des 30 premières minutes. Cependant, la réaction catalysée par **Ru-67** a atteint ses limites avec une conversion nettement inférieure à celle enregistrée avec **Ru-68** et **Ru-69**. Cela peut être attribué à des espèces catalytiques à 14 e⁻ plus stables formées à partir de ces derniers précatalysteurs par rapport à celles générées à partir de **Ru-67**. Fait intéressant, bien que **Ru-68** ait donné des conversions plus élevées que **Ru-69** dans la première heure de la réaction, après ce point, la tendance s'est inversée, conduisant à une conversion de 96 % avec **Ru-69** contre 91 % avec **Ru-68** après 5 heures (et 72 % pour le composé **Ru-67**).

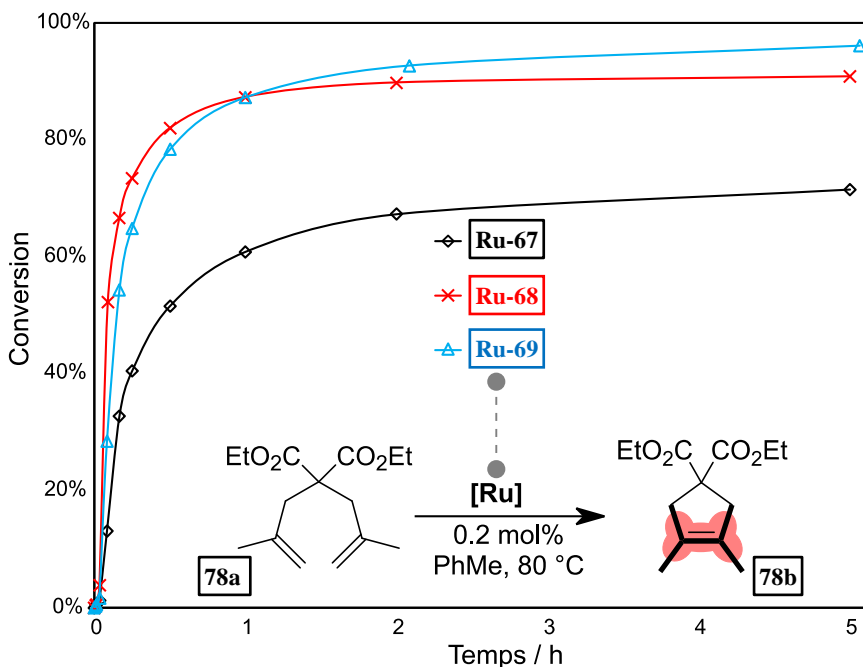


Figure 3 Courbes de conversion en RCM du diène **78a**. Conditions : Catalyseur 0,2 mol%, toluène, 80 °C sous argon. Mesuré par GC avec du 1,3,5-triméthoxybenzène ajouté comme étalon interne. Les lignes sont uniquement une aide visuelle.

Pour examiner plus en détail les différences de productivité du catalyseur, la réaction de **78a** décrite précédemment a été réessayée avec une charge de catalyseur deux fois inférieure égale à 0,1 mol% (Schéma 13). La tendance observée précédemment s'est maintenue et **Ru-67** a donné une conversion

plutôt faible pour une telle réaction (50 %), alors que **Ru-68** et **Ru-69** ont donné des conversions beaucoup plus élevées de 81 % et 92 % respectivement. Les trois catalyseurs de type BIPh ont ensuite été testés dans cinq réactions de RCM plus difficiles comportant la formation de doubles liaisons carbone-carbone tétrasubstituées. Une tendance similaire a été observée dans le cas de la formation du cycle à six chaînons (malonate **79b**) et du tosylamide **81b** à cinq chaînons, où les conversions enregistrées pour **Ru-68** et **Ru-69** sont jusqu'à 32 points de pourcentage (%p) supérieures à celles enregistrées pour **Ru-67**. Le complexe fluoré **Ru-69** a légèrement mais sensiblement dépassé les performances de **Ru-68** dans ces deux dernières réactions.

La supériorité des nouveaux catalyseurs **Ru-68** et **Ru-69** était encore plus prononcée dans la formation plus difficile d'un cycle à sept chaînons moins favorisée sur le plan thermodynamique (composés **80b** et **82b**). Dans ces derniers cas, une charge de catalyseur plus élevée de 2 mol% avec le malonate **80b** et 1 mol% avec le tosylamide **82b** ont été nécessaires pour atteindre des conversions appropriées. Cependant, une telle charge est toujours considérée comme faible dans le contexte de la formation difficile de liaisons carbone-carbone tétrasubstituées. Il convient de noter que **Ru-68** et **Ru-69** ont donné des conversions 4 à 8 fois supérieures à **Ru-67** et encore une fois, **Ru-69** était légèrement meilleur que **Ru-68**, ce qui est globalement en corrélation avec la tendance observée dans les tests de stabilité.

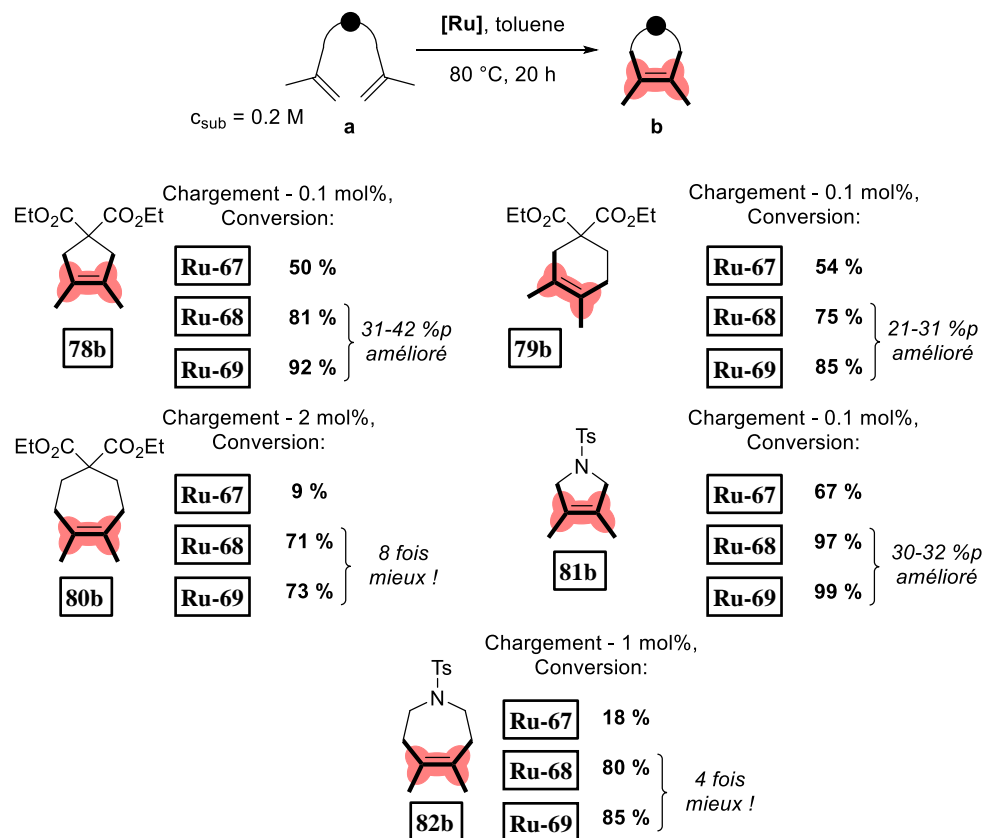


Schéma 13 Portée et limites des catalyseurs **Ru-67**, **Ru-68** et **Ru-69** dans les RCM de substrats difficiles.

Pour tous les substrats discutés jusqu'à présent, les produits RCM souhaités ont été obtenus en tant que produit unique. Cependant, la réaction RCM de l'éther **84a** a conduit à la formation d'un sous-produit réarrangé **84a'** résultant d'une migration de la double liaison le long de la chaîne alkyle (Figure 4A). Cela peut être dû aux produits de décomposition du catalyseur (probablement des espèces d'hydrure de ruthénium). La formation observée de **84a'** est en accord avec le rapport précédent de Grubbs et de ses collaborateurs, bien que ce produit d'isomérisation n'ait pas été caractérisé.

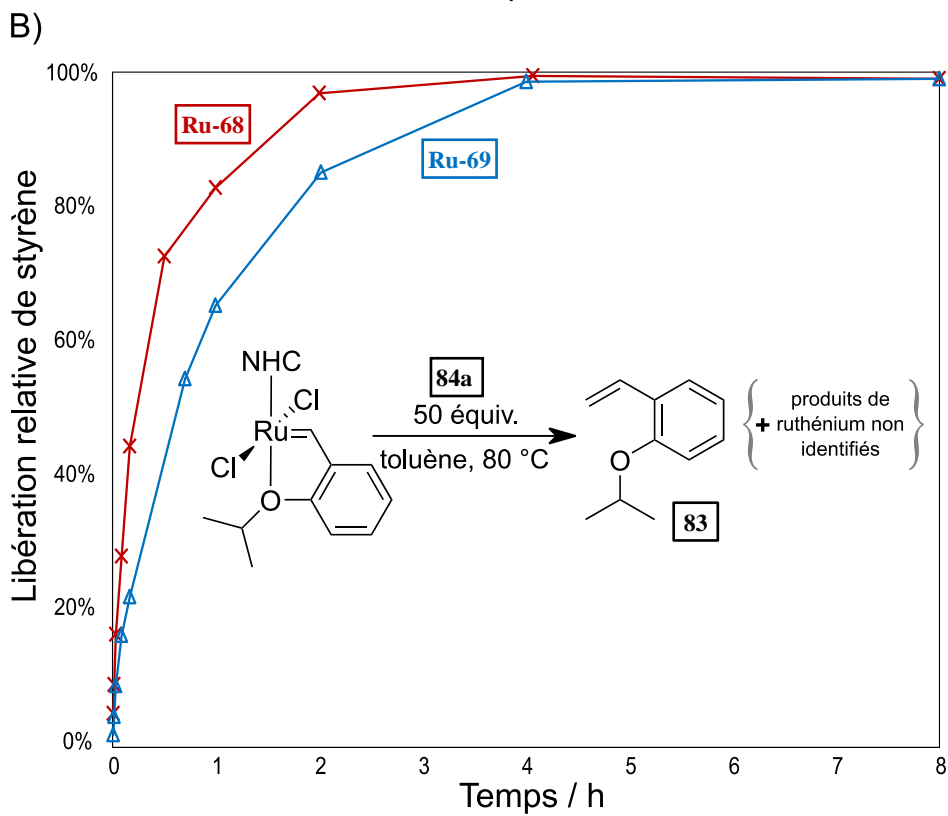
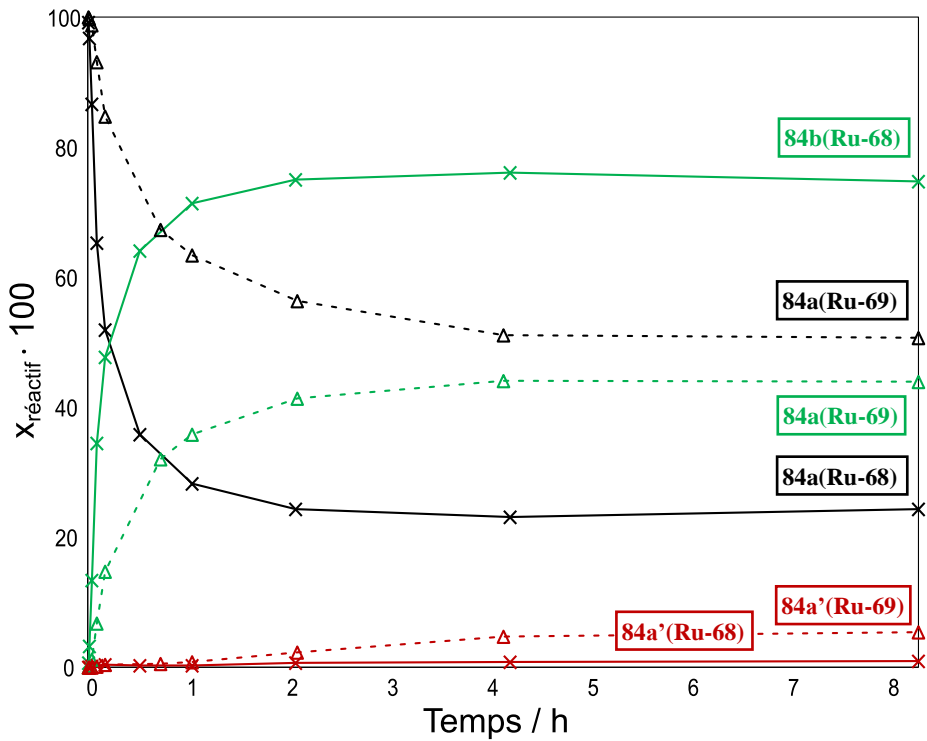
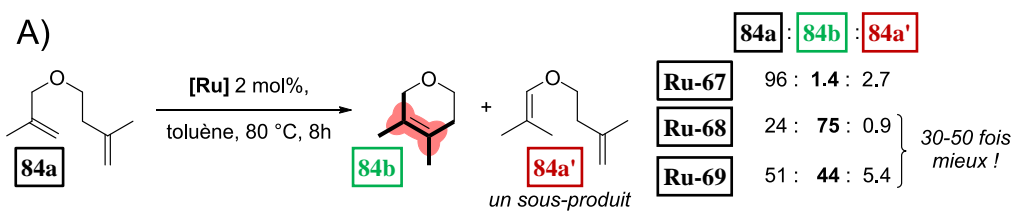


Figure 4 A) Profil de réaction du substrat **84a** RCM. B) libération d'o-isopropoxystyrène (**83**) dans le temps pendant **84a** RCM.

Le catalyseur **Ru-67** a conduit à une très mauvaise conversion de **84a**, formant **84b** et **84a'** en quantités comparables (rapport **84a : 84b : 84a'** de 96 : 1,4 : 2,7). Remarquablement, par rapport à **Ru-67**, les nouveaux catalyseurs **Ru-68** et **Ru-69** ont permis une formation du produit souhaité **84b** en quantité 30 à 50 fois supérieure. Fait intéressant, dans cet exemple, **Ru-68** a surpassé **Ru-69**, à la fois en termes de conversion et de sélectivité envers **84b** (le rapport **84a : 84b : 84a'** pour **Ru-68** a atteint 24:75:0,9 contre 51:44:5,4 pour **Ru-69** après 8 heures à 80 °C). Cette observation pourrait s'expliquer par la subtile différence d'activité entre **Ru-68** et **Ru-69** qui a été observée dans la réaction de RCM de **78a** (Figure 3).

Pour vérifier cette dernière hypothèse, le profil de réaction de la RCM de **84a** a été établi, en comparant les performances de **Ru-68** et **Ru-69** (Figure 4A). La différence d'activité du catalyseur est plus prononcée dans cet exemple difficile de RCM, et le complexe **Ru-68** est considérablement plus actif que **Ru-69** (le rapport **84a : 84b : 84a'** après 1 h atteint 28 : 71 : 0,3 avec **Ru-68** contre 63 : 36 : 0,8 avec **Ru-69**). Après la première heure de réaction, la formation de **84b** ralentit considérablement, indiquant que la plupart des espèces catalytiquement actives ont été épuisées. Après ce point, les complexes issus de la décomposition de l'espèce active commencent à isomériser **84a**, qui est disponible en quantité plus élevée dans le cas de la réaction avec **Ru-69**. Ces facteurs expliquent une quantité plus élevée de **84a'** observée avec **Ru-69** après 8 h.

Pour sonder davantage l'origine de l'activité supérieure de **Ru-68**, la libération d'*ortho*-isopropoxystyrene (**83**) (par rapport au dernier point mesuré à 8 h) en fonction du temps a été tracée (Figure 4A). La formation de **83** peut servir de mesure indirecte de la progression de l'initiation du catalyseur tout au long de la réaction. Pour les deux complexes, la libération de **83** se termine dans les 4 premières heures, bien que pour **Ru-68** la pente soit considérablement plus raide que pour **Ru-69**. Ceci est conforme à l'hypothèse selon laquelle **Ru-68** est un catalyseur plus actif que **Ru-69**, probablement en raison d'un taux d'initiation plus rapide résultant d'un effet *trans* plus élevé dû à la présence du ligand NHC plus donneur d'électrons dans BI*Ph.

Pour évaluer davantage la portée et les limites des catalyseurs **Ru-68** et **Ru-69**, plusieurs réactions de CM difficiles ont été étudiées (Schéma 14). Tout d'abord, nous avons étudié la réaction entre le chrysanthémate d'éthyle (**85**) et le Z-1,4-diacétoxy-2-butène (**86**). Les catalyseurs **Ru-68** et **Ru-69** ont donné des conversions similaires de **85**, 69 % et 73 % respectivement, donnant le produit **87** de manière sélective, alors que **Ru-67** n'a fourni que 26 % de conversion. Ensuite, la fonctionnalisation de la double liaison géminale carbone-carbone de la 4-méthylène-1-tosylpipéridine (**88**) avec **86** ou de l'amylène (**90**) a été testée. Dans le cas d'une réaction avec **86**, l'utilisation de **Ru-68** et **Ru-69** a permis des conversions jusqu'à 18 % de plus par rapport au complexe **Ru-67**, conduisant à une conversion de 76 % pour **Ru-69**.

Il convient de noter que dans l'exemple de CM de **88** avec l'amylène, les catalyseurs portant des NHC à deux étages **Ru-68** et **Ru-69** ont donné des conversions presque quantitatives de **88**, 93 % et 91 % respectivement, ce qui était 5 fois plus élevé que dans le cas de **Ru-67** atteignant seulement 18 %. Enfin et surtout, la métathèse très difficile de la 1,5-ényne **92** pour obtenir un dérivé de cyclobutène **93** encombré et constraint a été tentée. Une difficulté supplémentaire découlant de cette réaction est que sa sélectivité peut être compromise par une réaction d'auto-CM concurrente et par dégradation du produit résultant. Nous avons été heureux de constater que les catalyseurs **Ru-68** et **Ru-69** donnaient de bons rendements de 59 % et 53 % respectivement, ce qui était environ 10 fois plus élevé qu'avec **Ru-67**, ce dernier ne conduisant qu'à une très faible quantité de produit avec un rendement de 6 %. Fait intéressant,

comme dans le cas de la réaction RCM de **84**, dans cet exemple, le catalyseur **Ru-68** a visiblement mieux fonctionné que son homologue fluoré **Ru-69**, ce que nous attribuons à une activité **Ru-68** plus élevée. Remarquablement, l'utilisation des nouveaux catalyseurs a permis de diviser par deux la charge en catalyseur par rapport au complexe SIMes à usage général utilisé à une charge de 20 mol% pour cette transformation.

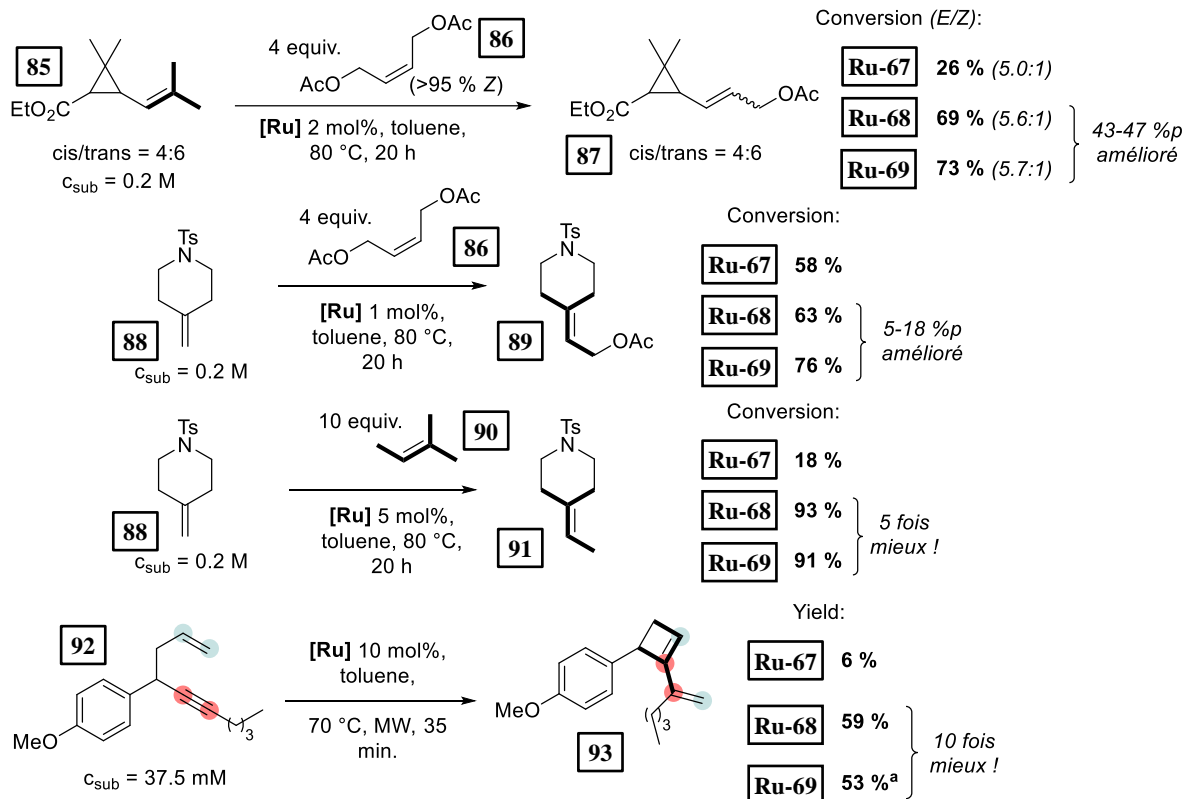


Schéma 14 Portée et limites des catalyseurs **Ru-67**, **Ru-68** et **Ru-69** en CM et cycloisomérisation de substrats difficiles. ^a - réaction réalisée dans du perfluorotoluène. %p – différence en points de pourcentage par rapport à **Ru-67**.

En résumé, nous avons développé les deux nouveaux ligands NHC de type biplan BI*Ph et BIF*Ph basés sur un noyau benzimidazolylidène, dont les ailes inférieures sont constituées de groupement *N*-phényle pour réduire l'encombrement stérique dans la première sphère de coordination et dont les ailes supérieures sont respectivement des cycles phényles ou pentafluorophényles. Les complexes Grubbs-Hoveyda **Ru-68** et **Ru-69** correspondants de deuxième génération ont été générés et l'effet de l'introduction du deuxième étage de cycles aromatiques sur leurs propriétés stéréoélectroniques, leur stabilité et leur efficacité catalytique a été évalué, en prenant le ligand BIPh non substitué de type monoplan comme référence. Selon la nature des cycles aromatiques, BI*Ph s'est révélé plus donneur d'électrons que BIPh, tandis que BIF*Ph est moins donneur d'électrons. À l'inverse, le deuxième étage aromatique a conduit dans les deux cas à des ligands NHC légèrement moins encombrés par rapport au BIPh en forçant les cycles *N*-phényles à rester dans une position plus orthogonale par rapport au noyau benzimidazolylidène.

Plus important encore, les complexes **Ru-68** et **Ru-69** se sont révélés significativement plus stables que le complexe **Ru-67** connu supporté par BIPh. Ce gain de stabilité a été rationalisé grâce à des calculs DFT des voies de décomposition. Bien que les cycles aromatiques du deuxième étage ne puissent pas arrêter la rotation des groupes *N*-phényle dans **Ru-68** et **Ru-69**, ils contribuent fortement à

l'augmentation de l'énergie de l'étape cinétiquement déterminante, en forçant une forte distorsion de l'hétérocycle carbénique par des contraintes stériques. L'étape clé de décomposition implique le transfert de protons de l'une des positions *ortho* dans les groupes *N*-phényle vers l'atome de carbone voisin du fragment benzylidène, suivie de la migration du proton benzylique vers le ruthénium avec formation simultanée de liaisons carbone-carbone. De plus, la stabilité accrue observée des précurseurs du ruthénium **Ru-68** et **Ru-69** s'est également traduite en une stabilité accrue des espèces actives et a permis leur mise en œuvre en tant que précatalyseurs stables et hautement efficaces dans des réactions difficiles de métathèse d'oléfines pour la formation de doubles liaisons carbone-carbone tri- et tétra-substituées. Le complexe **Ru-68** portant le ligand BI*Ph le plus donneur d'électrons et plus fortement inducteur d'effet *trans* s'est révélé également plus actif que son homologue **Ru-69** portant le ligand BIF*Ph le moins donneur d'électrons.

Les résultats présentés dans ce chapitre ont donné lieu à la publication (préprint) suivante : « P. Krzesiński, C. Dinoi, I. D. Rosal, L. Vendier, S. Bastin, V. César, A. Kajetanowicz, K. Grela, N-Heterocyclic Carbene Ligands as a Remedy for Low Reactivity of Crowded Substrates in Ruthenium Catalyzed Olefin Metathesis, *ChemRxiv*, 2023, Working Paper, DOI : 10.26434/chemrxiv-2023-b4btj ».

CM d'oléate de méthyle de qualité technique pour la synthèse de polyesters et polyamides biosourcés

Nous avons commencé avec la self-CM de **28(Z)** après sa simple distillation préalable à partir d'alumine activée pour diminuer la teneur en poisons du catalyseur. 100 ppm de **Ru-10** ont permis d'atteindre l'équilibre en 3 h (50 °C, sans solvant, entrée 1, Tableau 3). Même si le mélange réactionnel contenait plusieurs produits, dont des alcènes et monoesters internes (**28(E/Z)**, **30**, **95**, **96**, **97**, Schéma 15), nous avons été heureux de constater que le mélange à l'équilibre contenait principalement **29** sous forme de diester. En diminuant la charge du catalyseur, nous avons remarqué que le monoester **95** était également présent dans le mélange réactionnel et que la relation était inversement proportionnelle (entrées 1-3, Tableau 3). Cela suggère qu'à des charges inférieures à 100 ppm de **Ru-10**, l'équilibre réactionnel n'est pas atteint. Nous voulions éviter toute espèce monofonctionnelle telle que **28**, **94**, **95** ou **96** dans le produit isolé, car elles entraîneraient une masse moléculaire plus faible du polyester résultant, car les monoesters termineraient une chaîne polymère. De la chromatographie en phase gazeuse, nous avons déduit que les températures d'ébullition de **29** et **95** seraient très similaires, ce qui rendrait la purification de **29** difficile. Par conséquent, nous avons décidé de nous concentrer sur la minimisation de la formation de **95** comme objectif principal du criblage du catalyseur, plutôt que sur la maximisation de l'efficacité du catalyseur.

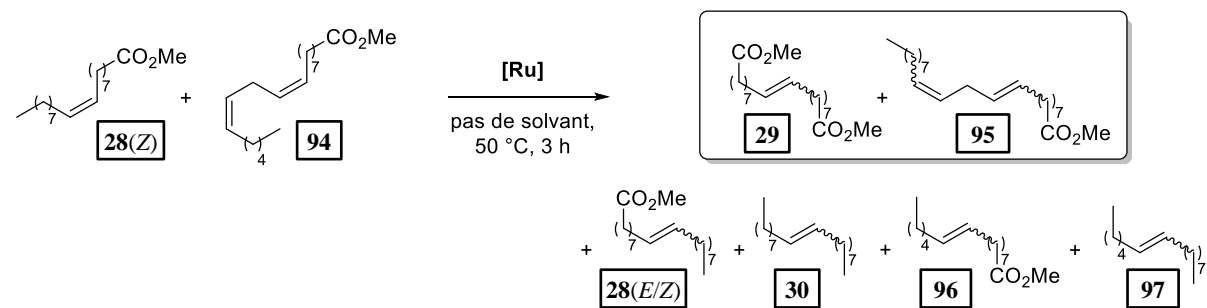


Schéma 15 Self-CM d'oléate de méthyle (**28**) avec 20 % en poids de linoléate de méthyle (**94**) et les produits observés.

Tous les complexes ont donné des conversions relativement similaires des substrats **28(Z)** et **94**, autour de 95 %, à l'exception de **Ru-69** qui a donné un taux inférieur de 91 %. Les catalyseurs **Ru-10**, **Ru-18**, **Ru-17** et **Ru-71** ont donné un rapport **29 : 95** supérieur à 90:10, **Ru-10** et **Ru-17** dépassant 95:5. **Ru-68** et **Ru-69** ont produit des quantités beaucoup plus élevées de **95**, ce qui peut être attribué à leur plus grande fragilité due à une protection stérique plus faible des NHC. **Ru-10** a donné un rendement en **29** légèrement supérieur à celui du catalyseur **Ru-17** (respectivement 54 % contre 49 %, le rendement maximal étant d'environ 50 % résultant de l'équilibre de la réaction) et il a donc été choisi de poursuivre le développement.

Tableau 3 Résultats du criblage du catalyseur.

Entrée	Catalyseur	Chargement [ppm]	Conversion de 28(Z) + 94 [%]	Rendement en 29 [%]	29 à 95 wt. rapport	E à Z rapport de 29
1		100	95	54	96:4	84:16
2	Ru-10	50	94	51	89:11	82:18
3		25	80	26	63:37	78:22
4	Ru-18		94	45	90:10	82:18
5	Ru-17		94	54	92:8	82:18
6	Ru-71	100	95	49	96:4	82:18
7	Ru-68		94	50	82:18	82:18
8	Ru-69		91	42	70:30	80:20

Conditions de réaction : sans solvant, 50 °C, 3 h.

Avec le catalyseur sélectionné, une self-CM d'oléate de méthyle a été réalisée avec 300 g de substrat. Après la réaction, le produit **29** a été isolé par distillation fractionnée puis purifié par cristallisation dans du méthanol à -30 °C. Il est intéressant de noter que ce protocole a donné le produit **29** pur contenant presque uniquement l'isomère *E* (rapport *E/Z* de 97 : 3) avec un rendement de 36 %.

Ayant le monomère **29** en main, nous avons tenté la réaction de polycondensation en fusion avec différents co-monomères (Schéma 16). Le *N*-butoxyde de titane a été utilisé comme catalyseur pour cette réaction. Il en résulte un solide rouge-brun insoluble dans tous les solvants les plus courants, y compris l'acide trifluoroacétique. Cela contredit les résultats rapportés par Warwel et al, dans lesquels les auteurs prétendaient caractériser les mêmes polyesters en utilisant la chromatographie par perméation de gel (GPC), bien qu'aucune donnée expérimentale n'ait été fournie à ce sujet. Pour confirmer la formation de macromolécules, la réaction a été arrêtée plus tôt et les oligomères formés (solubles dans les solvants organiques conventionnels) ont été caractérisés par spectroscopie RMN.

Les oligomères et polymères obtenus ont été caractérisés par calorimétrie différentielle à balayage (DSC) et analyse thermogravimétrique (TGA). Les polyesters obtenus ont des températures de fusion relativement basses comprises entre 9 et 42 °C (entrées 1 à 7, Tableau 4), caractéristique des polyesters aliphatiques linéaires. La température de fusion du polyamide (152 °C, entrée 8, Tableau 4) est nettement plus élevée, ce qui est dû à la formation de liaisons hydrogène par rapport aux polyesters. Les enthalpies de fusion varient de 25 à 73 J/g. Les polyesters aliphatiques présentaient des températures de

dégradation autour de 400 °C, cependant, le polyester contenant un bloc 1,4-cyclohexanediol présente une température de dégradation accrue de 446 °C en raison de la rigidité plus élevée du polymère qu'offre un tel monomère.

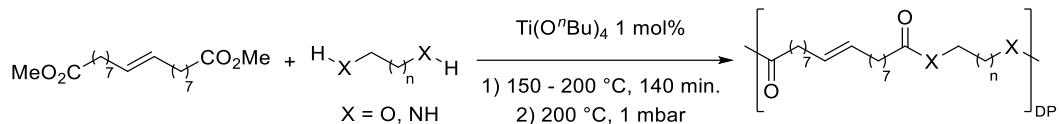


Schéma 16 Réaction de polycondensation pour obtenir des polyesters et des polyamides à partir du diester **29**.

Tableau 4 Polymérisation du monomère **29** et caractérisation des polyesters et polyamides obtenus.

Entrée	Polyester	Temps de vide	Rendement	DP ^a	M _n (g/mol) ^a	T _m (°C) ^b	ΔH (J/g) ^b	T _d (°C) ^c	perte de masse ^c
1		30 min.	51 %	1.7	592	42	64	403	97 %
2		19 h	52 %	n.d.	n.d.	14	25	413	96 %
3		225 min.	76 %	6.6	2238	34	72	395	98 %
4		21 h	81 %	n.d.	n.d.	11	55	398	97 %
5		180 min.	74 %	7.5	2539	38	73	397	98 %
6		21 h	88 %	n.d.	n.d.	10	60	398	96 %
7		19 h	24 %	n.d.	n.d.	9	35	446 ^d	78 % ^d
9		19 h	51 %	n.d.	n.d.	152	55	443	82 %

Conditions de réaction : $Ti(OBu)_4$ 1 mol%, sans solvant, 140 min. temps de fusion avec augmentation de la température de 150 à 200 °C. ^a - le degré de polymérisation (DP) et le poids moléculaire moyen en nombre (M_n) ont été calculés à partir de la RMN ¹H par analyse des groupes terminaux. ^b – déterminé par DSC. ^c – La T_d (température de décomposition) et la perte de masse des échantillons ont été déterminées par TGA. ^d – une perte de masse évidente de 50 % a été observée à une température de 353 °C. n.d. – non déterminé en raison de l'insolubilité du polymère.

En résumé, un nouveau procédé d'obtention de matériaux polymères fonctionnels à partir d'oléate de méthyle de qualité technique a été développé. La self-CM de l'oléate de méthyle en présence de quantités substantielles de linoléate de méthyle a été étudiée et la réaction a été optimisée pour obtenir de l'octa-déc-9-ènedioate de diméthyle avec une sélectivité et un rendement élevés. Une polycondensation ultérieure avec un co-monomère (diol ou diamine) a abouti à la formation de matériaux polymères qui ont été caractérisés par TGA et DSC.

Les résultats présentés dans ce chapitre ont donné lieu à la publication suivante : « P. Krzesiński, V. César, K. Grela, S. Santos, P. Ortiz, Cross-metathesis of technical grade methyl oleate for the synthesis of bio-based polyesters and polyamides, *RSC Sustain.*, **2023**, Advance Article, DOI : 10.1039/d3su00305a ».

List of abbreviations

%p	percent point	ⁱ Pr	isopropyl group
%V _{bur}	percent buried volume	IR	infrared
Ac	acetyl group	KHMDS	potassium hexamethyldisilazide
ADMET	acyclic diene metathesis	LEP	Lever electronic parameter
ATR	attenuated total reflectance	LiHMDS	lithium hexamethyldisilazide
BI*Ph	4,7-diphenyl-1,3-diphenylbenzimidazolylidene	LUMO	lowest occupied molecular orbital
BIF*Ph	4,7-di(pentafluorophenyl)-1,3-diphenylbenzimidazolylidene	Me	methyl group
BIPh	1,3-diphenylbenzimidazolylidene	Mes	mesityl group
CAAC	cyclic alkyl amino carbene	NBO	natural bond orbital
CC	column chromatography	NHC	N-heterocyclic carbene
CM	cross metathesis	NHO	N-heterocyclic olefin
COD	cyclooctadiene	NMR	nuclear magnetic resonance
Cy	cyclohexyl group	OM	olefin metathesis
DAC	diamidocarbene	Ph	phenyl group
dba	dibenzylideneacetone	quant.	quantitative
DCE	1,2-dichloroethane	RCEYM	ring-closing enyne metathesis
DCM	dichloromethane	RCM	ring-closing metathesis
DFT	density functional theory	RDI	rate determining intermediate
Dipp	2,6-diisopropylphenyl group	RDS	rate determining step
DMF	dimethylformamide	RDTS	rate determining transition state
DMSO	dimethyl sulfoxide	ROMP	ring-opening metathetic polymerization
DP	degree of polymerization	RS	resting state
DSC	differential scanning calorimetry	RU	repeat unit
equiv.	equivalent	SIMes	1,3-dimesitylimidazolinylidene
ESI	electrospray ionization	SIPr	1,3-di(2,6-diisopropylphenyl)imidazolylidene
Et	ethyl group	SPS	solvent purification system
EWG	electron withdrawing group	^t Bu	<i>tert</i> -butyl group
FAME	fatty acid methyl ester	TEP	Tolman electronic parameter
GC	gas chromatography	TGA	thermogravimetric analysis
HEP	Huynh electronic parameter	THF	tetrahydrofuran
HOMO	highest occupied molecular orbital	TLC	thin layer chromatography
HPLC	high performance liquid chromatography	TOF	turnover frequency
HRMS	high resolution mass spectrometry	TON	turnover number
HSQC	heteronuclear single quantum coherence	Ts	tosyl group
IMes	1,3-dimesitylimidazolylidene	XRD	X-ray diffraction
		Y	yield

Table of contents

1.	State-of-the-art overview.....	39
1.1.	General introduction to catalysis	39
1.2.	N-Heterocyclic carbene (NHC) ligands	40
1.2.1.	Carbene ligands	40
1.2.2.	A brief history of NHCs	40
1.2.3.	General properties of NHC ligands	41
1.2.4.	Methods for the synthesis of NHCs.....	42
1.2.5.	Determination of NHC's electronic parameters	43
1.2.6.	Determination of NHC's steric properties.....	45
1.3.	Olefin metathesis (OM).....	46
1.3.1.	Types of OM reactions	46
1.3.2.	Mechanism of OM.....	47
1.3.3.	Schrock type catalysts	49
1.3.4.	Classification of ruthenium-based OM catalyst	49
1.3.5.	Methods for the synthesis of ruthenium alkylidene complexes.....	50
1.3.6.	Mechanism of initiation of ruthenium-based precatalysts.....	51
1.3.7.	Impact of ligands on first generation catalysts	52
1.3.8.	Impact of ligands on second generation catalysts	53
1.4.	Stereoselective OM	55
1.4.1.	Thiophenolate Z-selective catalyst	56
1.4.2.	Z-selective catalyst bearing chelating LX-type NHC ligand.....	56
1.4.3.	Dithiocathecholate stereoretentive catalyst	58
1.5.	Formation of tetrasubstituted carbon-carbon double bonds using OM	60
1.5.1.	Mechanistic considerations	60
1.5.2.	Proposed decomposition pathways.....	62
1.5.3.	Methods to prevent catalyst deactivation	63
1.6.	Self-CM of methyl oleate	64
1.7.	Brief overview of the thesis.....	65
2.	Toward a robust Z-selective OM catalyst	67
2.1.	Objectives.....	67
2.2.	Axis A - ruthenium complexes supported by a chelating NHC ligand comprising a barbituric heterocycle.....	68
2.2.1.	Preliminary results.....	68
2.2.2.	Synthesis of ruthenium complexes with the chelating NHC ligand	69
2.2.3.	Installation of an alkylidene ligand and the attempted catalysis	73
2.2.4.	Conclusions	75
2.3.	Axis B – NHC-NHO ligand architecture.....	77
2.3.1.	Synthesis of an NHC-NHO ligand precursor	77

2.3.2.	Attempts to synthesize ruthenium OM catalyst containing the NHC-NHO ligand.....	78
2.3.3.	Synthesis of rhodium(I) NHC complexes	80
2.3.4.	Synthesis of palladium(II) NHC-NHO complex	85
2.3.5.	Conclusions	87
2.4.	Summary and prospects.....	89
3.	NHC ligands bearing parallelly-stacked aromatics for efficient OM catalysts in tetrasubstituted carbon-carbon double bond formation	91
3.1.	Objectives.....	91
3.2.	Synthesis of NHC precursors	91
3.3.	Synthesis of ruthenium catalysts	94
3.4.	Evaluation of electronic and steric properties of new NHC ligands and catalysts.....	95
3.5.	Precatalysts' stability.....	100
3.6.	Computational study.....	101
3.7.	Catalytic activity studies.....	105
3.8.	Conclusions	110
3.9.	Prospects.....	110
4.	CM of technical grade methyl oleate for the synthesis of bio-based polyesters and polyamides	
	113	
4.1.	Objectives.....	113
4.2.	Catalysts screening and synthesis of dimethyl octadec-9-enedioate	113
4.3.	Polycondensation studies.....	114
4.4.	Conclusions	115
5.	Experimental section	117
5.1.	Materials and methods.....	117
5.2.	Supporting information for Chapter 2	118
5.2.1.	Axis A.....	118
5.2.1.1.	General considerations	118
5.2.1.2.	Synthesis of ruthenium complexes Ru-56 – Ru-59	118
5.2.1.3.	Attempts to install an alkylidene moiety	121
5.2.1.4.	Synthesis of complex Ru-60.....	122
5.2.1.5.	Attempted catalysis	123
5.2.2.	Axis B	124
5.2.2.1.	General considerations	124
5.2.2.2.	Attempts to synthesize an NHC-NHO precursor 38.....	124
5.2.2.3.	Synthesis of the NHC-NHO precursor 48	125

5.2.2.4.	Attempts to synthesize ruthenium OM catalyst.....	128
5.2.2.5.	Synthesis of thiourea 49 and characterization of the side product 50	128
5.2.2.6.	Synthesis of rhodium-NHC complexes	129
5.2.2.7.	Synthesis of the NHC-NHO palladium complex Pd-3	130
5.3.	Supporting information for Chapter 3	131
5.3.1.	General considerations	131
5.3.2.	Synthesis of benzimidazolium precursors	132
5.3.2.1.	Synthesis of benzimidazolium salt 77	132
5.3.2.2.	Synthesis of the phenyl derived benzimidazolium salt 67.....	132
5.3.2.3.	Synthesis of <i>N</i> -phenylbenzimidazole 66 using Buchwald-Hartwig amination ...	135
5.3.2.4.	Synthesis of the pentafluorophenyl derived benzimidazolium salt 71	136
5.3.2.5.	Resolved synthetic obstacles during the synthesis of 71	139
5.3.3.	Synthesis of ruthenium catalysts	140
5.3.3.1.	Synthesis of Ru-67	140
5.3.3.2.	Synthesis of Ru-68	141
5.3.3.3.	Synthesis of Ru-69	142
5.3.4.	Synthesis of rhodium complexes.....	142
5.3.4.1.	Synthesis of rhodium-NHC-COD complexes	142
5.3.4.2.	Synthesis of rhodium-NHC-carbonyl complexes.....	144
5.3.5.	Synthesis of selenoureas.....	146
5.3.5.1.	Synthesis of compound Se-1	146
5.3.5.2.	Synthesis of compound Se-2	147
5.3.5.3.	Synthesis of compound Se-3	147
5.3.5.4.	Synthesis of compound Se-4	148
5.3.6.	Stability tests of ruthenium complexes.....	148
5.3.6.1.	CD ₂ Cl ₂ at ambient temperature	148
5.3.6.2.	C ₆ D ₆ at 80 °C.....	149
5.3.7.	Isolation of the decomposition product Ru-70	151
5.3.8.	Catalysis	152
5.3.8.1.	GC analysis.....	152
5.3.8.2.	RCM of 78a – time-conversion plots	154
5.3.8.3.	Substrate scope – RCM	156
5.3.8.4.	RCM of 84a	157
5.3.8.5.	Substrate scope – CM	159
5.3.8.6.	Substrate scope – enyne metathesis.....	162

5.4.	Supporting information for Chapter 4	164
5.4.1.	General considerations	164
5.4.2.	Self-CM of methyl oleate	164
5.4.2.1.	Catalysts screening – general procedure	164
5.4.2.2.	GC analysis.....	164
5.4.2.3.	Synthesis of dimethyl <i>E</i> -octadec-9-enedioate	166
5.4.3.	Polycondensation reactions	166
5.4.3.1.	General procedure	166
5.4.3.2.	End group analysis	168
6.	References	169

1. State-of-the-art overview

1.1. General introduction to catalysis

No doubt catalysis is one of the most relevant tools used in the chemical industry, allowing to obtain a myriad of sometimes otherwise inaccessible molecules. It has been estimated that 90 % of all chemical processes utilize catalysis.^[1] Homogeneous catalysis has the advantage of more precise characterization of catalysts and intermediates which makes it more suitable for rational design. Among various catalytic processes, transition metal catalyzed reactions have emerged as one of the most significant and promising paths to the affordable synthesis of complex organic frameworks. Catalyst's auxiliary ligands play a significant role in defining the activity, selectivity and stability of the resulting catalysts.^[2]

Almost all chemical reactions consist of a series of elementary steps, defined as a direct transformation of reactant molecules into products through a single transition state. Such a sequence of elementary steps is called a reaction mechanism and when it describes forms of catalyst, it is referred to as a catalytic cycle (Figure 1A). Another useful representation is the energy profile which contains additional information about the thermodynamic parameters associated with each elementary step as well as their reaction barriers (Figure 1B). A precatalyst is a stable compound that is used to generate the active catalyst *in situ* by a sort of activation process. An off-loop species is defined as a complex in equilibrium with a catalytic intermediate but itself not involved in the catalytic cycle. Finally, when the formation of an off-loop species is irreversible, catalyst deactivation takes place and the formed compound is called a dead or deactivated catalyst.^[3]

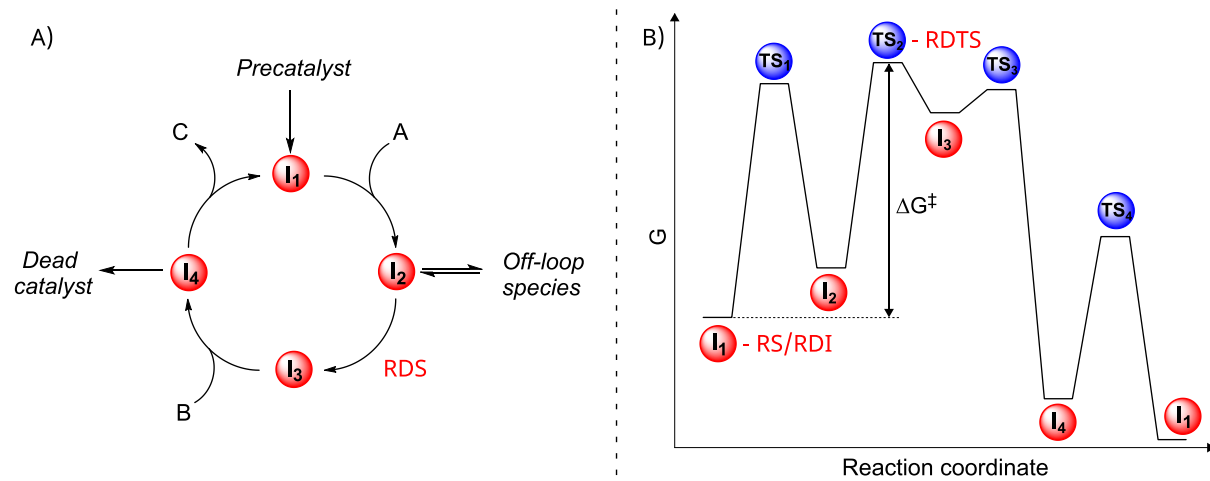


Figure 1 A) Graphical representation of a catalytic cycle. B) Energy profile of a representative catalytic cycle.

The rate-determining step (RDS) is the slowest step in the catalytic cycle. This step can be identified as the step associated with the highest free-energy transition state in the cycle (TS₂ on Figure 1B), however, the case is not always that simple. TS₂ is then called rate determining transition state (RDTS) and RDS is the transformation of I_2 to I_3 . Thus said, correct identification of RDS and RDTs is not always a straightforward exercise. Another important definition for a catalytic cycle is that of resting state (RS) sometimes referred to as rate determining intermediate (RDI). It is the form of the catalyst that is present at the highest concentration among all the catalytically active species and as such it has the highest chance of being experimentally observed. Identification of an RS can be deduced from an energy profile. In the considered example (Figure 1B), I_1 is RS since it is the only intermediate with lower free energy

than the proceeding and the following intermediates. The difference in energy between RDTs and RS is called cycle energy span (ΔG^\ddagger).^[3]

One measure of catalyst efficiency is the Turnover Number (TON). In the simplest case where only one molecule of substrate participates in the catalytic cycle, such as presented in Figure 1A, this can be defined as the number of moles of substrate that a mole of catalyst can convert (turn over) before becoming inactivated. The catalytic activity is defined by Turnover Frequency (TOF) as the number of substrate molecules converted per active site in a unit of time and can be defined as TON divided by time (equation 1).^[4] This parameter is usually time dependent and directly correlates to ΔG^\ddagger by Eyring equation (equation 2).^[3]

$$\text{TOF} = \frac{\text{TON}}{t} \quad (1)$$

$$\text{TOF} = \frac{k_B T}{h} e^{-\frac{\Delta G^\ddagger}{RT}} \quad (2)$$

1.2. N-Heterocyclic carbene (NHC) ligands

1.2.1. Carbene ligands

Carbenes are neutral divalent carbon species having six valence electrons. One can imagine the carbon atom being either linear or bent (Figure 2A). In the linear geometry, the carbene center is sp-hybridized with two nonbonding degenerate orbitals (p_x and p_y). In the bend molecule, the carbon atom changes to a sp^2 -type hybridization. The p_y orbital remains almost unchanged (it is usually called p_π), while the orbital that starts as pure p_x orbital is stabilized since it acquires some s character (it is therefore called σ). Most carbenes are bent and their frontier orbitals are systematically called σ and p_π . The carbene ground-state multiplicity is related to the relative energy of the σ and p_π orbitals. The singlet ground state is favored by a large σ - p_π separation, at least 2 eV energy difference is necessary to impose a singlet ground state, whereas a value below 1.5 eV leads to a triplet state carbene (Figure 2B). The ground-state spin multiplicity is a fundamental feature of carbenes that dictates their reactivity. Singlet carbenes possess a filled and a vacant orbital and therefore should have an ambiphilic character. On the other hand, triplet carbenes have two singly occupied orbitals and are generally regarded as diradicals.^[5]

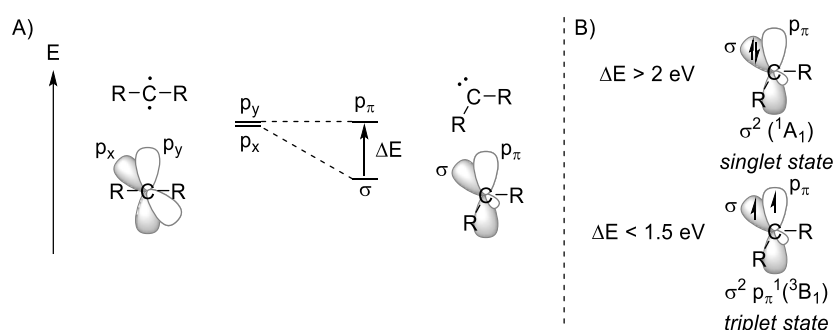


Figure 2 A) Relationship between the carbene bond angle and the nature of the frontier orbitals. B) Relationship between the ground-state multiplicity and the relative energy of σ and p_π orbitals of a carbon carbene atom.

1.2.2. A brief history of NHCs

Many carbenes are very short-lived species, depending on the nature of R groups. Indeed, nucleophilic carbenes were originally perceived as elusive laboratory curiosities. In 1962 Wanzlick postulated their

existence and proposed a method for their *in situ* formation.^[6] This led to their use as ligands in organometallic chemistry, as originally described in the seminal reports from 1968 by Wanzlick^[7] and Öfele.^[8] At last in 1988 was the first persistent singlet carbene **1** (Figure 3) isolated by Bertrand and coworkers.^[9] Three years later, this was followed by another milestone when Arduengo and coworkers obtained the first stable *N*-heterocyclic carbene (NHC) **2**.^[10] Since then, this area of chemistry has experienced tremendous growth finding many applications, e.g. in the field of transition metal catalysis.

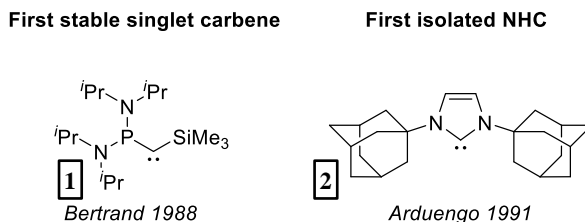


Figure 3 Structures of the first stable singlet carbene and the first isolated NHC.

1.2.3. General properties of NHC ligands

The electronic stabilization provided by the nitrogen atoms in the structure of an NHC is a very important factor. Nitrogen atoms adjacent to carbene carbon are at the same time σ -electron-withdrawing and π -electron-donating, stabilizing the structure both inductively by lowering the energy of the occupied σ -orbital and mesomerically by increasing the energy of p_{π} by donating electron density into the empty π -orbital (Figure 4A). As a result, the energy gap between the highest occupied molecular orbital (HOMO) and lowest unoccupied molecular orbital (LUMO) is substantial enough to render NHCs as singlet carbenes (Figure 4B). Moreover, the cyclic nature of NHCs forces the carbene carbon into a bent, more sp^2 -like arrangement which also helps to favor the singlet state.^[11]

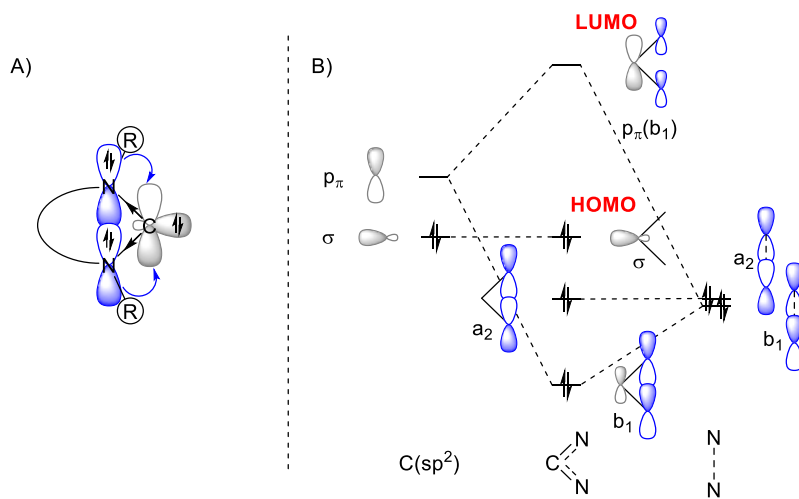


Figure 4 A) Ground-state electronic structure of an imidazol-2-ylidene, a most representative amongst NHCs. B) Simplified diagram of molecular orbitals of a diaminocarbene.

In general, all ligands are characterized by the electronic parameter, which contains major contributions from σ - or π -donation as well as π -accepting properties. With the rising energy of the HOMO of a ligand, its electron donating ability is increasing. Since the HOMO of an NHC is high in energy, those ligands are generally perceived as good σ -donors when coordinated to a metal (Figure 5A). Conversely, the electron acceptor capability of a ligand is characterized by the energy level of its LUMO. The lower the LUMO energy, the better the accepting property of a ligand. Originally NHC ligands were perceived as

not at all π -accepting. Now it is agreed that although their π - acidity is weak, the π -backbonding is not negligible (Figure 5B). As a result, the NHC-metal bond is considered singular with a delocalized double bond in the N-C-N unit of the NHC and throughout this thesis such representation is utilized (Figure 5C).^[12]

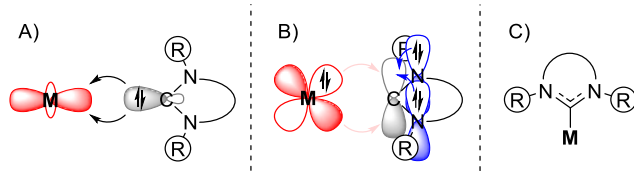
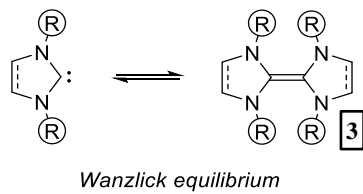


Figure 5 A) Strong σ -bonding of an NHC with metal. B) Weak π -accepting property of an NHC in a metal complex. C) Representation of an NHC-metal bond used throughout this thesis.

Free NHC can react with itself to form the dimeric form **3** (Scheme 1). The reaction equilibrium is influenced by the steric bulk of the R group,^[13,14] the nature of NHC (for example its backbone) and the way of its generation (as the reaction can be catalyzed by electrophiles).^[15] In the original work of Wanzlick only dimeric form was isolated^[6] whereas the groundbreaking work of Arduengo featured the free NHC form.^[10]



Scheme 1 Dimerization reaction of NHC.

There are other types of NHCs than the presented so far imidazol(in)ylidene. Figure 6 contains a non-exhaustive list of such examples. By changing the backbone either benzimidazolylidene, diamidocarbene (DAC) and triazolylidene can be obtained. Furthermore, the second nitrogen atom can be replaced by either a carbon atom to give cyclic alkyl amino carbene (CAAC) and abnormal carbene or by other heteroatoms such as sulfur (thiazolylidene) or oxygen (oxazolylidene).

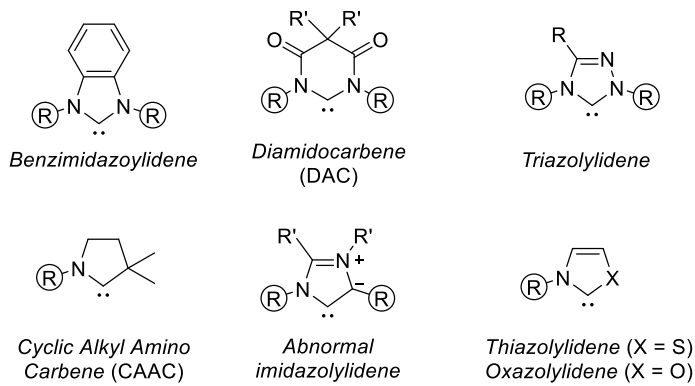
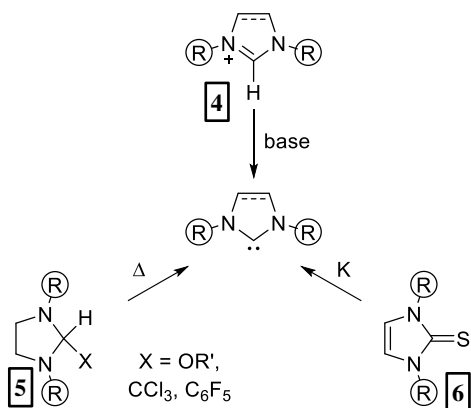


Figure 6 A non-exhaustive list of other NHC ligands.

1.2.4. Methods for the synthesis of NHCs

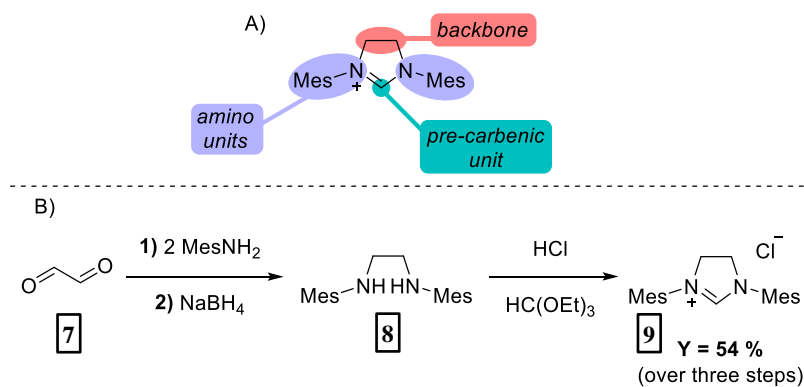
As reported by Wanzlick in his original work, NHCs can be obtained by thermal elimination of chloroform from 2-trichloromethylimidazolidine (**5**).^[6] Since then, examples of the removal of other volatile byproducts, e.g. alcohols or pentafluorobenzene, have been reported.^[16,17] This methodology appears

quite straightforward to obtain NHCs although it is limited to saturated imidazolinylidenes. Another method for NHC formation was reported by Kuhn and coworkers in 1993.^[18] This implied a reduction of corresponding NHC thiourea derivative **6** with potassium in boiling tetrahydrofuran (THF). Finally, in the pioneering work of Arduengo and coworkers, the 1,3-diadamantylimidazolylidene (**2**) was obtained by deprotonation of the corresponding imidazolium salt **4** using sodium hydride.^[10] Since there are numerous methods to synthesize azolium salts,^[19] their deprotonation is by far the most commonly utilized method to obtain NHCs. All three mentioned ways to synthesize NHCs were summarized in Scheme 2.



Scheme 2 Methods for the synthesis of NHCs.

An azolium NHC precursor is constructed by three distinct subunits, a pre-carbenic unit, an amino unit, and a backbone functionality (Scheme 3). Each synthon can be introduced at a different step, thus so far a myriad of synthetic protocols have been reported.^[19] An example of the synthesis of 1,3-dimesitylimidazolinium chloride (**9**) is presented in Scheme 3. Starting from backbone synthon – glyoxal (**7**), a connection with an amino unit (mesityl amine) is performed. In the second step, the resulting imine is reduced to the corresponding aniline **8**. At last, the imidazolinium cycle is introduced utilizing triethyl orthoformate, a very popular C1 synthon for such synthesis.^[20]



Scheme 3 An example of the synthesis of NHC precursor.

1.2.5. Determination of NHC's electronic parameters

Ligand electronic parameters are important factors determining the properties of resultant NHC-metal complexes. That is why much effort has been put into quantitative characterization and comparison of ligand electronic properties. In 1970 Tolman introduced a method that was later named Tolman electronic parameter (TEP).^[21] CO stretching frequency in tetrahedral complexes of the type Ni(CO)₃L is

measured which correlates with ligand electronic donation. A stronger net donor makes the complex more electron-rich, increasing the amount of backdonation from metal d orbital to π^* of CO and elongating the carbon-oxygen bond (Figure 7). Thus, a smaller wavenumber in infrared (IR) spectroscopy is obtained. Conversely, for a weaker electron donor higher wavenumber is observed. However, the notorious toxicity and low boiling point of $\text{Ni}(\text{CO})_4$ pose a severe limitation to this method. That is why much less toxic complexes *cis*- $\text{Rh}(\text{NHC})(\text{CO})_2$ or *cis*- $\text{Ir}(\text{NHC})(\text{CO})_2$ replaced the parent $\text{Ni}(\text{CO})_3\text{L}$. The new scales were correlated to TEP with linear regression (equation 3 and 4),^[22] which allowed for a direct comparison of a broader library of ligands and nowadays TEP is the most frequently reported electronic parameter for NHCs and other L-type ligands.

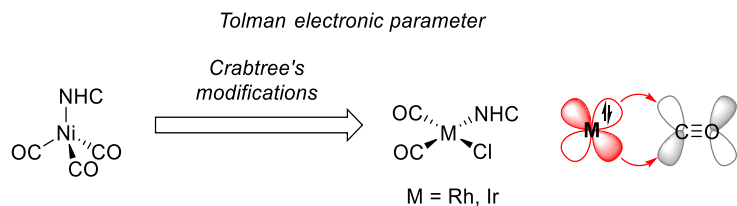


Figure 7 Tolman electronic parameter – a measure of NHC electronic donation.

$$\text{Rh to Ni: } \text{TEP}[\text{cm}^{-1}] = 0.8001 \cdot \tilde{\nu}_{\text{CO}}^{\text{av}}(\text{Rh})[\text{cm}^{-1}] + 420.0[\text{cm}^{-1}] \quad (3)$$

$$\text{Ir to Ni: } \text{TEP}[\text{cm}^{-1}] = 0.8475 \cdot \tilde{\nu}_{\text{CO}}^{\text{av}}(\text{Ir})[\text{cm}^{-1}] + 336.2[\text{cm}^{-1}] \quad (4)$$

TEP is a measure of ligand's net electronic donation, meaning σ -donation with subtracted π -accepting properties. To differentiate NHC electrophilicity (π -acidity) from nucleophilicity (σ -donation) other electronic parameters have been developed. To characterize NHC ligands π -acidity two nuclear magnetic resonance (NMR) scales were constructed based on either ^{31}P or ^{77}Se chemical shift of the corresponding chemical probes. NHC phenylphosphinidene adducts (Figure 8A)^[23] and selenoureas (Figure 8B)^[24] were employed as such probes. Both NMR scales are based on a similar concept. Two mesomeric forms A and B of NHC adducts can be envisaged. Weak π -acceptors would adopt an electronic situation closer to form B, leading to an electron rich phosphorus or selenium atom. This in turn would result in an upfield shift ^{31}P or ^{77}Se NMR signal. Form A is dominant with good π -acceptors leading to a deshielded nuclei and downfield shifted ^{31}P or ^{77}Se NMR signals are observed.

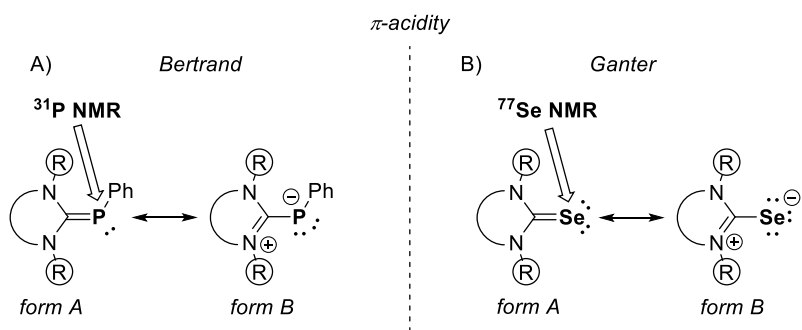


Figure 8 A) Mesomeric forms of NHC phenylphosphinidene adduct. B) Mesomeric forms of selenourea probe.

Attempts to quantify a ligand's sole σ -donation were also made. The method proposed by Huynh utilizes the ^{13}C chemical shift of the carbene carbon atom in palladium(II)-benzimidazolylidene complexes as a probe for the measurement of the σ -donor strength of the additional NHC ligand of interest (Figure 9A). It was found that a stronger donating ligand induces a downfield shift, while a weaker donor results in

an upfield shifted signal of the Huynh electronic parameter (HEP). Generally, ^{13}C NMR signals show very little line broadening when compared to bands in IR spectroscopy and arguably HEP is detected with greater accuracy.^[12,25,26] Ganter and coworkers proposed that the corresponding heteronuclear $^1\text{J}(\text{C}-\text{H})$ coupling constant of an azolium salt could be potentially used to determine the σ -donating ability of the corresponding NHC (Figure 9B).^[27] The magnitude of the $^1\text{J}(\text{C}-\text{H})$ coupling constants correlates to the s-character of the C–H bond and inversely correlates with the σ -donor strength of the parent NHC. Thus, a weaker donor would have a larger $^1\text{J}(\text{C}-\text{H})$ value indicating a larger s-character of the carbene lone pair (σ -orbital). $^1\text{J}(\text{C}-\text{H})$ coupling constants can be conveniently obtained from ^{13}C satellites of the ^1H NMR spectrum.^[28] It must be noted that both counteranions and solvents influence the chemical shift of the C–H bond in an azolium salt and possibly also its coupling constant. Thus, this data should be treated with caution to avoid misinterpretations. More detailed studies are required, but all future comparisons should only be systematically made among salts bearing the same anion, which are measured under identical conditions.^[12]

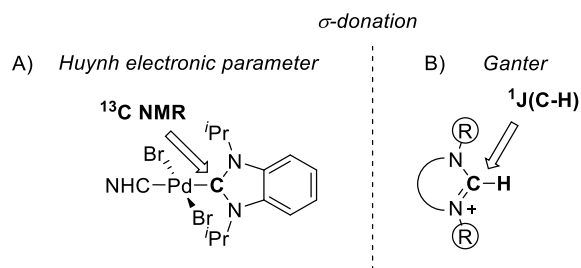


Figure 9 A) Huynh electronic parameter (HEP). B) $^1\text{J}(\text{C}-\text{H})$ coupling constant of an azolium salt as a measure of σ -donation.

The last described here electronic parameter was introduced by Lever and coworkers. The Lever electronic parameter (LEP) is based on the electrochemical E_0 value for various redox couples in a series of $\text{Ru}^{\text{III}}/\text{Ru}^{\text{II}}$ complexes containing the ligands of interest (Figure 10).^[29] Whereas LEP is widely employed to evaluate electronic properties of classical Werner-type ligands, it has not been determined for many NHC ligands.

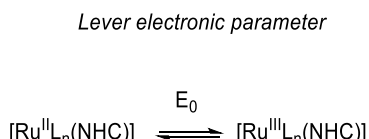


Figure 10 Lever electronic parameter (LEP).

1.2.6. Determination of NHC's steric properties

To determine a steric hindrance of phosphine ligands, cone angle is the most commonly utilized parameter.^[30] Since an NHC does not resemble a cone, the need has arisen for an another measure of such ligand steric bulk. The “buried volume” method, developed by Nolan, Cavallo, and co-workers, elegantly quantifies the steric demand of various NHCs using a single parameter only.^[31–34] Around the metal center a dome of 3.5 Å radius is constructed (Figure 11A). The percent buried volume (% V_{bur}) represents the part of the half-sphere that is buried by the atoms of the ligand under investigation. The more sterically demanding a ligand is, the larger the % V_{bur} value is. Ideally the % V_{bur} should be reported of a complex of linear geometry, such as (NHC)AuCl, (NHC)AgCl, or (NHC)CuCl, since the steric influence of additional spectator ligands on the metal center is minimized.^[35] Additionally to the value of % V_{bur} SambVca, a free web application, provides a topographic steric map (Figure 11B).^[36]

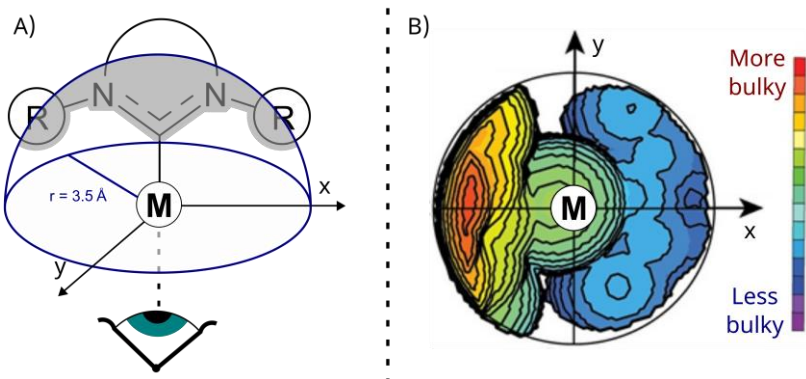
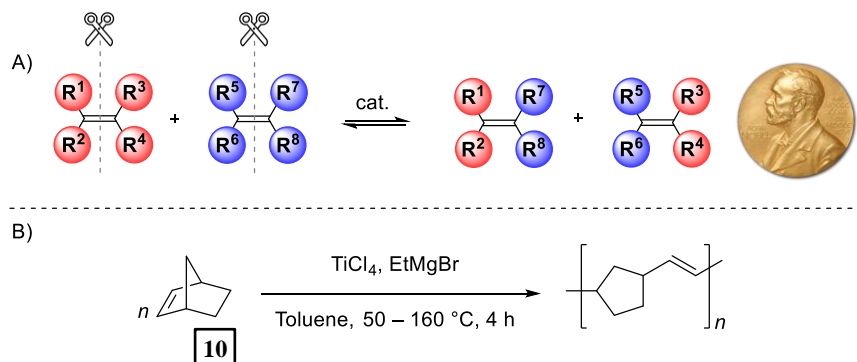


Figure 11 A) Graphical illustration of the buried volume (%Vbur) concept. B) Topographic steric map provided by the Sam-bVca web application.

1.3. Olefin metathesis (OM)

Olefin metathesis (OM), sometimes referred to as alkene metathesis, is a carbon skeleton redistribution around an unsaturated carbon-carbon double bond by its scission and regeneration (Scheme 4A). The reaction is catalyzed by a transition metal complex. OM is a reversible reaction and as such its chemical equilibrium is receptive to the change in conditions according to Le Chatellier's principle. This can be used to drive the reaction toward desired products. Historically, the first described example of OM reaction was the polymerization of norbornene (**10**) reported in 1955 in DuPont laboratories (Scheme 4B).^[37] Considering ruthenium-based OM catalyst, the impact made by NHC ligands on this domain was arguably the greatest of all when compared with other transition metal catalysis. In 2005 Chauvin, Grubbs and Schrock were honored with The Nobel Prize in Chemistry for the development of the metathesis method in organic synthesis.



Scheme 4 A) Reaction scheme of the olefin metathesis. B) Polymerization of norbornene (**10**).

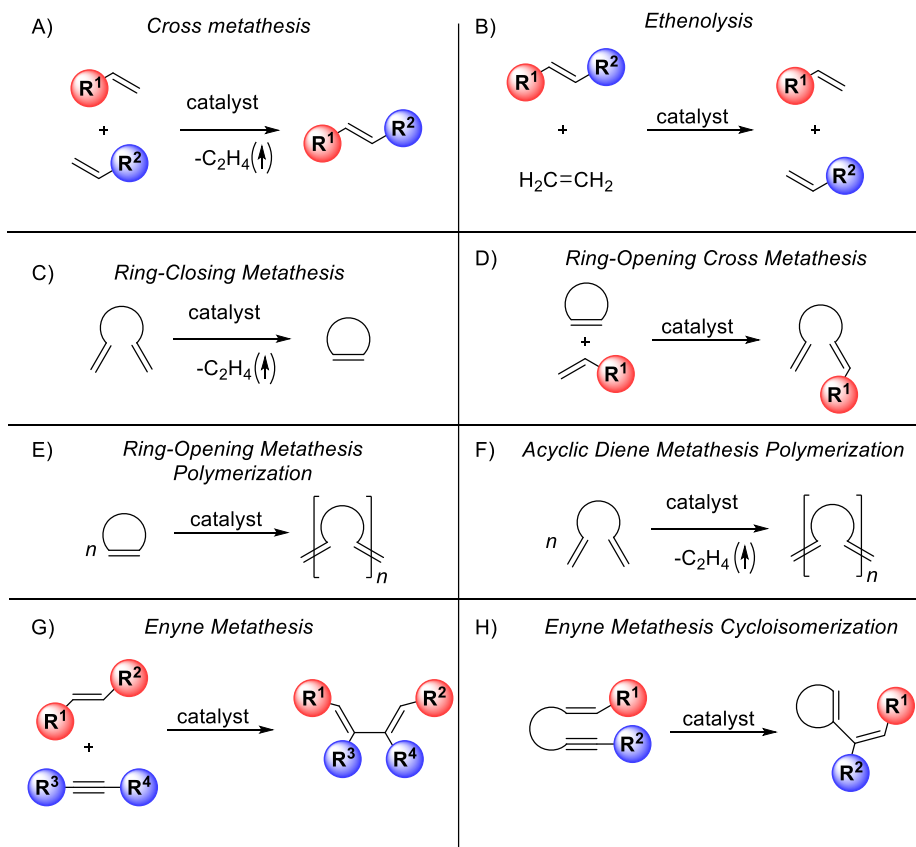
1.3.1. Types of OM reactions

Several types of OM have been distinguished based on the nature of substrates used for the reaction. Cross Metathesis (CM) is a reaction between two alkene molecules resulting in new products. The most common case is coupling between two α -olefins (Scheme 5A). The main driving force of this OM variant is the emission of a gas product – ethylene. Also, a popular variant is a reaction between α -olefin and internal alkene. In this case, the reaction equilibrium can be pushed by utilizing an excess of an internal olefin partner. A special case of CM is the reaction of internal olefin in a high pressure of ethylene which shifts reaction equilibrium towards α -alkene products. This variant is called an “ethenolysis” reaction (Scheme 5B).

Ring Closing Metathesis (RCM) is an intramolecular OM reaction that leads to a cyclic product formation (Scheme 5C). Frequently the ethylene release is the driving force of this OM variant. Additionally, the formation of thermodynamically favored five and six-membered cycles can help in pushing the reaction equilibrium toward products. Thus said, the synthesis of larger, even macrocyclic compounds, is known and utilized. The reversed reaction to RCM is ring-opening cross-metathesis (Scheme 5D). To drive the reaction towards a favorable outcome usually an excess of α -olefin is used together with the stress release of a cyclic substrate.

Polymerization with the use of OM is also known. The driving force can be either strain release of the cyclic substrate, the reaction is thus called ring-opening metathesis polymerization (ROMP, Scheme 5E), or ethylene emission – acyclic diene metathesis polymerization (ADMET, Scheme 5F).

Last but not least, is the example of enyne metathesis where alkene reacts with alkyne (Scheme 5G) and its intramolecular version – enyne metathesis cycloisomerization also known as ring-closing enyne metathesis (RCEYM, Scheme 5H).



Scheme 5 Classification of OM reactions.

1.3.2. Mechanism of OM

One of the greatest contributions to the elucidation of the mechanism of OM was made by Chauvin and his student Hérisson in 1971.^[38] The authors proposed that metal alkylidenes are able to catalyze this reaction going through a metallacyclobutane intermediates (Figure 12A). The first part of the hypothesis was confirmed by Casey and Burkhardt when in 1974 the authors reported tungsten alkylidene complex **W-1** that was able to exchange its carbene fragment giving with isobutene (**11**) 1,1-diphenylethylene (**12**), and with (1-methoxyvinyl)benzene (**13**) producing complex **W-2** and compound **12** (Figure

12B).^[39] The existence of metallacyclobutane intermediates was unambiguously proven in 1980 when Grubbs and coworkers reported that the stable titanacyclobutane **14** (Figure 12C) is able to slowly catalyze OM,^[40] thus rejecting other proposed intermediates.^[41–45]

In summary, the accepted mechanism constitutes of the following steps (Figure 12A). Once alkylidene intermediate **I**₁ is formed (through catalyst activation with a substrate molecule), the alkene substrate coordinates to the metal center to give **I**₂. Through metallacyclobutane intermediate **I**₃, **I**₄ is formed which contains a coordinated molecule of product. After a product is released, methylidene intermediate **I**₅ is formed which next coordinates a molecule of substrate to give **I**₆. Going through metallacyclobutane intermediate **I**₇, **I**₈ is formed, which after ethylene release regenerates intermediate **I**₁.

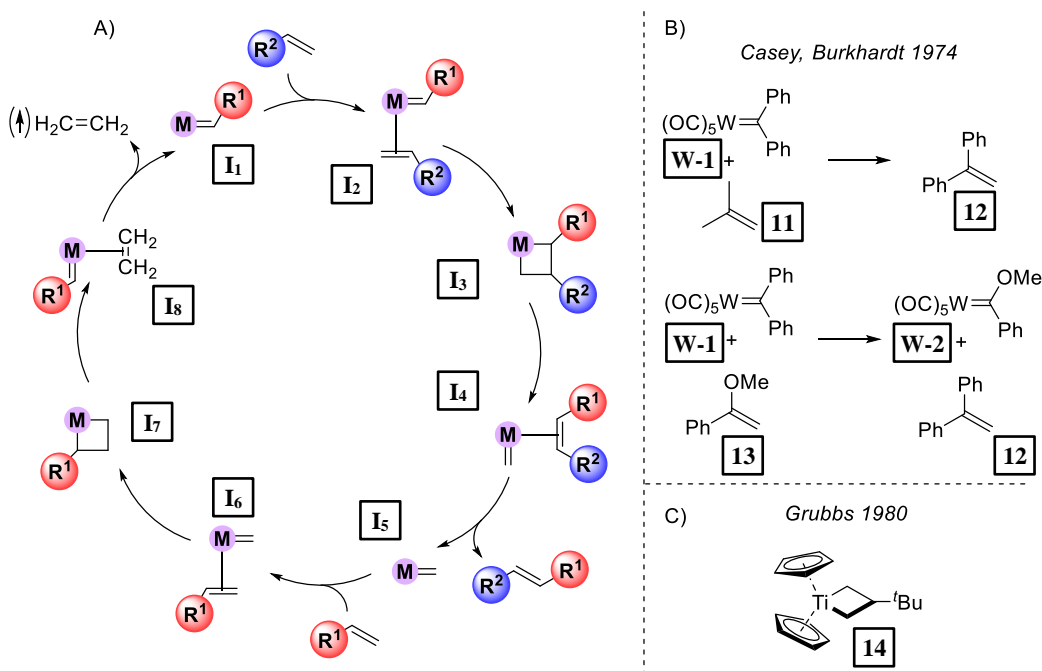
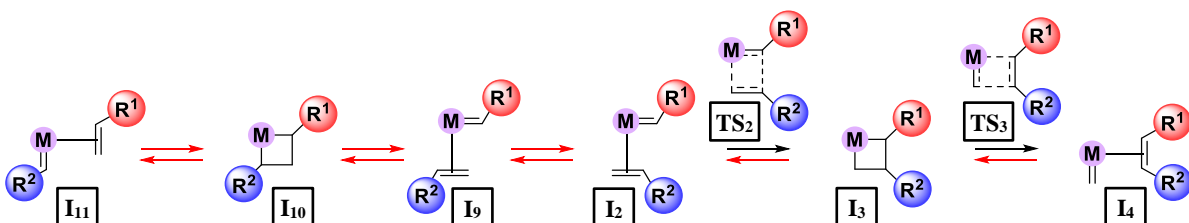


Figure 12 A) Mechanism of olefin metathesis. B) Evidence of carbene ligand exchange in a reaction with olefin. C) A stable titanacyclobutane able to slowly catalyze OM.

In general, RDTs of the reaction is connected to either formation or cycloreversion of metallacyclobutane intermediates (e.g. **TS**₂ or **TS**₃ on Scheme 6), although sometimes RDS can be a part of catalyst initiation. Every step of the mechanism is reversible, thus it is possible for metalacyclobutene intermediates (e.g. **I**₃) to undergo cycloreversion with the reformation of the starting alkylidene intermediate **I**₂.



Scheme 6 Productive versus degenerative metathesis events.

Additionally, one can also imagine a reverse orientation of olefin in the structure of **I**₉. In consequence, although this would lead to the formation of a new alkylidene species **I**₁₁, it would not lead to the formation of a new olefin. In general, any events which do not result in product formation are called non-productive or degenerate metathesis. The rate of nonproductive metathesis greatly exceeds that of the

productive and degenerate reactions can provide additional opportunities for a catalyst to decompose and, therefore, can decrease its efficiency.^[46]

1.3.3. Schrock type catalysts

Developed in Schrock laboratories in 1980, complex **W-3** (Figure 13) was the first example of a well-defined metal-alkylidene complex used to catalyze OM.^[47] Later on, other reports featured molybdenum-based alkylidene complexes (e.g. **15**, Figure 13).^[48] Customary tungsten and molybdenum-based alkylidene complexes are called Schrock catalysts and certainly represent a group of exceptionally active OM catalysts (14 e⁻ molybdenum complexes). However, arguably NHC ligands did not make a pronounced impact on this domain and because of it, the topic of Schrock catalysts will not be elaborated here any further.

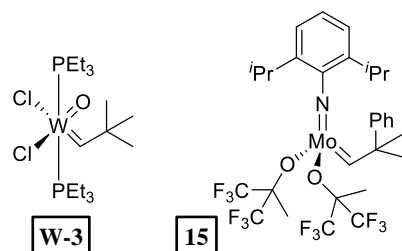


Figure 13 Examples of Schrock catalysts.

1.3.4. Classification of ruthenium-based OM catalyst

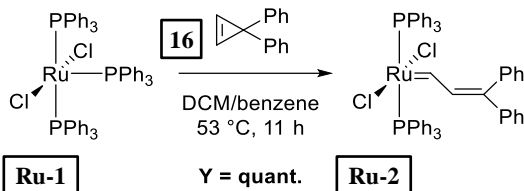
Ruthenium-based catalysts were classified based on their alkylidene and auxiliary ligands. Ruthenium(II) benzylidene complexes are commonly called Grubbs catalysts. Indenylidene catalysts feature 3-phenyl-1-indenylidene functionality and Hoveyda-Grubbs complexes bear a chelating *o*-isopropoxybenzylidene ligand. First generation features only phosphine ligands with PPh₃ and PCy₃ being the most common. The second generation of each catalyst group bears one NHC ligand. Naturally, every ligand has an impact on catalyst activity, stability and effectiveness, and those effects will be discussed later on. This quick overview of ruthenium-based catalysts is summarized in Figure 14.

	<i>Grubbs</i>	<i>Indenylidene</i>	<i>Hoveyda-Grubbs</i>
<i>1st Generation</i>	$L^1, L^2 = \text{PCy}_3 \text{ or } \text{PPh}_3$	$L^1, L^2 = \text{PCy}_3 \text{ or } \text{PPh}_3$	$L^1 = \text{PCy}_3 \text{ or } \text{PPh}_3$
<i>2nd Generation</i>	$L^1 = \text{NHC}$ $L^2 = \text{PCy}_3 \text{ or } \text{PPh}_3$	$L^1 = \text{NHC}$ $L^2 = \text{PCy}_3 \text{ or } \text{PPh}_3$	$L^1 = \text{NHC}$

Figure 14 Classification of ruthenium-based catalysts.

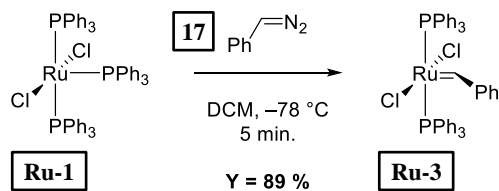
1.3.5. Methods for the synthesis of ruthenium alkylidene complexes

Historically, the first well-defined ruthenium-based alkylidene complex **Ru-2** was obtained by Grubbs and coworkers from $\text{RuCl}_2(\text{PPh}_3)_3$ (**Ru-1**) precursor and 3,3-diphenyl cyclopropene (**16**, Scheme 7).^[49] The major drawback of this synthetic protocol is the difficulty of the synthesis and stability of diphenyl cyclopropene,^[50] although alternative methods for the preparation of **Ru-2** type alkylidene complexes have been reported.^[51,52]



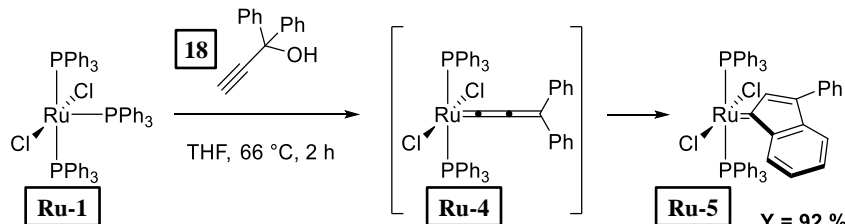
Scheme 7 Synthesis of the first ruthenium-based alkylidene complex **Ru-1**.

The second method to introduce alkylidene is the reaction of a ruthenium precursor **Ru-1** with diazo-methane derivative **17** (Scheme 8).^[53] This reaction brings certain risks during its scaleup due to the explosive nature of **17**. Nevertheless, the PCy_3 derivative of **Ru-3** (**Ru-8**, Scheme 11) is one of the most common, commercially available catalysts.



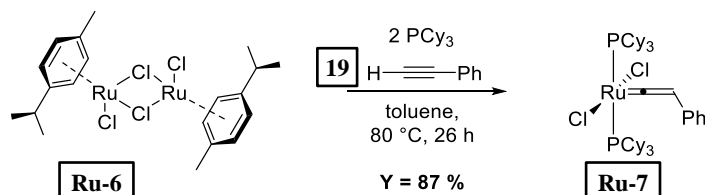
Scheme 8 Synthesis of ruthenium alkylidene catalyst using phenyldiazomethane (**17**).

One of perhaps the most industrially viable methods to obtain a ruthenium alkylidene complex is the reaction of **Ru-1** with propargyl alcohol **18** (Scheme 9). This reaction results in the formation of indenylidene catalyst **Ru-5** and not as initially thought allenylidene complex **Ru-4**,^[54] which is an intermediate *en route* to the formation of **Ru-5**.^[55] Thus said, methods for the preparation of 18e^- cationic allenylidene complexes by reaction with **18** are known.^[56-58]



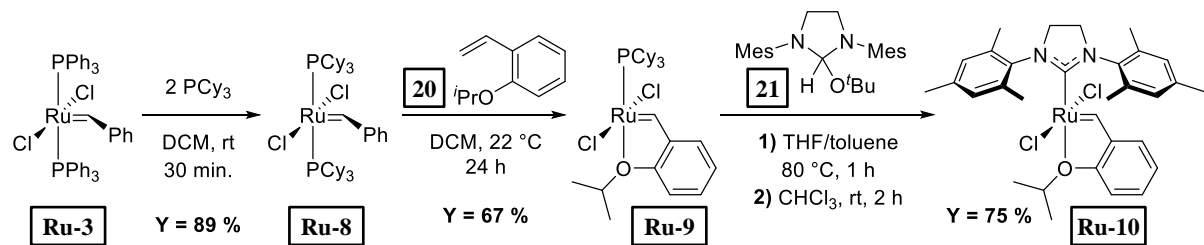
Scheme 9 Synthesis of indenylidene catalyst **Ru-5**.

The last method described here utilized dimer **Ru-6** as the ruthenium precursor to obtain vinylidene complex **Ru-7** in the reaction with phenylacetylene (**19**) and PCy_3 (Scheme 10).^[59]



Scheme 10 Synthesis of vinylidene ruthenium complex **Ru-7**.

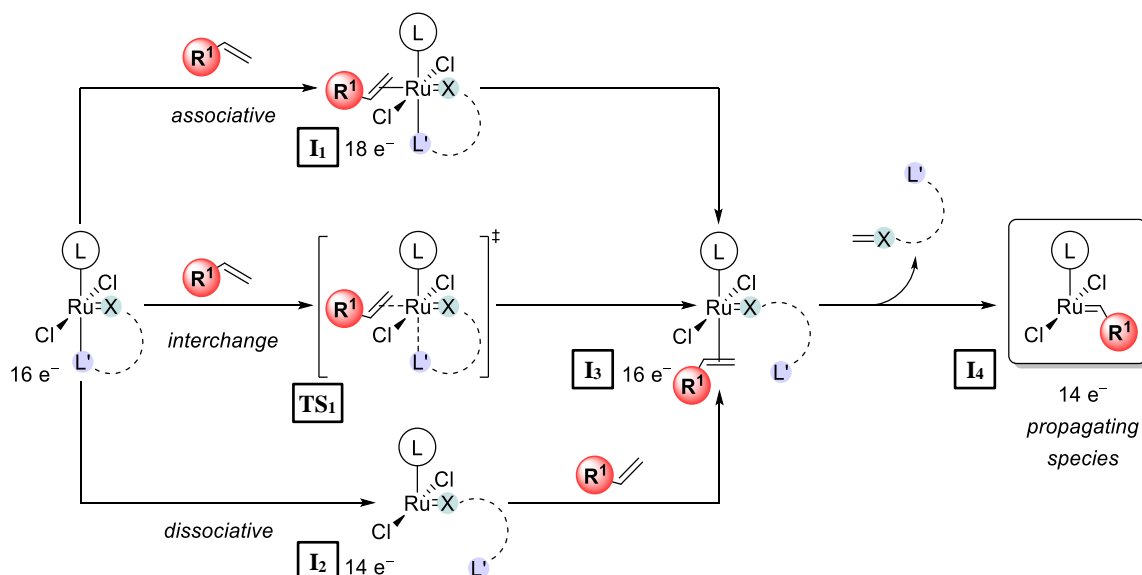
In summary, the four mentioned alkylidene precursors (**16 – 19**) can be used to obtain active OM catalysts (**Ru-2**, **Ru-3**, **Ru-5** and **Ru-7**). These complexes can serve as precursors for other OM catalysts, which can be obtained by straightforward ligand exchange. For example, **Ru-3** can react with PCy_3 to give complex **Ru-8** containing the new phosphine ligands.^[53] Furthermore, benzylidene in **Ru-8** structure can be exchanged to *o*-isopropoxybenzylidene in a reaction with *o*-isopropoxystyrene (**20**) to give Hoveyda-Grubbs complex **Ru-9**.^[60] Naturally, NHC ligands can be installed as well. The reaction of **Ru-9** and NHC precursor **21** at elevated temperature gives second generation Hoveyda-Grubbs catalyst **Ru-10** (Scheme 11),^[61] which is one of the most popular, general purpose NHC OM catalysts.



Scheme 11 Synthesis of the second generation Hoveyda-Grubbs catalysts **Ru-10**.

1.3.6. Mechanism of initiation of ruthenium-based precatalysts

Most precatalysts are 16e^- species that have to first lose a ligand to generate a 14e^- alkylidene **I₄** (Scheme 12), which is the propagating species participating in the catalytic cycle. The initiation rate of a precatalyst determines the rate at which active 14e^- species are generated, this factor has a significant impact on the overall rate of the reaction. For the sake of clarity, it is necessary to distinguish catalyst initiation referring to generation of **I₄**, from catalyst activity which generally refers to substrate consumption in time (defined with TOF).



Scheme 12 The mechanism of activation of ruthenium-based OM catalyst.

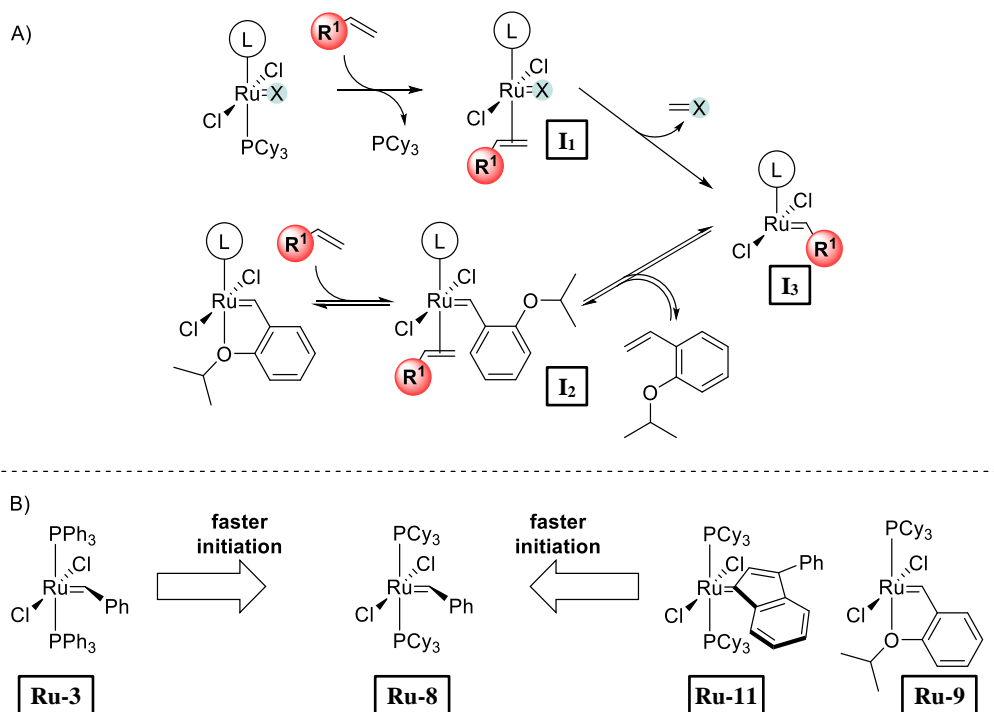
In the first step of catalyst initiation, olefin coordinates to ruthenium and a ligand is liberated to give intermediate **I₃** which can occur in three ways. Alkene can bind to a metal center forming 18e^- intermediate **I₁** which then liberates a ligand, this constitutes the associative pathway. Conversely, a ligand can first be released to give a 14e^- intermediate **I₂** which then binds olefin (dissociative pathway). Finally,

the interchange pathway assumes simultaneous alkene coordination and ligand de-coordination occurring through a single transition state **TS₁**. Once alkene-bonded intermediate **I₃** is formed (Scheme 12B), they undergo the first metathesis event releasing former alkylidene ligand in a form of an alkene and generating 14e⁻ propagating species **I₄** that enters a catalytic cycle, thus formerly constituting catalyst initiation.

1.3.7. Impact of ligands on first generation catalysts

The initiation of Grubbs-type complexes occurs *via* the dissociative pathway.^[50,62] In the case of first-generation, the initiation rate increases when bulkier and more electron donating phosphines are utilized. The effect of phosphine's Tolman angle (its bulkiness) is quite intuitive – more sterically challenging phosphine binds in a weaker fashion due to steric clash with other parts of the molecule. However, the electronic factor plays here a more important role. More electron donating phosphines exhibit a stronger *trans* effect and favor the dissociation of a second phosphine ligand by stabilizing 16e⁻ monophosphine olefin complex **I₁** (Scheme 13A), and more importantly the electron deficient 14e⁻ metallacyclobutane.^[63]

Compared to Grubbs benzylidene complexes, indenylidene moiety was shown to lead to a decrease in initiation rate. In fact, indenylidene catalysts are considered more thermally stable, exhibiting activity at increased temperatures. Importantly, introducing indenylidene moiety changes a catalyst initiation mechanism (formation of **I₁**) which varies from dissociative to interchange pathway, depending on the exact catalyst structure.^[64]



Scheme 13 A) Differences in catalyst activation. B) Impact of phosphine and alkylidene ligands on first generation catalysts.

The initiation mechanism of Hoveyda-Grubbs catalysts seems more complex and all three pathways were found to be operative, depending on the catalyst's exact structure, reaction conditions, substrate nature, etc. with the associative pathway being arguably the more common case.^[65–69] Interestingly,

contrary to Grubbs and indenylidene precatalysts, the activation of Hoveyda-Grubbs complexes occurs reversibly thus making precatalyst an off-loop species as well. Although a matter of former debate,^[70] proofs confirming the validity of this release-return or “boomerang” mechanism are quite conclusive.^[60,71–74] In general, the Hoveyda-Grubbs catalysts initiate slower than their Grubbs-type counterparts.^[75] This can be explained by the chelating nature of the *o*-isopropoxybenzylidene ligand and thus its lower lability than a monodentate phosphine.

1.3.8. Impact of ligands on second generation catalysts

Regardless of the nature of the precatalyst’s alkylidene ligand, the formed $14e^-$ propagating species are identical. Here the first advantage of NHC-based catalysts over the first generation can be explained. Compared with phosphines, NHCs bind stronger to metal providing more durable catalytic intermediates. Additionally, NHC’s *N*-substituents point towards the metal center offering higher steric protection than phosphine substituents ejected away from the metal. Having in mind the degenerate metathesis events this seems to have a pronounced impact ultimately resulting in more productive second-generation OM catalysts.

NHCs affect the catalyst activity as well. Although the second generation Grubbs catalyst **Ru-12** proved to be more active than the first generation **Ru-8**,^[76,77] later reports suggested that the initiation rate of the second generation is actually lower (Figure 15A).^[50,62] The kinetic results indicate that the initiation of **Ru-12** is so slow that it is rate determining whereas for **Ru-8** RDS occurs after catalyst initiation. The proposed explanation for this was that although phosphine dissociates faster in **Ru-8**, it can rebind more easily thus shifting reaction equilibrium towards off-loop species **I₂** (Figure 15B) when L is phosphine. Increased formation of off-loop species removes propagating species from the catalytic cycle thus impairing catalyst activity and productivity.^[50,78–80] This well explains why the second generation is more active although the initiation rates are lower when compared to the first generation.

However, the slower initiation of the second generation puzzled chemists for many years. Why does much stronger σ -donating than phosphine NHC ligand result in slower catalyst initiation? The relative *trans* effect should be higher than phosphines resulting in a weaker metal-phosphine bond. Even more confusion was added by the observation that more σ -donating than unsaturated 1,3-dimesitylimidazolylidene (IMes), saturated 1,3-dimesitylimidazolinylidene (SIMes) NHC ligand results in higher initiation rate of **Ru-13** (Figure 15A). Some propositions were made to explain those seemingly contradictory effects,^[80,81] with the report of Fogg and coworkers being perhaps the most elucidative.^[82] The authors proposed that long overlooked NHC π -acidity plays a crucial role in explaining those trends observed in catalyst initiation, as it impacts the π -backbonding of metal to phosphine. Compared with IMes, the SIMes ligand is more σ -donating with a $^1J(C-H)$ value of 206 Hz versus 225 Hz for IMes.^[27] Thus said, SIMes ligand is also more π -acidic with $\delta(^{77}Se)$ of the corresponding selenourea of 116 ppm versus 35 ppm for IMes.^[27] As a result, the net electronic donation of SIMes is slightly decreased since the TEP value for SIMes is 2051.5 cm⁻¹ and 2050.7 cm⁻¹ for IMes.^[83] More π -acidic NHC results in a weaker metal to phosphine π -backbonding and higher lability of phosphine ligand in **Ru-13**. Furthermore, NHCs are much less π -accepting when compared with phosphines thus explaining why **Ru-12** (or **Ru-13** for that matter) initiated slower than **Ru-8**. In summary, the ligand π -acidity well correlates with the observed trend in initiation rates.

Since for the second-generation the initiation step is RDS, there is room for improvement of catalytic activity by increasing the initiation rate. This can be achieved in several different ways (Figure 15C). It was found that more sterically demanding 1,3-di(2,6-diisopropylphenyl)imidazolinylidene (SIPr) NHC results in a faster initiation of catalyst **Ru-14**.^[84,85] Since Grubbs-type catalysts initiate via the dissociative mechanistic pathway, bulkier NHCs result in facilitated phosphine dissociation thus increasing catalyst initiation rate. Moreover, modifying phosphine ligands changes catalyst activity as well. Similar to the first generation, increasing phosphine's steric bulk increases the catalyst's initiation rate. Moreover, the electronic factors play a more important role, however, in a reversed manner than in the first generation. Less electron donating PPh_3 phosphine results in higher initiation of **Ru-15** due to a weaker ruthenium-phosphorous bond.^[50] Furthermore, perhaps one of the most outstanding approaches was reported by Grubbs and coworkers where the authors removed phosphine ligand entirely from the picture, replacing it with two pyridine ligands (**Ru-16**, Figure 15C).^[86] Pyridine ligands, especially those bearing electron withdrawing group (EWG) in meta position, are very labile and thus the catalytic activity of **Ru-16** increases.

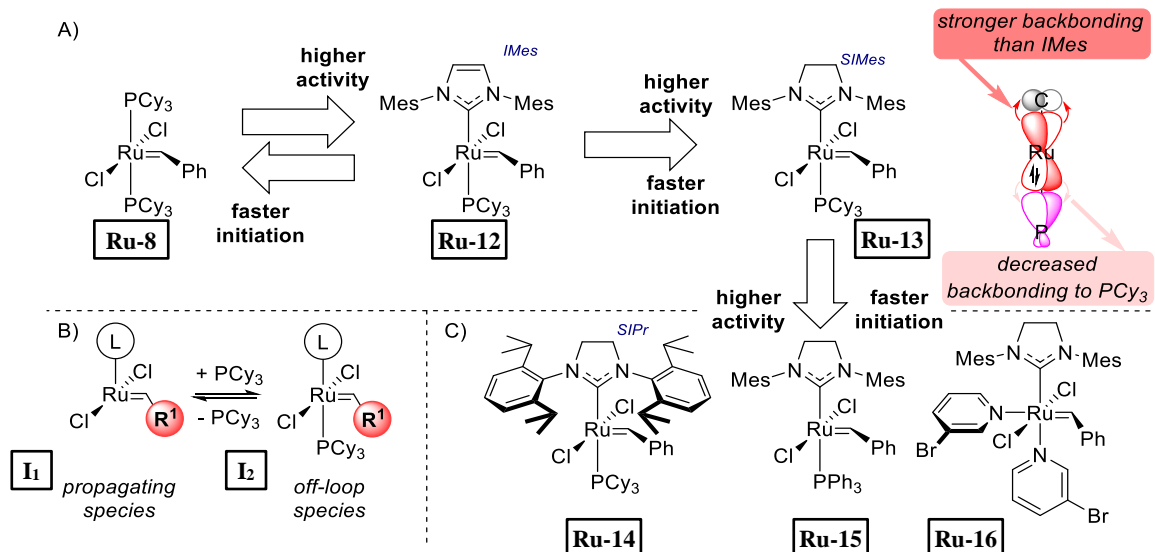


Figure 15 A) Impact of NHC ligands on second generation Grubbs catalysts. B) Catalyst deactivation by the formation of off-loop species. C) Methods to improve the initiation rate of Grubbs second generation catalysts.

However, the impact of NHC's electronic properties on the activity of the Hoveyda-Grubbs catalyst family is a subdomain that needs more systematic studies. It seems as though the scientific community has taken the solution of saturated NHCs, which worked well for second generation Grubbs complexes, and directly applied it to a second generation of Hoveyda-Grubbs complexes. In fact, it is difficult to find studies using IMes-derived Hoveyda-Grubbs catalysts^[87,88] or bearing other unsaturated NHC analogs. Clearly, increased π - acidity of saturated NHCs cannot be beneficial for the lability of metal-ether interaction since p_{π}^* orbitals of oxygen cannot interact with d orbitals of metal. In other words, the ether ligand can be considered a pure σ -donor, which is certainly not the case for phosphines. Thus said, possibly such an approach was not wrong since higher σ -donation and π - acidity of a saturated NHC should result in a stronger ruthenium-carbon bond thus giving more productive catalysts.

Nevertheless, the steric factors of NHCs have been examined. It was found that more sterically demanding SIPr NHC results in catalyst **Ru-17** (Figure 16) with hampered initiation when compared with SIMes analog **Ru-10**, although the catalytic productivity was improved.^[89] This observation would indicate the associative pathway of initiation since increased NHC's bulkiness would destabilize sterically congested

$18e^-$ intermediate. Such an effect is exactly opposite to Grubbs second generation catalysts for which more sterically demanding NHC increases catalysts initiation rate. However, as mentioned before for Hoveyda-Grubbs catalysts all three mechanistic pathways of initiation were reported to be operative under different reaction conditions.

Much more attention was put on the tuning of a benzylidene ligand (Figure 16). Installation of EWG (**Ru-18**) or bulky substituent (**Ru-19**) in the structure of benzylidene-ether ligand results in a more labile ruthenium-oxygen bond and faster catalyst initiation.^[89–92] Furthermore, the impact of the release-return mechanism on catalyst productivity was quite thoroughly examined. Postulated in the past was the hypothesis that the boomerang mechanism contributes to increased productivity of phosphine-free **Ru-10** when compared with its phosphine-containing counterpart **Ru-13**. Fogg and coworkers clearly demonstrated that the precatalyst **Ru-10** is indeed its RS, thus validating the occurrence of the release-return mechanism. Thus said, the same report disclosed that the impact of precatalyst reformation during catalysis does not contribute to **Ru-10** higher productivity. As mentioned previously, the increased formation of off-loop species removes propagating species from the catalytic cycle. Instead, the authors proposed that the higher productivity of **Ru-10** lies in the lack of a phosphine ligand. Phosphines can bind to propagating species thus creating off-loop species (**I₂**, Figure 15B). The difference is that those off-loop species are less prone to re-enter the catalytic cycle than the off-loop precatalyst **Ru-10**.^[73]

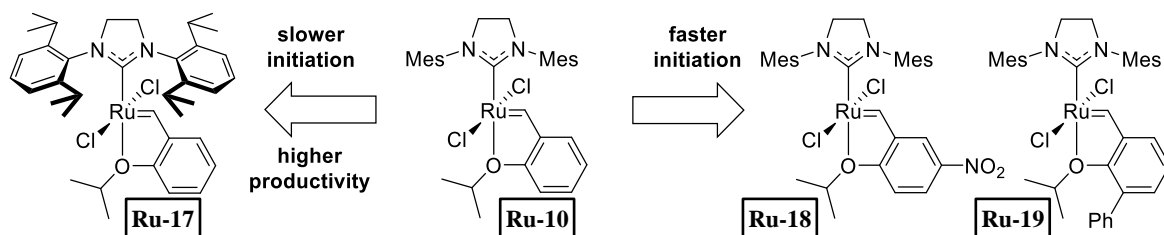
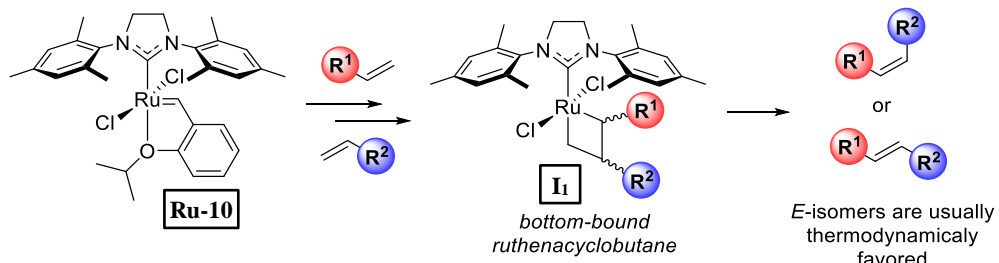


Figure 16. Impact of ligands on second generation Hoveyda-Grubbs catalysts.

1.4. Stereoselective OM

Olefin binding in catalytic intermediates can occur in two forms. One in which the alkene is bound *trans* to the L-type ligand (bottom-bound) and one in which the olefin is bound *cis* (side-bound). Naturally, the subsequently formed ruthenacyclobutane intermediates can also be either bottom-bound or side-bound. Research indicates that for standard NHC catalysts, the bottom-bound ruthenacyclobutanes **I₁** (Scheme 14) are predominant over the side-bound.^[93–95] Second-generation precatalysts tend to lead to higher *E*-selectivities in CM reactions, due to their ability to equilibrate *E/Z* mixtures of products to the thermodynamically favorable *E*-isomer (Scheme 14). However, the exact *E/Z* product ratio varies depending on the structure of an NHC ligand and the substrate reacted.^[85,96,97]

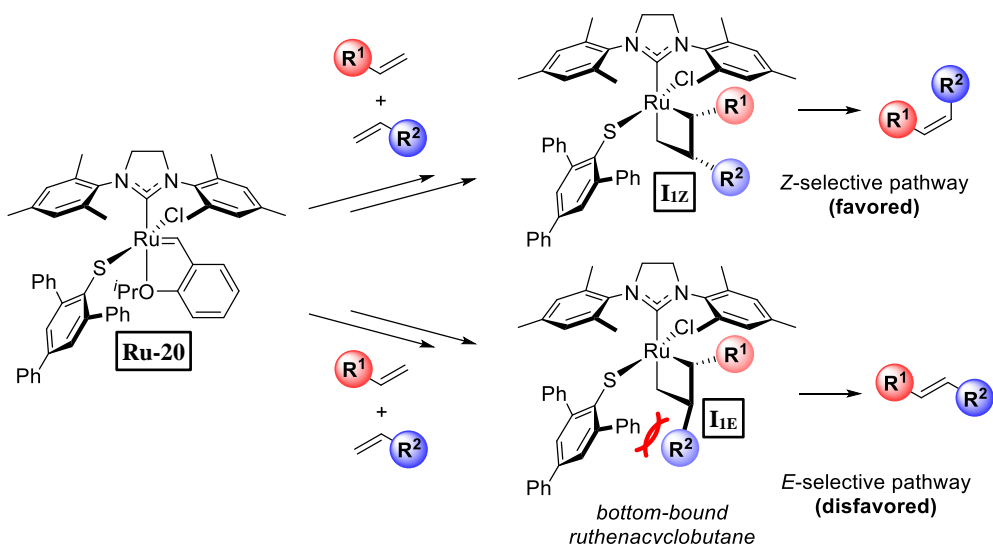


Scheme 14 Simplified mechanism of CM highlighting the challenge of the stereocontrol on product formation.

E/Z selectivity is one of the key aspects in OM since one isomer is typically desired in synthetic applications. Moreover, in polymer chemistry selectivity is necessary for a regular repeating structure. This chapter describes solutions for kinetically controlled stereoselective OM.

1.4.1. Thiophenolate Z-selective catalyst

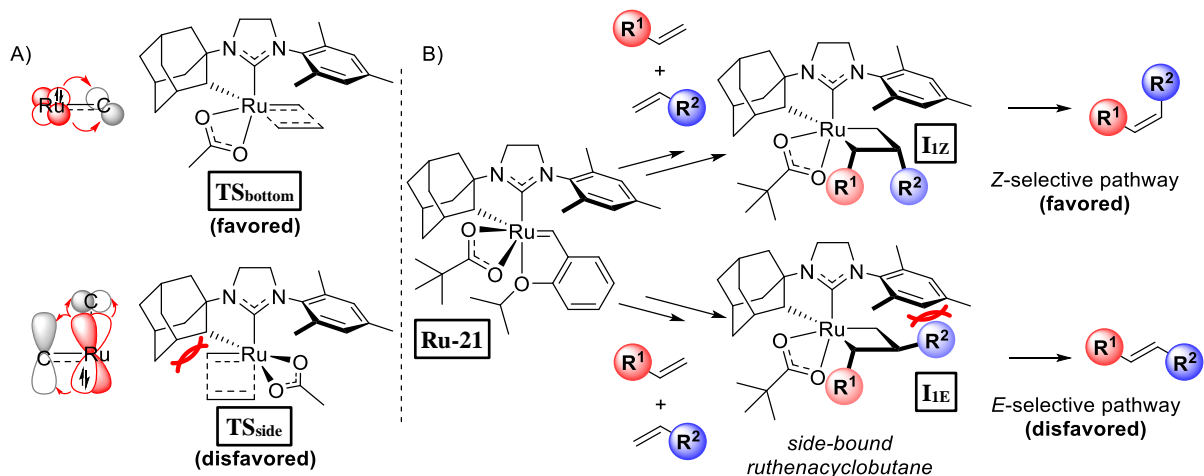
Jensen and coworkers proposed in 2013 a method for obtaining a *Z*-selective OM catalyst.^[98] In his approach, one of the chloride ligands in Hoveyda-Grubbs second generation catalyst **Ru-10** is replaced by the much bulkier X-type 2,4,6-triphenylthiophenolate ligand (complex **Ru-20**). The thiophenolate ligand imposes a steric hindrance on ruthenacyclobutanes **I_{IZ}** and **I_{IE}** (Scheme 15). As a result, the steric clash in the *E*-selective pathway disfavors the formation of *E*-products as opposed to the *Z*-selective pathway.^[99] This strategy led to the development of other types of *Z*-selective OM catalysts.^[100,101]



Scheme 15 Mechanistic explanation of thiophenolate catalyst **Ru-20** *Z*-selectivity.

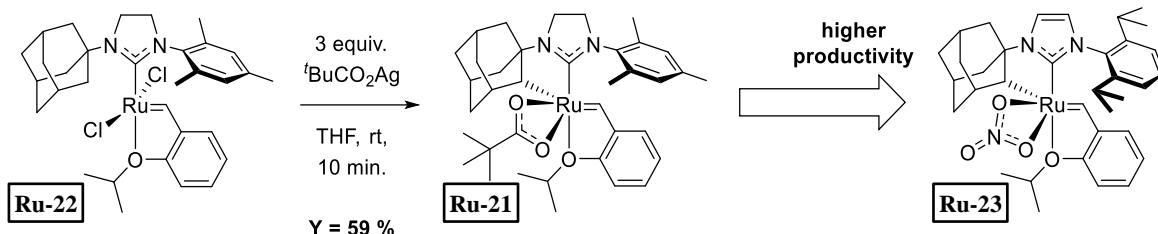
1.4.2. *Z*-selective catalyst bearing chelating LX-type NHC ligand

Arguably the most outstanding approach for *Z*-selective OM catalyst was presented by Grubbs and coworkers in 2011 when they obtained a second generation Hoveyda-Grubbs catalyst bearing a chelating LX-type NHC ligand.^[102] Compared to standard, monodentate NHCs, the chelating NHC results in the formation of side-bound ruthenacyclobutanes **I_{IZ}** and **I_{IE}** (Scheme 16B). There are two reasons for this preference over bottom-bound intermediates (Scheme 16A). On the one hand, it could be explained by the steric effect. In the **TS_{bottom}**, which leads to bottom-bound ruthenacyclobutanes, the *syn* orientation of the metallacyclobutane and adamantyl groups results in unfavorable van der Waals interactions between adamantyl and metallacycle protons. Electronic factor also plays a role, and in the **TS_{bottom}** one d metal orbital participates in the backdonation to the NHC and alkylidene π^* orbitals. Conversely, leading to side-bound metalacyclobutanes **TS_{side}** has two separate metal d orbitals engaged in backdonation, one for the NHC and another for alkylidene. The strong preference for the side-bound ruthenacyclobutanes offers unique control through steric interactions. The steric hindrance of an *N*-aryl group disfavors the *E*-selective pathway and *Z*-olefins are formed (Scheme 16B).^[103] As the result, complexes of type **Ru-21** are very *Z*-selective^[104-108] and today commercially available^[109].



Scheme 16 A) Transition states explaining the preferred formation of side-bound ruthenacyclobutanes. B) Simplified mechanistic explanation of the observed complex **Ru-21** Z-selectivity.

Originally, the chelated catalyst **Ru-21** was obtained from dichloride complex **Ru-22** in a cyclometalation reaction with silver pivalate (Scheme 17).^[102] Changing *tert*-butylate to nitrate^[110] and mesityl *N*-substituent to bulkier 2,6-diisopropylphenyl (Dipp) resulted in a more efficient catalyst.^[111] Moreover, Mauduit and coworkers reported catalyst **Ru-23** (Scheme 17) bearing unsaturated NHC backbone which improved NHC precursor and catalyst synthesis (yield and number of steps) and can be considered as the state-of-the-art Z-selective catalyst.^[112]

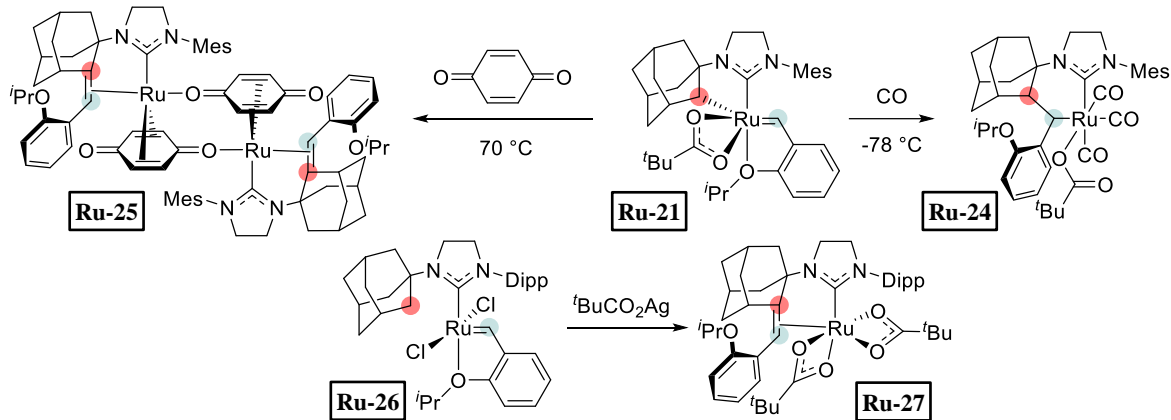


Scheme 17 Synthesis of cyclometalated catalyst **Ru-21** and improvements in the design of efficient Z-selective catalyst bearing a chelating NHC.

However, the concept of a chelating NHC OM catalyst did not prove to be universal in terms of ligand design on the adamantyl NHC side. Grubbs and coworkers reported several examples of complexes with NHC bearing other *N*-chelating groups,^[113–116] ultimately arriving at the conclusion that the original choice of chelated *N*-1-adamantyl was the best. César and coworkers reported Z-selective catalyst **Ru-28** (Scheme 19) bearing chelating *N*-(9-methylfluorenyl)NHC which proved to be highly fragile under catalytic conditions.^[117]

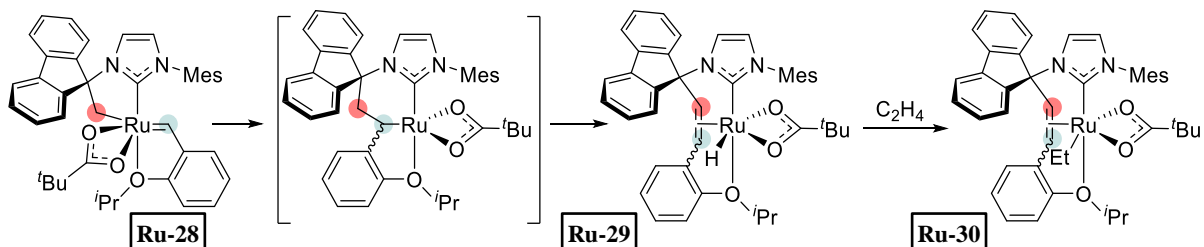
The decomposition pathways of Z-selective catalysts were studied by Grubbs and coworkers (Scheme 18).^[118] The authors found that complex **Ru-21** reacts with carbon monoxide giving complex **Ru-24** in which alkylidene is inserted into the ruthenium–alkyl bond of the cyclometalated adamantyl group. It was subsequently hypothesized that also in the absence of CO, this alkylidene insertion phenomenon could be common for C–H activated catalysts. Indeed, the authors also found that complexes analogous to **Ru-24** can be intermediates that could undergo β -hydride elimination reactions. In the reaction of **Ru-21** with *p*-benzoquinone complex **Ru-25** was isolated, in which alkylidene ligand was inserted into the ruthenium–alkyl bond and subsequent β -hydride elimination gave η^2 -coordinated olefin. Furthermore, when the same synthetic protocol for cyclometallation that worked with **Ru-22** (Scheme 17) was utilized

for Dipp substituted **Ru-26** only complex **Ru-27** was isolated (Scheme 18). Again, the same reactivity pattern was observed where the alkylidene ligand was inserted into the ruthenium-alkyl bond and β -hydride elimination gave η^2 -coordinated olefin. Ultimately, the Dipp derivative of **Ru-21** can be obtained by using sodium pivalate instead of silver.



Scheme 18 Studies of the decomposition of Z-selective complexes, highlighting the primary step of alkylidene insertion into the ruthenium–alkyl bond of the cyclometalated adamanyl group.

The decomposition pathways of Z-selective catalysts were also explored by César and coworkers (Scheme 19).^[117] The authors were able to isolate and characterize hydride complex **Ru-29**, whose formation stands in agreement with the decomposition mechanism proposed by Grubbs and coworkers. Furthermore, it was found that in presence of ethylene **Ru-28** gives complex **Ru-30**, in which ethylene is inserted into the ruthenium-hydride bond. Clearly, the conclusion can be drawn that the presence of ruthenium-alkyl bond accounts for high catalyst fragility. The high reactivity of the non-stabilized alkyl moiety of other metal cyclometalated complexes usually accounts for its high sensitivity to reagents/substrates.^[119–121] However, to have Z-selective properties it seems crucial to have cyclometalated NHC complexes bearing a ruthenium-carbon(sp³) bond.

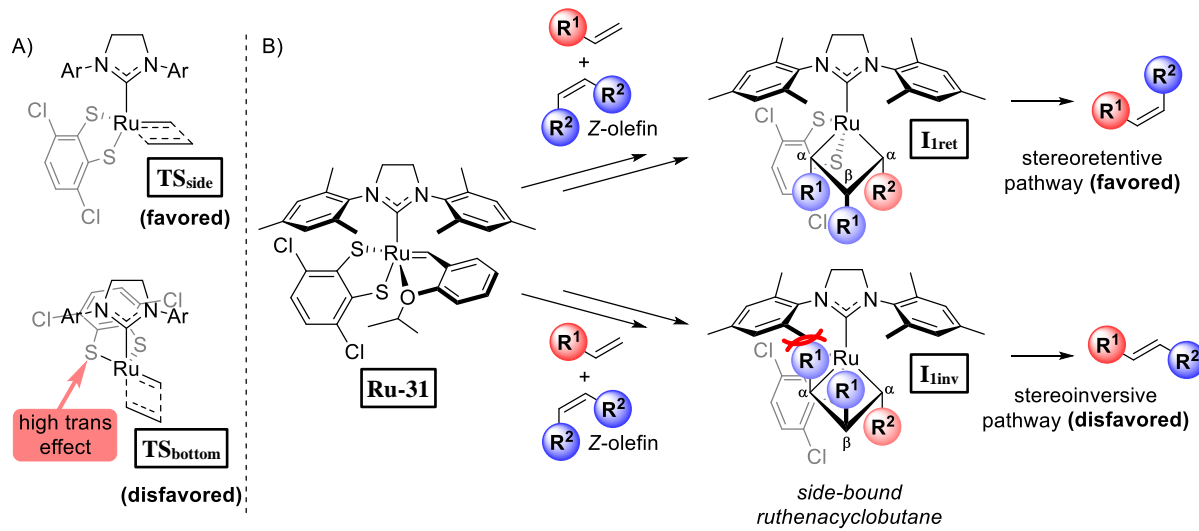


Scheme 19 Studies of the decomposition of Z-selective catalyst **Ru-28** bearing the chelating *N*-(9-methylfluorenyl)NHC.

1.4.3. Dithiocathecholate stereoretentive catalyst

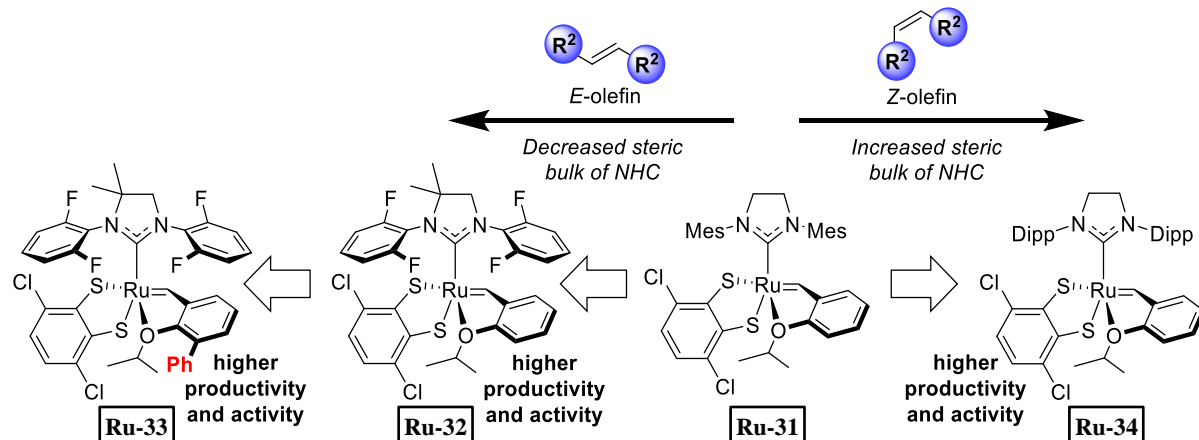
The last example of stereoselective OM catalyst derives from the ruthenium dithiocathecholate catalyst **Ru-31** obtained by Hoveyda in 2015.^[122] Initially, Hoveyda described complex **Ru-31**, or its previous derivatives bearing other dithiolate ligands, as Z-selective catalysts.^[122,123] However, subsequent studies by Pederson, Grubbs and coworkers showed that ruthenium dithiolate catalysts are not stereoselective but stereoretentive,^[124] which means that the original geometric configuration of a substrate is preserved. This feature derives from the fact that similarly in this case, the side-bound ruthenacyclobutane intermediates **I_{1ret}** and **I_{1inv}** (Scheme 20B) are formed. As the result of the high *trans* effect of sulfur atoms in the dithiocathecholate ligand, the **TS_{bottom}** is destabilized and thus disfavored over **TS_{side}** (Scheme 20A).^[123,125,126] Consequently, **I_{1inv}** requires either one of the substrate groups at α position to point

upwards resulting in a steric clash with NHC ligand. **I_{1inv}** is thus disfavored over **I_{1ret}** and Z-olefin products are formed (Scheme 20B).^[126]



Scheme 20 A) Transition states explaining the preferred formation of side-bound metalacyclobutanes with ruthenium dithiocatecholate catalyst. B) Simplified mechanistic explanation of the observed complex **Ru-31** stereoretentivity.

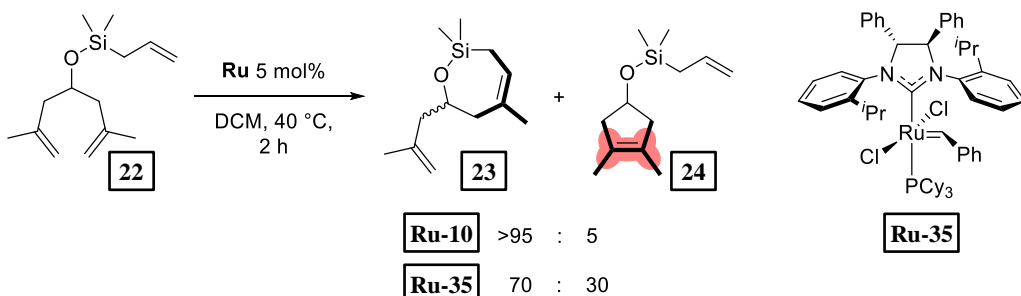
Naturally, if an *E*-alkene substrate is used then the *E*-product can be formed. This requires the substituent in β position in **I_{1ret}** to point up towards NHC, which was proven with density functional theory (DFT) calculations to be possible since there is an open space between NHC *N*-aryls.^[126] Thus said, the rotation of NHC ligand around carbon-metal bond is not entirely precluded, although it is to some extent blocked for saturated NHCs due to stronger metal-NHC backbonding.^[82] Consequently, the productivity of *E*-stereoretentive catalysts is quite low, although it can be improved to a moderate extent by using NHC complexes bearing sterically reduced *N*-aryl groups (**Ru-32**, Scheme 22).^[124] More importantly, this is the first and only example of a ruthenium-based kinetically *E*-selective OM.^[127] Moreover, it was found that catalyst activation presented a major obstacle, which was resolved by using a Blechert-type benzylidene ligand (**Ru-33**) ultimately giving good productivity although still high catalyst loadings have to be employed.^[128] On the other hand, installation of more sterically challenging NHC results in *Z*-stereoretentive catalyst **Ru-34** of improved productivity and activity.^[124] Compared with classical dichloro complexes (**Ru-10**), dithiocatecholate ligand makes the catalyst extremely oxygen sensitive.^[129]



Scheme 21 Improvements in the design of efficient *Z* or *E*-stereoretentive ruthenium dithiocatecholate catalyst.

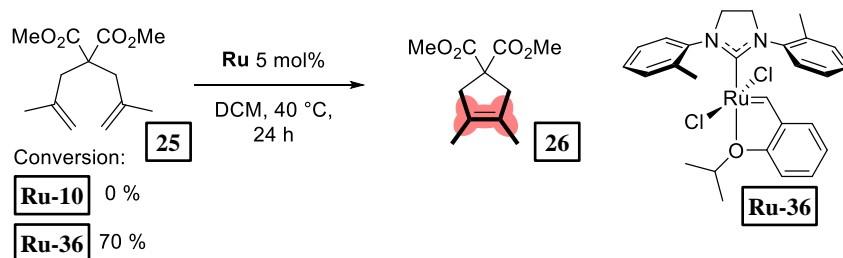
1.5. Formation of tetrasubstituted carbon–carbon double bonds using OM

Another important aspect of OM is the formation of tetrasubstituted or crowded carbon–carbon double bonds. This transformation is a challenge for general-purpose catalysts (e.g. **Ru-10**). In 2007 Grubbs and coworkers reported an interesting observation encountered during their research on enantioselective OM catalyst **Ru-35** (Scheme 22).^[130] The authors noted that when triene **22** was subjected to RCM, whereas SIMes bearing **Ru-10** gave mostly the desired chiral product **23** having a trisubstituted double bond, catalyst **Ru-35**, which had an NHC bearing mono-*ortho* substituted *N*-aryl groups, gave a mixture of **23** and tetrasubstituted olefin **24**. The authors hypothesized that the smaller demand of the “chopped” NHC ligand allows for more facile coordination of sterically crowded olefins to ruthenium metal center,^[130] which was later validated by DFT calculations.^[131]



Scheme 22 First reported example of the formation of tetrasubstituted double bond using ruthenium OM catalyst.

Such NHC ligand design proved to be a versatile approach and in time led to several other efficient catalysts for the formation of highly substituted double bonds. Remarkably, Grubbs, Schrodi and coworkers reported that whereas **Ru-10** gave no conversion of **25** to give tetrasubstituted **26**, catalyst **Ru-36**, now commercially available,^[132] bearing NHC with *ortho*-tolyl *N*-aryls gave 70 % conversion (Scheme 23).^[133]



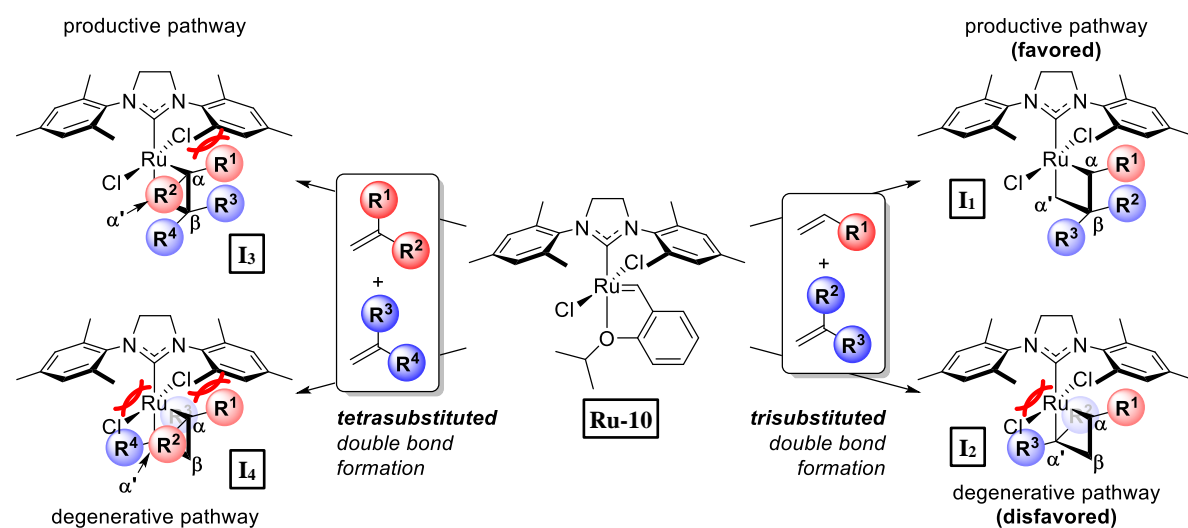
Scheme 23 An example of the formation of a tetrasubstituted double bond using a tailored ruthenium OM catalyst.

1.5.1. Mechanistic considerations

In contrast to the tetrasubstituted double bond formation by RCM, which is a challenge for SIMes bearing **Ru-10**, the formation of trisubstituted double bonds can be fairly easily performed with **Ru-10**. This can be explained by the fact that in **I₁** (Scheme 24, right) it is always preferred for the α position to be occupied by only one substrate substituent (R^1) than more sterically encumbered two substrate substituents (R^2 and R^3). As a result, more sterically protecting NHC provides more durable catalytic species and **Ru-10** performs better than **Ru-36**.^[134] Additionally, bulkier NHCs disfavor the degenerative pathway by imposing steric bulk on α' position in **I₂**. Although, in RCM (for obvious reasons) formation of **I₂** is already precluded (at least when small rings are formed), disfavoring the degenerative metathesis

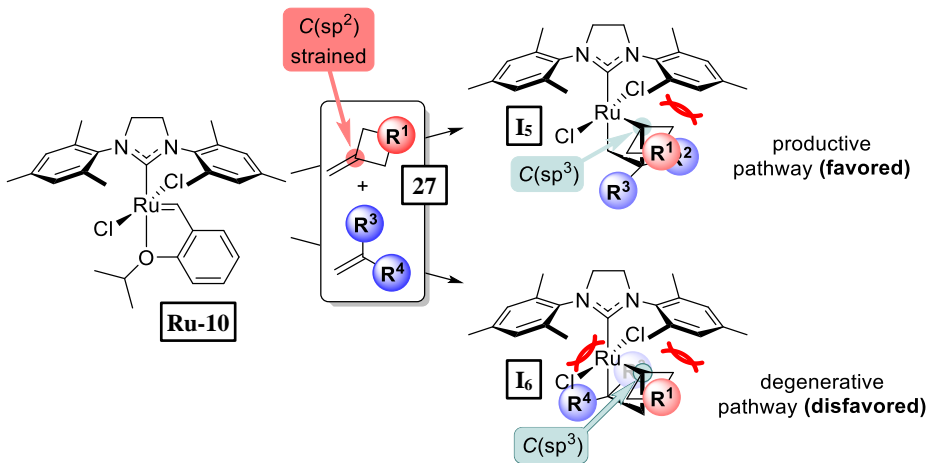
has a tremendous impact on CM. Consequently, SIPr bearing **Ru-17** performs better than **Ru-10** in this transformation, which performs better than **Ru-36**.^[135]

The situation changes dramatically when tetrasubstituted double bond formation is considered. In this case, α position in either **I₃** or **I₄** (Scheme 24, left) is always occupied by two substrate substituents (either R¹ and R² or R³ and R⁴), which due to steric clash poses a significant challenge to SIMes bearing **Ru-10**. However, contradictory to the positive effect imposed on α position, the reduced steric bulk of NHC has deleterious consequences. On one hand, less sterically protecting NHCs result in less durable catalytic intermediates and this will be discussed in depth in the next chapter. Furthermore, when CM is considered such NHCs do not disfavor the degenerative pathway. In conclusion, for the formation of tetrasubstituted double bonds, the catalyst must overcome two opposing factors and this transformation proved efficient only for RCM which by default disfavors degenerative metathesis (only when the formed ring size is small).



Scheme 24 Simplified mechanistic explanation of trisubstituted (right) and tetrasubstituted (left) carbon-carbon double bond formation.

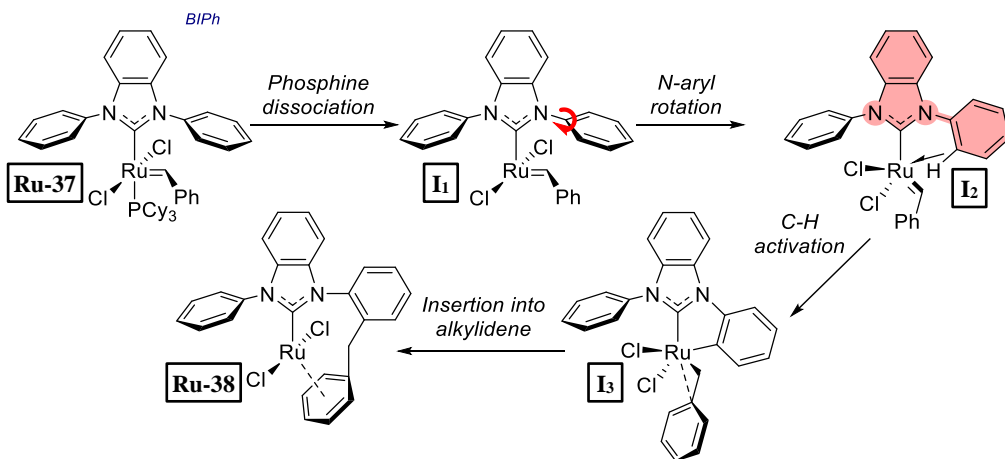
Although the tetrasubstituted double bond formation is uncommon by CM, special examples can be found in the literature utilizing methylene-functionalized substrates bearing four-membered rings (**27**, Scheme 25). All arguments discussed so far remain valid, however, strain release from sp² carbon in the structure of substrate **27** to sp³ carbon in ruthenacyclobutanes (**I₅** or **I₆**) provides an additional driving force that allows to overcome the negative effect of steric repulsion with NHC ligand. As well as for other CM examples, disfavoring the degenerative metathesis is a crucial factor and bulkier NHCs perform better in this transformation, thus **Ru-17** is more productive than **Ru-10** which is more productive than **Ru-36**.^[136,137]



Scheme 25 Simplified mechanistic explanation of tetrasubstituted carbon–carbon double bond formation with CM of substrate **27**.

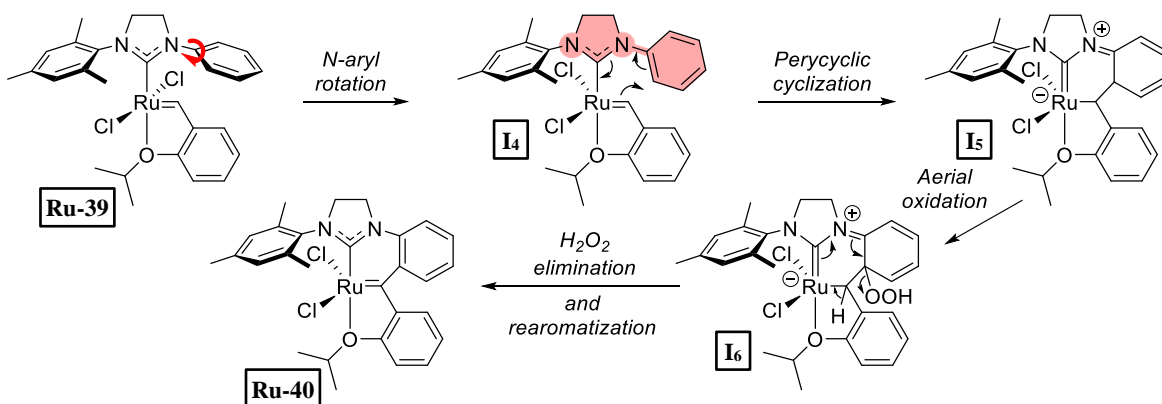
1.5.2. Proposed decomposition pathways

Although the catalysts bearing small-NHCs were more efficient than popular general-purpose tools in the formation of tetrasubstituted olefins by RCM, it was quickly noted that they strongly suffer from decreased stability. Particularly, Grubbs and coworkers reported the deactivation of second-generation Grubbs catalyst **Ru-37** bearing 1,3-diphenylbenzimidazolylidene (BIPh) NHC ligand (Scheme 26).^[138] The originally proposed mechanism was later validated using DFT calculations.^[139,140] In the first step PCy_3 ligand dissociates to form 14e^- **I**₁. Next, one of the *N*-phenyls rotates until it is coplanar with the benzimidazolylidene fused ring, forming **I**₂ stabilized by C–H agostic interaction. The following CH activation step gives cyclometalated **I**₃ and in the last step, the C–H activated *N*-phenyl group undergoes insertion into the ruthenium–carbon bond of what was formerly the benzylidene ligand. Ultimately, metathesis inactive complex **Ru-38** was isolated.



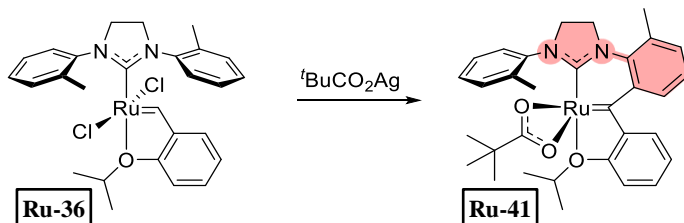
Scheme 26 Deactivation pathway of BIPh-base Grubbs second generation catalyst.

Blechert and coworkers investigated the mechanism of deactivation of **Ru-39** (Scheme 27).^[141] The authors proposed it consists of sequential *N*-phenyl rotation and pericyclic cyclization to give **I**₅. Subsequent aerial oxidation gives **I**₆ and elimination-rearomatization yields the metathesis-inactive product **Ru-40**. Although this mechanism assumes oxidation in the air (**Ru-39** does not decompose in solution in oxygen-free conditions), it bears a resemblance to the first deactivation pathway.



Scheme 27 Deactivation pathway of Hoveyda-Grubbs complex bearing *N*-phenyl substituent.

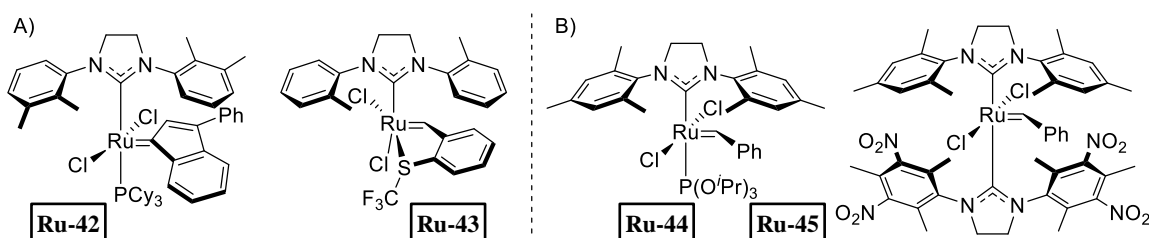
Moreover, during their study on the decomposition of *Z*-selective catalysts Grubbs and coworkers reported cyclometallation of the *ortho*-aryl position of NHC's *ortho*-tolyl *N*-substituents in **Ru-36** to give alkylidene inserted complex **Ru-41**.^[118] It becomes clear that for the catalysts with sterically-reduced NHCs, the crucial step in its decomposition is *N*-aryl rotation until it is coplanar with the NHC heterocycle.



Scheme 28 C-H functionalization of *ortho*-tolyl *N*-aryl group by cyclometalation with silver pivalate.

1.5.3. Methods to prevent catalyst deactivation

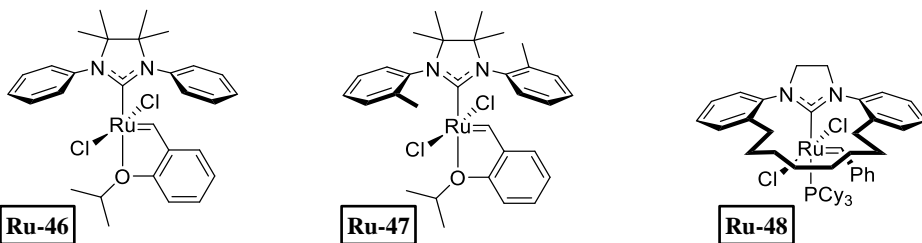
The overall stability of the small-NHC bearing complexes can be to some extent improved by using indenylidene (**Ru-42**)^[142] or thioether benzylidene (**Ru-43**)^[143] ligands that are known to increase the thermodynamic stability of ruthenium catalysts and harsher reaction conditions can be applied (Scheme 29A). A conceptually similar idea for forcing reactivity of crowded olefins is to use specially reinforced catalysts (**Ru-44**, **Ru-45**, Scheme 29B) at very high temperatures (up to 140 °C) at which SIMes-bearing complexes are active for tetrasubstituted carbon–carbon bonds formation.^[144,145]



Scheme 29 Methods to stabilize a precatalyst so that it can work at elevated temperatures.

Considering that the deleterious catalyst decomposition process requires the rotation of the *N*-aryl arm of the NHC ligand, more interesting were efforts to synthesize NHC complexes with restricted *N*-aryl rotation and maintained low steric demand of the ligand (**Ru-46**, **Ru-47**, Scheme 30).^[134,146] In theory, such an approach would yield a more robust catalyst with high activity at mild conditions. Grela and

coworkers reported the most recent example where such an approach merits higher catalyst stability and productivity (catalyst **Ru-48**).^[147]

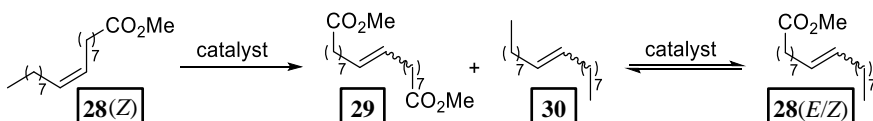


Scheme 30 Increasing catalyst productivity by restricting NHC's *N*-aryl rotation.

1.6. Self-CM of methyl oleate

Fossil fuels are the main source of raw materials for the chemical industry.^[148] However, as we move towards a net zero scenario, renewable feedstocks will take the place of fossil fuels as the starting material for the synthesis of chemicals. This transition is especially urgent in the case of polymers, which account for the largest volume of chemical industry products.^[148] Biomass is currently the main source of renewable feedstocks, and among the different types of biomass, vegetable oils are the most widely used in the chemical industry, due to their availability, affordability, and functionality.^[149–152] Transesterification of vegetable oils with methanol yields fatty acid methyl esters (FAMEs) with concomitant production of glycerol. Both feed-stocks have already found applications in the production of cosmetics, detergents, plasticizers, and other products.^[149,153,154]

OM has already been proven useful in the synthetic modifications of FAMEs.^[155,156] Notably, CM of 1-butene with FAME or vegetable oil can be utilized to produce higher-value products.^[157] Also, the ethenolysis reaction of FAMEs has gained significant interest, since it gives access to valuable terminal olefins.^[158,159] Last but not least, the self-CM of methyl oleate, **28(Z)**, which is the most abundant unsaturated FAME found in natural oil, affords dimethyl octadec-9-enedioate (**29**, Scheme 31) and the internal alkene **30** – both desirable products. The reaction gives equilibrium mixtures of **29**, **30** and **28(E/Z)** formed in an approximate molar ratio of 1:1:2.^[156,160–163]



Scheme 31 Self-CM of methyl oleate.

When anticipating a large-scale application of a homogeneous catalyst, it is important to have high TONs to render the process profitable. The TON is significantly dependent on the substrate quality, and thus, several protocols to remove catalyst poisons (peroxides, phosphates, sulfates, soap, etc.) from methyl oleate have been developed.^[164] This usually assumes thermal substrate pretreatment under vacuum with a variety of different sorbents (aluminum oxide, magnesium silicate/celite, or bleaching earths).^[164]

However, procuring pure methyl oleate is not a straightforward task.^[165] Vegetable oils are tri-glycerides composed of different fatty acids which leads to mixtures of FAMEs after trans-esterification. Concerning OM transformations of FAMEs, this can be particularly problematic when a mixture of unsaturated FAMEs is formed. So far, reports concerning self-CM of methyl oleate mainly focused on the use of pure, refined **28**, but this cannot be a viable raw material for industrial scale due to high purification

costs.^[160,166] The use of pretreated but non-refine methyl oleate was also studied in the context of catalyst TON, however, still a FAME material with a low content of polyunsaturated fatty acids was utilized.^[164]

Historically, methyl oleate with a low content of polyunsaturated FAMEs could be procured by selective hydrogenation of polyunsaturated fatty acids.^[167] Nowadays **28** with low content of polyunsaturated FAMEs is produced from high oleic safflower oil. Such raw material is obtained from genetically modified crops, which are safflower plants into which one or several genes coding have been inserted through the process of genetic engineering.^[168,169] However, to develop a process susceptible to potential future industrialization raw material availability must be considered. Consequently, it is desirable to move from highly oleic safflower oil towards more broadly available vegetable oil sources such as regular sunflower or rapeseed oil. This area has been largely unexplored.

1.7. Brief overview of the thesis

The material of this thesis is divided into three parts. The first one describes attempts to obtain a robust Z-selective OM catalyst. In the second presented are advancements in the formation of tetrasubstituted carbon-carbon double bonds using OM. The last part describes a potential application of the obtained catalytic systems in the synthesis of bio-based polyesters and polyamides. For clarity, exact objectives are introduced at the beginning of each chapter.

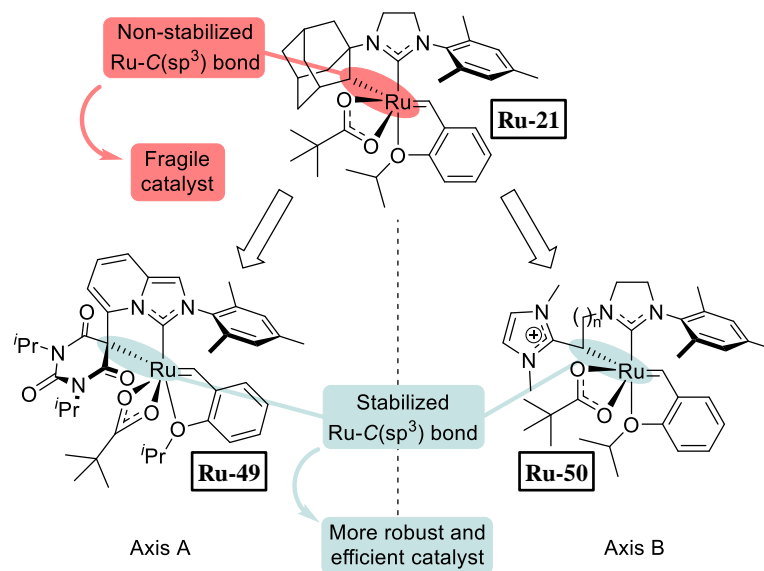
2. Toward a robust Z-selective OM catalyst

2.1. Objectives

This chapter describes attempts to synthesize a robust Z-selective catalyst bearing a chelating LX-type NHC ligand. The foundations on which the concept of this work was based are presented in Chapter 1.4. Since the biggest weakness of Z-selective catalysts derives from the presence of a ruthenium-alkyl bond, we aimed at obtaining an OM catalyst bearing chelating NHC with a more stable ruthenium-carbon(sp^3) bond. We envisaged that changing the adamantyl group to a more stabilized carbon ligand would result in more durable catalyst. Having those objectives in mind, we diversified the strategy into two axes. On the one hand, we investigated the synthesis of OM catalyst bearing a bidentate NHC ligand comprising a barbituric heterocycle (axis A). Axis B constitutes the synthesis of catalyst bearing chelating NHC ligand with *N*-heterocyclic olefin (NHO) moiety (Scheme 32).

The imidazopyridinylidene NHC containing a barbituric heterocycle was chosen since it has proven a versatile LX platform for d^6 [Ru(II), Mn(I)] or d^8 [Pd(II), Rh(I), Ir(I), Au(III)] transition-metal centers, giving access to stable metal complexes.^[170]

However, the NHC-NHO ligand architecture is a completely novel approach and thus also interesting from the basic science perspective than application. Furthermore, the domain of NHO ligands is much less explored than the NHC field and examples of well-defined metal NHO complexes remain rather rare in literature.^[117,171–179] The NHO ligand is a carbon-based donor composed of an alkylidene moiety appended to an NHC frame of the general formula $NHC=CR_2$. Because of the highly polarized nature of the alkylidene in NHO, the zwitterionic imidazolium ylide form $(NHC)^+-CR_2^-$ is predominant in coordination chemistry, where the NHO ligand acts as a globally neutral two electron σ -donor with negligible π -acidity.^[180–185]

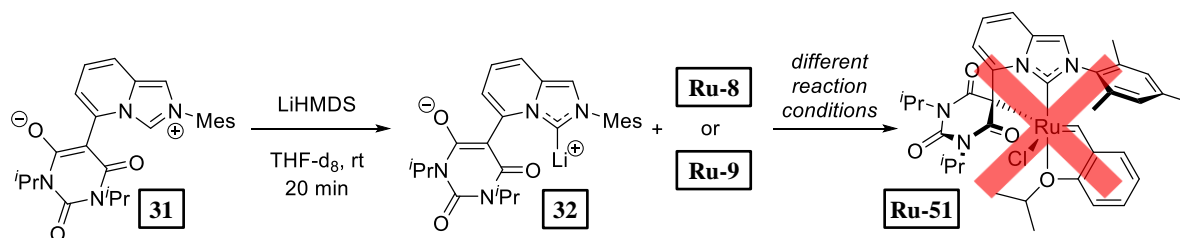


Scheme 32. The concept for a robust Z-selective OM catalyst.

2.2. Axis A - ruthenium complexes supported by a chelating NHC ligand comprising a barbituric heterocycle

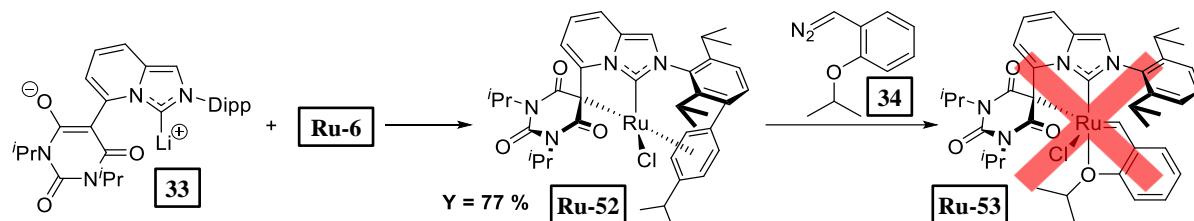
2.2.1. Preliminary results

Prior to the work described in this thesis, Gajda attempted the synthesis of a complex of type **Ru-51**, bearing the targeted chelating NHC ligand.^[186] However, the screening of several ruthenium-alkylidene complexes did not give the desired second generation complex. Upon my arrival in the group of César, I tried this synthetic route ultimately arriving at the same conclusion that it cannot be synthesized through this way (Scheme 33). The deprotonation of zwitterionic salt **31** gives the corresponding anionic NHC, most probably in the form of lithium complex **32**.^[170] However, upon mixing **32** with ruthenium precursor **Ru-8** or **Ru-9**, no formation of the expected complex **Ru-51** was detected, with starting **32** and ruthenium precursors remaining unchanged.



Scheme 33 First attempts to synthesize the Hoveyda-Grubbs complex bearing the targeted chelating NHC ligand.

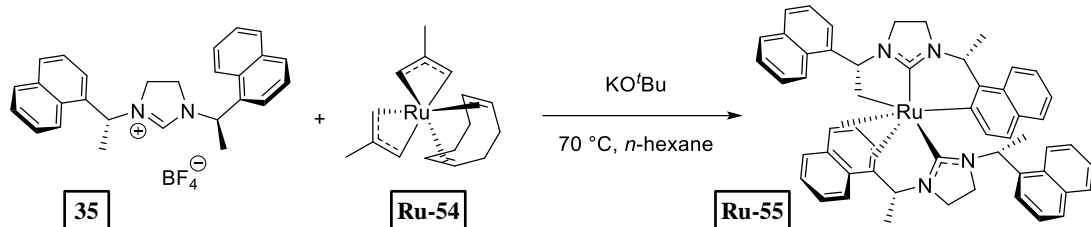
Facing those obstacles, Gajda tried a modified synthetic protocol. The concept of this new approach was to first coordinate the desired NHC ligand to a ruthenium metal center and then to install a benzylidene moiety. Such an approach worked for the synthesis of SIMes complex **Ru-10** from its *p*-cymene NHC derivative.^[187] It was possible to obtain the ruthenium-*p*-cymene complex **Ru-52** bearing the targeted NHC ligand,^[170] however, subsequent reaction with diazomethane derivative **34** did not give the corresponding ruthenium-NHC-alkylidene complex **Ru-53**.^[186]



Scheme 34. Alternated synthetic route for the Hoveyda-Grubbs complex bearing the targeted chelating NHC ligand.

We assumed that the unforeseen lack of reactivity of **Ru-52** with **34** might originate from a decreased lability of *p*-cymene ligand being the impact of the chelating NHC. Although the synthesis of the stable IMes version of **Ru-52** was reported many years ago,^[188] only recently devised was an efficient protocol to obtain the very unstable SIMes derivative.^[187] This highlights how a relatively small difference in NHC structure can influence the corresponding NHC-*p*-cymene complex reactivity by modulating the lability of the *p*-cymene ligand. Considering the arguments mentioned above, we turned our attention towards other auxiliary ligands which hopefully would be more labile than *p*-cymene and allow the installation of an alkylidene moiety. We decided to start from complex **Ru-54** as a potential metal precursor. Additionally, as demonstrated by Glorius and coworkers (Scheme 35)^[121] methylallyl ligands in

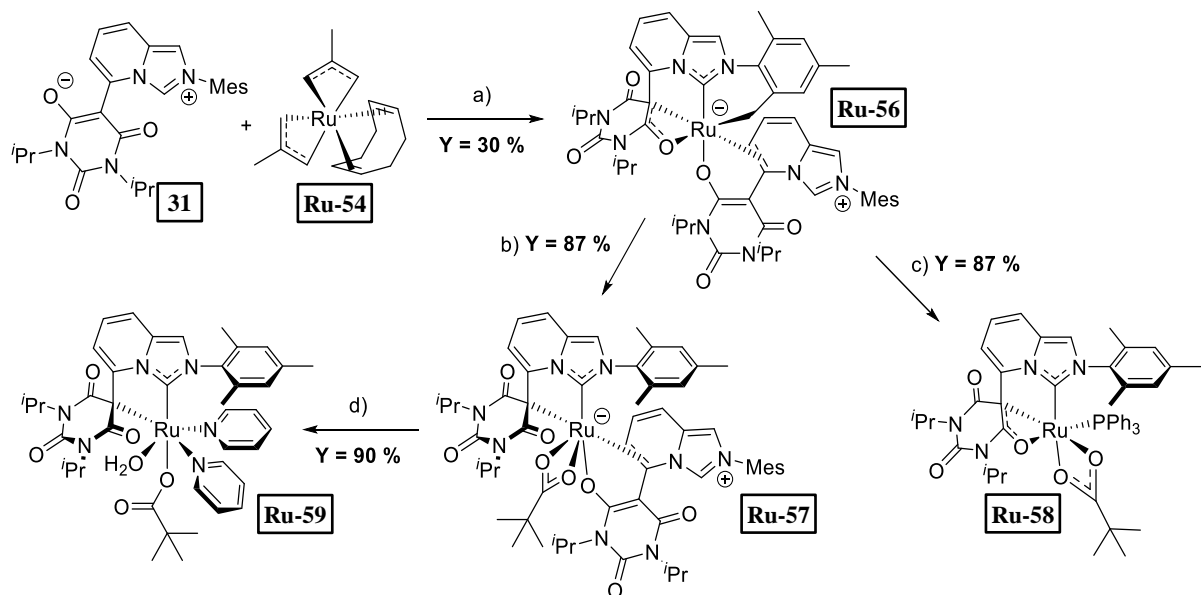
the **Ru-54** structure can serve as internal bases and we wanted to explore whether it can be used to deprotonate the imidazopyridinium precursor **31** to form a ruthenium-NHC complex.



Scheme 35 Example of utilizing complex **Ru-54** as a metal precursor for a ruthenium-NHC complex.

2.2.2. Synthesis of ruthenium complexes with the chelating NHC ligand

The reaction of complex **Ru-54** with two equivalents of precursor **31** led to the formation of the stable, red complex **Ru-56** isolated in 30 % yield using column chromatography (CC) (Scheme 36). Indeed, the methallyl moiety of **Ru-54** served as an internal base to deprotonate the azonium position of **31** and form a desired ruthenium-NHC complex. However, the reaction did not stop after the first protonolysis step and the second methallyl group was spent on the cyclometallation of the *ortho*-methyl group of the mesityl *N*-substituent. As evidenced by distortionless enhancement by polarization transfer (DEPT) ¹³C NMR, the cyclometallation resulted in a formation of the CH₂ group observed at δ_{C} 24.1 ppm. Consequently, this resulted in a diastereotopic CH₂ proton group as the two protons reside in a different chemical environment and one of its signals was observed in the ¹H NMR spectrum as doublet at δ_{H} 4.11 ppm (the other ¹H signal of this group being concealed within a multiplet 5.13 – 4.85 ppm). Surprisingly, rather than retaining the cyclooctadiene (COD) ligand, the metal center was stabilized by coordination of a second molecule of imidazopyridinium precursor **31**, which was indicated by compound's molecular weight (indicated by high-resolution mass spectrometry – HRMS), supplemented with a relatively deshielded ¹H NMR doublet signal at δ_{H} 8.38 ppm (low coupling constant of 1.1 Hz resulted from long range coupling) characteristic of an azolium salt.



Scheme 36 Synthesis of ruthenium complexes **Ru-56**–**Ru-59** bearing the chelating NHC ligand. Reaction conditions: a) 2 equiv. of **31**, 1 equiv. of **Ru-54**, THF, 90 °C, 2 h; b) 2.2 equiv. *t*BuCO₂H, THF, 80 °C, 15 h; c) 1.2 equiv. PPh₃, 1.2 equiv. *t*BuCO₂H, dichloroethane (DCE), 80 °C, 6 h; d) dry pyridine (excess), 80 °C, 2 h.

Gratifyingly, it was possible to grow monocrystals of **Ru-56** suitable for X-ray diffractometry (XRD), by layering a dichloromethane (DCM) complex solution with pentane (Figure 17). The crystal structure revealed a distorted square bipyramidal coordination geometry of ruthenium with C_{NHC} and oxygen atoms of NHC precursor **31** occupying axial positions. Interestingly, to stabilize the coordination sphere by forming an 18e⁻ complex, the carbon–carbon–oxygen part of the malonate coordinated *via* an η³ mode. In the report of César and coworkers for seven transition metal complexes containing a similar NHC ligand only η¹ coordination mode was observed through the central malonate carbon atom (C_{mal}).^[170] The η³ coordination was denoted by relatively short Ru–C_{C=O} and Ru–O_{C=O} bond lengths of 2.380 and 2.235 Å respectively (Figure 18 and Table 1, entries 3–4). Ruthenium atom is displaced out of the N–C_{NHC}–N plane of NHC’s heterocycle by a distance of 0.303 Å (parameter γ denoted in Figure 18, Table 1, entry 10), presumably as a result of Ru–O_{C=O} or Ru–C_{C=O} bonds pulling it away from the plane. Moreover, the cyclometalated mesityl group resulted in a short Ru–C_{NHC} bond distance of 1.928 Å, which was shorter than any other metal–C_{NHC} bonds among the corresponding series.^[170] Notably, the yaw angle, reflecting a distortion of the metal–C_{NHC} bond relative to the bisector of the N₂C unit (parameter θ denoted in Figure 18, Table 1, entry 6),^[189] was relatively low when compared with corresponding complexes from the literature.^[170] Moreover, the degree of pyramidalization of C_{mal} atom ($\Sigma = 353.43^\circ$, Figure 18, Table 1, entry 8) was found less pronounced compared to related metal complexes bearing ligand **32** with a η¹-coordination of the barbiturate ligand ($\Sigma = 336\text{--}344^\circ$).^[170]

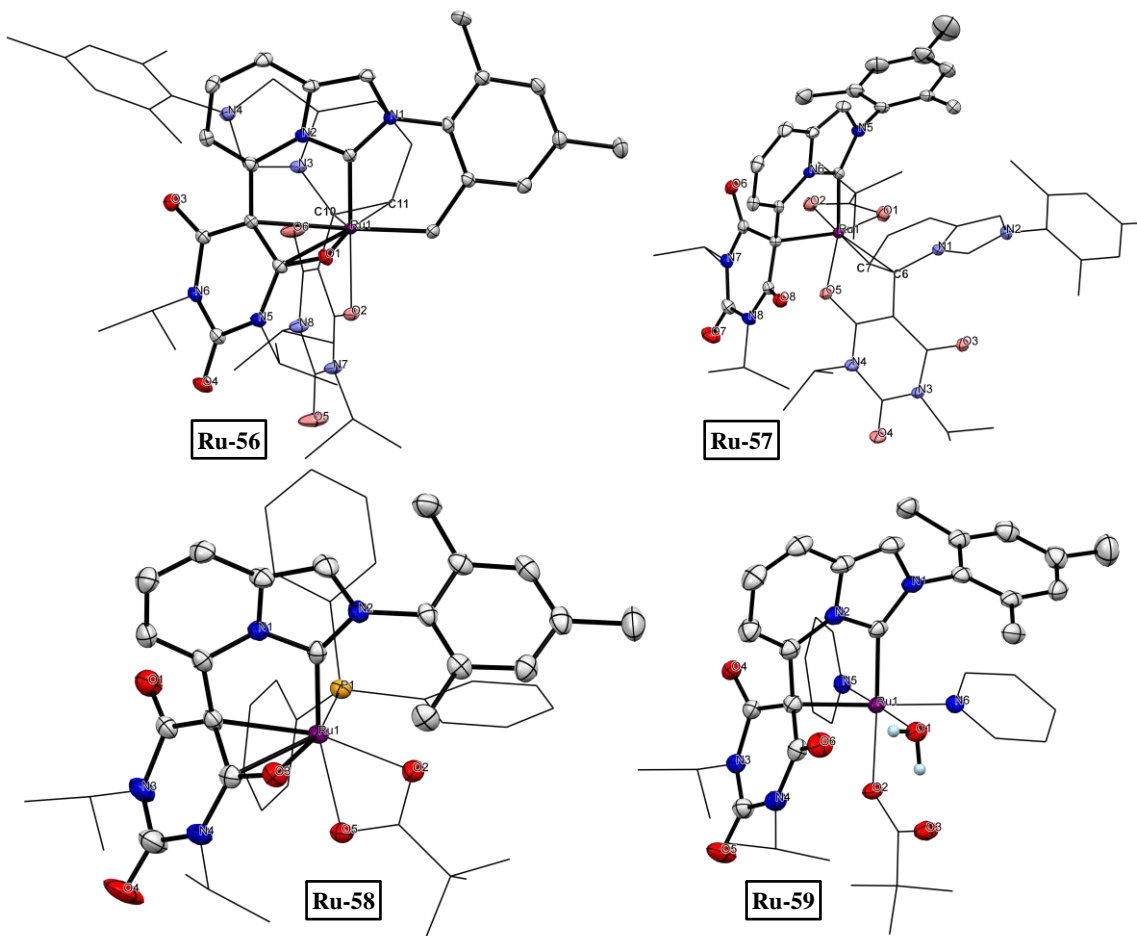


Figure 17 XRD crystal structures of the obtained complexes, ellipsoids are drawn at 50 % probability, hydrogens were omitted for clarity.

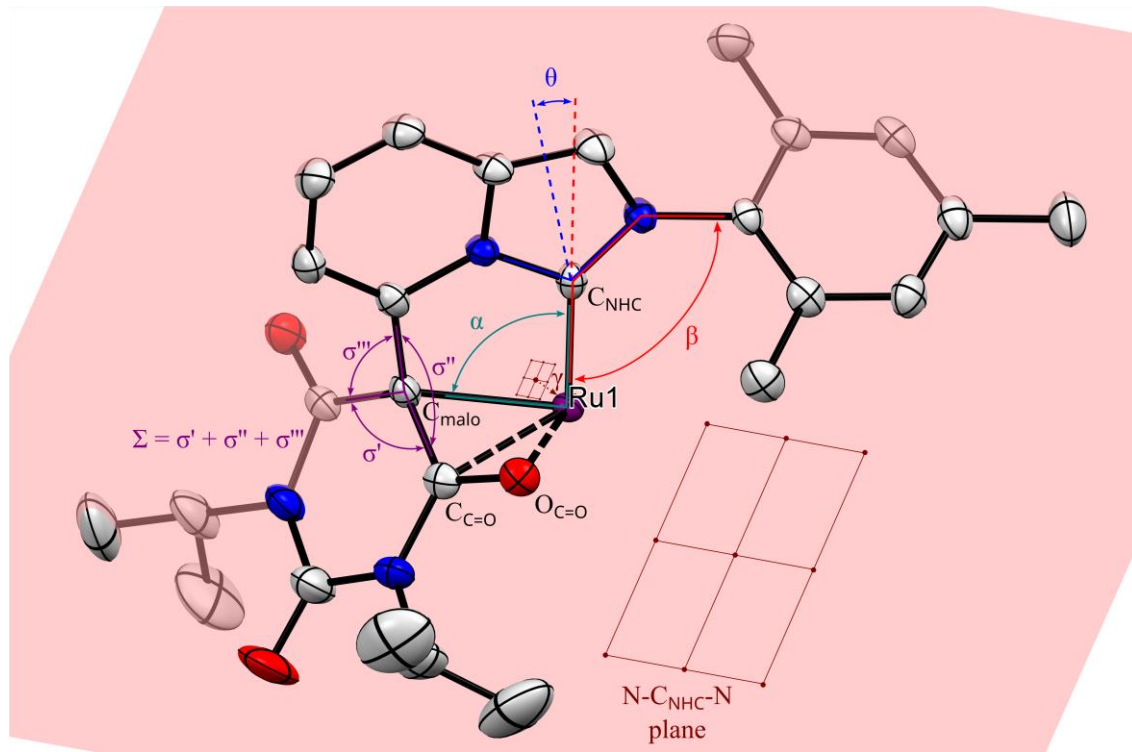


Figure 18 Graphical representation of selected structural parameters. α – bite angle. θ – yaw angle. Σ – degree of pyramidalization of C_{malo} atom. Torsion angle β depicting the N -mesityl group displacement out of the NHC's heterocycle plane. γ – ruthenium distance out of $N-C_{NHC}-N$ plane of NHC's heterocycle.

Table 1 Selected, corresponding bond lengths (\AA) and angles (deg) in X-ray crystal structures of complexes **Ru-56–Ru-59**.

		Ru-56	Ru-57	Ru-58	Ru-59
1	Ru–C _{NHC}	1.928(2)	2.0243(15)	1.987(3)	1.9827(19)
2	Ru–C _{malo}	2.488(2)	2.2392(15)	2.222(3)	2.301(2)
3	Ru–C _{C=O}	2.380(2)	2.818	2.262(3)	2.999
4	Ru–O _{C=O}	2.2349(17)	3.420	2.2443(19)	3.538
5	α	78.85(9)	79.79(6)	79.51(10)	80.32(8)
6	θ	7.67	15.16	11.46	12.66
8	Σ	353.43	338.68	346.19	341.25
9	β	9.77	21.12	9.09	17.45
10	γ	0.303	0.038	0.248	0.251
11	Ru1–C54		Ru1–O5	Ru1–P1	Ru1–N5
		2.088(2)	2.1402(11)	2.2485(7)	2.0658(16)
12	Ru1–O2		Ru1–O1	Ru1–O2	Ru1–N6
		2.1833(17)	2.1430(11)	2.1279(19)	2.1176(17)
13	Ru1–C10		Ru1–O2	Ru1–O5	Ru1–O1
		2.103(2)	2.1561(11)	2.2315(19)	2.1599(14)
14	Ru1–C11		Ru1–C6		Ru1–O2
		2.157(2)	2.1200(15)		2.1654(13)
15			Ru1–C7		
			2.2280 (15)		

α – bite angle. θ – yaw angle. Σ – degree of pyramidalization of C_{malo} atom. Torsion angle β depicting the N -mesityl group displacement out of the NHC's heterocycle plane. γ – ruthenium distance out of $N-C_{NHC}-N$ plane of NHC's heterocycle.

In the next step, we attempted to cleave the ruthenium-alkyl bond with the use of pivalic acid. Gratifyingly, the reaction gave cleanly a red complex **Ru-57** isolated in 87 % yield by CC. Indeed, the protonolysis resulted in a free *N*-mesityl group as indicated by the disappearance of characteristic signals of the CH₂ group in ¹H and ¹³C NMR spectra with simultaneous emergence of singlet signal at δ_{H} 0.88 ppm assigned to *tert*-butyl group of the pivalate ligand. Crystals of **Ru-57** suitable for XRD experiments were grown by layering a hexafluorobenzene complex solution with heptane. The crystal structure revealed a distorted square bipyramidal coordination geometry with C_{NHC} and oxygen atom **31** remaining at apical positions. However, the coordination mode of barbituric heterocycle had changed from η^3 to η^1 as evidenced by longer Ru–C_{C=O} and Ru–O_{C=O} distances of 2.818 and 3.420 Å respectively. Presumably in consequence, the ruthenium atom resides closer to the plane of NHC's heterocycle ($\gamma = 0.038$ Å). Moreover, freeing the *N*-mesityl arm elongated Ru–C_{NHC} bond to 2.0243 Å, which is more alike to other metal-NHC complexes of the series, and significantly increased the yaw angle to 15.16°, which is the highest value in the series.^[170] The degree of pyramidalization ($\Sigma = 338.68^\circ$) reflects higher sp³ hybridization of C_{malo}, which also fits closely to the previously reported series.^[170] Similarly, the bite angle (parameter α denoted in Figure 18, Table 1, entry 5) of 79.79° well correlates with the series.^[170] Moreover, the introduction of pivalate anion inflicted significant congestion within the complex as indicated by *N*-mesityl group repulsion out of the NHC's heterocycle plane (torsion angle β , Figure 18, Table 1, entry 9) by 21.12°.

Furthermore, when PPh₃ was added along with pivalic acid, this resulted in the formation of a yellow-orange complex **Ru-58** isolated in 87 % yield by CC. Similarly, the protonolysis to generate the *N*-mesityl group could be observed by the disappearance of characteristic signals of the CH₂ group in ¹H and ¹³C NMR spectrums and emergence in ¹H NMR of singlet signal at δ_{H} 0.57 ppm characteristic for pivalate ligand. The addition of PPh₃ ligand resulted in the replacement of the imidazopyridinium compound **31** by the PPh₃ as evidenced by the disappearance of the characteristic signal of an azolium salt and emergence of a singlet signal at δ_{P} 67.23 ppm in ³¹P NMR spectrum of **Ru-58**. Surprisingly enough, the complex's crystal structure revealed η^3 coordinated barbiturate, with Ru–C_{C=O} and Ru–O_{C=O} bond lengths of 2.262 and 2.2443 Å respectively. Once more a distorted octahedral coordination geometry was observed, with C_{NHC} and phosphorous ligands residing in *cis* positions to one another, rather than *trans* which was disfavored probably due to steric clash of both ligands. Ruthenium atom is displaced out of the N–C_{NHC}–N plane of NHC's heterocycle by a distance of 0.248 Å. The degree of pyramidalization ($\Sigma = 346.19^\circ$) was significantly higher than in the case of **Ru-56** thus conveying a more delocalized bond character of the carbon-carbon-oxygen part of the malonate in **Ru-58**. Compared to **Ru-56**, the Ru–C_{NHC} bond elongated to 1.987 Å accompanied by a yaw angle slight increase to 11.46°, presumably due to cleavage of the ruthenium-C_{Mes} bond.

At last, we attempted the installation of a pyridine ligand in the hope of having a labile functionality suitable for the introduction of an alkylidene ligand. Indeed, the reaction of **Ru-57** with dry pyridine gave the complex **Ru-59** isolated in 90 % yield using CC. Although the complex is stable when stored in a protective atmosphere in the form of a brown solid, the CC had to be performed with dried and degassed solvents as otherwise **Ru-59** readily decomposed on silica gel. As indicated by the integration of signals in an aromatic range of ¹H NMR spectrum and by the number of aromatic signals in ¹³C NMR, **Ru-59** contained in its structure two molecules of pyridine that replaced the imidazopyridinium compound **31**. However, the crystal structure of **Ru-59** revealed a molecule of water coordinated as well, and a monodentate coordination mode of pivalate ligand, that both stabilized the structure due to *i*

creation of near perfectly octahedral geometry and *ii*) hydrogen bonding between the water protons and oxygen atoms of pivalate (O3) and barbiturate (O6) ligands. Hydrogen bonds are evidenced by a low distance between proton and bond acceptor of 1.625 and 1.944 Å with corresponding angles of 170.74 and 153.34° for O3 and O6 atoms respectively. However, the exact structure in solution could not be determined as the water protons could not be unambiguously assigned. Moreover, a quite significant broadening of signals in both ¹H and ¹³C NMR spectra indicates an equilibrium process of water or pyridine coordination and decoordination. Since dry pyridine was used for the reaction, most probably the water was introduced during the working up of the reaction.

Complex **Ru-59** bears an η^1 coordinated barbiturate with long Ru–C_{C=O} and Ru–O_{C=O} distances of 2.999 and 3.538 Å respectively. Ru–CNHC bond length of 1.9827 Å, bite and yaw angles, and the degree of pyramidalization ($\alpha = 80.32^\circ$, $\theta = 12.66^\circ$, $\Sigma = 341.25^\circ$) well correlate with **Ru-57** and **Ru-58** and with other corresponding metal-NHC complexes.^[170] However, the ruthenium atom is displaced out of the N–CNHC–N plane of NHC's heterocycle by a distance of 0.251 Å, similar to complex **Ru-58** with η^3 coordinated barbiturate. Clearly, the parameter γ is not only determined by barbiturate coordination mode but also influenced by the interaction of NHC with other co-ligands. Notably, the *N*-mesityl group is bent out of the NHC's heterocycle plane with a torsion angle β of 17.45° which is a result of π - π stacking interaction between the *N*-mesityl group and the bottom pyridine ligand that forces both in parallel displacement to match their partial charges for attractive electrostatic interaction. The π - π interaction can be evidenced by a near parallel alignment of *N*-mesityl and pyridine planes (the planes intersect at a very acute angle of 8.65°), and a small centroids distance of 3.570 Å.

2.2.3. Installation of an alkylidene ligand and the attempted catalysis

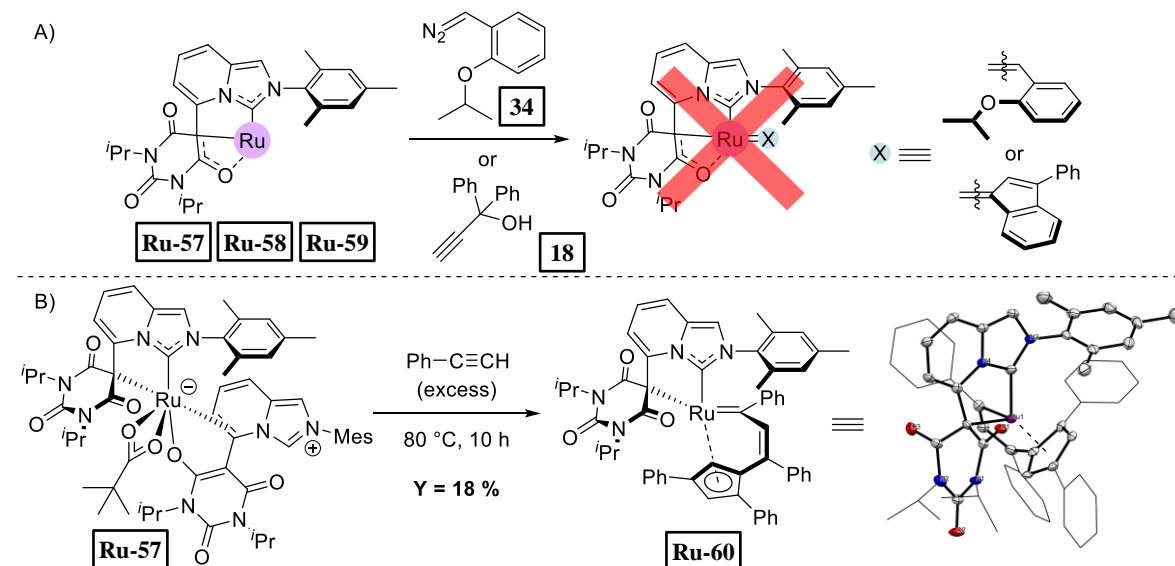
With the small library of ruthenium complexes bearing the targeted NHC ligand, the introduction of an alkylidene ligand was attempted (for methods of alkylidene installation refer to Chapter 1.3.5). First, the reaction of complexes **Ru-57**–**Ru-59** with diazo compound **34** was tried, however, no reactivity was observed with the starting complexes remaining unchanged (Scheme 37A). Even the very promising pyridine derivative **Ru-59** exhibited no reactivity with **34**. Next, we attempted a reaction with propargyl alcohol **18** at 80 °C. This time a reactivity of the starting complexes was observed, however, no product could have been isolated and characterized because a complex mixture of unidentified species was formed.

At last, we turned our attention to phenylacetylene (**19**) as an alkylidene precursor. Quite similar reactivity pattern was observed to the reaction with **18** in the sense that a mixture of products was formed. However, this time it was possible to isolate using CC the major product **Ru-60** in 18 % yield from the reaction of **Ru-57** with **19** (Scheme 37B). Indeed, **Ru-60** contained an alkylidene functionality in its structure as indicated by a very deshielded signal in ¹³C NMR at δ_C 282.7 ppm, a characteristic of ruthenium-alkylidene complexes. Moreover, evidenced was the imidazopyridinium compound **31** decoordination, as indicated by the disappearance of the characteristic signal of an azolium salt in the ¹H NMR spectrum and also, surprisingly, the decoordination of pivalate ligand as evidenced by the disappearance of singlet characteristic of *tert*-butyl group.

Gratifyingly, it was possible to grow single crystals of **Ru-60** suitable for XRD experiments by vapor-liquid diffusion crystallization of the complex's THF solution submerged in pentane vapors. Surprisingly, the crystal structure revealed an unexpected tetramerization of phenylacetylene to form a

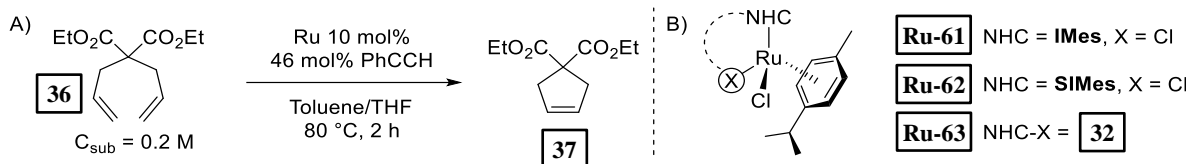
cyclopentadienyl unit whose η^5 coordination replaced the pivalic anion giving the piano stool complex **Ru-60**. The more common η^1 coordination mode of barbiturate ligand was observed with long Ru–C_{C=O} and Ru–O_{C=O} distances of 3.026 and 3.564 Å respectively. Ru–C_{NHC} bond length of 2.049 Å, bite and yaw angle, and the degree of pyramidalization ($\alpha = 77.81^\circ$, $\theta = 12.95^\circ$, $\Sigma = 334.68^\circ$) well correlate with the series, especially with the other half-sandwich ruthenium-NHC-barbiturate complex **Ru-52**.^[170] Ruthenium atom resides relatively close to the plane of NHC's heterocycle ($\gamma = 0.044$ Å), similar to the structure of **Ru-57**. Notably, the *N*-mesityl group is bent out of the NHC's heterocycle plane with a torsion angle β of 14.73°, similar to the structure of **Ru-59** as a result of π - π stacking interaction between the *N*-mesityl group and the bottom phenyl group of the alkylidene-cyclopentadiene tetrameric ligand. Likewise to the complex **Ru-59**, the π - π interaction can be evidenced by a near parallel alignment of *N*-mesityl and phenyl planes (the planes intersect at a very acute angle of 5.51°) and a small centroids distance of 3.720 Å.

Although the phenylacetylene tetramerization was quite unexpected, still **Ru-60** contained an alkylidene moiety and its activity in RCM of **36** was assessed. However, the complex **Ru-60** did not provide any formation of RCM product **37** (Table 2, entry 1). We suspected that **Ru-60** inactivity might be the consequence of cyclopentadienyl ligand which saturates the coordination site of metal restricting substrate coordination. We pondered whether a vinylidene (or other alkylidene intermediate) with a free coordination site might be formed *en route* to the formation of **Ru-60**. Such an intermediate should be active in OM.^[190]



Scheme 37 A) Attempts of reaction of complexes **Ru-57**–**Ru-59** with either diazomethane derivative **34** or propargyl alcohol derivative **18**. B) Reaction of complex **Ru-57** with phenylacetylene and XRD crystal structure of the formed product **Ru-60** (ellipsoids are drawn at 50 % probability, hydrogens were omitted for clarity).

To test the postulated hypothesis the previously obtained ruthenium-NHC complexes **Ru-56**–**Ru-59** were mixed with substrate **36** and phenylacetylene that served as an activator to form an alkylidene intermediate that could catalyze OM (Scheme 38A). However, no formation of product **37** was observed in all of the cases (Table 2, entries 2–5). To test the validity of this experimental approach, IMes and SIMes monodentate NHC-ruthenium-*p*-cymene complexes (Scheme 38B) **Ru-61** and **Ru-62** were tested in this methodology, resulting in a quantitative formation of the RCM product **37** (Table 2, entries 6–7) whereas the complex **Ru-63** bearing the chelating NHC gave no observable amount of **37** (Table 2, entry 8).



Scheme 38 A) RCM reaction of **36** catalyzed by ruthenium complexes with additive **19**. B) Structures of ruthenium-NHC-p-cymene complexes used in the study.

Table 2 Results of RCM reaction of **36** catalyzed by ruthenium complexes with additive **19**.

Entry	Complex	Yield of 37 (%) ^a
1	Ru-60 ^b	0
2	Ru-56	0
3	Ru-57	0
4	Ru-58	0
5	Ru-59	0
6	Ru-61 ^c	98
7	Ru-62 ^c	>99
8	Ru-63 ^c	0

Reaction conditions: complex 10 mol%, **19** 46 mol%, toluene/THF mixture, 80 °C, 2 h. ^a – yield determined by gas chromatography (GC). ^b – 1 mol% of **Ru-60**, no **19** added. ^c – complex generated prior to metathesis reaction from **Ru-6** and corresponding carbene, complex not isolated.

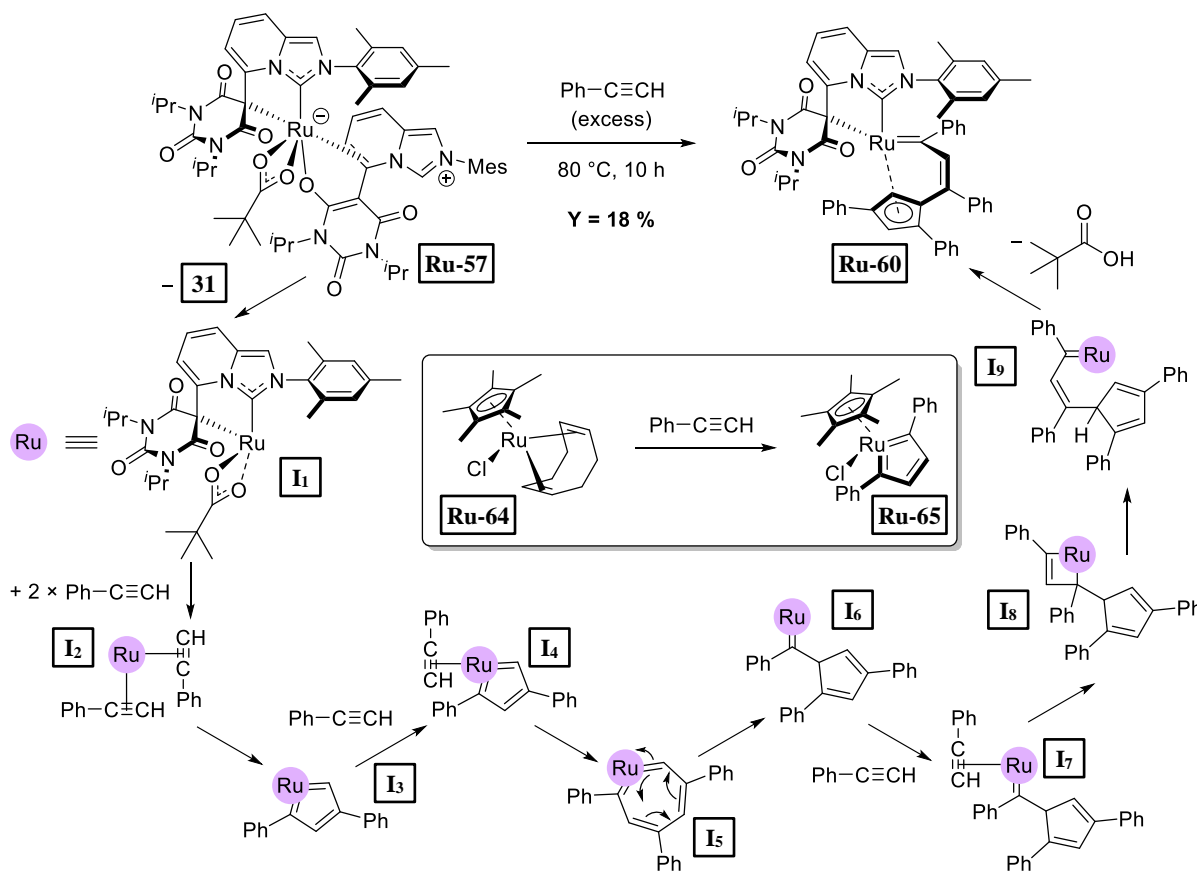
2.2.4. Conclusions

In summary, several ruthenium complexes bearing the targeted chelating NHC-barbiturate ligand were successfully synthesized. Depending on the nature of the other ligands present in the structure it was found that the barbiturate-derived NHC can flexibly accommodate between η^1 coordination mode *via* malonate carbon and η^3 *via* carbon-carbon-oxygen part of the malonate in order to stabilize the coordination sphere. Furthermore, the NHC-barbiturate ligand can even adopt a tetradentate coordination mode when one of the *ortho*-methyl groups of the *N*-mesityl substituent is cyclometalated (structure **Ru-56**). The complexes have been fully characterized using NMR and XRD.

It was possible to install an alkylidene ligand to a ruthenium complex bearing the chelating NHC-barbiturate ligand, however, an unexpected tetramerization of phenylacetylene occurred leading to the formation of a cyclopentadienyl co-ligand (complex **Ru-60**). Regrettably, no catalytic activity in OM was observed either of complex **Ru-60** or when an *in situ* alkylidene ligand generation was attempted with phenylacetylene.

The lack of catalytic activity in OM with the attempted *in situ* catalyst generation has prompted us to postulate that an expected vinylidene intermediate was never formed from **Ru-57**. This has led us to the proposition of the following reaction mechanism (Scheme 39). Certainly, the first step is the de-coordination of the presumably labile imidazopyridinium precursor **31** to liberate metal coordination sites forming **I₁**. Next, two molecules of phenylacetylene might coordinate to form intermediate **I₂** which then can form the dicarbene intermediate **I₃**. However uncommon is such reactivity, several precedencies of forming ruthenium dicarbene complexes (e.g. **Ru-65**) from ruthenium-cyclopentadienyl-COD-chloride complexes (e.g. **Ru-64**) can be found in the literature.^[191–193]

In the next step, another molecule of phenylacetylene might coordinate (**I**₄) to expand the ruthenacyclopentatriene ring forming **I**₅. The following cycloreversion reaction forms a cyclopentadiene ring leaving one carbene ligand (**I**₆). Next, the fourth molecule of phenylacetylene coordinates (**I**₇) and the cycloaddition reaction gives ruthenacyclobutane **I**₈ whose cycloreversion reaction gives **I**₉. In the last step, **I**₉ undergoes intramolecular protonolysis reaction to deprotonate cyclopentadiene unit and de-coordinate pivalic acid forming the isolated **Ru-60**.

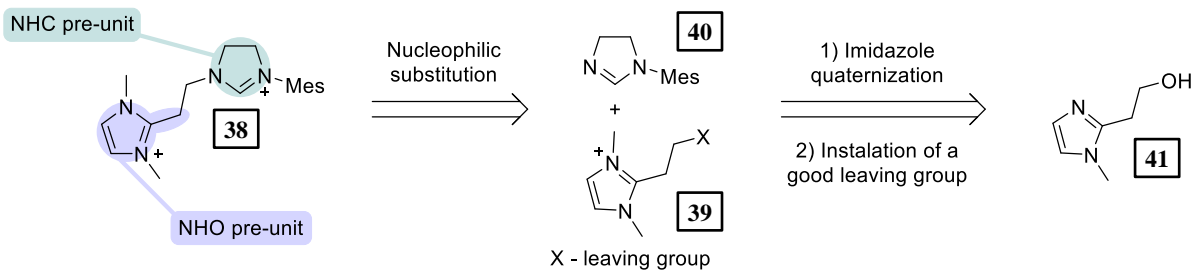


Scheme 39 A proposed mechanism of the formation of complex **Ru-60** and the reported formation of the dicarbene ruthenium complex **Ru-65**.

The proposed mechanism explains why no catalytic activity in OM was observed. Rather than forming a vinylidene intermediate from **I**₁, it prefers to form the dicarbene intermediate **I**₃ which presumably should not be active in OM. However, the explanation for why the formation of dicarbene intermediates would be preferred with the chelating NHC-barbiturate ligand remains unclear. Perhaps validating the proposed mechanism with DFT calculations would shed more light on the matter.

2.3. Axis B – NHC-NHO ligand architecture

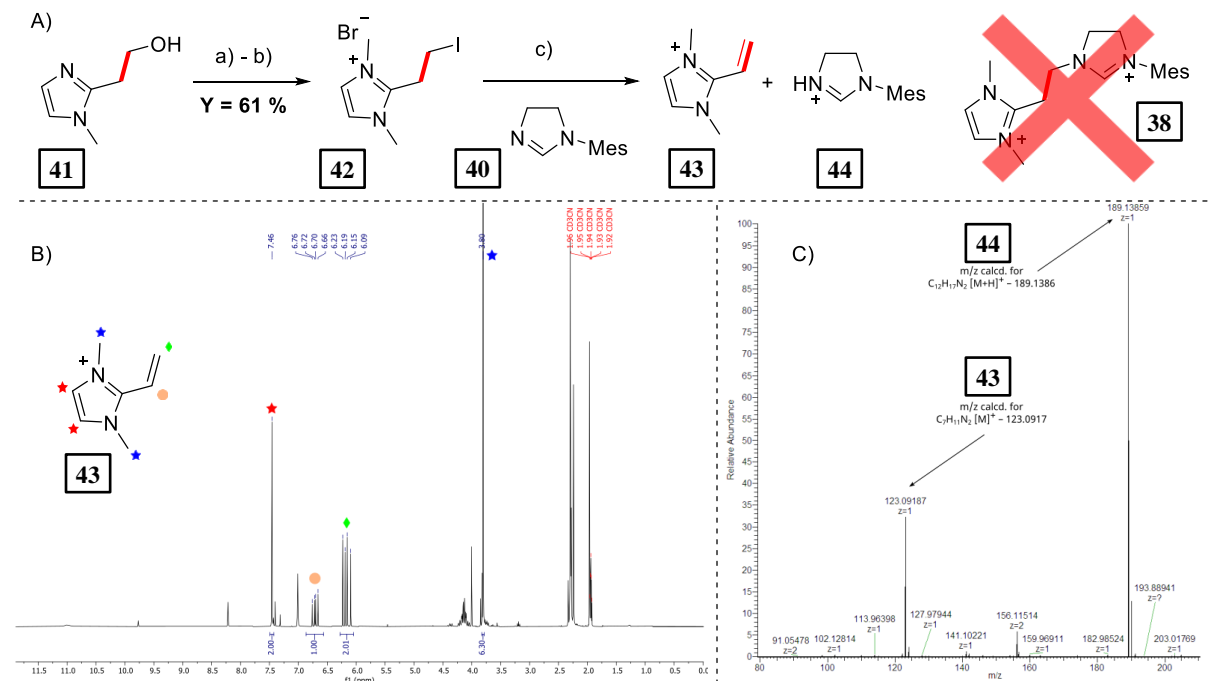
Originally, we envisaged the structure of an NHC-NHO ligand precursor with NHC and NHO pre-units connected with a CH₂ unit (**38**, Scheme 40) as the corresponding NHC-NHO complex would form a targeted five-membered metallacycle.^[113,116] The synthetic route described in Scheme 40 was proposed where **38** is formed by coupling of the 2-imidazolium derivative **39** bearing the desired CH₂-CH₂ skeleton with *N*-mesitylimidazoline (**40**). We planned to obtain the precursor **39** from compound **41** whose synthesis was reported in the literature.^[194]



Scheme 40 Proposed retrosynthetic route to obtain the NHC-NHO ligand precursor.

2.3.1. Synthesis of an NHC-NHO ligand precursor

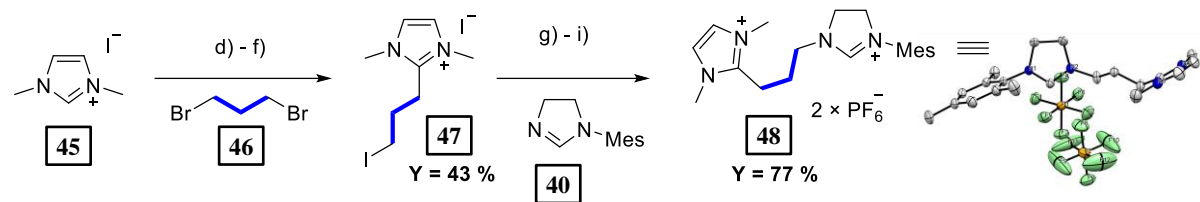
We started off by quaternization of nitrogen atom in **41** structure with the use of methyl iodide and the subsequent Apple reaction allowed for the replacement of the OH group to an iodide leaving group, giving compound **42** in a 61 % isolated yield. However, the following nucleophilic substitution with *N*-mesitylimidazoline (**40**) was not successful as the competing elimination of hydrogen iodide was preferred (Scheme 41A). The olefin **43** was identified in the crude reaction mixture by the presence in ¹H NMR spectrum (Scheme 41B) of characteristic signals for a vinyl group at δ_H 6.71 ppm (doublet of doublets, CH_{olefinic}) and at δ_H 6.21 and 6.12 ppm (two doublets, CH_{2olefinic}). This was supported with HRMS (Scheme 41C), in which a peak at m/z = 123.0918 assigned to **43** (calcd. m/z = 123.0917) was identified.



Scheme 41 A) Attempts to synthesize the first NHC-NHO ligand precursor **38**; reaction conditions: a) methyl iodide (excess), 80 °C, 15 min.; b) 1.1 equiv. of CBr₄, 1.1 equiv. PPh₃, dimethylformamide (DMF), rt, 2 h; c) 1.05 equiv. of **40**, MeCN, 90 °C,

overnight. B) ^1H NMR spectrum of a crude reaction mixture and signal assignments of the elimination product **43**. C) HRMS spectrum of crude reaction mixture.

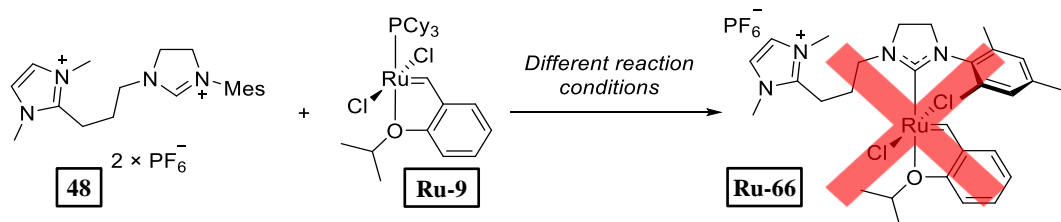
Due to the encountered obstacle, the structure of the targeted ligand was altered. To circumvent the undesired elimination reaction, we decided to introduce an additional CH_2 unit in between NHC and NHO pre-functionalities (structure **48**, Scheme 42). From dimethylimidazolium iodide (**45**) the corresponding dimethylimidazolylidene IMe was formed by deprotonation with lithium hexamethyldisilazide (LiHMDS) and was next engaged in a nucleophilic substitution reaction with 1,3-dibromopropane (**46**). The subsequent Finkelstein reaction gave the expected compound **47** in 43 % yield. At last, ligand precursor **48** was obtained through the nucleophilic substitution reaction of the precursor **47** with *N*-mesitylimidazoline. The structure of **48** was determined with NMR spectroscopy and unambiguously confirmed by XRD (Scheme 42).



Scheme 42 The synthesis of the second NHC-NHO ligand precursor **48** and its XRD structure (ellipsoids are drawn at 50 % probability, hydrogens were omitted for clarity); reaction conditions: d) 1.05 equiv. of LiHMDS, THF, rt, 80 min.; e) 20 equiv. of **46**, -80 °C to rt, overnight. f) 5 equiv. of NaI, acetone, rt, overnight; g) 1.3 equiv. of **40**, MeCN, 90 °C, overnight; h) 3.4 equiv. of AgCl, water, rt, 30 min.; i) 5.6 equiv. of KPF₆, DCM, 40 °C, 7 days.

2.3.2. Attempts to synthesize ruthenium OM catalyst containing the NHC-NHO ligand

With the NHC-NHO ligand precursor **48** in hand, the synthesis of the corresponding NHC-ruthenium OM catalyst **Ru-66** was attempted (Scheme 43). In this approach, we investigated the commonly utilized PCy₃ to NHC ligand replacement in the structure of metal precursor **Ru-9**. However, the complex **Ru-66** could not be obtained by this way. Since the exploration of other less common ruthenium precursors was not fruitful in the case of NHC-barbiturate catalyst synthesis (Chapter 2.2), we decided to shift at this point from the attempts to synthesize the corresponding ruthenium NHC catalysts and focus on a general study of the novel NHC-NHO ligand type architecture. As explained previously in Chapter 2.1, such ligand architecture is a completely novel approach and a more general study of it is still compelling, and evidently required prior to a future application study.

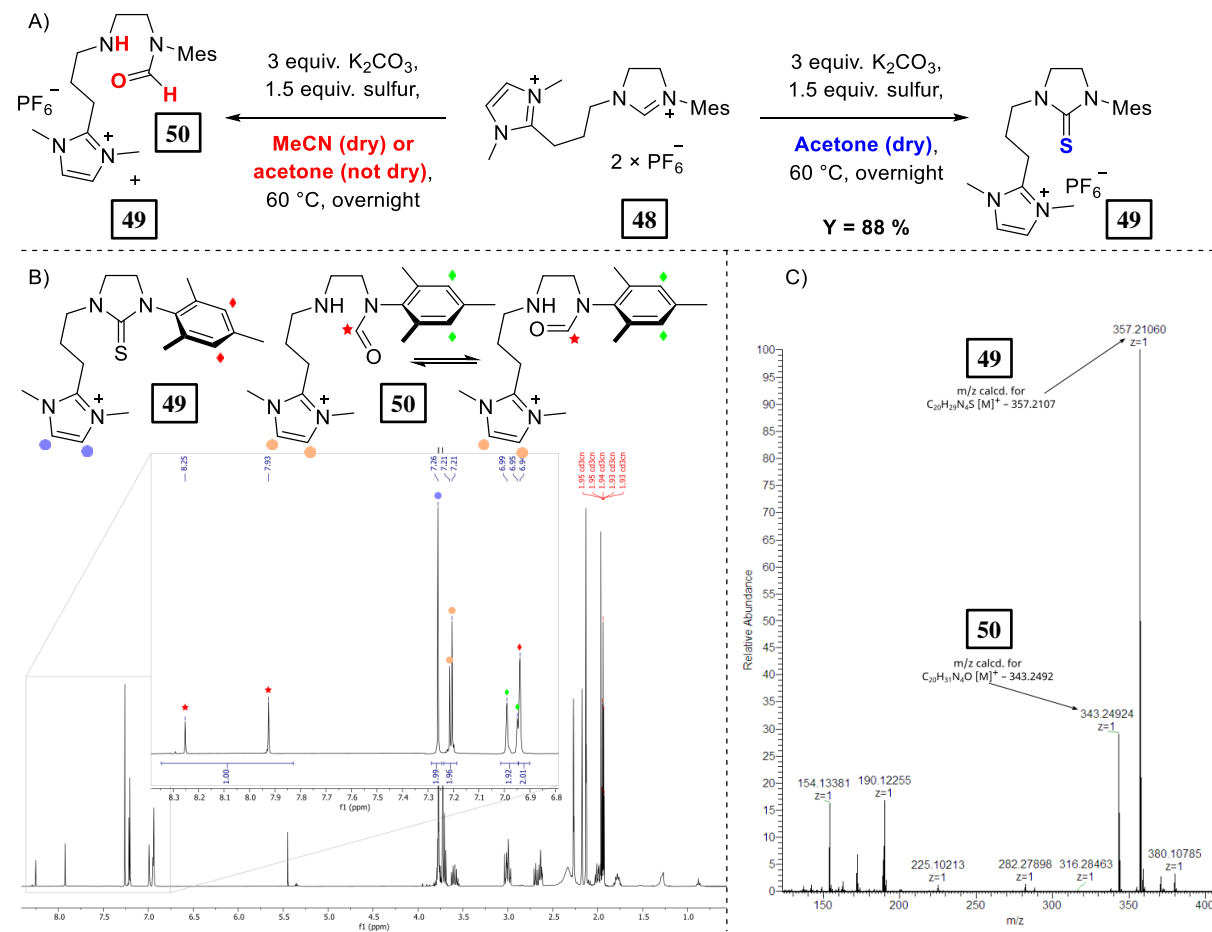


Scheme 43 The attempted synthesis of **Ru-66**.

To better understand why the complex **Ru-66** was not formed, reactivity studies of the precursor **48** were performed by investigation of the formation of thiourea **49**. While, when performed in dry acetone, the reaction gave quite cleanly the expected **49** (isolated in 88 % yield by crystallization, Scheme 44A), when either non-dried acetone [high-performance liquid chromatography (HPLC) grade] or dry MeCN (10 ppm of water was detected using Karl-Fisher titration) were used, it resulted in a significant

formation of side product **50**. Compound **50** could be identified in a crude reaction mixture by the presence in the ^1H NMR spectrum of upfield shifted signals at δ_{H} 8.25 and 7.93 ppm corresponding to the $\text{CH}_{\text{formyl}}$ proton of the two rotamer forms of **50** (Scheme 44B). Furthermore, the same pattern was observed in the aromatic region with the two rotameric forms of **50** giving the signals at δ_{H} 7.21 and 7.21 ppm ($\text{CH}_{\text{imidazolium}}$) and 6.99 and 6.95 ppm (CH_{Mes}). Moreover, the m/z ratio characteristic for **50** was identified with HRMS (Scheme 44C).

The formation of **50** could only result from the ring opening of the imidazolinylidene carbene formed from precursor **48**. Saturated NHCs (imidazolinylidenes) can suffer from ring opening of the heterocycle, although the reaction mechanism involves water.^[195] It seems peculiar that the reaction performed in MeCN containing 10 ppm of water would give **49** and **50** formed in equimolar ratio, whereas while dry acetone was used (the water content of ketones cannot be determined by classical Karl-Fisher titration, however, dry acetone certainly contained significantly more than 100 ppm of water)^[196] the desired thiourea **49** was isolated in 88 % yield. Probably, the solvent affects the rates of the two competing reactions, although this matter requires more investigation.

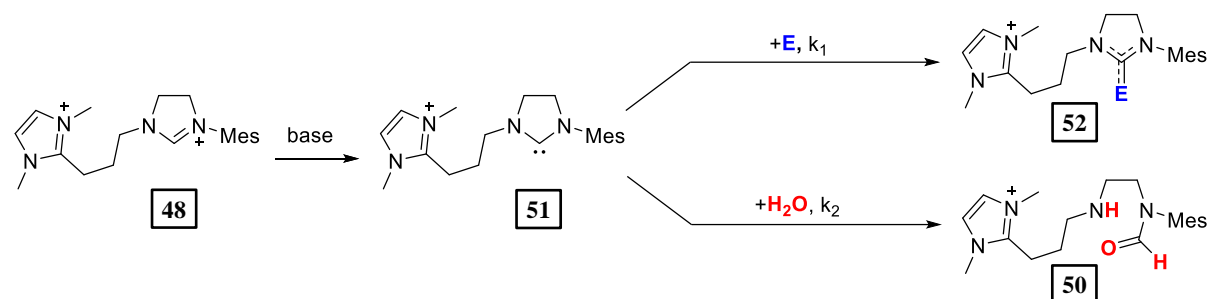


Scheme 44 A) Screening of the basic reactivity for the formation of the NHC thioadduct **49**. B) ^1H NMR spectrum of crude reaction mixture containing **49** and **50** (when dry MeCN was used). C) HRMS (ESI) mass spectrum of crude reaction mixture containing **49** and **50** (when dry MeCN was used).

The reactivity with sulfur has led us to propose the reactivity pattern of the precursor **48** (Scheme 45). Once the azolium position of **48** is deprotonated, the formed NHC **51** can undergo two competing reactions. **51** can either form the desired complex with the electrophile (**52**) or the imidazolinylidene ring

can open in the presence of traces of water giving *N*-formylated product **50**. Presumably, the solvent affects the ratio of the competing reaction rates (k_1 to k_2 , Scheme 45).

It becomes clear at this point why the synthesis of the ruthenium-NHC complex **Ru-66** had failed. The energy barrier of PCy_3 replacement with an NHC ligand in the structure of **Ru-9** is usually relatively high as heating is required. Consequently, the formation of the side product **50** is preferred instead. Noteworthy, the reaction conditions that gave selectively thiourea **49** (K_2CO_3 , dry acetone, 60°C) were also attempted for the synthesis of complex **Ru-66**, however, with no positive outcome. Moreover, neither did the use of a stronger base (LiHMDS), however, since in this case the selectivity of the deprotonation of either NHC or NHO pre-functionalities cannot be modulated, this approach was rejected at the early beginning.



Scheme 45 Proposed explanation for the observed reactivity of carbene **51**.

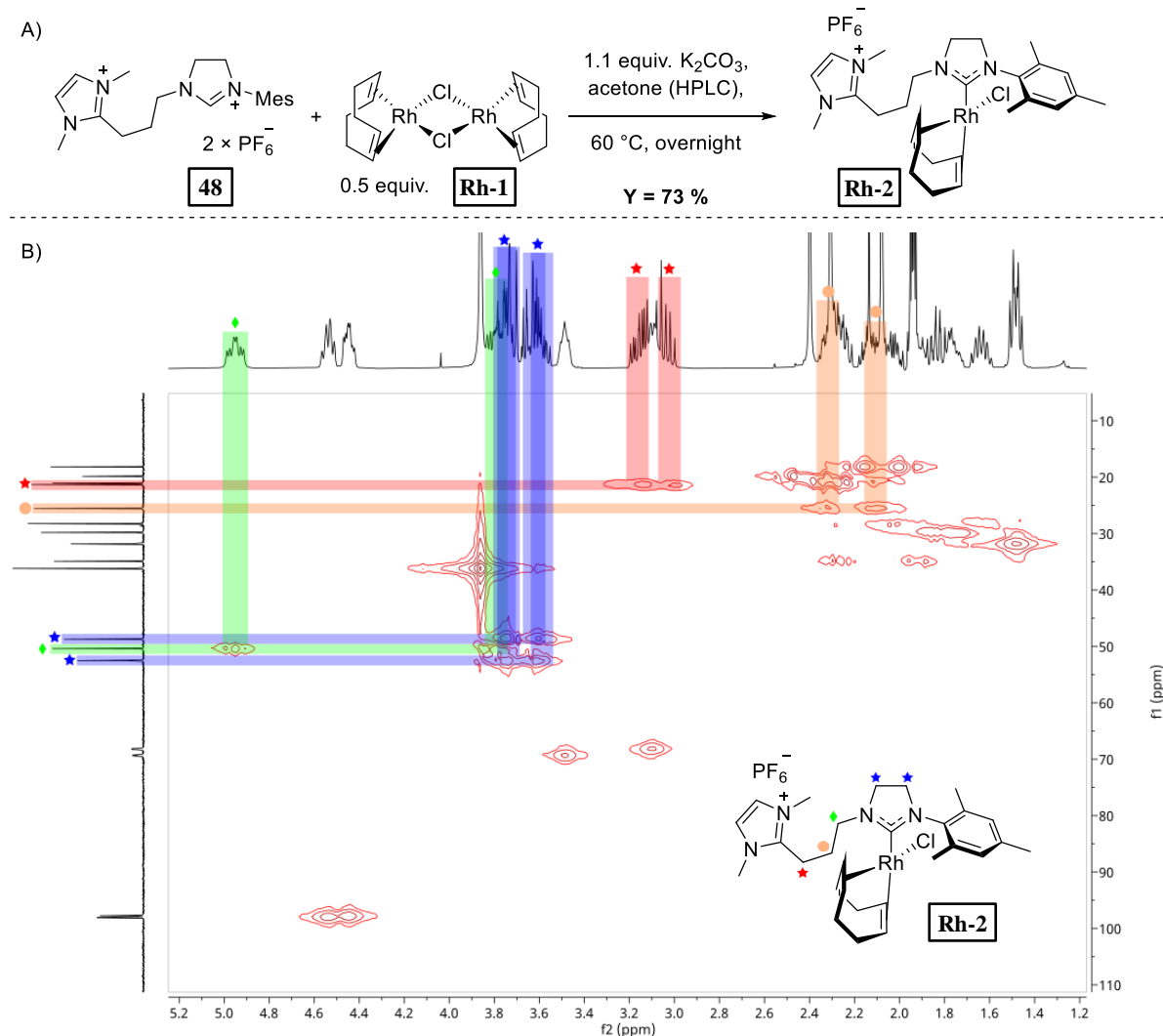
2.3.3. Synthesis of rhodium(I) NHC complexes

Learning the general reactivity pattern of our ligand, we set off to synthesize a metal complex bearing the targeted ligand coordinated in a monodentate mode through NHC and next attempt the coordination of the NHO moiety. We hypothesized that a dimeric structure of metal precursor might be reactive enough to give a metal-NHC complex in a good yield whilst the formation of **50** would be much slower. Rhodium(I) metal center was chosen as the corresponding NHC complex should be air-stable, isolable by CC and after installation of CO ligands allow for measuring the ligand's electronic properties (TEP).

Indeed, utilizing dimeric rhodium precursor **Rh-1** proved to be a good strategy and gave the rhodium-NHC complex **Rh-2** isolated by CC in 73 % yield (Scheme 46A). The formation of **Rh-2** was initially evidenced by the disappearance of the characteristic signal in the ^1H NMR spectrum of the imidazolinium proton. Furthermore, the ^{13}C NMR spectrum revealed the downfield shifted doublet signal at δ_{C} 212.0 ppm [$^1J(\text{C}-\text{Rh}) = 47.3$ Hz] characteristic of carbenic carbon atom coordinated to rhodium. The signal multiplicity resulted from the coupling of the carbon atom with the ^{103}Rh isotope. The structure of **Rh-2** was confirmed by XRD (Figure 19A).

The complex **Rh-2** ^1H NMR spectrum revealed three singlet signals at δ_{H} 2.40, 2.31 and 2.08 ppm, as well as two singlet signals in the aromatic region at δ_{H} 7.01 and 6.95 ppm, which is a characteristic of a mesityl group with broken C_2 symmetry (two-fold rotational symmetry). However, this could be an effect of blocked rotation around either nitrogen- C_{Mes} as well as rhodium- C_{NHC} bonds. Blocked rotation around the rhodium- C_{NHC} bond in the structure of **Rh-2** would result in diastereotopic CH_2 groups, as the two protons of each CH_2 would reside in a different chemical environment. Although the ^1H NMR spectrum of **Rh-2** is too complicated to unambiguously distinguish diastereotopic proton groups, the ^1H - ^{13}C heteronuclear single quantum coherence (HSQC) spectrum clearly indicates that in each CH_2 unit, one carbon signal correlates with two proton groups, as depicted in Scheme 46B (for CH_2 units in

the NHC ligand). This thus conveys that at ambient temperature, in CD_3CN solution the rhodium- C_{NHC} bond rotation is blocked.

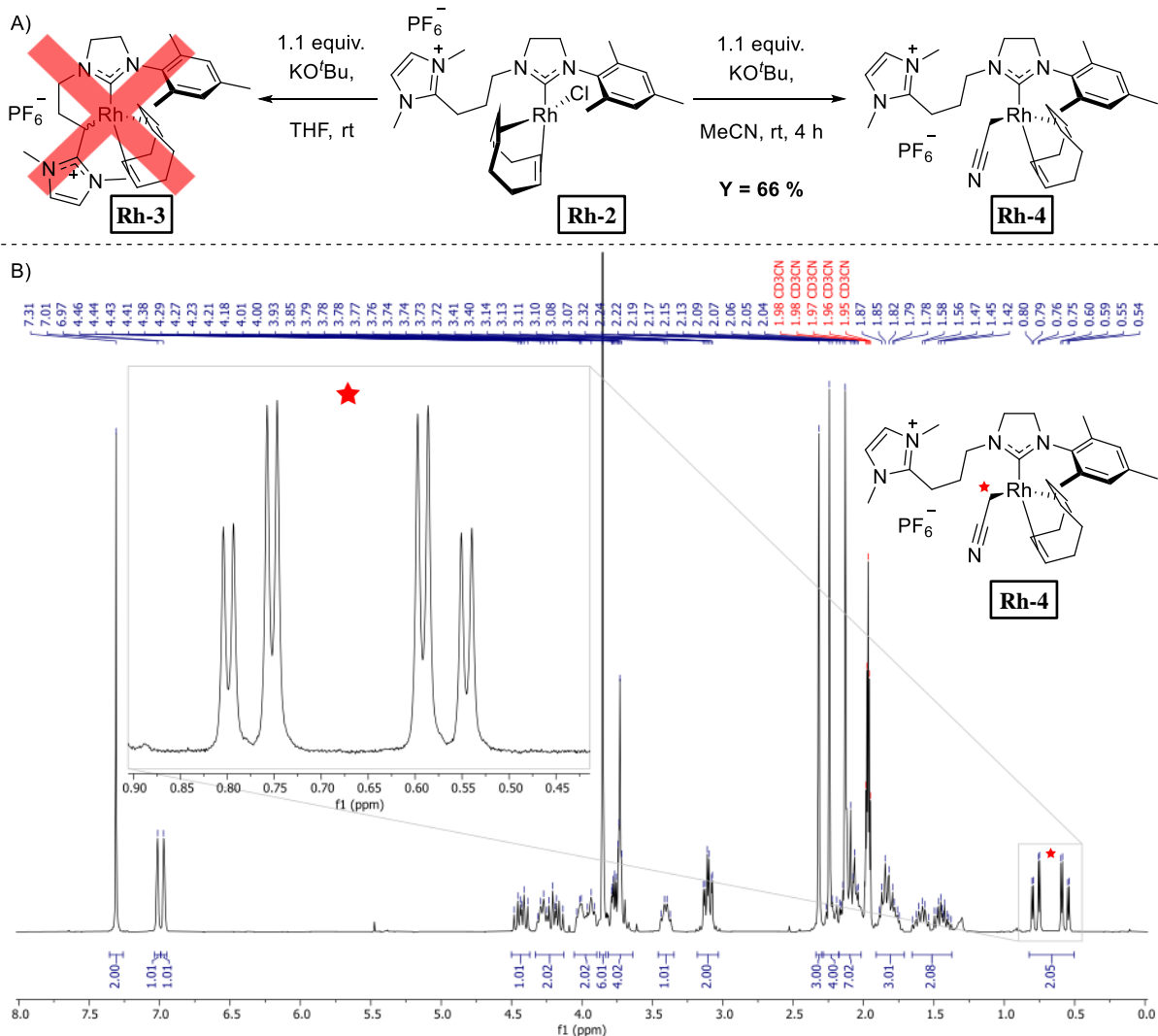


Scheme 46 A) Synthesis of rhodium-NHC complex **Rh-2**. B) ¹H-¹³C HSQC spectrum of complex **Rh-2** with the marked correlation between carbon signals in NHC's CH_2 units and diastereotopic proton groups.

In the next step, deprotonation of α -imidazolium position (NHO pre-functionality) was attempted in the hope of forming the corresponding NHO complex. When the reaction was performed in THF, although complex **Rh-2** reactivity was observed, no rhodium-NHC-NHO complex **Rh-3** could have been isolated (Scheme 47A, left). Most probably an alkoxy ligand replaced chloride, however, for unclear reasons the desired product **Rh-3** was not formed.

Strikingly, when the same reaction was attempted in acetonitrile, the complex **Rh-4** was isolated in which a deprotonated acetonitrile (cyanomethyl) ligand replaced the chloride ligand (Scheme 47A, right). This was evidenced by the appearance in ¹H NMR of a peculiar, shielded doublet of doublet signal at δ_{H} 0.67 ppm (Scheme 47B) assigned to the CH_2 group of the newly formed cyanomethyl ligand. The observed signal multiplicity derives from coupling with ¹⁰³Rh isotope and a diastereotopic CH_2 group, which similarly to the complex **Rh-2** results from a blocked rhodium- C_{NHC} bond. The corresponding signal in ¹³C NMR of the discussed CH_2 group was observed as a doublet at δ_{C} -8.4 ppm [$J(\text{C}-\text{Rh}) = 25.8$ Hz]. The signal assigned to C_{NHC} was slightly downfield shifted with

respect to **Rh-2**, at δ_{C} 219.0 ppm. Although rather unstable in the air or in solution, complex **Rh-4** was fully characterized by NMR and it was possible to grow single crystals suitable for XRD, by layering MeCN complex solution with Et₂O (Figure 19B).



Scheme 47 A) Attempts to synthesize the rhodium-NHC-NHO complex **Rh-3** and the synthesis of rhodium-NHC-cyanomethyl complex **Rh-4**. B) ¹H NMR spectrum of rhodium-NHC-cyanomethyl complex **Rh-4**.

The crystal structures of **Rh-2** and **Rh-4** were then closely examined (Table 3). Both complexes exhibit a square-planar coordination geometry, a classical case for rhodium(I) 16e⁻ complexes. Rhodium-C_{NHC} bond lengths in the two complexes do not differ by more than three estimated standard deviations and well correlate with examples of other rhodium-NHC complexes reported in the literature.^[170,189,197] Similarly, rhodium-carbon bond lengths of COD ligand's carbon atoms *trans* to the NHC (C3 and C4 in Figure 19) do not differ between **Rh-2** and **Rh-4** and from the literature, varying from 2.180 to 2.207 Å. Reflecting a stronger *trans* effect of an NHC ligand *versus* the X-type chloride or cyanomethyl ligand, in both complexes rhodium-carbon bond lengths of COD ligand's carbon atoms *cis* to the NHC (C2 and C5 in Figure 19) decrease significantly to 2.109, 2.113 and 2.142, 2.162 Å for complexes **Rh-2** and **Rh-4** respectively. Moreover, the longer bond lengths in **Rh-4** indicate a stronger *trans* effect of cyanomethyl ligand when compared with chloride.

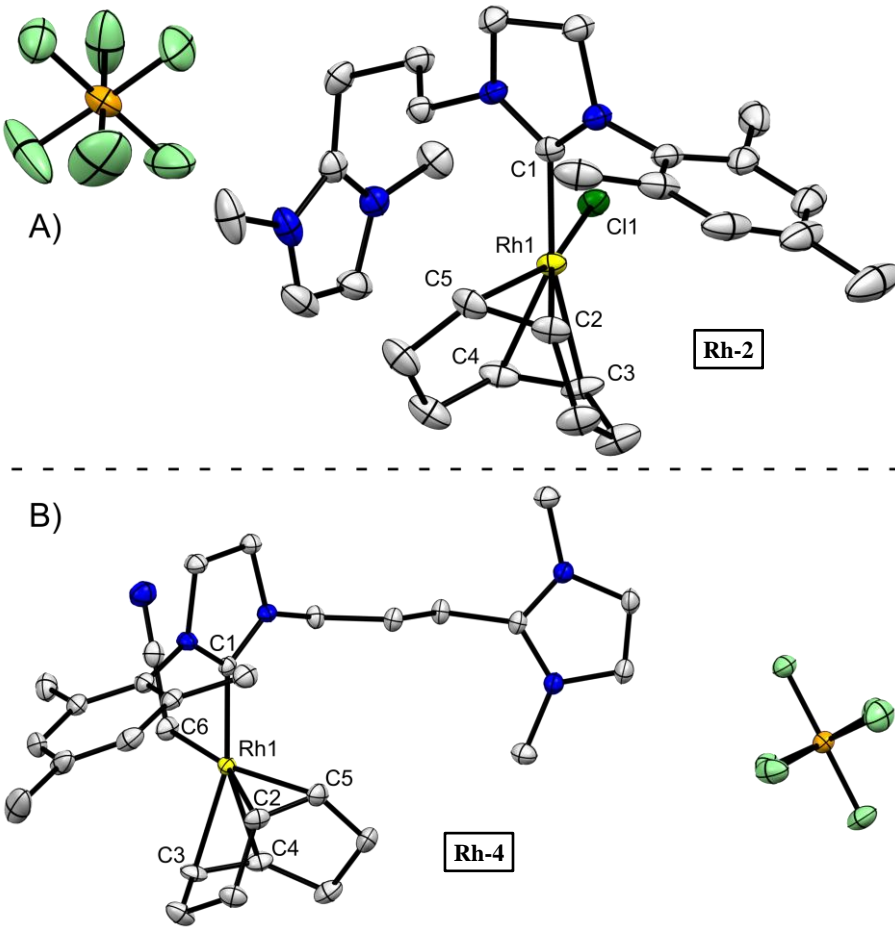


Figure 19 XRD crystal structures of **Rh-2** and **Rh-4**, ellipsoids are drawn at 50 % probability, hydrogens were omitted for clarity. Atom labeling does not correspond to cif files.

Table 3 Selected bond lengths of complexes **Rh-2** and **Rh-4**. Atom labeling corresponds to Figure 19 and not to cif files.

Entry	Bond	Rh-2	Rh-4
1	Rh1-C1	2.039(3)	2.027(2)
2	Rh1-C2	2.113(3)	2.162(2)
3	Rh1-C3	2.195(3)	2.180(2)
4	Rh1-C4	2.207(3)	2.202(2)
5	Rh1-C5	2.109(3)	2.142(2)
6	Rh1-C6	-	2.154(2)

The unexpected reluctance of the complex **Rh-2** cyclometallation and the formation of **Rh-4** prompted us to examine the literature in search of a possible explanation. Certainly potassium *tert*-butoxide is not basic enough (pKa of *tert*-butanol equals 16.5)^[198] to deprotonate acetonitrile (pKa of acetonitrile equals 28.9),^[199] however, evidenced here is the facilitation of this process in the rhodium coordination sphere. A few examples of transition metal cyanomethyl complexes can be found in the literature, based on gold,^[200] nickel,^[201,202] palladium,^[203] platinum,^[204,205] iridium,^[206,207] iron,^[208] rhenium^[209] and copper^[210] metals. To the best of our knowledge, no cyanomethyl rhodium complex has been reported so far.

Furthermore, two strategies to synthesize such complexes have been reported. On one hand, acetonitrile can be deprotonated using a strong base such as *n*-butyllithium and the corresponding LiCH₂CN can be reacted with a transition metal precursor. Moreover, an oxidative addition of either ClCH₂CN or acetonitrile could be performed giving chloro- or hydrido-cyanomethyl complexes. However, to the best of our knowledge, no cyanomethyl complex was obtained using a relatively weak base as potassium *tert*-butoxide. However, it remains unclear why the complex **Rh-4** was formed instead of **Rh-3** since the pKa of α -imidazolium position and acetonitrile should be similar (DFT calculated pKa of structurally related compound **53** being 28.1, Figure 20).^[180]

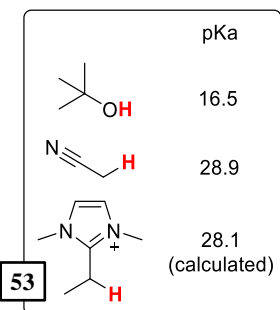
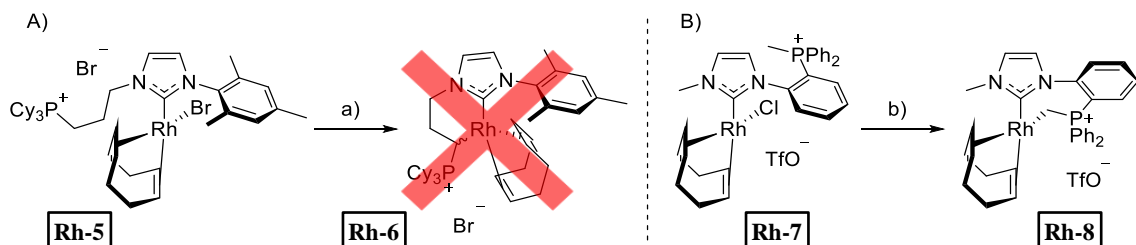


Figure 20 Relative acidities of *tert*-butanol, acetonitrile and **53**.

Canac and coworkers reported the synthesis of NHC-rhodium complex **Rh-5**, structurally very closely related to **Rh-2**. Similarly, attempts of cyclometallation gave a mixture of products and no rhodium-NHC-phosphonium ylide complex **Rh-6** was isolated (Scheme 48A).^[197] Conversely, an earlier report by Canac and coworkers described the synthesis of complex **Rh-8** which was obtained by treating the rhodium-NHC complex **Rh-7** with potassium *tert*-butoxide (Scheme 48B).^[211] Perhaps the unobstructed **Rh-8** formation might result from more steric availability of CH₂ ylidic functionality rather than substituted CH ylide of the anticipated complex **Rh-6**. However, more significant seems the formation of a seven-membered metallacycle in **Rh-8** versus six-membered in **Rh-6** (as explained below).



Scheme 48 A) Failed synthesis of related rhodium-NHC-phosphonium ylide complex **Rh-6**, reported by Canac and coworkers; reaction conditions: a) *t*BuOK, THF, -78 °C to rt, 2 h. B) Synthesis of complex **Rh-8**, reported by Canac and coworkers; reaction conditions: a) *t*BuOK, THF, -78 °C to rt, 1 h.

XRD structures of the rhodium-NHC complexes **Rh-2**, **Rh-4** and **Rh-5** reveal that the square-planar coordination sphere of the metal and NHC's heterocycle orient in a quasi-orthogonal fashion, with C11-Rh1-C20-N1 in **Rh-2**, C35-Rh1-C19-N2 in **Rh-4** and C11-Rh1-C1-N2 in **Rh-5** torsion angles being 67.8, 73.9 and 80.5° respectively (Figure 21). Exchanging the COD ligand in **Rh-8** structure for CO ligands gave complex **Rh-9** which was characterized using XRD. **Rh-9** crystal structure revealed that also in this case such orientation of the two planes is preferred, with the C23-Rh1-C1-N1 torsion angle being 62.4° (Figure 21). It seems likely that such preferred orientation results from steric repulsion of NHC's *N*-substituents with other co-ligands, thus hindering the rotation around the rhodium-C_{NHC} bond as evidenced earlier with NMR spectroscopy. Possibly, due to this blocked rotation only the seven-

membered metallacycle could be formed as it allows the ylide ligand to reach the metal coordination site without twisting the NHC heterocycle to a coplanar arrangement, which presumably results in a steric clash within the molecule.

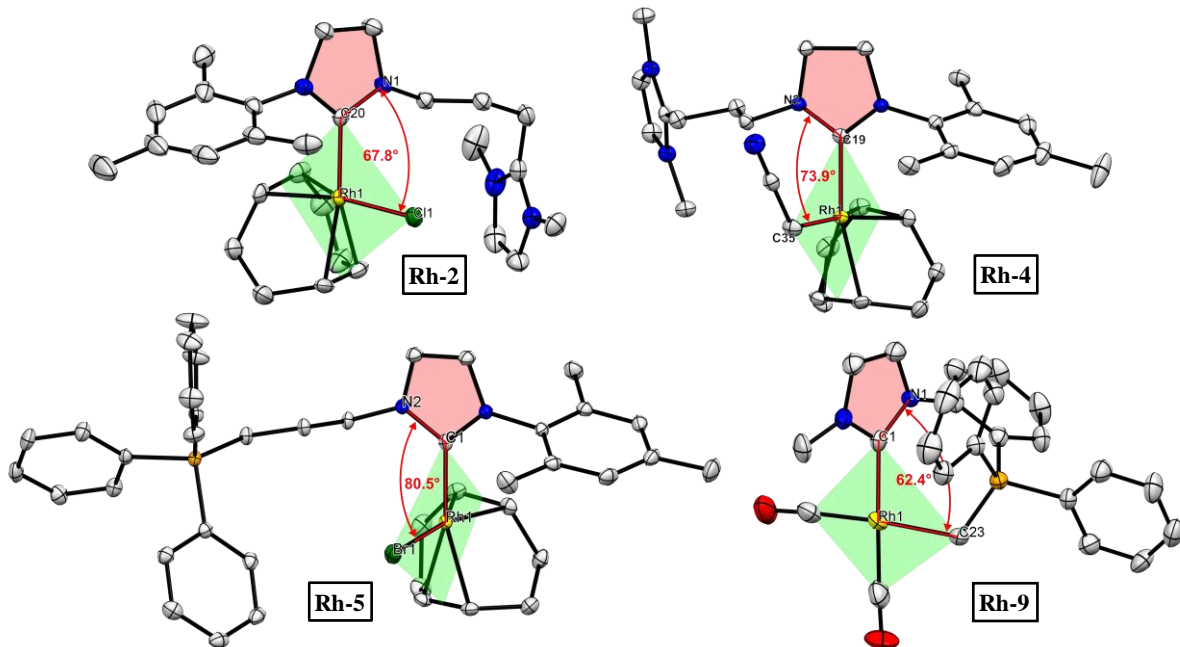


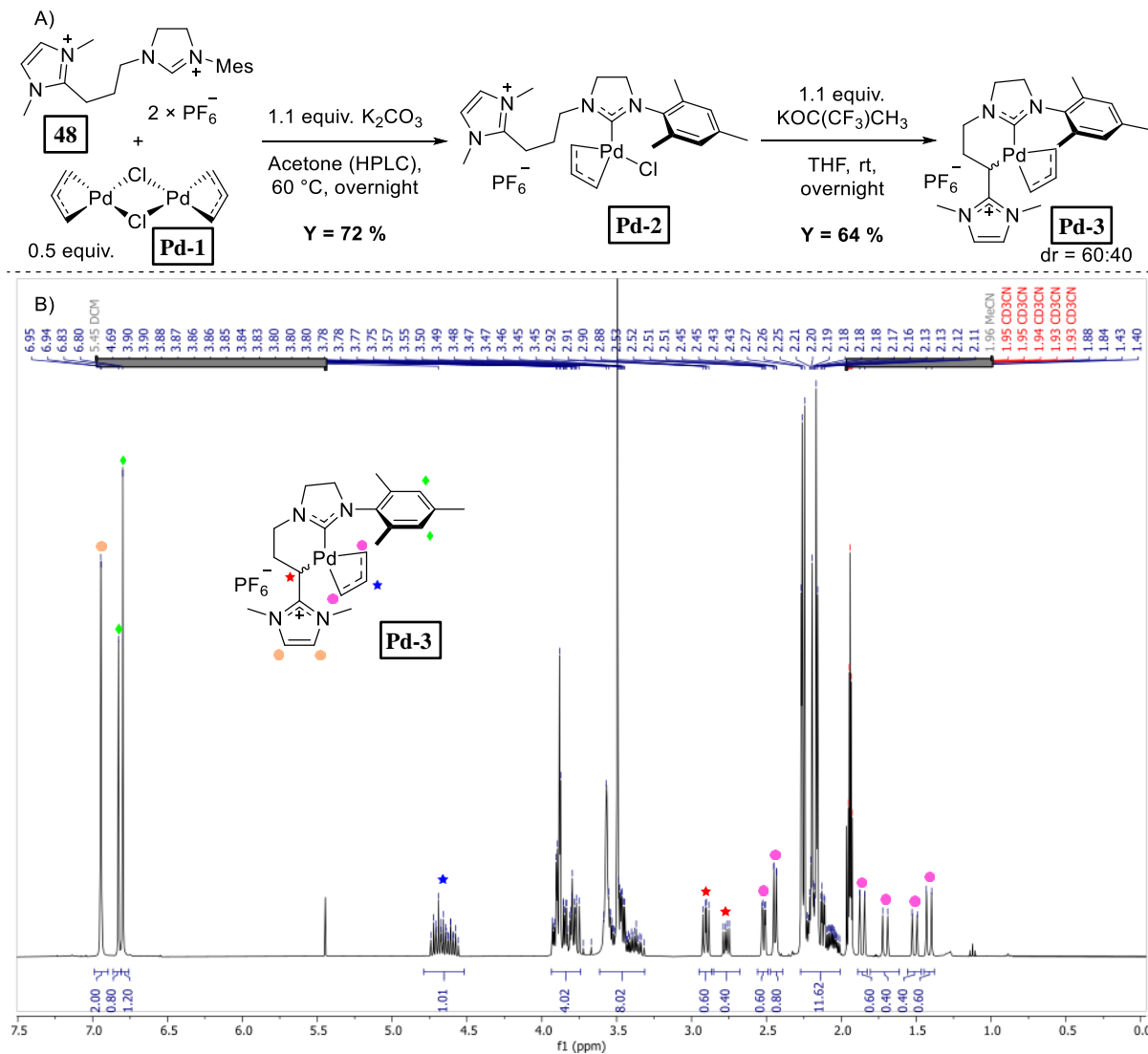
Figure 21 Crystal structures of complexes **Rh-2**, **Rh-4**, **Rh-5**, **Rh-9** and with indicated key structural parameters. Ellipsoids were drawn at 50 % probability. Hydrogen atoms and counter ions were omitted for clarity.

2.3.4. Synthesis of palladium(II) NHC-NHO complex

In view of the difficulties in the cyclometallation of a rhodium complex, we next turned our attention to palladium metal in the hope that it would be possible to obtain a palladium-NHC-NHO complex. Similarly to the case of **Rh-1**, utilizing a dimeric palladium precursor **Pd-1** gave the desired palladium-NHC complex **Pd-2** in a good yield of 72 % (Scheme 49A). Formation of an NHC complex was evidenced by the disappearance of the characteristic signal in the ¹H NMR spectrum of the imidazolinium proton, supported by the emergence in the ¹³C NMR spectrum of the downfield shifted broad signal at δ_{C} 210.2 – 209.1 ppm characteristic for C_{NHC} of an imidazolinylidene complex. Both ¹H and ¹³C NMR spectra of **Pd-2** exhibited a very significant line broadening, obscuring the multiplicity of all signals recorded in ¹H NMR and preventing the recording of ¹³C NMR with sharp signals. This most probably results from the hindered π - σ -allyl rearrangement (sometimes referred to as flip of π -allyl ligand)^[212,213] which slow rate constant compared to the NMR time scale accounts for the line broadening. Notably, recording the spectra at varied temperatures did not improve their resolution.

Gratifyingly, deprotonation of α -imidazolium position in **Pd-2** gave the expected cyclometalated palladium-NHC-NHO complex **Pd-3** in 64 % yield (Scheme 49A). Resulting from the presence of an asymmetric carbon atom and blocked flip of π -allyl ligand, complex **Pd-3** occurs in forms of diastereomers formed in a ratio of 60:40 (determined by ¹H NMR, Scheme 49B). The signals assigned to C_{NHC} were recorded at δ_{C} 200.8 and 202.3 ppm. Signals of the CH_{NHO} group were recorded in ¹H NMR as doublets of doublets at δ_{H} 2.90 and 2.77 ppm, and in ¹³C NMR at δ_{C} 16.1 and 16.4 ppm. Naturally, every CH₂ group is diastereotopic which was evidenced in the ¹H-¹³C HSQC NMR spectrum with CH₂ protons of allyl ligand characteristically scattered as doublets (sometimes concealed within other multiplets) from

δ_H 2.55 to 1.41 ppm. Notably, in the aromatic region, only two signals corresponding to the CH_{Mes} group were observed at δ_H 6.83 and 6.80 ppm, which indicates unhindered rotation around the nitrogen- C_{Mes} bond.



Scheme 49 Synthesis of the palladium-NHC-NHO complex **Pd-3**.

The structure of **Pd-3** was confirmed by XRD (Figure 22A). The palladium atom resides in a quasi-square-planar environment. Diastereomers of **Pd-3** cocrystallized which led to crystallographic disorder observed in the XRD structure. Palladium- C_{NHC} bond distance measuring 2.030 Å well correlates with values reported for other palladium-NHC complexes.^[197,213] Palladium- C_{NHO} bond distances measured 2.152, 2.181 Å, which was slightly higher than in other palladium-NHO complexes reported in the literature ranging from 2.037 to 2.136 Å.^[173,174] Furthermore, the bond lengths of palladium- C_{allyl} are also in agreement with other palladium-allyl complexes reported in the literature.^[197,213] Notably, the palladium- C_{allyl} bond of carbon atom in *trans* position to the NHO ligand (Pd1-C2, Table 4, entry 2) was slightly longer when compared to the carbon atom *trans* to the NHC ligand (Pd1-C4, Table 4, entry 4). This is well explained by a stronger *trans* effect of NHO ligand resulting from its stronger σ -donation. Importantly, as defined in Figure 22B the relevant torsion angle measured 31.4° , which presumably was attainable due to lower steric repulsion of the NHC-NHO ligand with other co-ligands than in the case

of the rhodium coordination sphere. Investigations on this subject using DFT calculations would be highly insightful.

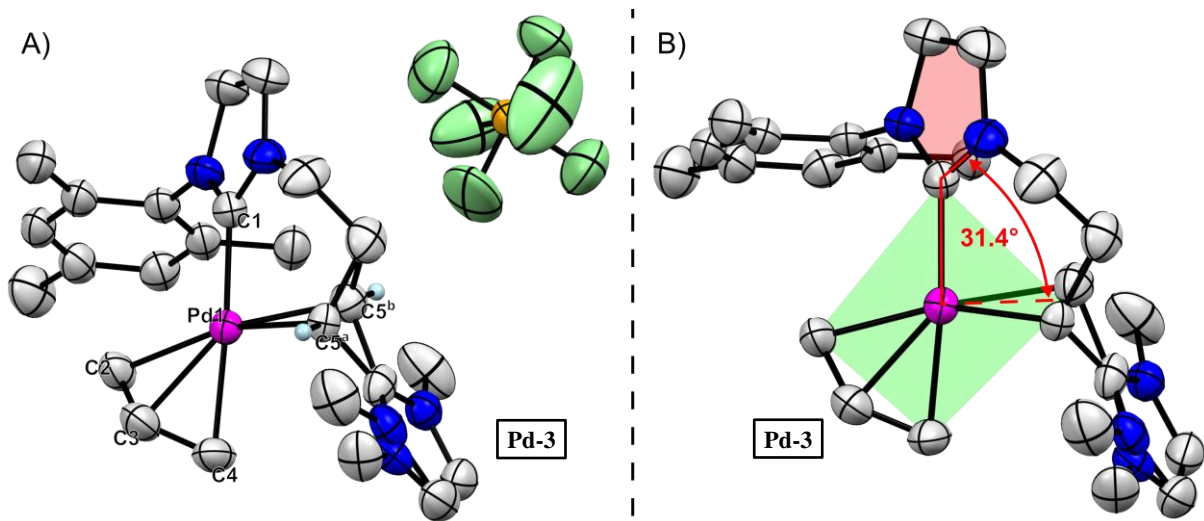


Figure 22 A) XRD crystal structure of the palladium-NHC-NHO complex **Pd-3** (ellipsoids are drawn at 30 % probability, hydrogens were omitted for clarity). Atom labeling does not correspond to the cif file. B) Explanation of a key structural parameter of complex **Pd-3** crystal structure.

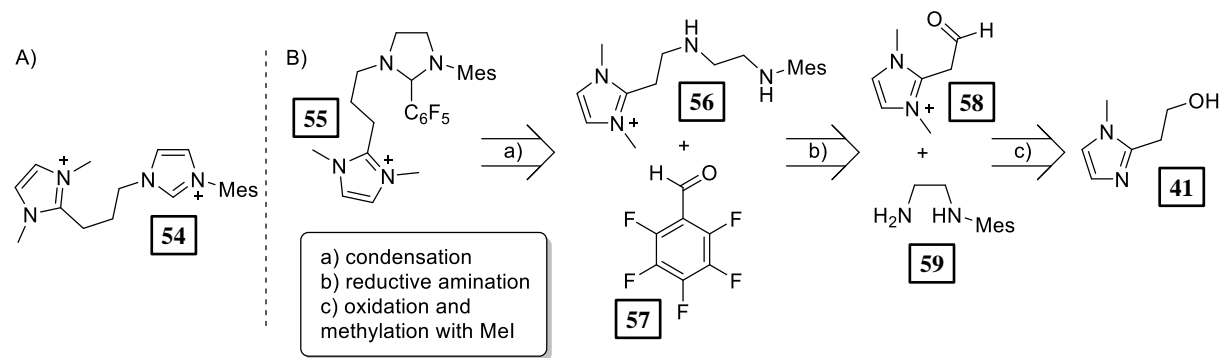
Table 4 Selected bond lengths of complex **Pd-3**. Atom labeling corresponds to Figure 22A and not to cif files.

Entry	Bond	Distance (Å)
1	Pd1-C1	2.030(4)
2	Pd1-C2	2.212(4)
3	Pd1-C3	2.152(5)
4	Pd1-C4	2.167(5)
5	Pd1-C5 ^a	2.152(7)
6	Pd1-C5 ^b	2.181(10)

2.3.5. Conclusions

An NHC-NHO ligand precursor **48** with NHC pre-unit and NHO pre-unit linked with two membered alkyl chain was successfully obtained (Scheme 42). However, the selected synthetic route was not successful in the synthesis of the initially chosen NHC-NHO precursor **38** due to a competing elimination reaction to form alkene **43** (Scheme 41). Furthermore, it was discovered that the NHC generated from **48** undergoes a competing ring opening of the imidazolinylidene heterocycle precluding the formation of the ruthenium-NHC complex **Ru-66** (Scheme 43). Certain conclusions can be drawn from those results to prevent the undesired side reactions and obtain an analog of **Ru-66**. On the one hand, the unsaturated NHC derivative of **48** should not undergo the heterocycle ring opening since it is a feature of saturated NHC analogs.^[195] The proposed structure of **54** (Scheme 50A) could be obtained using a similar synthetic methodology to the one utilized in the synthesis of **48**. On the other hand, a different synthetic protocol to generate a free NHC could be utilized. An imidazolinylidene NHC could be obtained by thermolysis of a proper precursor (see Chapter 1.2.4) and such an approach proved to be successful when the deprotonation of an azolium salt does not yield a desired metal-NHC complex.^[214,215] However, this implies a significant altering of the initially envisaged synthetic protocol (Scheme 40),

although it allows for the circumvention of the undesired elimination reaction met during the synthesis of **38**. The proposed retrosynthetic route to obtain the NHC-NHO precursor **55** is shown in Scheme 50B.



Scheme 50 A) The proposed NHC-NHO ligand precursor **54** to prevent imidazolinylidene ring opening. B) A proposed synthetic route to obtain the NHC-NHO precursor **55**.

Nevertheless, it was possible to obtain metal complexes bearing the desired NHC coordinated to rhodium(I) and palladium(II) metal centers by the utilization of dimeric metal precursors. The subsequent cyclometallation reaction to generate a metal NHC-NHO complex was successful in the case of the palladium platform (Scheme 49) leading to the formation of the first metal NHC-NHO complex **Pd-3**. However, it was not possible to obtain rhodium-NHC-NHO complex **Rh-3**, allegedly due to block rotation around the rhodium-C_{NHC} bond. Furthermore, when the cyclometallation reaction of **Rh-4** was attempted in acetonitrile an intermolecular protonolysis reaction was preferred leading to the formation of the first cyanomethyl rhodium complex **Rh-4**. This suggests that although the synthesis of a ruthenium-NHC complex similar to **Ru-66** is undoubtedly within reach (by utilizing the modified synthetic approach discussed above), the corresponding cyclometallation reaction to obtain an NHC-NHO catalyst is certainly not guaranteed.

2.4. Summary and prospects

Several ruthenium complexes bearing the targeted NHC-barbiturate ligand were successfully synthesized. However, the planned subsequent installation of an alkylidene ligand proved particularly problematic and the corresponding OM catalyst could not be obtained. The reactivity with phenylacetylene was explored which resulted in the isolation of a ruthenium-NHC-barbiturate complex bearing a tetramerized phenylacetylene chelating ligand coordinated through an alkylidene and cyclopentadiene parts. A mechanism was proposed for the formation of this unexpected complex, consisting of a formation of dicarbene intermediates rather than an expected vinylidene complex.

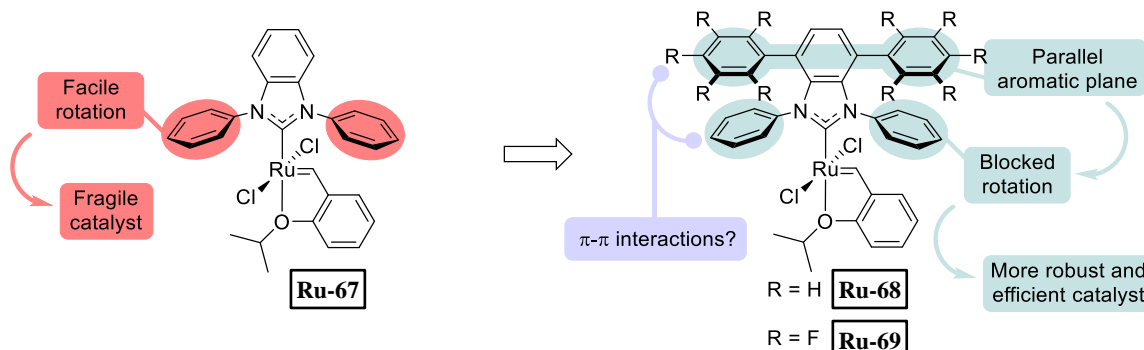
Next, the synthesis of an NHC-NHO OM catalyst was attempted. A ligand precursor was obtained with the means of classical organic synthesis. However, the formation of the corresponding ruthenium-NHC complex was precluded due to an unexpected ring opening of the formed imidazolinylidene heterocycle. The reactivity of the novel class NHC-NHO ligand was explored in the coordination chemistry of rhodium and palladium metal centers, ultimately leading to the synthesis of the first NHC-NHO complex based on a palladium platform. Furthermore, the first rhodium-cyanomethyl complex supported with the NHC ligand was obtained.

Unfortunately, none of the two strategies resulted in an OM catalyst, however, several intriguing reactivities were explored during this work leading to interesting conclusions. We believe that the work reported here represents a significant contribution to the field of organometallic and coordination chemistry. The endeavors on both subjects shall continue in the group of César.

3. NHC ligands bearing parallelly-stacked aromatics for efficient OM catalysts in tetrasubstituted carbon-carbon double bond formation

3.1. Objectives

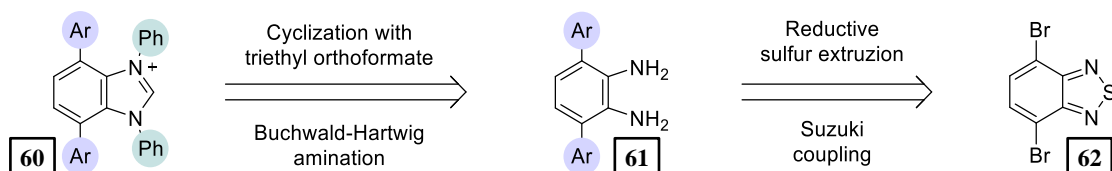
Within this chapter, robust and efficient catalysts for the formation of tetrasubstituted carbon-carbon double bonds are described. Benzimidazolylidene ruthenium catalysts (e.g. **Ru-67**, Scheme 51) did not gain much interest perhaps owing to their limited applications deriving from complexes' high fragility (as described in Chapter 1.5). Delaude and coworkers reported, in their scholarly work, the synthesis of ruthenium catalysts having benzimidazolylidene NHC ligand with *ortho*-tolyl and mesityl *N*-substituents.^[216,217] We reasoned that such ligand architecture would be ideal for the installation of a second decker of aromatic rings, which would hinder the rotation of *N*-aryl rings and would lead to a more robust and efficient OM catalyst. We also wanted to explore whether π - π stacking interactions would contribute to blocking the rotation. For those purposes, the installation of phenyl groups into the backbone (**Ru-68**) was attempted, since the synthesis should be relatively feasible, but also pentafluorophenyl groups (**Ru-69**) since it should result in stronger π - π interactions (Scheme 51).



Scheme 51 The concept for robust OM catalyst for the formation of tetrasubstituted carbon-carbon double bonds.

3.2. Synthesis of NHC precursors

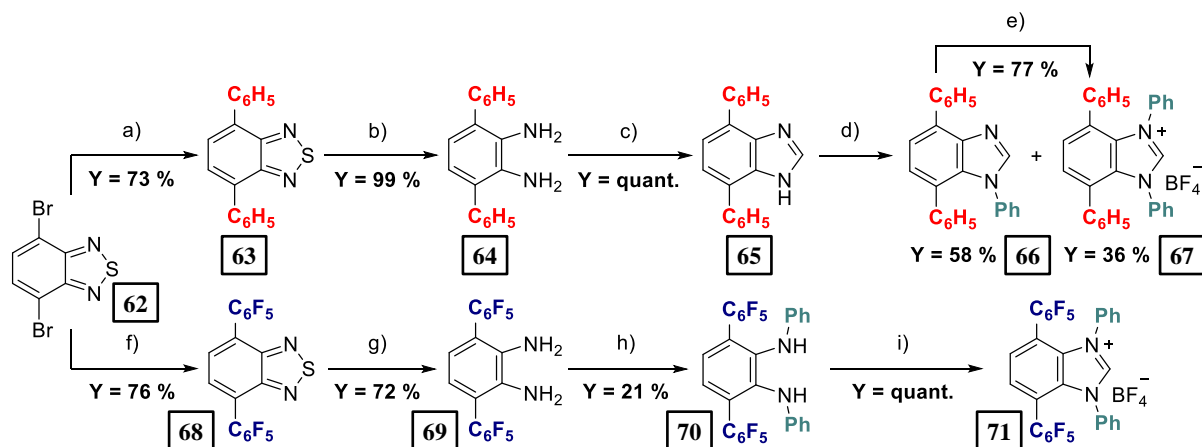
Initially, we envisaged the following synthetic route to synthesize the benzimidazolium precursors **60** (Scheme 52). Starting from dibromobenzothiadiazole (**62**) aromatic groups would be installed using Suzuki-Miyaura coupling, and the intermediary *o*-phenylenediamine derivatives **61** would be obtained after reductive sulfur extrusion. Next, using Buchwald-Hartwig amination phenyl *N*-substituents would be installed and at last after the cyclization with triethyl orthoformate the desired benzimidazolium salts **60** would be isolated.



Scheme 52 A proposed synthetic route to obtain the desired NHC precursors.

However, the final synthetic protocol deviated from the initial plans (Scheme 53) and obstacles met on the way will be discussed later on. Suzuki coupling allowed for the installation of phenyl groups in the backbone motif giving functionalized benzothiadiazole **63** in 73 % yield and subsequent reductive sulfur extrusion gave access to the *o*-phenylenediamine derivative **64** in 99 % yield. Next, the bicyclic benzimidazole skeleton was obtained using standard cyclization protocol with triethyl orthoformate, affording **65** in quantitative yield. Products **63**, **64** and **65** were obtained on a gram scale without any purification steps by CC. In the final step, the desired benzimidazolium salt **67** was obtained using copper-catalyzed arylation with diphenyliodonium tetrafluoroborate. Although examples of *N*-R substituted imidazoles arylations to corresponding imidazolium salts can be found in the literature,^[218] as well as arylations from NH imidazoles to corresponding *N*-aryl imidazoles,^[219] worth highlighting is that such direct arylation of NH imidazole to imidazolium salt has never been reported in the literature. This protocol gave a mixture of the desired *N,N'*-diphenylbenzimidazolium salt **67** (36 % isolated yield) and neutral *N*-phenylbenzimidazole **66** (58 % isolated yield) which were separated using CC. The succeeding arylation of isolated **66** gave salt **67** in 77 % yield, therefore the two subsequent arylation reactions led to an overall yield of 81 % in compound **67**.

Synthesis of pentafluorophenyl substituted derivative **71** presented more synthetic challenges. A Ku-mada-Corriu coupling was successfully employed to graft pentafluorophenyl groups into the benzothiadiazole motif giving **68** in 76 % yield. The subsequent reductive sulfur extrusion step gave the *o*-phenylenediamine derivative **69** in 72 % yield. Unlike the synthesis of salt **67**, the *N*-phenyl groups were first installed through a Buchwald-Hartwig amination, giving compound **70** in 21 % isolated yield. In a final step, the benzimidazolium salt **71** was obtained in quantitative yield using a modified cyclization protocol using triethyl orthoformate in the presence of HBF₄·Et₂O.

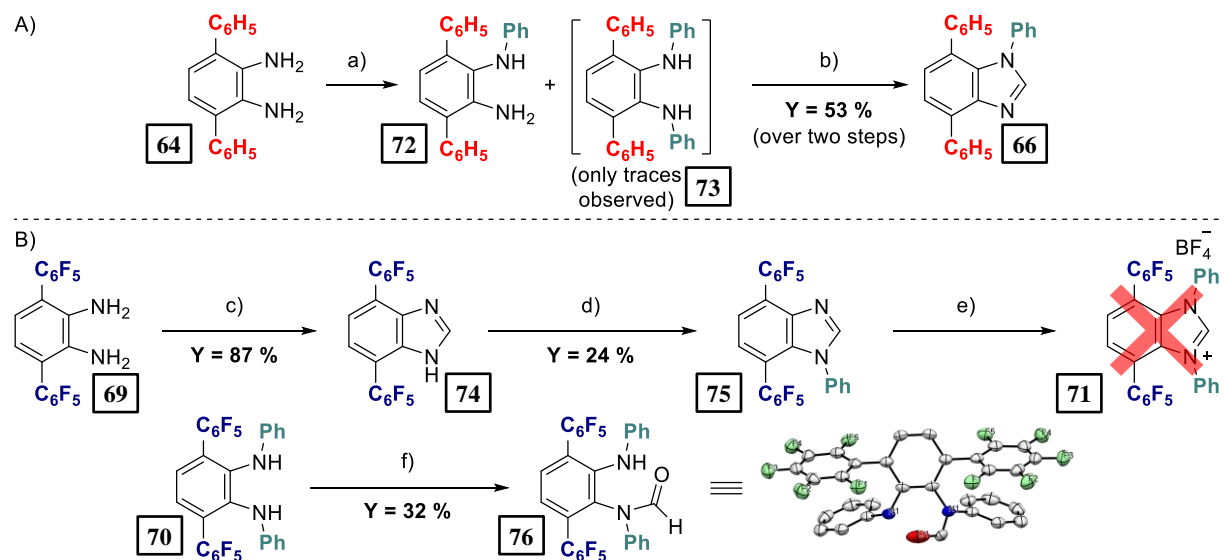


Scheme 53 Synthesis of benzimidazolium salts **67** and **71**; reaction conditions: a) 2.1 equiv. of PhB(OH)₂, 4 equiv. of K₂CO₃, 0.8 mol% Pd(PPh₃)₄, toluene/water 2.5 : 1 v/v, reflux, overnight; b) 9 equiv. of NaBH₄, 6 mol% CoCl₂·6H₂O, EtOH/THF 3:1 v/v, reflux, 3 h; c) (EtO)₃CH (excess), 6 equiv. of HClaq, reflux, overnight; d) 2 x 2 equiv. of Ph₂IBF₄, 2 x 5 mol% Cu(OAc)₂·H₂O, DMF, 100 °C, 24 h, then 48 h; e) 2 equiv. of Ph₂IBF₄, 7.5 mol% Cu(OAc)₂·H₂O, DMF, 100 °C, overnight; f) 3 equiv. of BrMgC₆F₅, 10 mol% Pd(PPh₃)₃, THF, 70 °C, overnight; g) 3 equiv. of NaBH₄, 7 mol% CoCl₂·6H₂O, EtOH/THF 3:1 v/v, 50 °C, 1 min. 30 sec.; h) PhBr (excess), 2.5 mol% Pd₂(dba)₃, 7.5 mol% P'Bu₃, 1.5 equiv. of potassium hexamethyldisilazide (KHMDs), 160 °C, 30 min.; i) (EtO)₃CH (excess), 1 equiv. of HBF₄·Et₂O, 60 °C, 30 min.

As mentioned previously, the original synthetic protocol needed several amendments. During the synthesis of **67**, we found that Buchwald-Hartwig amination is not efficient in installing phenyl *N*-substituents (Scheme 54A). At relatively high palladium catalyst loading (10 mol%) it was possible to obtain *N*-phenyl derivative **72**, giving after cyclization with triethyl orthoformate the neutral *N*-phenylbenzimidazole **66** in moderate isolated yield of 53 %. However, only traces of the desired *N,N'*-diphenyl

derivative **73** were formed. In this respect, the copper-catalyzed arylation with diphenyliodonium tetrafluoroborate performed much more efficiently while avoiding the use of using an expensive palladium catalyst at high catalyst loading.

Even more interesting were perturbations during the synthesis of the pentafluorophenyl substituted derivative **71**. First of all, Kumada coupling had to be employed as the initially planned Suzuki coupling did not give the expected benzothiadiazole **68**. Next, we decided to directly move to the synthetic strategy employing the arylation with an iodonium salt since it worked so well in the synthesis of **67**. The benzimidazole **74** was obtained in 87 % using standard protocol for the cyclization with triethyl orthoformate, however, the corresponding arylation with diphenyliodonium tetrafluoroborate gave only the neutral *N*-phenylbenzimidazole **75** in 24 % yield (Scheme 54B). Moreover, when the same arylation protocol was employed on the isolated **75** the expected benzimidazolium salt **71** was not observed. Surprisingly, for the pentafluorophenyl functionalized **69** the Buchwald-Hartwig amination worked relatively efficiently (considering the difficulty of this transformation) giving the expected *N,N'*-diphenyl derivative **70** in 21 % isolated yield at relatively low palladium catalyst loading (5 mol%). The last obstacle was encountered during the cyclization with the orthoformate step when standard protocol utilizing HCl_{aq} was employed. Surprisingly, this protocol when attempted with **70** gave *N*-formyl derivative **76** isolated in 32 % yield (Scheme 54B). Fortunately, changing the acid from HCl_{aq} to HBF₄·Et₂O resulted in the formation of the expected benzimidazolium tetrafluoroborinate **71**.



Scheme 54 A) Synthetic obstacles encounter during the synthesis of **67**; reaction conditions: PhBr (excess), 5 mol% Pd₂(dba)₃, 15 mol% P'Bu₃, 2 equiv. of KOBu, 160 °C, 3 days; b) (EtO)₃CH (excess), 6 equiv. of HCl_{aq}, reflux, overnight, 53 %. B) Synthetic obstacles encountered during the synthesis of **71** and XRD crystal structure of compound **76** (ellipsoids are drawn at 50 % probability, hydrogens were omitted for clarity); reaction conditions: c) (EtO)₃CH (excess), 6 equiv. of HCl_{aq}, reflux, overnight; d) 4 equiv. of Ph₂IBF₄, 20 mol% Cu(OAc)₂·H₂O, DMF, 100 °C, 20 h, microwave heating; e) 4 equiv. of Ph₂IBF₄, 20 mol% Cu(OAc)₂·H₂O, DMF, 100 °C, 20 h; f) (EtO)₃CH (excess), 6 equiv. of HCl_{aq}, reflux, 3 days.

Compound **76** was fully characterized using NMR spectroscopy, which through ¹⁹F NMR indicated two inequivalent pentafluorophenyl groups, of which only one was C₂ symmetric. Gratifyingly, it was possible to grow monocrystals of **76** suitable for XRD experiments by vapor-liquid diffusion crystallization of the compound's DCM solution submerged in pentane vapors. Interestingly, the examined monocrystal of **76** exhibited a peculiar packing of molecules with the formyl group residing interchangeably connected to either one or the other nitrogen atom, as simulated in Figure 23A. As a result, the resolved

asymmetric unit contained only half of the molecule, as shown in Figure 23B. Importantly, the crystal structure indicated π - π stacking interactions between phenyl and pentafluorophenyl groups both within the molecule of **76** and of intermolecular character. This was as evidenced by reasonably low angle of 18.74° of the intersection of the aromatic planes. Similarly, a small centroids' distances were observed of 3.593 and 3.985 Å respectively for intra- and intermolecular π - π stacking interactions.

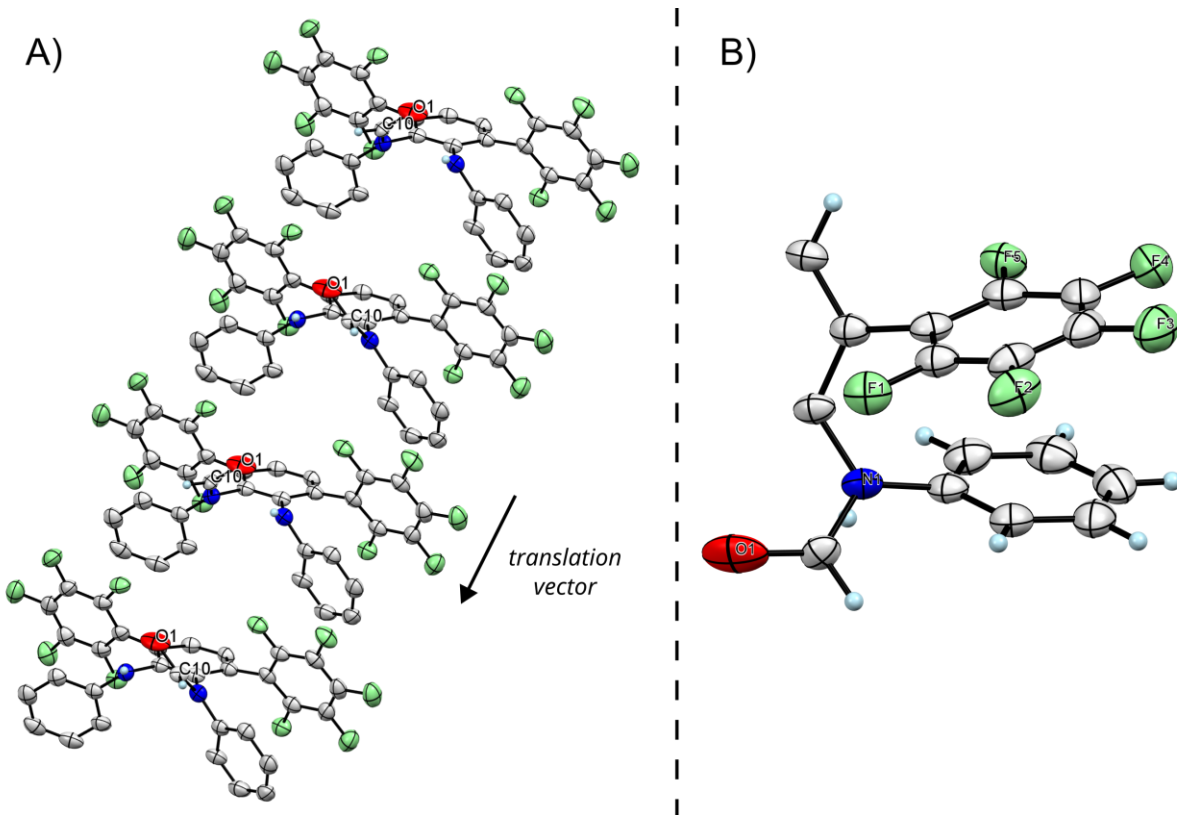
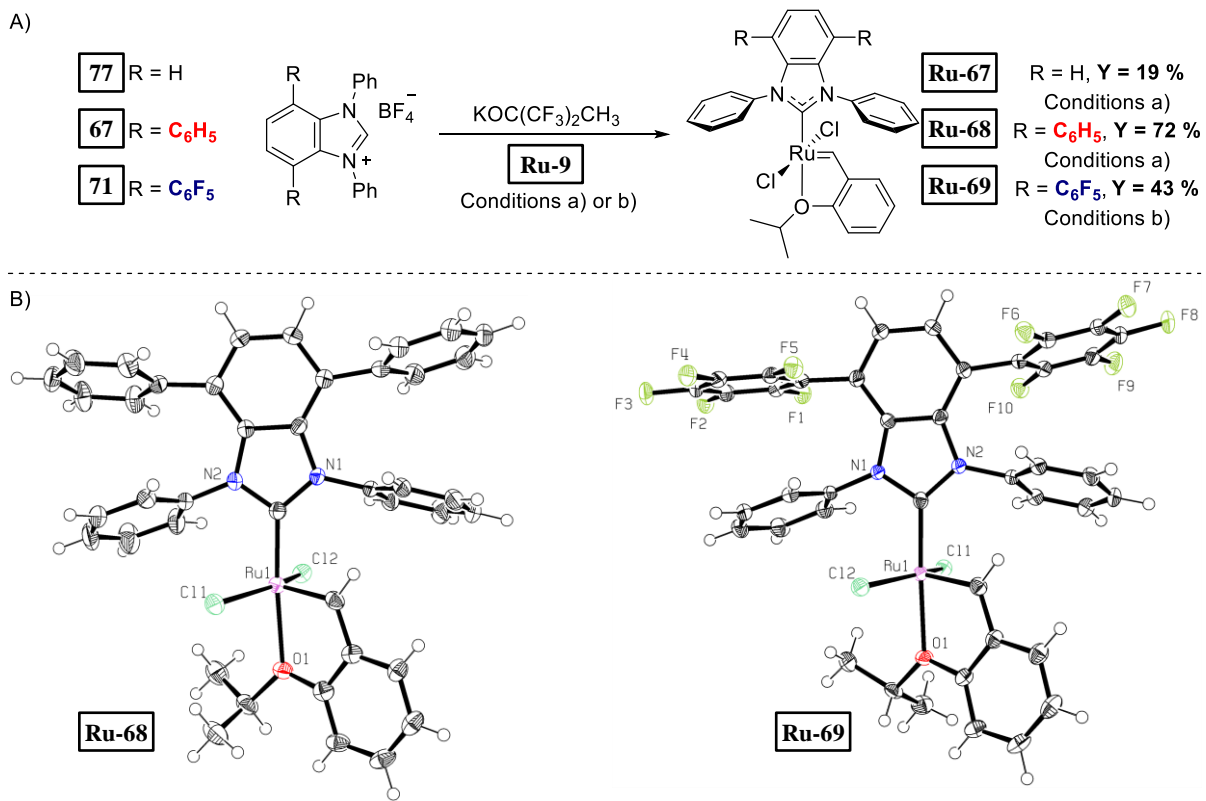


Figure 23 A) Simulation of packing in crystals of **76**, indicating an interchangeable position of the formyl group (translation vector along one axis of the cell, ellipsoids are drawn at 50 % probability, hydrogens were omitted for clarity). B) The asymmetric unit of the compound's **76** crystal structure (ellipsoids are drawn at 50 % probability).

3.3. Synthesis of ruthenium catalysts

The corresponding Hoveyda-Grubbs complexes were obtained by displacement of the PCy_3 ligand in **Ru-9** ruthenium precursor by the free NHCs generated using $\text{KOC}(\text{CF}_3)\text{CH}_3$ as a base (Scheme 55A). Complex **Ru-68** was isolated using column chromatography, whereas complex **Ru-69** was purified by simple crystallization from a tetrahydrofuran-pentane mixture. Both complexes (brown-orange solids) are stable for months when stored in a protective atmosphere. It is noteworthy that upon a synthesis of known **Ru-67**^[130], we noticed its fragility when column chromatography was performed with regular solvents. Even with carefully degassed dry solvents, complex **Ru-67** was obtained in 19% yield only, which is considerably lower than in the case of **Ru-68** and **Ru-69**, 72% and 43% respectively. The molecular structures of complexes **Ru-68** and **Ru-69** were confirmed by XRD experiments on single crystals grown by layering DCM complex solutions of **Ru-68** and **Ru-69** with pentane, respectively (Scheme 55B).

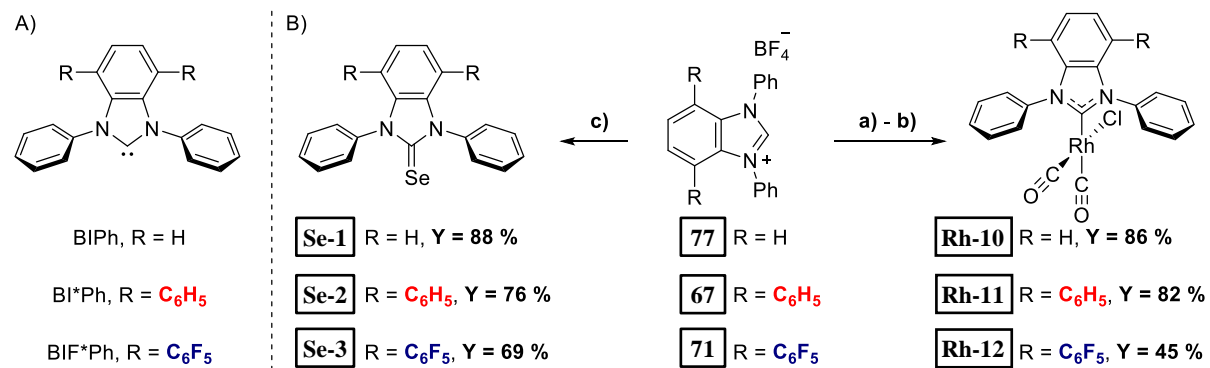


Scheme 55 A) Synthesis of **Ru-67**, **Ru-68** and **Ru-69**; reaction conditions: a) 1.75 equiv. of **77** or **67**, 1.75 equiv. $\text{KOC}(\text{CF}_3)_2\text{CH}_3$, benzene, rt, 30 min. then 1 equiv. **Ru-9**, 60 °C, 1 h; b) 1.75 equiv. of **71**, 2 equiv. of $\text{KOC}(\text{CF}_3)_2\text{CH}_3$, benzene, rt, 15 min. then 1 equiv. of **Ru-9**, 60 °C, 30 min. B) XRD structure of **Ru-68** and **Ru-69**, ellipsoids are drawn at 50% probability.

3.4. Evaluation of electronic and steric properties of new NHC ligands and catalysts.

An in-depth characterization of the electronic properties of the three ligands was then carried out (Scheme 56 and Table 5, see Chapter 1.2.5 and 1.2.6 for reference on this subject). Utilized henceforth are abbreviations of names of new NHCs listed on Scheme 56A. The overall electron-donating ability of the NHC ligands was first quantified by recording the average stretching frequency ($\nu_{\text{CO}}^{\text{av}}$) of the carbonyl ligands in complexes **Rh-10-Rh-12** (Scheme 56B, right), which is correlated to the TEP value of the ligand by a linear correlation (equation 3, Chapter 1.2.5). Furthermore, the σ -donating and the π -accepting abilities of the NHCs were independently assessed by measuring the ${}^1\text{J}(\text{C}-\text{H})$ coupling constant between the carbon and the hydrogen atoms on the pre-carbenic position in azolium precursors (**77**, **67** and **71**) and by recording the chemical shift of ${}^{77}\text{Se}$ nuclei in the seleno adducts **Se-1-Se-3** (Scheme 56B, left), respectively. Additionally, those electronic parameters of the imidazole-based congener IMes were reproduced and compared with the values previously reported in the literature. The experimental data revealed that the three benzimidazole-based NHCs are less donating than IMes and less or similarly donating as SIMes (values of $\nu_{\text{CO}}^{\text{av}}$ for SIMes-derived rhodium carbonyl complex are not consistent in the literature)^[220,221] when overall electronic donation is considered. Within the benzimidazolylidene series, the presence of the two distal phenyl groups in BI*Ph slightly increased its σ -donation but also its π - acidity relative to the unsubstituted BIPh, leading to a slightly stronger overall electronic donation with a TEP value of 2052.2 cm⁻¹. In contrast, perfluorination of the backbone-aryl groups induced a noticeable decrease in electronic donation with a TEP value ranging from 2052.2 cm⁻¹ for BI*Ph to 2056.2 cm⁻¹ for BIF*Ph, as could be anticipated in view of the strong electron-withdrawing

effect of fluorine atoms. Overall, starting from the unsubstituted BIPh, the installation of the second aryl layer at the rear of the benzimidazolyl core generates the more electron-donating BI*Ph ligand and the less electron-donating BIF*Ph ligand.



Scheme 56 A) Structures and abbreviations of NHC ligands studied herewith. B) Synthesis of rhodium carbonyl complexes and selenoureas; reaction conditions: a) 2.2 equiv. of **77** or **67** or **71**, 2.2 equiv. of KOC($\text{CF}_3)_2\text{CH}_3$, THF, rt, 30 min. then 1 equiv. of **Rh-1**, overnight; b) CO (excess), DCM, rt, 30 min.; c) 1 equiv. of **77** or **67** or **71**, 1 equiv. of KOC($\text{CF}_3)_2\text{CH}_3$, THF, rt, 30 min. then 2 equiv. of Se, overnight.

Table 5 Stereoelectronic parameters of SIMes, IMes, BIPh, BI*Ph and BIF*Ph.

Ligand	$\nu_{\text{CO}}^{\text{av}}$ [cm ⁻¹] ^a	TEP [cm ⁻¹] ^b	$^1\text{J}(\text{C}-\text{H})$ ^c	$\delta(^{77}\text{Se})$ [ppm] ^d	%V _{bur} [%] ^e
SIMes	lit. 2040.5 ^[221]	2052.6	lit. 206 ^[27]	lit. 110 ^[222]	33.7 ^f
	lit. 2037.5 ^[220]	2050.2			
IMes	2037.5	2050.2	225	27	n.a. ^g
	(lit. 2037.6) ^[223]	(2050.3)	(lit. 225) ^[27]	(lit. 27) ^[222]	
BIPh	2043.0	2054.6	224	127	32.9 ^h
BI*Ph	2040.0	2052.2	222	160	31.6
BIF*Ph	2045.0	2056.2	226	198	31.6

^a – Recorded IR average CO stretching frequency of corresponding Rh(NHC)(CO)₂Cl complexes measured in DCM. ^b – Calculated using equation 3. ^c – Recorded $^1\text{J}(\text{C}-\text{H})$ coupling constant of corresponding azolium salts procured from ^{13}C satellites of the ^1H NMR spectrum. ^d – ^{77}Se chemical shift of corresponding selenoureas measured in CDCl₃. ^e – Calculated from XRD structures of the corresponding Grubbs-Hoveyda complexes. ^f – Crystal structure obtained from ref. ^[224] (CCDC 1100116). ^g – n.a. = not available, no single crystal XRD structure of IMes-derived Grubbs-Hoveyda complex has been reported. ^h – Crystal structure obtained from ref. ^[130] (CCDC 605939).

Selected bond lengths and angles of complexes **Ru-68** and **Ru-69** are presented in Table 6, along with the corresponding ones for the previously reported complex **Ru-67**, which may serve as the reference compound. The geometrical parameters describing the structures of complexes **Ru-68** and **Ru-69** correlate well with the one of reference **Ru-67**, as illustrated by the superimposed structures (Figure 24B). The lengths of the ruthenium-carbon(NHC) and the ruthenium-carbon(alkylidene) (entries 1 and 2, Table 6) in the three complexes do not differ by more than three estimated standard deviations, as well as the geometry index (τ_5),^[225] which characterizes the distortion of the square-pyramidal geometry [**Ru-67**: 0.35; **Ru-68**: 0.38; **Ru-69**: 0.40]. However, ruthenium-oxygen bond distances (entry 3, Table 6) significantly increase in order **Ru-69**, **Ru-67**, **Ru-68**, respectively, which perfectly correlates with the NHCs electronic donation abilities (overall and σ -donation) rising in this order BI*FPh < BIPh <

BI^*Ph , reflecting an increasing structural *trans* effect from BI^*FPh to BIPh and to BI^*Ph .^[226] Interestingly, such observation differs from phosphine derived second generation OM catalysts where the increased π - acidity of NHC ligand accounts for a stronger *trans* effect as the resulting metal-phosphine π -backdonation weakens (see Chapter 1.3.8). This supports the previous supposition that since the isopropoxy ligand is a pure σ -donor, the stronger σ -donating NHC will have a stronger *trans* effect. To the best of our knowledge, no such assumption has been made so far.

The relative steric constraints of the parent unsubstituted BIPh and of the two new double-decker BI^*Ph and BIF^*Ph ligands were quantified by establishing their topographical steric maps in complexes **Ru-67**, **Ru-68**, and **Ru-69** respectively (Figure 24A and Table 5), using the SambVca 2 web application (see Chapter 1.2.6 for reference), and were compared to the steric hindrance brought by the SIMes ligand in the general-purpose catalyst **Ru-10** (Table 5). As expected, all three benzimidazolylidene ligands provide a lower steric pressure than the standard SIMes ligand [$\% V_{\text{bur}}(\text{SIMes}) = 33.7\%$], due to the presence of less bulky *N*-phenyl groups. Interestingly, it appeared that the substitution of the benzimidazolyl backbone led to a slight decrease of the $\% V_{\text{bur}}$ from 32.9% for BIPh in **Ru-67** to 31.6% for BI^*Ph and BIF^*Ph in **Ru-68** and **Ru-69**, which arises from higher orthogonality of the *N*-phenyl groups relative to the benzimidazolyl heterocycle, characterized by the increase of the dihedral angles C7-N2-C8-C9 and C2-N1-C10-C11 (entries 6 and 7, Table 6) from 48.21° and 62.91° in **Ru-67** to 69.23° and 77.17° in **Ru-68** and 77.30° and 66.24° in **Ru-69**. This may be ascribed to the substitution of the backbone of the benzimidazolyl ring by phenyl and pentafluorophenyl rings in **Ru-68** and **Ru-69** respectively, which hinders the *N*-phenyl rotation as hypothesized. This through-space effect of the backbone substitution is the opposite of the buttressing effect observed in amino-decorated NHC catalysts, in which the bulky amino substituents on the backbone forced the *N*-aryl groups to be twisted.^[223,227]

Furthermore, when **Ru-68** and **Ru-69** are compared, although dihedral angles between the *N*-phenyl groups and the benzimidazolyl ring do not clearly stand out one from another, dihedral angles between NHC core and phenyl or pentafluorophenyl upper deck substituents (C5-C6-C14-C15 and C4-C3-C12-C13, entries 8 and 9, Table 6) explicitly increase from 62.50°, 63.79° to 70.32°, 79.38°, respectively. This observation could be explained by stronger π - π interactions between the two aromatic planes in the structure of **Ru-69**. Moreover, in the structure of **Ru-68** the upper and bottom aromatic planes intersect at slightly higher angles of 27.62 and 18.75° when compared with those of **Ru-69** crossing at 27.34 and 16.03°. Similarly, the centroids' distances were slightly higher in **Ru-68** at 3.901 and 3.734 Å whereas in **Ru-69** they measured at 3.704 and 3.597 Å. In conclusion, there is evidence of stronger π - π stacking interactions in the structure of **Ru-69** when compared with **Ru-68**, which we next tried to validate with DFT calculations.

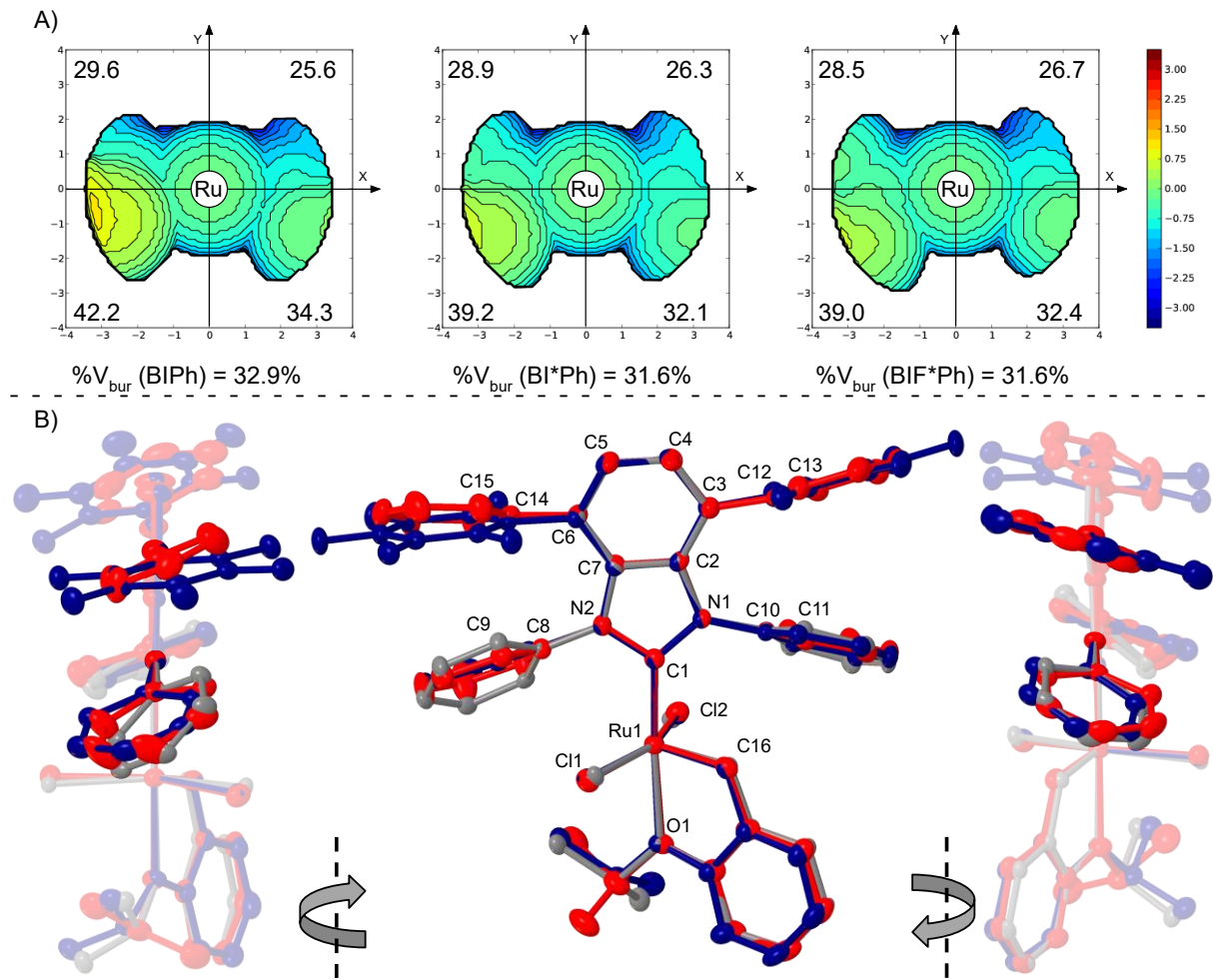


Figure 24 A) Steric maps of NHC ligands in complexes: left—**Ru-67**, center—**Ru-68**, right—**Ru-69**. Values in the four corners of the maps are the $\%V_{bur}$ of the NHC ligand in the corresponding quadrant. B) Superimposed structures of **Ru-67** (gray), **Ru-68** (red) and **Ru-69** (blue).

Table 6 Selected, corresponding bond lengths (\AA) and angles (deg) in X-ray crystal structures of complexes **Ru-67**, **Ru-68**, and **Ru-69**. Atom labeling corresponds to Figure 24B and not to cif files.

Entry	Atoms	Ru-67	Ru-68	Ru-69
1	Ru1-C1	1.9618(10)	1.968(3)	1.9585(17)
2	Ru1-C16	1.8365(11)	1.830(3)	1.8326(17)
3	Ru1-O1	2.2692(7)	2.2807(19)	2.2539(12)
4	C1-Ru1-O1	176.19(4)	175.61(9)	177.09(5)
5	Cl1-Ru1-Cl2	155.303(10)	153.04(3)	153.163(14)
6	C7-N2-C8-C9	48.21	69.23	77.30
7	C2-N1-C10-C11	62.91	77.17	66.24
8	C5-C6-C14-C15	-	62.50	79.38
9	C4-C3-C12-C13	-	63.79	70.32

The DFT computations reported here were carried out by Chiara Dinoi and Iker del Rosal.

In order to rationalize the effect of the insertion of a phenyl or pentafluorophenyl ring in the backbone of the benzimidazolyl group of **Ru-68** and **Ru-69** respectively, a DFT study was carried out at the B3PW91-D3 level of theory. The calculated bond distances and angles for optimized structures of **Ru-68** and **Ru-69** (**optRu-68** and **optRu-69**, Figure 25) were compared with those observed experimentally. The computed bond distances and angles accurately reproduce the experimental values with variations of less than 0.04 Å between the computed and the experimental bond lengths. Taking into account the free rotation of both the *N*-phenyl and the benzimidazolyl-phenyl or pentafluorophenyl rings, the disparities observed in the torsion angles between the experimental and computed structures are likely to be attributed to packing interactions within the crystal lattices.

To better characterize the interactions between the *N*-phenyl and the benzimidazolyl-phenyl or pentafluorophenyl rings, the natural charges of **optRu-68** and **optRu-69** have been computed by natural bond orbital (NBO) analysis. In **optRu-68** (Figure 25A), the carbon atoms of both the *N*-phenyl and benzimidazolyl-phenyl rings display negative charges (in the range -0.235 to -0.249 and -0.227 to -0.250 for the *N*-phenyl and benzimidazolyl-phenyl groups respectively). Conversely, in **optRu-69** (Figure 25B), while the carbon atoms of the *N*-phenyl display negative charges (in the range -0.230 to -0.254), those of the pentafluorophenyl rings display positive charges (in the range 0.300 to 0.393). According to the model proposed by Hunter and Sanders,^[228] the electron-withdrawing F substituents would reduce the negative quadrupole moment of the second-decker aromatic rings, thereby favoring parallel displaced sandwich conformations in **optRu-69**.

In order to check for the possible presence of π - π orbital interactions between the *N*-phenyl and the backbone-phenyl or -pentafluorophenyl rings, molecular orbital analysis of compounds **optRu-68** and **optRu-69** was also carried out. As previously suggested,^[229] when two aromatic rings are near enough to each other, their π orbital overlapping may provide an additional binding force to their stacking interaction. While for **optRu-68**, no π orbital overlapping between the *N*-phenyl and the backbone-phenyl rings is observed, on the other hand, in **optRu-69** the HOMO-15 orbital (Figure 25C) displays a small π orbital overlapping between the *N*-phenyl and the backbone-pentafluorophenyl rings.

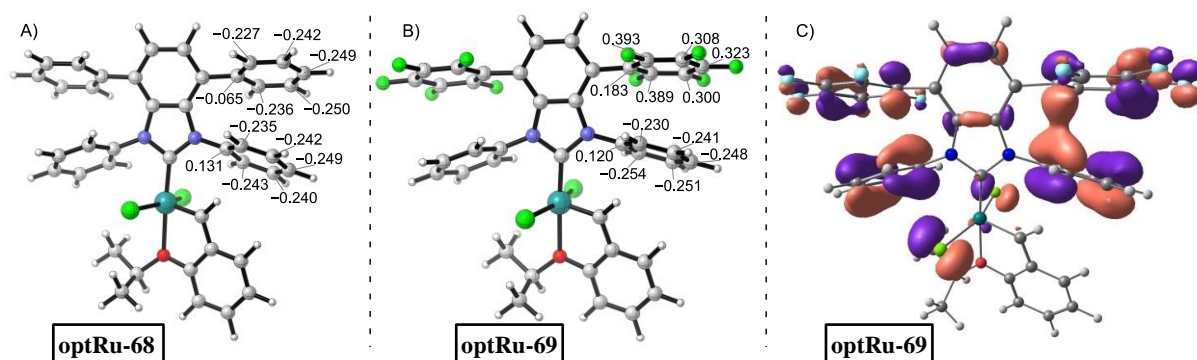


Figure 25 A) DFT optimized structure of **Ru-68** with marked natural charges for selected carbon atoms. B) DFT optimized structure of **Ru-69** with marked natural charges for selected carbon atoms. C) HOMO-15 of **optRu-69** indicating a small π orbital overlapping between the *N*-phenyl and the backbone-pentafluorophenyl rings.

In summary, the interaction between the *N*-phenyl and the second decker-phenyl or pentafluorophenyl rings was investigated. Therefore, by comparing their different *i*) centroid's distances (3.607 and 3.427 Å for **optRu-68** and **optRu-69** respectively), *ii*) quadrupole moments and *iii*) π orbital

overlapping suggests that the *N*-phenyl ring interacts more strongly with the backbone-pentafluorophenyl ring in **optRu-69** than with the backbone-phenyl ring in **optRu-68**.

3.5. Precatalysts' stability

The stability of the two newly obtained biplane-type NHC ruthenium complexes **Ru-68** and **Ru-69** was then quantitatively monitored and compared with the benchmark **Ru-67**. Since NHC ligand remains coordinated to the metal center throughout the entire catalytic cycle, the differences in complexes' stability should directly translate to the stability of actual propagating species, thus conveying their effectiveness in catalysis. Gratifyingly, **Ru-68** and **Ru-69** remained perfectly unchanged for approximately three weeks in solution at ambient temperature, while **Ru-67** slowly degraded to around 50% of the initial amount (Figure 26A). This fact confirmed our previous observation that upon isolation the top-covered complexes **Ru-68** and **Ru-69** are considerably more stable than **Ru-67**. Furthermore, the differences in stability were even more pronounced at a higher temperature (Figure 26B), where **Ru-67** disappeared completely after about 27 hours while **Ru-68** and **Ru-69** were still detectable even after more than 100 hours in solution at 80 °C. Furthermore, the elevated temperature allowed to distinguish **Ru-68** from **Ru-69** in terms of stability and **Ru-69** proved to be the more stable precatalyst, which we assign to the beneficial impact of the π-π interactions between *N*-phenyl groups and pentafluorophenyl backbone motifs.

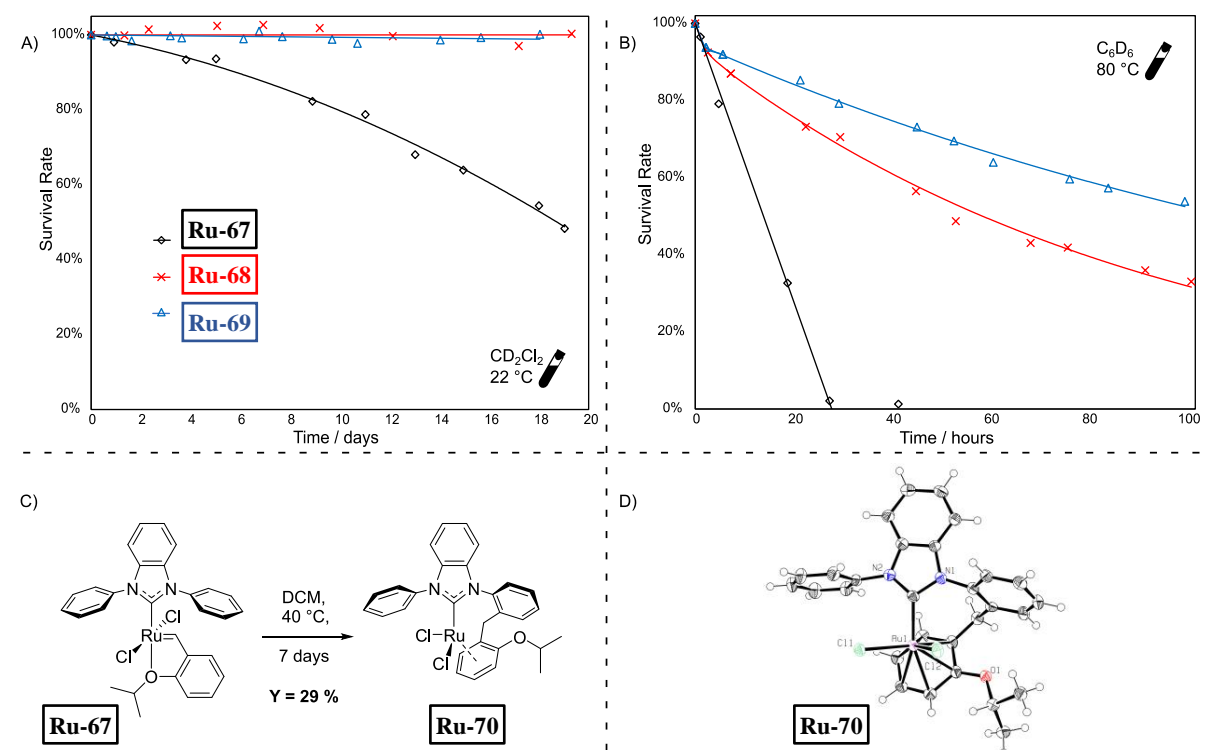


Figure 26 A) Stability tests in CD₂Cl₂ at 22 °C, measured by NMR (1,3,5-trimethoxybenzene added as reference), lines are visual aid only. B) Stability tests in C₆D₆ at 80 °C, measured by NMR. C) study of the decomposition of the complex **Ru-67** into the complex **Ru-70**. D) XRD structure of complex **Ru-70** (ellipsoids are drawn at 50% probability).

To unambiguously confirm the nature of the catalyst deactivation pathway, we attempted to isolate the degradation product of **Ru-67**. The previous report featuring isolation and characterization of the decomposition product from BiPh ruthenium OM catalyst described only its PCy₃ derivative **Ru-37** (see Chapter 1.5.2).^[138] After stirring **Ru-67** in dichloromethane at 40 °C for one week, the expected, tethered

η^6 -arene-NHC ruthenium complex **Ru-70** was isolated (Figure 26C), whose formation should proceed through the activation of an *ortho* C-H bond of one *N*-phenyl group followed by insertion into the alkylidene. The molecular structure of complex **Ru-70** was confirmed by XRD experiments on single crystals grown by layering dichloromethane complex solution with pentane (Figure 26D).

3.6. Computational study

The DFT computations reported here were carried out by Chiara Dinoi and Iker del Rosal.

In order to explain the slower decomposition kinetics of complexes **Ru-68** and **Ru-69** compared to that of **Ru-67**, we hypothesized that the insertion of an aromatic plane parallel to the *N*-aryl rings could prevent the rotation of the *N*-phenyl group, thus hampering or at least restraining the aromatic CH activation process leading to decomposition. Therefore, starting from optimized structures **optRu-67**, **optRu-68** and **optRu-69** the transition state Gibbs free energy barriers associated with the *N*-phenyl rotation (Figure 27) were computed by DFT calculations at the B3PW91-D3 level of theory. **TS_{rot}Ru-68** and **TS_{rot}Ru-69** display higher energies (19.3 and 22.7 kcal·mol⁻¹) than **TS_{rot}Ru-67** (17.4 kcal·mol⁻¹), which may be ascribed to the increased steric hindrance imposed on *N*-phenyl groups in structures **optRu-68** and **optRu-69** when compared to that of their simpler analog **optRu-67**. Moreover, in agreement with the higher π - π stacking interaction expected between the *N*-phenyl and the second decker-pentafluorophenyl rings, the energy of the rotation of the *N*-phenyl group is 3.4 kcal·mol⁻¹ higher for **optRu-69** than for **optRu-68**.

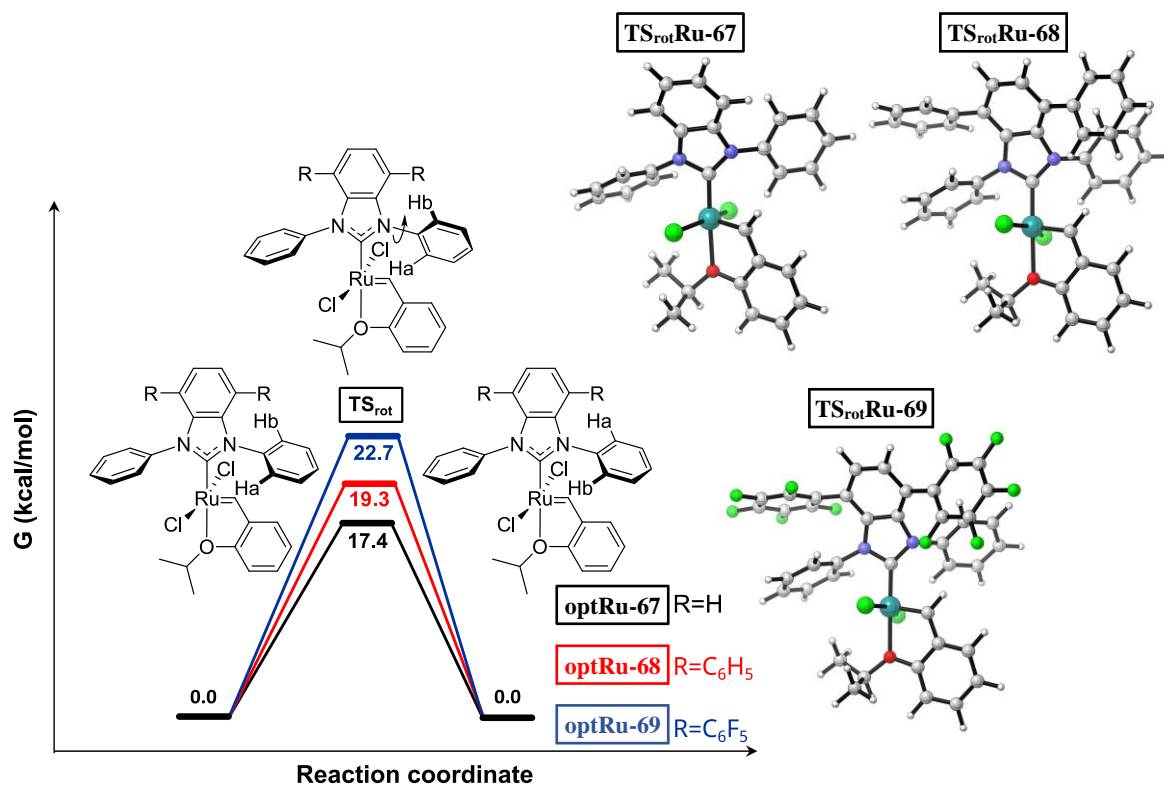


Figure 27 Gibbs free energy barriers associated with the rotation of the *N*-phenyl substituent in complexes **optRu-67**, **optRu-68** and **optRu-69**, computed at the B3PW91-D3 level of theory.

However, the complexes' deactivation cannot be ascribed to this straightforward *N*-phenyl rotation process as the corresponding transition state Gibbs free energy barriers can be easily overcome at room temperature, unlike what was observed experimentally. Therefore, we wondered whether the

experimentally observed decomposition kinetics could be instead explained by a particular step in the deactivation mechanism.

Inspired by the reports of Cavallo and coworkers explaining the decomposition of PCy₃ derivative **Ru-37**,^[131,140] the calculation of the whole decomposition pathway for complexes **Ru-67**, **Ru-68** and **Ru-69** was performed. For the sake of clarity in the comparison, their corresponding Gibbs free energy profiles are overlapped in Figure 28 and Figure 29.

Starting from compounds **optRu-67**, **optRu-68** and **optRu-69**, the first step involves a Berry pseudo rotation of the alkylidene O*i*Pr arm bringing the O*i*Pr group in *trans* position to one of the chloride ligands (intermediates **I**₁). The reaction is endergonic by 6.1, 10.1 and 8.8 kcal·mol⁻¹, with an associated barrier of 28.8, 33.8 and 33.4 kcal·mol⁻¹, for **TS**₁**Ru-67**, **TS**₁**Ru-68** and **TS**₁**Ru-69** respectively. Through a second Berry pseudo rotation process, one of the *N*-phenyl rings may then move in *trans* position to the alkylidene O*i*Pr arm, engaging one of its *ortho*-C–H bonds into an agostic interaction with the ruthenium metal center. The reaction is endergonic by 24.2 and 28.1 kcal·mol⁻¹ for **I**₂**Ru-67** and both **I**₂**Ru-68** and **I**₂**Ru-69**, respectively, and the corresponding barriers were calculated at 27.6, 29.3 and 30.3 kcal·mol⁻¹ for **TS**₂**Ru-67**, **TS**₂**Ru-68** and **TS**₂**Ru-69**, respectively.

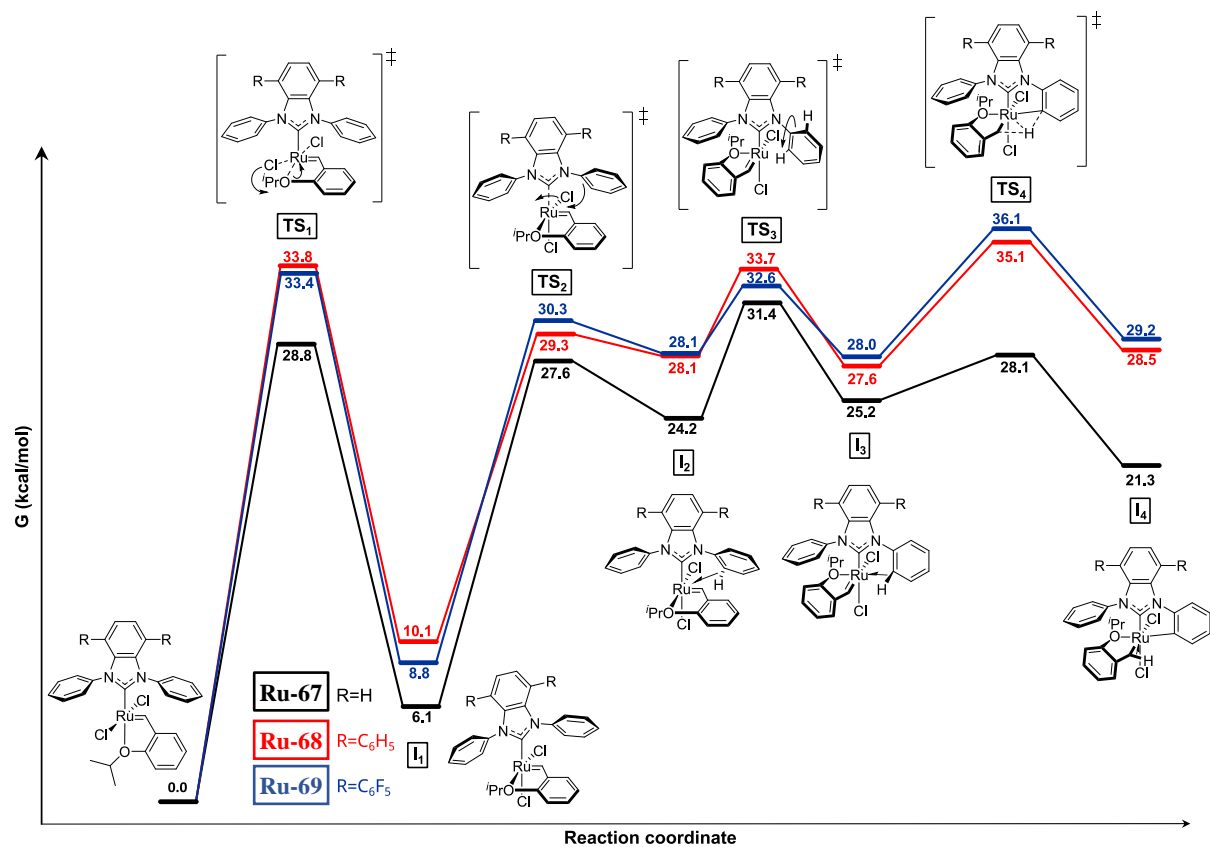


Figure 28 First part of the Gibbs Free energy profile for the deactivation reaction of catalysts **Ru-67** (black), **Ru-68** (red) and **Ru-69** (blue), computed at the B3PW91-D3 level of theory.

To prepare the H transfer from the *N*-phenyl cycle to the benzylidene group, the *N*-phenyl ring must undergo a rotation, allowing the reformation of an *ortho* C–H agostic interaction with the metal on the same side as the Ru-alkylidene bond. This rotation process is an equilibrium reaction, with the **I**₃ intermediates lying at +1.0, -0.5 and -0.1 kcal·mol⁻¹ relative to the **I**₂ intermediates, for complexes **Ru-67**, **Ru-68** and **Ru-69** respectively. In the next step, the transfer of the agostic activated proton to the nearby

α -carbon atom of the benzylidene group may then occur, affording a ruthenium-benzyl complex containing a new σ -bond between the ruthenium center and the *ortho*-carbon atom of the NHC *N*-phenyl ring. Interestingly, while the barrier for the formation of the Ru \cdots C–H agostic interaction through **TS**₃ is almost identical between compound **Ru-67** and compounds **Ru-68** and **Ru-69** (31.4, 33.7 and 32.6 kcal \cdot mol $^{-1}$, respectively), the barrier for the transfer of the agostic activated proton to the benzylidene group through **TS**₄ is considerably higher for complexes **Ru-68** and **Ru-69** (35.1 and 36.1 kcal \cdot mol $^{-1}$) than for **Ru-67** (28.1 kcal \cdot mol $^{-1}$). This difference of 7.0 and 8.0 kcal \cdot mol $^{-1}$ between the **TS**₄ energy of **Ru-68** and **Ru-69** with that of **Ru-67** is probably due to the presence of the two parallelly stacked aryl rings on the benzimidazolylidene backbone which rigidify the NHC skeleton, thus reducing the flexibility of the *N*-phenyl group during the proton transfer process through **TS**₄. In the corresponding products **I**₄, lying at 21.3, 28.5 and 29.2 kcal \cdot mol $^{-1}$ for complexes **Ru-67**, **Ru-68** and **Ru-69** respectively, the benzylidene group is transformed into a benzyl group and a new ruthenium-carbon bond with an *ortho* position of the *N*-phenyl group is created.

From intermediates **I**₄, a Berry pseudo rotation brings the benzyl OⁱPr arm in *trans* position to the NHC ring, affording intermediates **I**_{4'} by an equilibrium process (Figure 29). The following step involves simultaneously *i*) the transfer of an α hydrogen from the benzyl group to the ruthenium atom and *ii*) the insertion of the formerly benzyl group into the σ -bond between ruthenium and carbon of the *N*-phenyl ring. For complexes **Ru-67**, **Ru-68** and **Ru-69** respectively, this elementary step is exergonic by 6.9, 10.4 and 13.8 kcal \cdot mol $^{-1}$, with the corresponding transition state measuring 29.7, 34.7 and 33.7 kcal \cdot mol $^{-1}$.

The resulting intermediates **I**₅ may then undergo a reductive elimination step which breaks the ruthenium–hydride bond, by transferring the hydrogen to the formerly benzylic carbon center. This leads to intermediates **I**₆ with associated barriers of 20.2, 22.4 and 24.4 kcal \cdot mol $^{-1}$ for complexes **Ru-67**, **Ru-68** and **Ru-69** respectively. **I**₆ are only kinetic intermediates to the decomposition products **I**₈, which can be reached through a series of haptotropic shifts involving the ruthenium atom and the Ph group of the formerly benzylidene moiety, as confirmed by the XRD structure of complex **Ru-70** (Figure 26D). The formation of **I**₈ is slightly exergonic by only –3.2, –0.2 and –2.3 kcal \cdot mol $^{-1}$ for compounds **Ru-67**, **Ru-68** and **Ru-69** respectively, in contrast to the stability of about 20 kcal \cdot mol $^{-1}$ obtained for the analog of complex **Ru-67**, which contains the same benzylidene ligand without the OⁱPr substituent (**Ru-37**).^[140] This difference is likely to be ascribed to the decoordination of the OⁱPr ligand during the formation of the final η^6 product **I-8**, which destabilizes the system with respect to the starting compound.

Considering the full mechanistic profile, the path between intermediates **I**₃ and **I**₅ involves transition states with the Gibbs free energy values for **Ru-68** and **Ru-69** considerably higher than those for **Ru-67**. This indicates that the influence of the insertion of an aromatic plane parallel to the *N*-phenyl rings seems to have a particularly significant impact on the **TS**₄ and **TS**₅ transition states. Therefore, we carried out a geometrical analysis of structures of those key transition states for compounds **Ru-67**, **Ru-68** and **Ru-69** displaying in Figure 30 the most significant geometrical parameters.

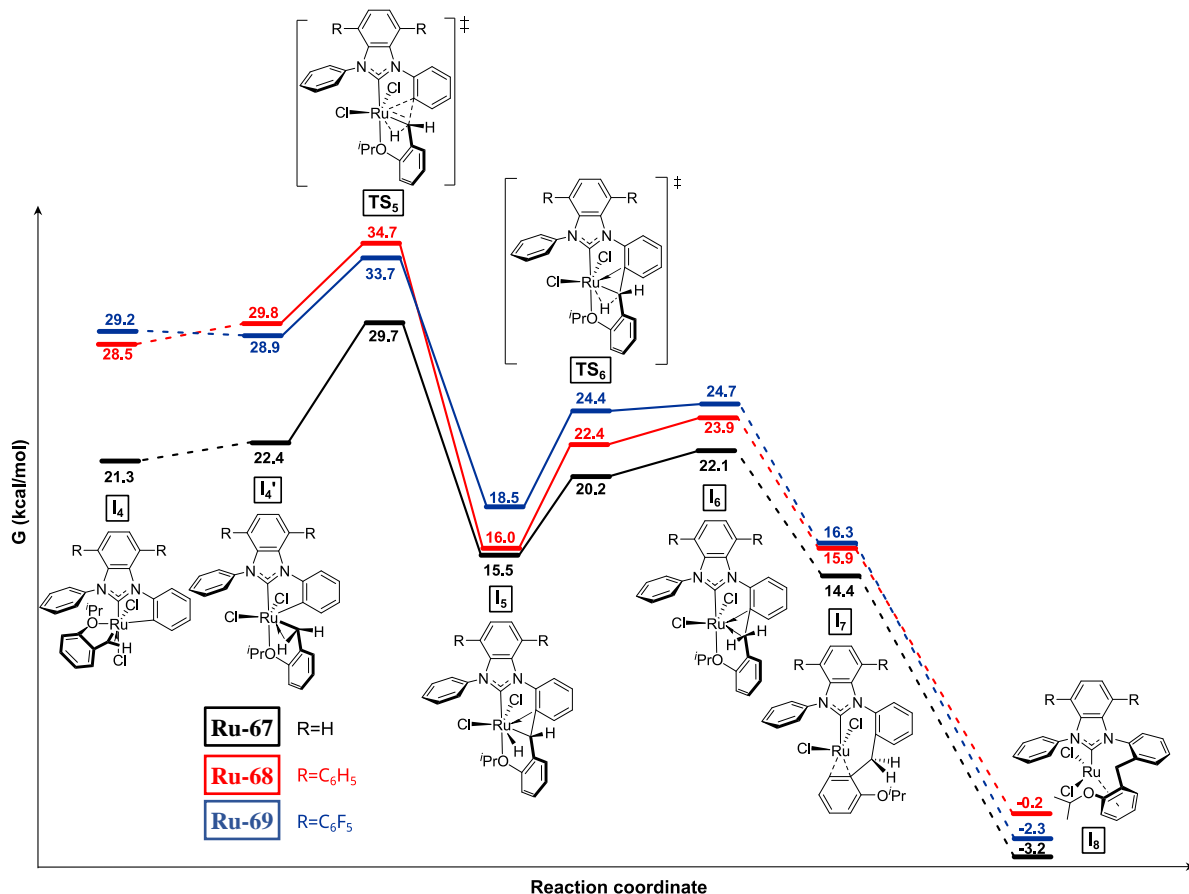


Figure 29 Second part of the Gibbs Free energy profile for the deactivation reaction of precatalysts **Ru-67** (black), **Ru-68** (red) and **Ru-69** (blue), computed at the B3PW91-D3 level of theory.

In all the three **TS₄** transition states (Figure 30A), the aromatic N-phenyl ring is heavily rotated, so that the activated C–H bond can properly interact with the ruthenium center and thus be transferred to the alkylidene moiety, the C9–H and C49–H bond distances measuring 2.023, 2.092, 2.056 Å and 1.645, 1.599, 1.616 Å for complexes **Ru-67**, **Ru-68** and **Ru-69** respectively. As a consequence, the N-phenyl ring arranges in a quasi-coplanar fashion with respect to the benzimidazolylidene heterocycle and any substitution on the benzimidazolylidene moiety results in a steric clash that increases the **TS₄** energy. This increased steric repulsion is geometrically traduced by an out-of-plane distortion of the two rings of the benzimidazolylidene core. Indeed, while in **TS_{4Ru-67}** the two rings of the bicyclic benzimidazolylidene are almost perfectly planar (dihedral angles N2-C7-C2-N1 = 0.5°, C6-C7-C2-C3 = 0.9°), they clearly deviate from planarity in **TS_{4Ru-68}** and **TS_{4Ru-69}** (N2-C7-C2-N1 = 5.7° and 5.5°, C6-C7-C2-C3 = 9.5° and 10.3° respectively). Therefore, the crossing of this transition state requires more energy for complexes **Ru-68** and **Ru-69** than for **Ru-67**, reflecting their slower experimental decomposition shown in Figure 26.

Figure 30B shows the geometry of the transition states **TS₅** of compounds **Ru-67**, **Ru-68** and **Ru-69**. While for **TS_{5Ru-67}** the carbon–carbon bond formation occurs once the benzylic proton has been already transferred to the ruthenium center, in the case of **Ru-68** and **Ru-69** these two processes occur simultaneously. As previously seen for **TS₄**, the kinetic barrier associated with **TS₅** is considerably higher for complexes **Ru-68** and **Ru-69** (34.7 and 33.7 kcal·mol⁻¹) than for **Ru-67** (29.7 kcal·mol⁻¹), and arises

from the same distortion of the benzimidazolylidene core due to steric clash between the stacked exocyclic aryl groups.

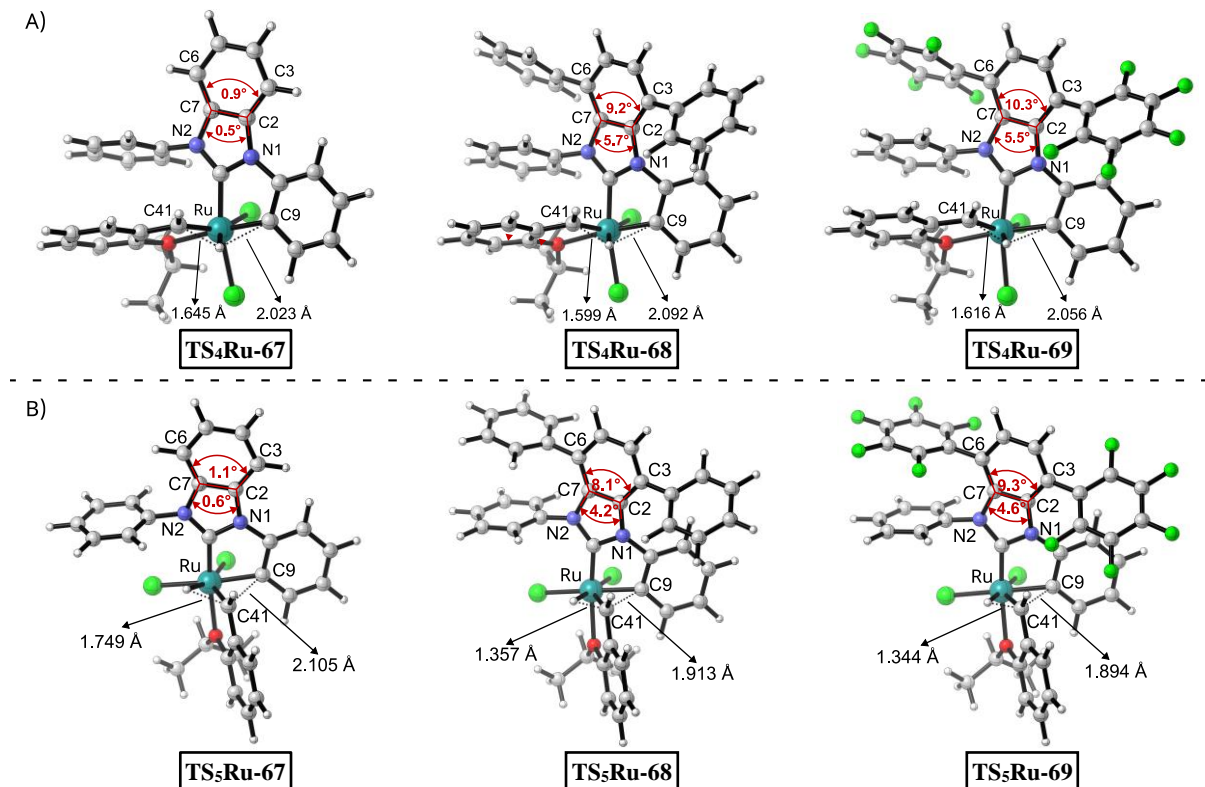


Figure 30 A) Significant geometrical parameters of the TS_4 structure of precatalysts **Ru-67**, **Ru-68** and **Ru-69**. A) Significant geometrical parameters of the TS_5 structure of precatalysts **Ru-67**, **Ru-68** and **Ru-69**.

In conclusion, the computed decomposition profile indicates that the steric repulsion between the *N*-phenyl and the second decker phenyl- and pentafluorophenyl groups strongly affects the rate-determining step of the reaction which involves *i*) the transfer of the *N*-phenyl agostic proton to the nearby α -carbon atom of the benzylidene group (through TS_4) and *ii*) the transfer of the benzylic proton to ruthenium coupled with the carbon-carbon bond formation (through TS_5). The corresponding kinetic barrier is thus considerably higher for compounds **Ru-68** and **Ru-69** than for **Ru-67**, in accordance with the decomposition kinetics reported in Figure 26.

3.7. Catalytic activity studies

The catalytic performance of the new, biplane-type complexes was compared with the known benchmark **Ru-67** using a set of model reactions. Firstly, we checked their activity in RCM with tetrasubstituted carbon-carbon double bond formation. For that purpose diethyl 2,2-di(2-methylallyl)malonate (**78a**) was chosen as the model substrate and the time-conversion plots of its RCM reaction were constructed with 0.2 mol% of each catalyst, in toluene, at 80 °C (Figure 31). All complexes exhibited high activity, affording considerable conversions within the first 30 minutes, however, the reaction catalyzed by **Ru-67** reached its limits at a significantly lower conversion than the one recorded with **Ru-68** and **Ru-69**. This can be attributed to a more stable 14 e⁻ catalytic species formed from the latter precatalysts versus those generated from **Ru-67**. Interestingly, although **Ru-68** gave higher conversions than **Ru-69** within the first hour of the reaction, after this point the trend reversed leading to 96 % conversion with **Ru-69** versus 91 % with **Ru-68** after 5 hours (and 72 % for the benchmark **Ru-67**).

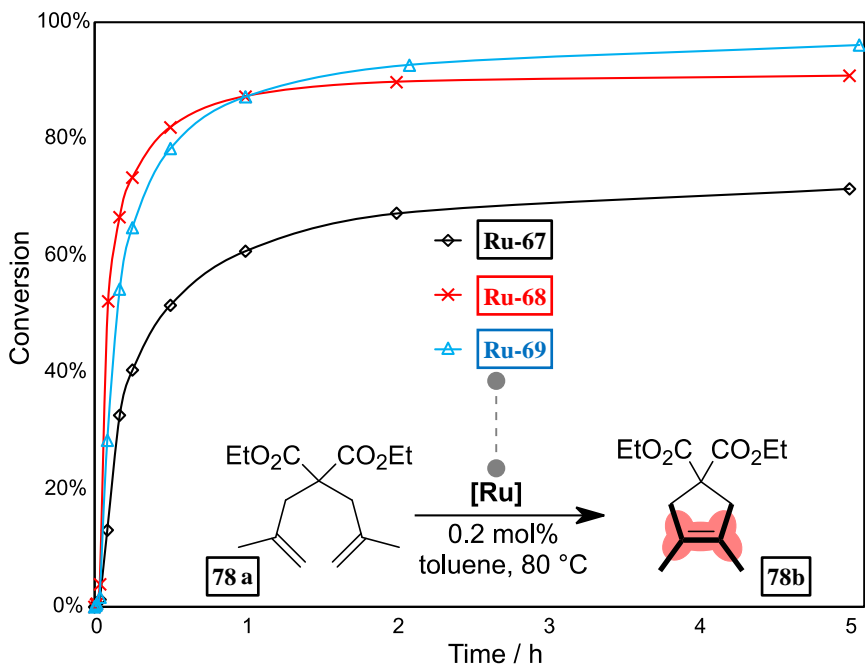
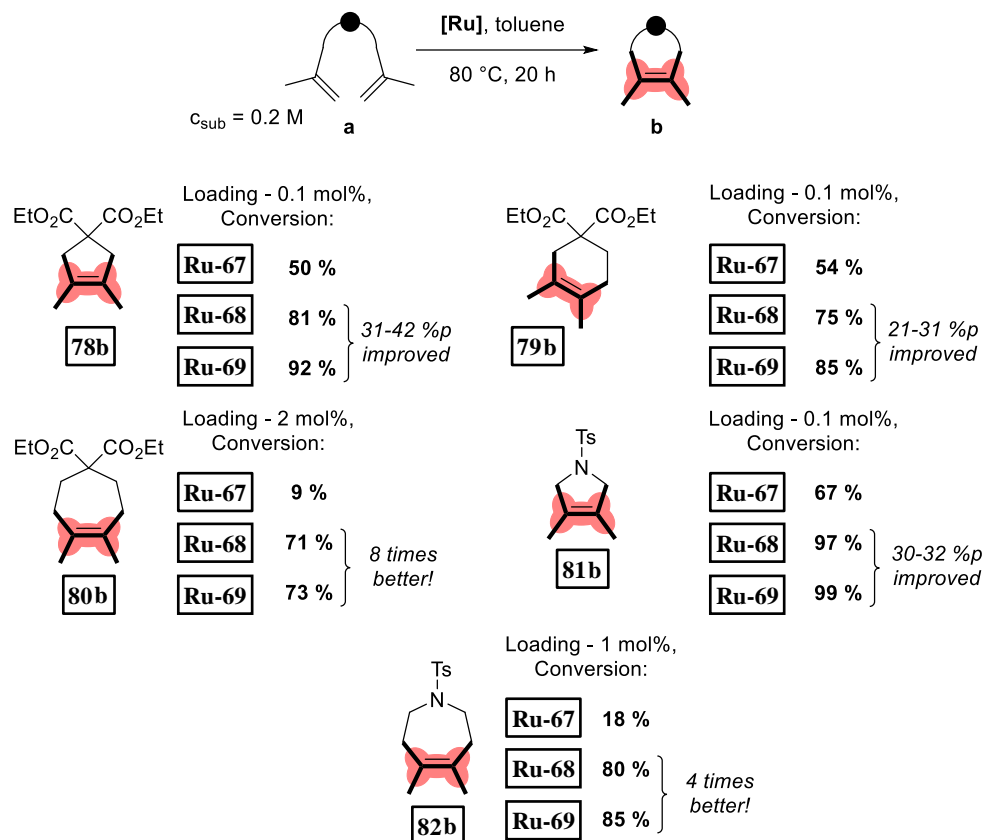


Figure 31 Time-conversion curves in RCM of diene **78a**. Conditions: Catalyst 0.2 mol%, toluene, 80 °C under argon. Measured by GC with 1,3,5-trimethoxybenzene added as internal standard. Lines are visual aid only.

To further examine the differences in catalyst productivity, the previously described reaction of **78a** was reattempted at two times lower catalyst loading of 0.1 mol% (Scheme 57). The trend observed earlier was maintained and **Ru-67** gave a rather poor conversion for such a reaction (50 %), whereas **Ru-68** and **Ru-69** gave much higher conversions of 81 % and 92 % respectively. The three BIPh-type catalysts were further tested in five more challenging RCM reactions featuring tetrasubstituted double carbon–carbon bond formation. Similar was the case of the formation of the six-membered ring (malonate **79b**) and five-membered tosylamide **81b**, where **Ru-68** and **Ru-69** gave up to 32 percentage points (%p) higher substrate conversions compared to **Ru-67**. The fluorinated complex **Ru-69** slightly but noticeably outperformed **Ru-68** in those two latter reactions. The superiority of the new catalysts **Ru-68** and **Ru-69** was even more pronounced in the more challenging formation of a less thermodynamically favored seven-membered ring (compounds **80b** and **82b**). In these latter cases, a higher catalyst loading of 2 mol% with malonate **80b** and 1 mol% with tosylamide **82b** was required to reach suitable conversions, however, such loading is still considered low in the context of the challenging formation of carbon–carbon tetrasubstituted bonds.^[230,231] Noteworthy, **Ru-68** and **Ru-69** gave conversions 4 to 8 times higher than **Ru-67** and again **Ru-69** was slightly better than **Ru-68** which overall correlates with the observed trend in stability tests.

For all substrates discussed so far, the desired RCM products were obtained as a sole product. However, the RCM reaction of ether **84a** led to the formation of a rearranged byproduct **84a'** resulting from a double bond migration along the alkyl chain (Figure 32A). This can be caused by catalyst decomposition products (probably ruthenium hydride species).^[232–234] The observed formation of **84a'** stands in agreement with the previous report of Grubbs and coworkers, although this isomerization product was not characterized there.^[130] Catalyst **Ru-67** offered a very poor conversion of **84a**, forming **84b** and **84a'** in comparable amounts (**84a**: **84b** : **84a'** ratio of 96:1.4:2.7). Remarkably, when compared with **Ru-67** the new catalysts **Ru-68** and **Ru-69** allowed for 30 to 50 times improved formation of the desired product **84b**. Interestingly, in this example **Ru-68** outperformed **Ru-69**, both in terms of conversion and

selectivity toward **84b** (**84a** : **84b** : **84a'** ratio for **Ru-68** reached 24:75:0.9 *versus* 51:44:5.4 for **Ru-69** after 8 hours at 80 °C). This observation could be explained by the subtle difference in activity between **Ru-68** and **Ru-69** that was observed in RCM of **78a** (Figure 31).



Scheme 57 Scope and limitations of catalysts **Ru-67**, **Ru-68** and **Ru-69** in RCM of challenging substrates.

To verify the latter hypothesis, the reaction profile for **84a** RCM was established, comparing **Ru-68** performance with **Ru-69** (Figure 32B). The difference in catalyst activity is more pronounced in this challenging RCM example, and complex **Ru-68** is considerably more active than **Ru-69** (**84a** : **84b** : **84a'** ratio after 1 h reached 28:71:0.3 with **Ru-68** *versus* 63:36:0.8 with **Ru-69**). After the first hour of the reaction, the formation of **84b** slows down significantly, indicating that most of the catalytically active species have been spent. After that point, the compounds resulting from the decomposition of the catalyst start to isomerize **84a**, which is available in a higher quantity in the case of the reaction with **Ru-69**. Those factors account for a higher amount of **84a'** observed with **Ru-69** after 8 h.

To further probe the origin of the higher activity of **Ru-68**, the release of *ortho*-isopropoxystyrene (**83**) (relative to the last point measured at 8 h) *versus* time was plotted (Figure 32C). The formation of **83** can serve as an indirect measure of how catalyst initiation progresses throughout the reaction. For both complexes, **83** release finishes within the first 4 h, although for **Ru-68** the slope is considerably steeper than for **Ru-69**. This is in line with the hypothesis that **Ru-68** is a more active catalyst than **Ru-69** probably due to a faster initiation rate resulting from a higher *trans* effect of more electron donating BI*Ph NHC ligand.

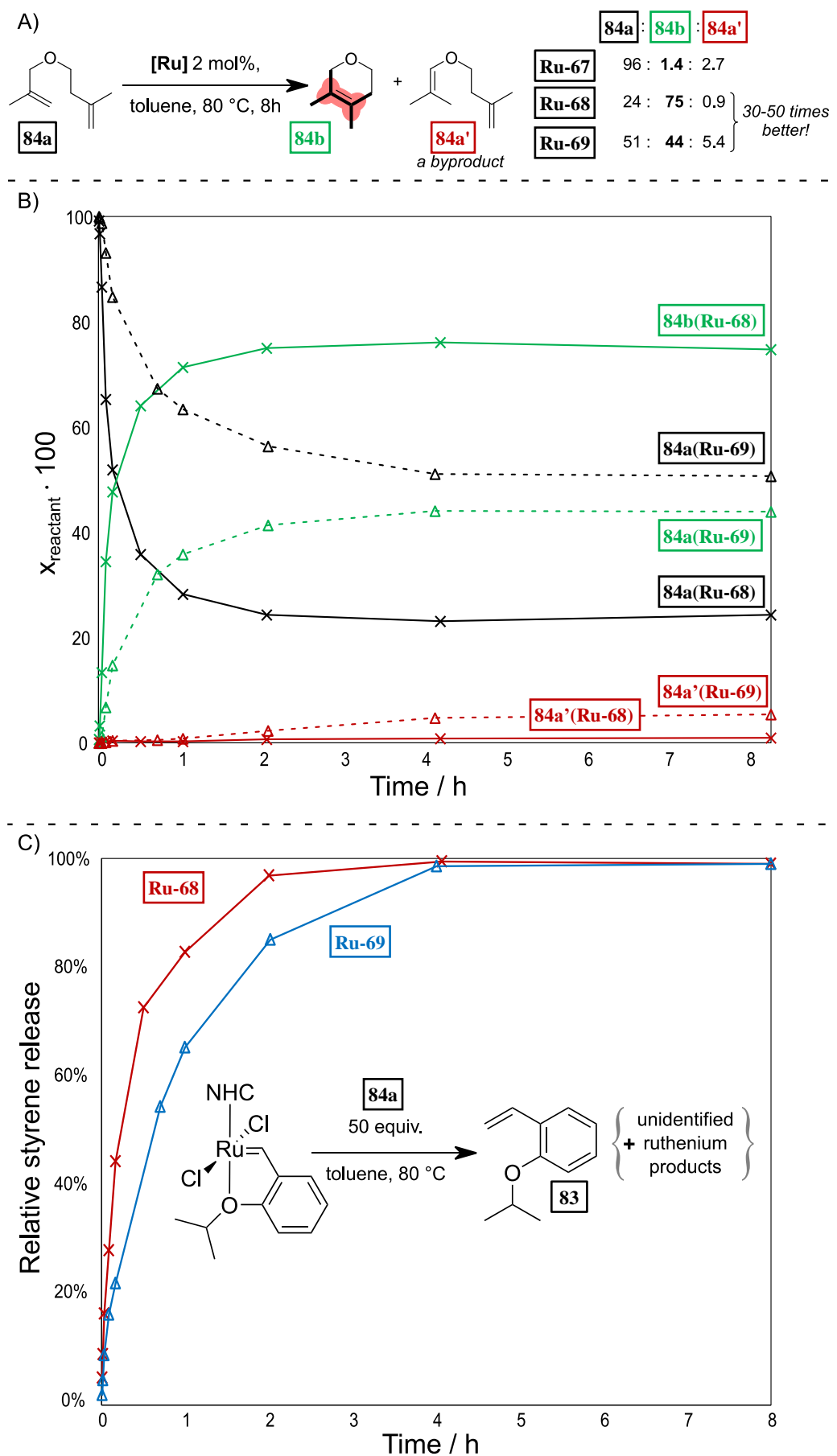
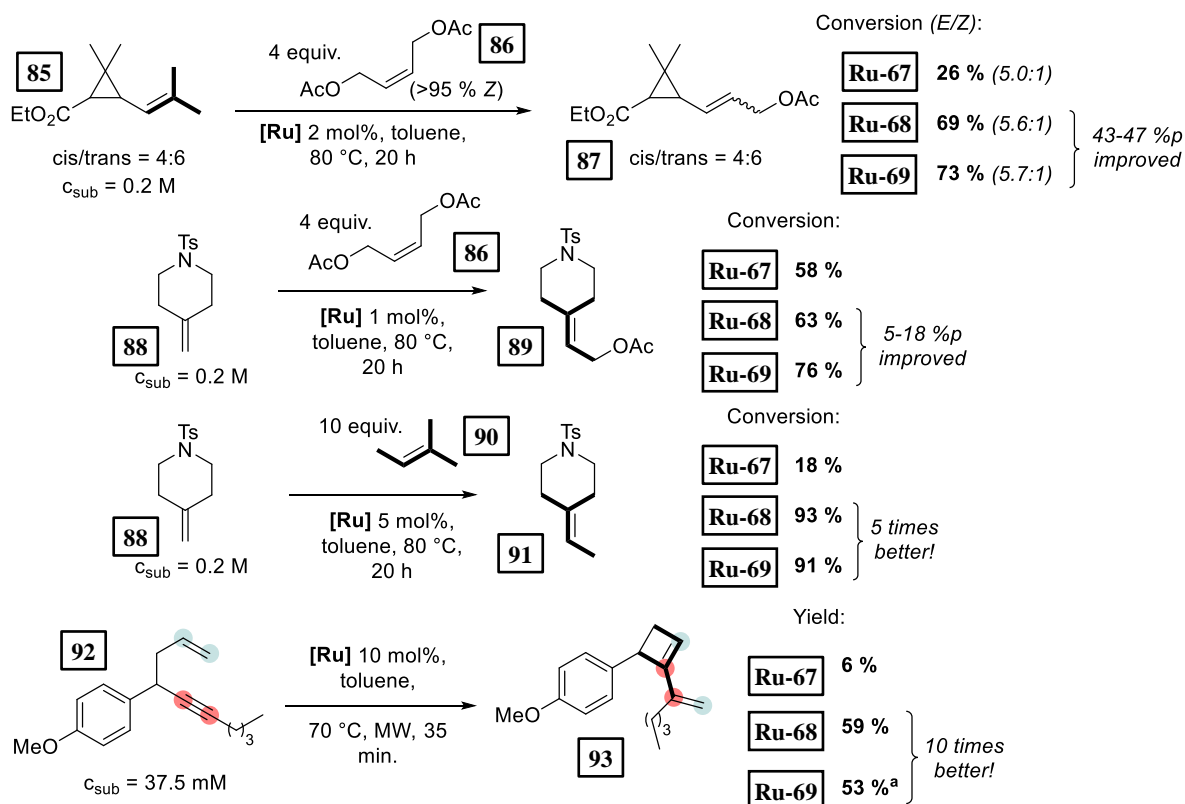


Figure 32 A) Reaction profile of substrate **84a** RCM. B) *o*-isopropoxystyrene (**83**) release in time during **84a** RCM.

To further evaluate the scope and limitations of catalysts **Ru-68** and **Ru-69**, several challenging CM reactions were investigated (Scheme 58). First, we studied the reaction between ethyl chrysanthemate (**85**) and Z-1,4-diacetoxy-2-butene (**86**). Catalysts **Ru-68** and **Ru-69** gave similar conversions of **85**, 69 % and 73 % respectively, giving product **87** selectively, whereas known **Ru-67** provided only 26 % of conversion. Next, the functionalization of the geminal carbon-carbon double bond of 4-methylene-1-tosylpiperidine (**88**) with either **86** or amylene (**90**) was probed. In the case of reaction with **86**, the use of **Ru-68** and **Ru-69** allowed for conversions up to 18 %^p higher compared to benchmark **Ru-67**, leading to 76 % conversion for **Ru-69**.

Noteworthy, in the example of CM of **88** with amylene, the biplane-type NHC catalysts **Ru-68** and **Ru-69** gave almost quantitative conversions of **88**, 93 % and 91 % respectively, which was 5 times higher than in the case of **Ru-67** reaching only 18 %. Last but not least, the highly challenging 1,5-eyne metathesis of substrate **92** to obtain crowded and strained cyclobutene derivative **93** was attempted.^[235] An additional difficulty arising in this reaction is that its selectivity can be compromised by a competing self-CM side reaction and by degradation of the resulting highly strained product. We were pleased to find that catalysts **Ru-68** and **Ru-69** gave good yields of 59 % and 53 % respectively, which was around 10 times higher than with **Ru-67** forming only traces of product which amounted to a 6 % yield. Interestingly, similarly to the case of the RCM reaction of **84a**, in this example, catalyst **Ru-68** performed visibly better than its fluorinated counterpart **Ru-69**, which we attribute to **Ru-68** higher activity. Remarkably, the use of the new catalysts allowed for a two-fold diminution in catalyst loading compared to the general-purpose SIMes complex **Ru-10** used at 20 mol% loading for this transformation.^[235]



Scheme 58 Scope and limitations of catalysts **Ru-67**, **Ru-68** and **Ru-69** in CM and cycloisomerisation of challenging substrates.
^a – reaction conducted in perfluorotoluene. %p – percentage point difference from **Ru-67**.

3.8. Conclusions

In summary, we developed the two new biplane-type NHC ligands BI*Ph and BIF*Ph based on a benzimidazolylidene core, whose lower wings are set as *N*-phenyl rings to reduce their steric hindrance on the first coordination sphere and whose upper wings are phenyl or pentafluorophenyl rings, respectively. The corresponding second-generation Grubbs-Hoveyda complexes **Ru-68** and **Ru-69** were generated and the effect of the introduction of the second decker of aromatic rings on their stereoelectronic properties, stability, and catalytic efficiency was evaluated, taking the monoplane-type, unsubstituted BIPh ligand as a reference. According to the nature of the aromatic rings, BI*Ph was shown to be more electron-donating than BIPh, while BIF*Ph was less donating. Conversely, the second aromatic decker led in both cases to slightly less hindered NHC ligands compared to BIPh by forcing the *N*-phenyl rings to stay in a more orthogonal position relative to the benzimidazolylidene core.

More importantly, both complexes **Ru-68** and **Ru-69** were shown to be significantly more stable than the known BIPh-supported complex **Ru-67**. This stability gain was rationalized through DFT calculations of the decomposition pathways. Although the aromatic rings of the second decker cannot stop the rotation of the *N*-phenyl groups in **Ru-68** and **Ru-69**, they strongly contribute to the increase in energy of the rate-determining step, by forcing a strong distortion of the carbenic heterocycle through steric constraints. The rate-determining step involves proton transfer of one of the *ortho* positions in the *N*-phenyl groups to the nearby carbon atom of the benzylidene moiety followed by migration of the benzylic proton to ruthenium with the simultaneous carbon-carbon bond formation. Moreover, the observed increased stability of the ruthenium precursors **Ru-68** and **Ru-69** was translated to the active species and enabled their implementation as highly efficient, stable precatalysts in challenging olefin metathesis reactions for the formation of tri- and tetra-substituted carbon-carbon double bonds. Complex **Ru-68** bearing the more electron-donating and *trans* effect inducing BI*Ph ligand revealed also more active than its **Ru-69** counterpart bearing the less electron donating BIF*Ph ligand.

The results presented in this chapter led to the following publication (preprint): P. Krzesiński, C. Dinoi, I. D. Rosal, L. Vendier, S. Bastin, V. César, A. Kajetanowicz, K. Grela, Unhindered Biplane-Shaped N-Heterocyclic Carbene Ligands as a Remedy for Low Reactivity of Crowded Substrates in Ruthenium Catalyzed Olefin Metathesis, *ChemRxiv*, 2023, Working Paper, DOI: 10.26434/chemrxiv-2023-b4btj.

3.9. Prospects

Overall, while it is well known that ruthenium catalysts bearing NHC ligands with low steric demand are more fragile, which impairs their productivity, we showed here that the adjunction of a second decker of aromatic groups in the NHC scaffold is a viable and promising strategy to access very stable and efficient olefin metathesis catalysts. Because the formation of sterically hindered olefins has always been the Achilles' heel of the ruthenium-catalyzed metathesis, this special trait exhibited by the newly obtained complexes appears of paramount importance. We believe that the present report will open up new possibilities for further developments of olefin metathesis catalysts and will significantly extend applications of this transformation in natural product synthesis and medicinal chemistry.

Furthermore, the special design of the developed NHC ligands could be applied to other fields than the formation of tetrasubstituted carbon-carbon double bonds or even outside of the field of OM to catalysis with other NHC-metal complexes. First of all, a structure could be envisaged of an *E*-stereoretentive catalyst bearing the NHC ligands BI*Ph or BIF*Ph (Figure 33A). As described in Chapter 1.4.3, to

facilitate the formation of the desired ruthenacyclobutane intermediates the targeted NHC should bear *N*-aryl groups with small *ortho* substituents. Therefore, the new NHC ligands might improve the stability and productivity of the corresponding *E*-stereoretentive catalysts by preventing the deleterious rotation of the *N*-aryl arm of the NHC.

Moreover, switching from phenyl *N*-substituents to aromatics with broken C₂ symmetry (e.g. *ortho*-tolyl or 2, 5-dimethylphenyl, Figure 33B) will induce axial chirality in the NHC ligand. Assuming that stable atropoisomers will be formed, this could potentially lead to the implementation of NHC ligands with the novel biplane-type architecture in enantioselective catalysis. The design could be implemented outside of OM's scope to enantioselective catalysis with other transition metals like palladium, rhodium, copper, gold, etc. The work on those subjects continues in the group of Grela.

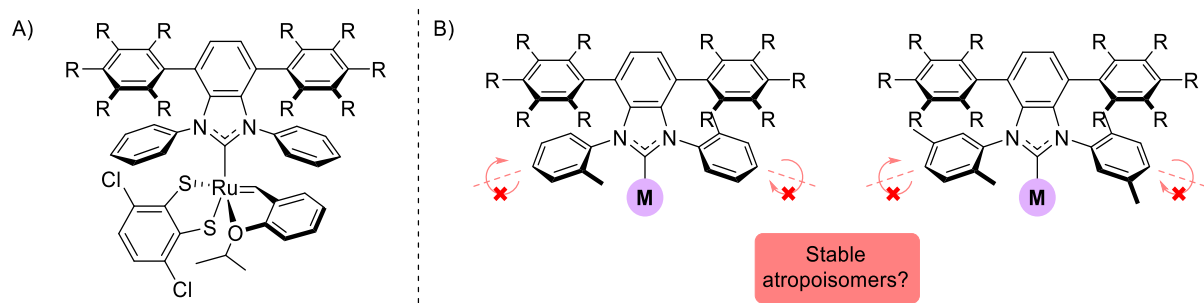
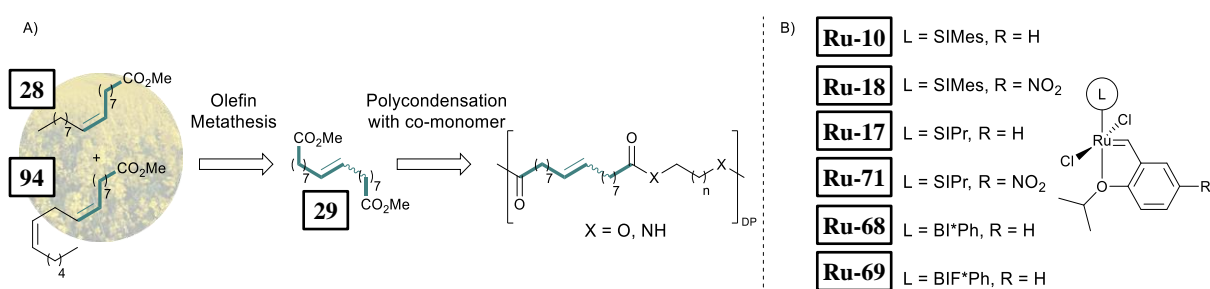


Figure 33 A) Proposition of an *E*-stereoretentive catalyst of improved stability and efficiency. B) Proposed atropoisomeric NHC metal complexes.

4. CM of technical grade methyl oleate for the synthesis of bio-based polyesters and polyamides

4.1. Objectives

At last, we embarked on the search for a process of synthesis of bio-based polyesters and polyamides, having in mind the relevant state-of-the-art outlined in Chapter 1.6. To demonstrate the applicability of this study, a technical grade methyl oleate (**28**) was used as a starting material for the self-cross metathesis step. Such material derives from broadly available sunflower or rapeseed oil and contains a substantial amount (20 wt%) of methyl linoleate (**94**), which is the most abundant polyunsaturated FAME. The resulting dimethyl octadec-9-enedioate (**29**) was used in a subsequent polycondensation to obtain polymeric materials (Scheme 59A). In this research, we used commercially available catalysts **Ru-10**, **Ru-18**, **Ru-17**, **Ru-71** and catalysts developed in Chapter 3, **Ru-68**, **Ru-69** (Scheme 59B).



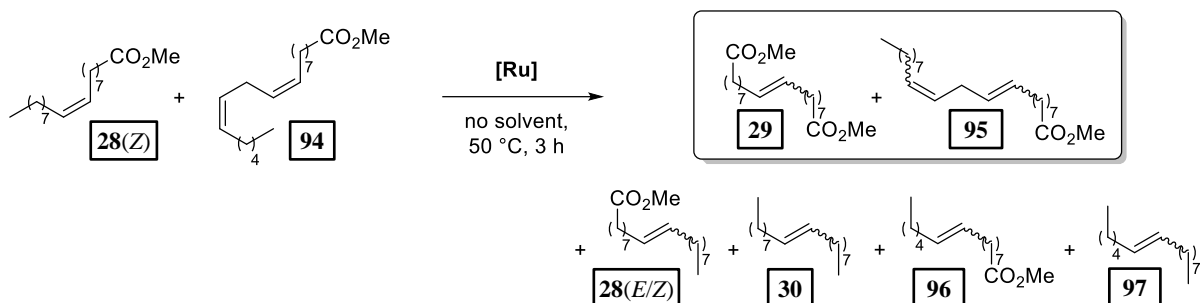
Scheme 59 A) Proposed process of the synthesis of biobased polyesters and polyamides by self-CM of technical grade methyl oleate (**28**) and subsequent polycondensation reaction. B) Catalysts used in the study.

4.2. Catalysts screening and synthesis of dimethyl octadec-9-enedioate

We started off with the self-CM of **28(Z)** after its prior simple distillation from activated alumina to decrease the content of catalyst poisons. 100 ppm of **Ru-10** allowed to reach equilibrium in 3 h (50 °C, no solvent, entry 1, Table 7). Even though the reaction mixture contained a variety of products including several internal alkenes and monoesters (**28(E/Z)**, **30**, **95**, **96**, **97**, Scheme 60), we were pleased to find that the equilibrium mixture contained predominantly **29** as a diester species. Upon decreasing the catalyst loading, we noticed that monoester **95** was also present in the reaction mixture and that the relation was inversely proportional (entries 1-3, Table 7). This suggests that at loadings lower than 100 ppm of **Ru-10** the reaction equilibrium is not reached. We wanted to avoid any monofunctional species such as **28**, **94**, or **95** in the isolated product since they would lead to a lower molecular mass of the resulting polyester, as monoesters would terminate a polymer chain. From GC, we deduced that boiling temperatures of **29** and **95** would be very similar (see Figure 49, Chapter 5.4.2.2), which would make the purification of **29** challenging. Hence, we decided to focus on minimizing the formation of **95** as the primary objective of catalyst screening, rather than maximizing catalyst efficiency.

All of the complexes gave reasonably similar conversions of substrates **28(Z)** and **94** around 95 %, except for **Ru-69** giving a lower 91 %. Catalysts **Ru-10**, **Ru-18**, **Ru-17** and **Ru-71** gave a ratio of **29** to **95** above 90:10, with **Ru-10** and **Ru-17** exceeding 95:5. **Ru-68** and **Ru-69** yielded much higher amounts of **95**, which can be attributed to their higher fragility due to lower steric protection of the NHCs. **Ru-10** gave a slightly higher yield of **29** than catalyst **Ru-17** (54 % versus 49 % respectively, the maximal

yield being approximately 50 % resulting from the reaction equilibrium) and therefore it was chosen to continue with the development.



Scheme 60 Self-CM of methyl oleate (**28**) with 20 wt% of methyl linoleate (**94**) and the observed products.

Table 7 Results of catalyst screening.

Entry	Catalyst	Loading [ppm]	Conversion of 28(Z) + 94 [%]	Yield of 29 [%]	29 to 95 wt. ratio	<i>E</i> to <i>Z</i> ratio of 29
1		100	95	54	96:4	84:16
2	Ru-10	50	94	51	89:11	82:18
3		25	80	26	63:37	78:22
4	Ru-18		94	45	90:10	82:18
5	Ru-17		94	54	92:8	82:18
6	Ru-71	100	95	49	96:4	82:18
7	Ru-68		94	50	82:18	82:18
8	Ru-69		91	42	70:30	80:20

Reaction conditions: no solvent, 50 °C, 3 h.

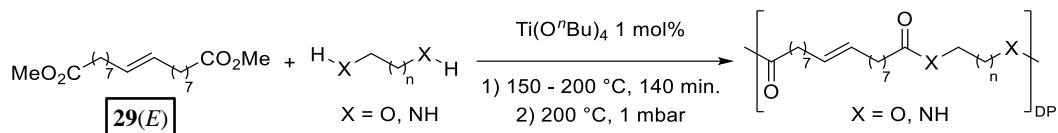
With the selected catalyst, self-CM of methyl oleate was conducted with 300 g of substrate. After the reaction, product **29** was isolated by fractional distillation and subsequently purified by crystallization from methanol at -30 °C. Interestingly, this protocol gave pure **29** containing almost only *E* isomer (*E/Z* ratio of 97:3) in 36 % yield.

4.3. Polycondensation studies

Having monomer **29** in hand, we attempted the melt polycondensation reaction with different co-monomers (Scheme 61). Titanium *n*-butoxide was used as the catalyst for this reaction.^[236] This resulted in a red-brown solid insoluble in all the most common solvents including trifluoroacetic acid. This stood in contradiction to the findings reported by Warwel and coworkers,^[236] where authors claimed to characterize the same polyesters using gel permeation chromatography (GPC), although no experimental data was provided therein. To confirm the formation of macromolecules, the reaction was stopped at an earlier stage and the formed oligomers (soluble in conventional organic solvents) were characterized by NMR spectroscopy.

The obtained oligomers and polymers were characterized by differential scanning calorimetry (DSC) and thermogravimetric analysis (TGA). The obtained polyesters have relatively low melting temperatures between 9 and 42 °C (entries 1 – 7, Table 8), which is characteristic of linear aliphatic polyesters.

Significantly higher was the melting temperature for polyamide (152 °C, entry 8, Table 8), which is due to the formation of hydrogen bonds in comparison to polyesters. Heats of fusion varied from 25 to 73 J/g. Aliphatic polyesters exhibited degradation temperatures around 400 °C, however, the polyester containing 1,4-cyclohexanediol block unit showed an increased degradation temperature of 446 °C due to the higher rigidity that such a monomer provides for the corresponding polymer.



Scheme 61 Polycondensation reaction to obtain polyesters and polyamides from diester **29**.

Table 8 Polymerization of monomer **29** and characterization of obtained polyesters and polyamides.

Entry	Polyester	Vacuum time	Yield	DP ^a	M _n (g/mol) ^a	T _m (°C) ^b	ΔH (J/g) ^b	T _d (°C) ^c	mass loss ^c
1		30 min.	51 %	1.7	592	42	64	403	97 %
2		19 h	52 %	n.d.	n.d.	14	25	413	96 %
3		225 min.	76 %	6.6	2238	34	72	395	98 %
4		21 h	81 %	n.d.	n.d.	11	55	398	97 %
5		180 min.	74 %	7.5	2539	38	73	397	98 %
6		21 h	88 %	n.d.	n.d.	10	60	398	96 %
7		19 h	24 %	n.d.	n.d.	9	35	446 ^d	78 % ^d
9		19 h	51 %	n.d.	n.d.	152	55	443	82 %

Reaction conditions: Ti(O*n*Bu)₄ 1 mol%, no solvent, 140 min. melt time with temperature increase from 150 to 200 °C. ^a – degree of polymerization (DP) and number average molecular weight (M_n) were calculated from ¹H NMR by end group analysis. ^b – determined by DSC. ^c – T_d (decomposition temperature) and mass loss of the samples were determined by TGA. ^d – evident mass loss of 50 % was observed at temperature 353 °C. n.d. – not determined due to polymer insolubility.

4.4. Conclusions

In summary, a novel process of obtaining functional polymer materials from technical grade methyl oleate was developed. Self-CM of methyl oleate (**28**) in the presence of substantial amounts of methyl linoleate was investigated and the reaction was optimized to obtain dimethyl octadec-9-enedioate (**29**) with high selectivity and yield. Subsequent polycondensation with a co-monomer (diol or diamine) resulted in the formation of polymeric materials which were characterized using TGA and DSC.

The results presented in this chapter had led to the following publication: P. Krzesiński, V. César, K. Grela, S. Santos, P. Ortiz, Cross-metathesis of technical grade methyl oleate for the synthesis of bio-based polyesters and polyamides, *RSC Sustain.*, **2023**, Advance Article, DOI: 10.1039/d3su00305a.

5. Experimental section

5.1. Materials and methods

All reactions requiring the exclusion of oxygen and moisture were carried out in dry glassware with dry solvents under a dry and oxygen free argon or nitrogen atmosphere using either Schlenk techniques or inside an mBraun Glovebox. Analytical thin layer chromatography (TLC) was performed on Merck Silica gel 60 F₂₅₄ precoated aluminum sheets. Components were visualized by observation under ultra violet light (254 nm or 365 nm) or dyed by an aqueous KMnO₄ reagent. Column chromatography was carried out using silica gel (40-63 µm or 60-200 µm), purchased from Merck.

Commercially available solvents (HPLC grade) and reagents were used as received unless stated otherwise. Dry solvents (DCM, toluene, Et₂O, hexane) were obtained using solvent purification system (SPS) MBRAUN SPS-800 and stored in Ar over activated 4 Å molecular sieves for at least 12 h prior to use. Dry THF was obtained by distillation under Ar with sodium and benzophenone and stored in Ar over activated 4 Å molecular sieves for at least 12 h prior to use. Dry MeCN was obtained by distillation under Ar with P₂O₅ and stored in Ar over activated 3 Å molecular sieves for at least 12 h prior to use. Dry acetone was prepared by adding activated 4 Å molecular sieves (5 % wt./v), storing for 6 h and after sieves removal subsequently distilled in Ar.^[196] Dry pentane was obtained by distillation with sodium under Ar and stored in Ar over activated 4 Å molecular sieves for at least 12 h prior to use. Dry DCE and EtOAc were freeze/pump/thaw degassed and stored in Ar over activated 4 Å molecular sieves for at least 12 h prior to use. DMF was degassed by bubbling N₂ or Ar for 15 min. and stored over activated 4 Å molecular sieves for at least 12 h prior to use.

The NMR spectra were recorded on Bruker AV300, AV400, Ultrashield III 300 MHz or Agilent 400 MHz spectrometers at 22 ± 2 °C. Chemical shifts are reported in parts per million (ppm) and referenced against the residual proton or carbon signal of a solvent: CDCl₃ (¹H = 7.26 ppm, ¹³C = 77.16 ppm), CD₂Cl₂ (¹H = 5.32 ppm, ¹³C = 53.84 ppm), DMSO-d₆ (¹H = 2.50 ppm, ¹³C = 39.52 ppm), CD₃CN (¹H = 1.94 ppm, ¹³C = 1.32, 118.26 ppm), C₆D₆ (¹H = 7.16 ppm). Coupling constants J are given in hertz (Hz). Data are reported as follows: chemical shift, multiplicity, coupling constant, integration.

GC measurements were recorded using a PerkinElmer Clarus 580 chromatograph equipped with InertCap 5MS-Sil column or Shimadzu 2010plus equipped with Zebron ZB-5 column or Shimadzu 2014 equipped with SLBTM-5MS.

Infrared (IR) spectrums were recorded on a Perkin-Elmer Spectrum One FTIR spectrometer or Perkin-Elmer Spectrum 100 FTIR spectrometer.

HRMS were recorded either by mass spectrometry service of the Institute of Chemistry of Toulouse on Xevo G2 QToF, Waters, electrospray ionization (ESI) mode; or by Environmental Laboratory of Mass Spectrometry of Institute of Biochemistry and Biophysics of the Polish Academy of Sciences (Warsaw) on QTOF Premier, Waters, ESI mode. Low resolution mass spectroscopy was recorded on a Shimadzu QP2010 Ultra GC-MS, electron impact (EI) mode.

Elemental analysis was performed either by C H N Elemental Analysis service of Laboratory of Coordination Chemistry (Toulouse) using Perkin Elmer 2400 series II analyzer; or by Elementary Analysis

Laboratory of Organic Chemistry Institute of Polish Academy of Sciences (Warsaw) using UNICube, Elementar analyzer.

XRD data was collected either by X-ray diffraction service of Laboratory of Coordination Chemistry (Toulouse) on the Agilent Gemini, Bruker Nonius, Bruker Kappa Apex II with either Cu K α ($\lambda = 1.54180 \text{ \AA}$) or Mo K α ($\lambda = 0.71073 \text{ \AA}$) radiation source; or by Laboratory of Structural and Biochemical Research, University of Warsaw Biological and Chemical Research Centre on the SuperNova Single, Double Source Rigaku Oxford Diffraction with Cu K α radiation source ($\lambda = 1.54180 \text{ \AA}$).

TGAs were performed on a TGA/DSC1 manufactured by Mettler-Toledo to determinate the degradation temperatures and mass losses of the materials synthetized oligomers. Such temperatures were determined based on the onset point of the slope of the thermogravimetric curve. The equipment is calibrated yearly for temperatures using nickel (purity > 99.99%) as a reference standard. The samples of around 15 mg were placed in open alumina crucibles and were submitted to heating ramps of 10 °C/min from room temperature to 700 °C using 50 mL/min of nitrogen as atmosphere. The experimental error supplied by the manufacturer is $\pm 3\%$ for both temperature determination and weight.

DSC was recorded using a DSC2 from Mettler-Toledo in order to determine the melting and any other thermal phenomena of the samples from the obtained thermograms (heat flow vs temperature). Melting temperatures of oligomers were given by the onset point of the endothermic signals. The calibration of heat flow and temperature is carried out monthly by using high purity indium standard (purity > 99.99%), so the accuracy of the given temperatures of melting is about $\pm 0.6 \text{ }^{\circ}\text{C}$. The enthalpies of melting are calculated by integration of the endothermic peaks assuming a linear baseline, and the accuracy of the determination is about $\pm 5\%$. The samples of around 10 mg were measured inside closed aluminum crucibles which were submitted to three cycles of heating/cooling at 5 °C/min from -80 °C to 300 °C in a controlled atmosphere of nitrogen.

5.2. Supporting information for Chapter 2

5.2.1. Axis A

5.2.1.1. General considerations

Commercially available substrates were used as received unless stated otherwise. Compounds **18**, **19**, and **Ru-54** were commercially available. Phenyl acetylene (**19**) was purified by CC (eluent: pentane), freeze/pump/thaw degassed and stored under Ar over activated 4 Å molecular sieves in a refrigerator. Compounds **31**,^[237] **34**,^[60] **36**,^[238] and **Ru-6**^[239] were synthesized according to literature procedures. Additionally, the OM substrate **36** was purified by distillation, properly degassed under a dynamic vacuum and stored over activated neutral Al₂O₃.

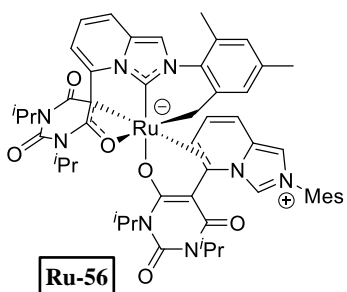
5.2.1.2. Synthesis of ruthenium complexes **Ru-56 – Ru-59**

The syntheses refer to Scheme 36, Chapter 2.2.2.

- **Synthesis of complex Ru-56**

Inside a glovebox, ligand precursor **31** (510 mg, 1.14 mmol, 2 equiv.) was mixed with complex **Ru-54** (182.4 mg, 0.571 mmol, 1 equiv.) in a 200 mL Fisher-Porter vessel. To the tube, 44 mL of dry and deoxygenated THF was added. The tube was heated at 90 °C for 2 h. Next, the solvent was removed *in vacuo* and the crude product was washed with dry pentane (50 mL). The crude reaction mixture was

solubilized in DCM and the obtained solution was put on a short silica gel pad, which was then washed with DCM. The solvent was removed *in vacuo* and the product was taken up with minimal amount of DCM. The product was precipitated with pentane (50 mL) and the supernatant was filtered off. The obtained precipitate was dried under the reduced pressure of an oil pump for several minutes. This procedure gave 288 mg of red crystals obtained as a mixture of complex **Ru-56** and recovered **31** in a 1 to 1.5 molar ratio (as determined by NMR). This corresponds to 172 mg (0.173 mmol) of pure **Ru-56** and 30 % yield. Such a mixture of **Ru-56** and **31** was used for the following synthetic steps. Analytically pure **Ru-56** was procured as deep red crystals by CC using as eluents EtOAc/hexane mixture from (5 to 15 %). Crystals of **Ru-56** suitable for XRD experiments were grown by layering a DCM complex solution with pentane.



¹H NMR (300 MHz, CD₂Cl₂) δ 8.38 (d, *J* = 1.1 Hz, 1H), 7.63 – 7.46 (m, 2H), 7.04 (s, 1H), 7.00 (s, 1H), 6.97 – 6.89 (m, 3H), 6.66 (dd, *J* = 9.1, 6.8 Hz, 1H), 6.38 (d, *J* = 6.6 Hz, 1H), 6.35 (d, *J* = 1.5 Hz, 1H), 5.49 (d, *J* = 9.7 Hz, 1H), 5.21 (dd, *J* = 9.7, 6.0 Hz, 1H), 5.13 – 4.85 (m, 5H), 4.11 (d, *J* = 10.3 Hz, 1H), 2.98 (d, *J* = 5.9 Hz, 1H), 2.47 (s, 3H), 2.44 (s, 3H), 2.34 (s, 3H), 2.14 (s, 3H), 1.65 (s, 3H), 1.47 (d, *J* = 6.9 Hz, 3H), 1.44 – 1.37 (m, 9H), 1.32 (d, *J* = 7.0 Hz, 3H), 1.25 (dd, *J* = 6.8, 2.9 Hz, 9H).

¹³C{¹H} NMR (101 MHz, CD₂Cl₂) δ 182.3, 167.7, 167.4, 161.0, 157.5, 151.7, 151.2, 147.1, 141.4, 140.9, 137.7, 137.2, 136.4, 136.2, 135.9, 134.2, 132.2, 130.3, 129.8, 129.6, 129.6, 129.4, 128.2, 127.9, 124.7, 114.5, 113.8, 112.5, 109.2, 102.6, 87.8, 77.5, 73.2, 51.8, 47.7, 46.0, 44.4, 44.1, 24.1, 22.4, 21.3, 21.1, 20.5, 20.2, 20.1, 20.0, 19.9, 19.9, 17.6, 17.4.

HRMS (ESI): m/z calcd. for C₅₂H₅₉N₈O₆Ru [M+H]⁺ 993.3615, found 993.3628.

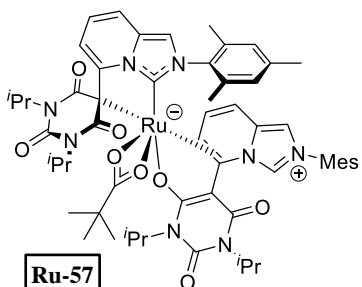
IR (ATR) ν / cm⁻¹ 2964, 2925, 2872, 1693, 1679, 1630, 1607, 1547, 1502, 1440, 1373, 1341, 1261.

Elemental analysis calcd. for C₅₂H₅₈N₈O₆Ru: C, 62.95; H, 5.89; N, 11.29. Found C, 62.49; H, 6.01; N, 10.87.

• Synthesis of complex **Ru-57**

92.1 mg of the mixture of complex **Ru-56** and **31** (1 to 1.5 molar ratio), which corresponds to 55.0 mg (55.4 µmol, 1 equiv.) of pure **Ru-56**, was dissolved in 4 mL of anhydrous THF in a Schlenk flask. Pivalic acid (12.2 mg, 0.122 mmol, 2.2 equiv.) was added and the flask was heated at 80 °C for overnight. Solvents were removed *in vacuo* and the product was isolated using CC (eluent: EtOAc in hex from 30 % to 50 %). After solvent evaporation, the complex **Ru-57** was dried under the reduced pressure of an oil pump for several minutes. The product was isolated as a light-red precipitate (53 mg, 48.4 µmol) in 87 % yield. Crystals of **Ru-57** suitable for XRD experiments were grown by layering a hexafluorobenzene complex solution with heptane.

¹H NMR (400 MHz, CD₂Cl₂) δ 8.28 (s, 1H), 7.14 (d, *J* = 9.2 Hz, 1H), 7.04 (dd, *J* = 15.1, 6.1 Hz, 3H), 6.96 (s, 1H), 6.74 (d, *J* = 6.6 Hz, 2H), 6.57 (d, *J* = 11.0 Hz, 2H), 6.36 (dd, *J* = 9.6, 5.8 Hz, 1H), 6.14 (d, *J* = 9.7 Hz, 1H), 5.02 (hept, *J* = 6.7 Hz, 1H), 4.83 (ddp, *J* = 33.6, 13.4, 6.7 Hz, 3H), 4.31 (d, *J* = 5.7 Hz, 1H), 2.35 (s, 3H), 2.20 (s, 3H), 2.10 (s, 3H), 1.83 (d, *J* = 7.6 Hz, 6H), 1.69 (s, 3H), 1.63 (d, *J* = 7.0 Hz,



3H), 1.38 (d, $J = 6.7$ Hz, 3H), 1.32 (dd, $J = 6.8, 3.5$ Hz, 6H), 1.25 – 1.18 (m, 9H), 0.96 (d, $J = 7.0$ Hz, 3H), 0.88 (s, 9H).

$^{13}\text{C}\{\text{H}\}$ NMR (101 MHz, CD_2Cl_2) δ 194.8, 175.2, 173.8, 169.6, 166.6, 161.5, 151.9, 151.4, 145.4, 143.2, 141.5, 138.5, 138.2, 136.7, 136.3, 135.1, 134.9, 132.4, 132.2, 131.8, 130.6, 130.0, 129.9, 129.4, 128.5, 125.7, 114.4, 114.3, 112.6, 112.6, 106.4, 95.3, 90.6, 58.8, 46.4, 45.7, 44.2, 43.9, 40.2, 26.9, 21.2, 21.1, 20.9, 20.6, 20.3, 20.2, 20.1, 19.9, 19.9, 19.5, 18.6, 17.9, 17.8, 17.2.

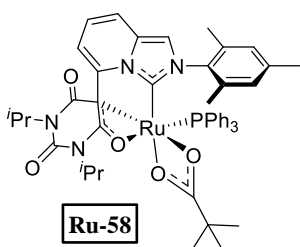
HRMS (ESI): m/z calcd. for $\text{C}_{57}\text{H}_{69}\text{N}_8\text{O}_8\text{Ru} [\text{M}+\text{H}]^+$ 1095.4298, found 1095.4312.

IR (ATR) ν / cm^{-1} 3060, 2976, 2928, 1706, 1684, 1646, 1627, 1608, 1579, 1538, 1471, 1437, 1378, 1361, 1335, 1260, 1168, 764.

Elemental analysis calcd. for $\text{C}_{57}\text{H}_{68}\text{N}_8\text{O}_8\text{Ru}$: C, 62.56; H, 6.26; N, 10.24. Found C, 62.31; H, 6.32; N, 10.25.

• Synthesis of complex Ru-58

268.0 mg of the mixture of complex **Ru-56** and **31** (1 to 1.5 molar ratio), which corresponds to 160.0 mg (0.161 mmol, 1 equiv.) of pure **Ru-56**, was dissolved in 5 mL of anhydrous DCE in a Schlenk flask. PPh_3 (50.8 mg, 0.194 mmol, 1.2 equiv.) and pivalic acid (19.8 mg, 0.194 mmol, 1.2 equiv.) were added and the flask was heated at 80 °C for 6 h. After solvent removal *in vacuo*, the product was isolated by CC using EtOAc in hexane 15 % as eluent. After solvent evaporation, the product was dried under the reduced pressure of an oil pump for several minutes. The product was isolated as an orange solid in 87 % yield (127 mg, 0.140 mmol). Crystals of **Ru-58** suitable for XRD experiments were grown by layering a DCM complex solution with pentane.



^1H NMR (300 MHz, CD_2Cl_2) δ 7.32 – 7.06 (m, 9H), 6.92 (ddt, $J = 13.4, 9.1, 6.3$ Hz, 9H), 6.41 (dd, $J = 6.6, 0.7$ Hz, 1H), 6.17 (ddd, $J = 10.6, 8.3, 1.2$ Hz, 2H), 4.90 (h, $J = 6.8$ Hz, 1H), 4.22 (hept, $J = 6.7$ Hz, 1H), 2.46 (s, 3H), 2.15 (s, 3H), 1.59 (d, $J = 6.8$ Hz, 3H), 1.42 (d, $J = 6.8$ Hz, 3H), 1.11 (d, $J = 6.9$ Hz, 3H), 1.00 (d, $J = 6.8$ Hz, 3H), 0.95 (s, 3H), 0.57 (s, 9H).

$^{13}\text{C}\{\text{H}\}\{\text{P}\}$ NMR (101 MHz, CD_2Cl_2) δ 194.3, 174.4, 174.2, 151.5, 147.4, 140.7, 139.3, 138.7, 136.8, 135.6, 135.4, 135.1, 135.0, 134.4, 133.6, 132.4, 131.1, 129.8, 129.7, 129.7, 129.2, 128.5, 128.1, 128.1, 127.4, 125.4, 114.2, 112.8, 112.6, 46.4, 46.0, 39.5, 26.3, 21.3, 20.9, 20.4, 20.0, 20.0, 18.6, 16.5.

^{31}P NMR (162 MHz, CD_2Cl_2) δ 67.23.

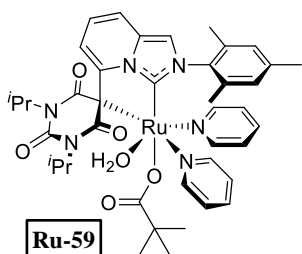
HRMS (MALDI): m/z calcd. for $\text{C}_{49}\text{H}_{53}\text{N}_4\text{O}_5\text{PRu} [\text{M}]^+$ 910.2811, found 910.2847.

IR (ATR) ν / cm^{-1} 3057, 2957, 2923, 2861, 1698, 1650, 1526, 1502, 1483, 1431, 1404, 1373, 1361, 1342, 1320, 1274, 1210, 1093, 1053, 989, 903, 787, 765, 750.

Elemental analysis calcd. for $\text{C}_{49}\text{H}_{53}\text{N}_4\text{O}_5\text{PRu}$: C, 64.67; H, 5.87; N, 6.16. Found C, 64.68; H, 5.85; N, 6.14.

- **Synthesis of complex Ru-59**

Starting complex **Ru-57** (40.0 mg, 36.6 µmol, 1 equiv.) was dissolved in 2 mL of anhydrous pyridine (excess) in a Schlenk flask. The flask was heated at 80 °C for 2 h. Next, the pyridine was evaporated *in vacuo*. The product was isolated by filtration through silica gel (dried in an oven at 120 °C, prior to use) with eluent EtOAc in pentane 50 % (dry solvents). It was imperative to use dry solvents for CC as otherwise the complex readily decomposed. The solvents were evaporated *in vacuo* and a minimal amount of anhydrous DCM was added to solubilize the substance. The product was precipitated with 10 mL of anhydrous pentane and the supernatant was removed. The obtained precipitate was washed with dry pentane (3 × 5 mL) and dried under the reduced pressure of an oil pump for several minutes. The complex **Ru-59** was obtained as a brown powder in 90 % yield (27.0 mg, 32.8 µmol). Crystals of **Ru-59** suitable for XRD experiments were grown by layering an Et₂O/DCM complex solution with pentane.



¹H NMR (400 MHz, CD₂Cl₂) δ 9.02 (d, *J* = 5.2 Hz, 1H), 7.70 (d, *J* = 6.1 Hz, 1H), 7.38 (tt, *J* = 7.4, 1.5 Hz, 2H), 7.21 (tt, *J* = 7.5, 1.6 Hz, 2H), 7.15 (dd, *J* = 9.3, 1.0 Hz, 1H), 7.11 – 6.61 (m, 6H), 6.57 (s, 1H), 6.26 – 6.14 (m, 2H), 5.05 (hept, *J* = 6.8 Hz, 1H), 4.20 – 3.57 (brs, 1H), 2.06 (s, 3H), 1.88 (s, 3H), 1.73 (s, 3H), 1.41 (dd, *J* = 6.9, 2.0 Hz, 6H), 1.19 (d, *J* = 6.9 Hz, 3H), 0.95 (d, *J* = 7.0 Hz, 3H), 0.92 (s, 9H).

¹³C{¹H} NMR (101 MHz, CD₂Cl₂) δ 191.3, 182.1, 178.3, 174.0, 160.6, 156.1, 154.9, 151.9, 144.9, 138.6, 137.5, 137.2, 134.4, 133.4, 133.3, 133.0, 129.3, 128.6, 125.9, 123.1, 123.1, 123.0, 123.0, 114.6, 112.6, 112.2, 46.1, 45.4, 40.4, 28.3, 21.2, 20.8 (d, *J* = 3.4 Hz), 20.3, 19.4, 18.3, 17.6.

HRMS (ESI): m/z calcd. for C₄₁H₅₀N₆O₆Ru [M]⁺ 824.2847, found 824.2803; for C₄₁H₄₈N₆O₅Ru [M-H₂O]⁺ 806.2730, found 806.2740; for C₃₆H₄₆N₅O₆Ru [M-C₅H₅N+H]⁺ 746.2486, found 746.2408; for C₃₆H₄₃N₅O₅Ru [M-C₅H₅N-H₂O]⁺ 727.2308, found 727.2317.

IR (ATR) ν / cm⁻¹ 2962, 2924, 2871, 1689, 1633, 1608, 1583, 1479, 1428, 1411, 1346, 1323, 792, 764, 751.

Elemental analysis calcd. for C₄₁H₅₀N₆O₆Ru: C, 59.77; H, 6.12; N, 10.20. Found C, 60.28; H, 6.32; N, 9.83.

5.2.1.3. Attempts to install an alkylidene moiety

The syntheses refer to Scheme 37A, Chapter 2.2.3.

- **With diazomethane derivative 34**

Freshly prepared diazomethane derivative **34**^[60] (0.131 mmol, 4 equiv.) was dissolved in 2 mL of dry pentane in a Schlenk flask. In a separate Schlenk flask, a starting complex (**Ru-57–Ru-59**) (32.8 µmol, 1 equiv.) was dissolved in 2 mL of dry DCM. Both Schlenk flasks were cooled down to -78 °C and **34** solution was transferred through a cannula to a complex solution. The reaction was stirred at this temperature allowing it to warm up to room temperature over several hours. The reaction was monitored by TLC, which showed no formation of a product with a starting complex remaining unchanged.

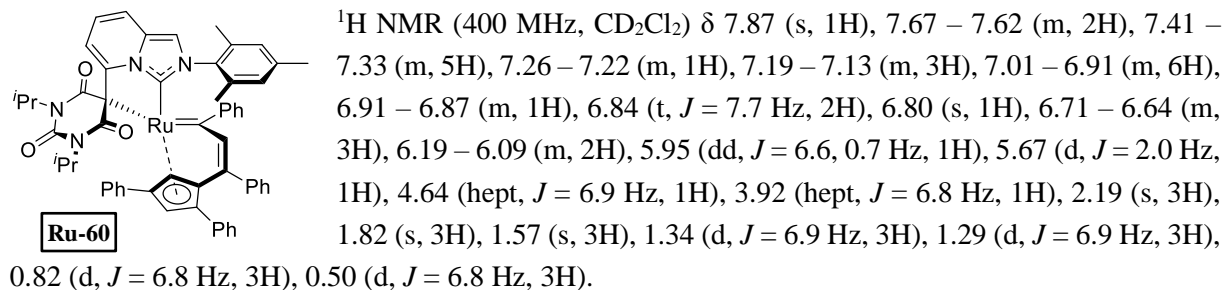
- With propargyl alcohol derivative **18**

Inside a glovebox, a starting complex (**Ru-57–Ru-59**) (30 µmol, 1 equiv.) was placed in a 1.5 mL vial equipped with a magnetic stir bar and **18** (18.7 mg, 90 µmol, 3 equiv.) was added followed by dry THF. The content of the vial was stirred at 80 °C for overnight. The reaction was monitored by TLC, which showed consumption of a starting complex, however, a variety of products were formed whose isolation and characterization were challenging.

5.2.1.4. Synthesis of complex **Ru-60**

The synthesis refers to Scheme 37B, Chapter 2.2.3.

In a Schlenk flask starting complex **Ru-57** (100 mg, 91.4 µmol, 1 equiv.) was dissolved in 2 mL of phenylacetylene (excess). The flask was heated at 80 °C for 10 h (after that time TLC showed full conversion of **Ru-57**). The excess of phenylacetylene was evaporated *in vacuo* and the product was isolated using CC (eluent from 0 to 15 % EtOAc in hexane). After solvent removal, the product was dried under the reduced pressure of an oil pump for several minutes. The complex **Ru-60** was obtained as a deep red powder in 18 % yield (16.0 mg, 16.8 µmol). Crystals of **Ru-60** suitable for XRD experiments were obtained by vapor-liquid diffusion crystallization from THF solution placed around pentane vapors.



¹³C{¹H} NMR (101 MHz, CD₂Cl₂) δ 282.7, 176.2, 176.0, 174.8, 162.1, 159.5, 151.8, 147.5, 146.3, 138.7, 138.4, 136.3, 136.1, 134.6, 134.2, 133.9, 132.3, 130.0, 129.7, 129.2, 128.6, 128.6, 127.8, 127.7, 127.4, 127.3, 127.2, 127.1, 126.6, 126.0, 124.2, 121.0, 119.0, 108.2, 99.0, 94.3, 47.5, 47.2, 21.7, 21.2, 21.2, 20.1, 18.9, 18.4.

HRMS (ESI): m/z calcd. for C₅₈H₅₂N₄O₃Ru [M]⁺ 954.3077, found 954.3088.

IR (ATR) *v* / cm⁻¹ 3153, 3055, 2965, 2924, 2870, 1707, 1638, 1596, 1492, 1419, 1393, 1328, 1313, 1195, 1172, 1160, 1068, 985.

5.2.1.5. Attempted catalysis

The procedures refer to Table 2, Chapter 2.2.3.

- **GC analysis**

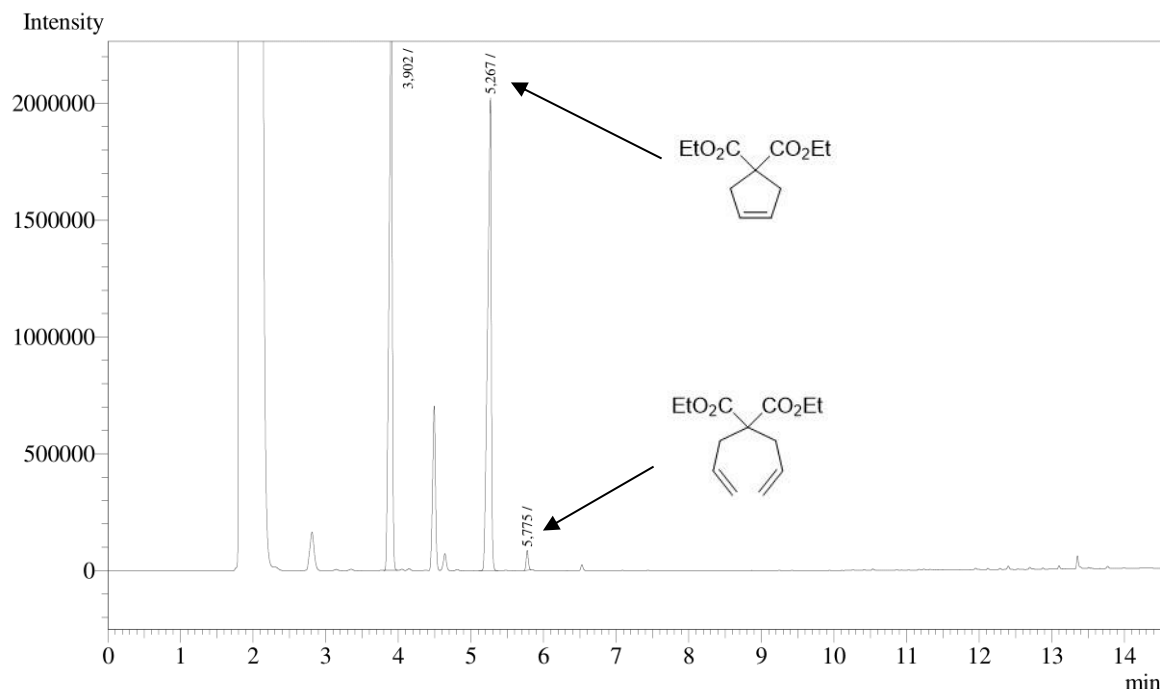


Figure 34 Gas chromatogram of an exemplary reaction mixture from RCM of **36**. Oven temperature program – 120 °C for 1 min.; then 10 °C/min. to 200 °C; then 20 °C/min. to 270 °C; then 30 °C/min. to 300 °C for 1.5 min.

Yield of **37** was calculated according to the following equation:

$$Yield = \frac{f_{(37/36)} \cdot A_{37}}{f_{(37/36)} \cdot A_{37} + A_{36}} \quad (5)$$

Where: A – signal area; **37** – from product **37**; **36** – from product **36**; $f_{(37/36)} = 1.255$.

- **With complex Ru-60**

Into a 1.5 mL vial equipped with a magnetic stir bar, 1.0 mg (1.05 µmol, 1 mol%) of complex **Ru-60** was weighted. The vial was transferred into a glovebox, in which substrate **36** stock solution in toluene (0.53 mL of 0.2 M, 0.106 mmol, 1 equiv.) was added. The content of the vial was mixed at 80 °C for overnight and the sample was analyzed by GC.

- **With NHC complexes Ru-56 – Ru-59, general procedure**

Into a 1.5 mL vial equipped with a magnetic stir bar, 10 µmol (10 mol%) of a corresponding ruthenium NHC complex was placed (the mass depended on complex molecular weight). The vial was transferred into a glovebox and the complex was dissolved in dry THF (0.25 mL). Next, 0.25 mL of substrate **36** (0.4 M, 0.100 mmol, 1 equiv.) and phenylacetylene (**19**) (0.184 M, 0.046 mmol, 46 mol%) stock solution in dry toluene was added (the substrate **36** and **19** were dissolved in the same stock solution and their molar concentrations were 0.4 and 0.184 M respectively). The content of the vial was stirred for 2 h at 80 °C and the sample was analyzed by GC.

- With NHC *p*-cymene complexes Ru-61 – Ru-63, general procedure

Into a 1.5 mL vial equipped with a magnetic stir bar, 20 µmol (10 mol%) of a corresponding azolium salt (an NHC precursor) was placed (the mass depended on complex molecular weight). The vial was transferred into a glovebox and dry THF (0.46 mL) was added followed by 40 µL of LiHMDS stock solution in toluene (0.5 M, 20 µmol, 10 mol%). The content of the vial was stirred for 30 min. at ambient temperature. The *p*-cymene ruthenium precursor **Ru-6** (6.1 mg, 10 µmol, 5 mol%) was added and everything was stirred for 1 h at ambient temperature.

Next, 0.50 mL of substrate **36** (0.4 M, 0.200 mmol, 1 equiv.) and phenylacetylene (**19**) (0.184 M, 0.092 mmol, 46 mol%) stock solution in dry toluene was added (the substrate **36** and **19** were dissolved in the same stock solution and their molar concentrations were 0.4 and 0.184 M respectively). The content of the vial was stirred for 2 h at 80 °C and the sample was analyzed by GC.

5.2.2. Axis B

5.2.2.1. General considerations

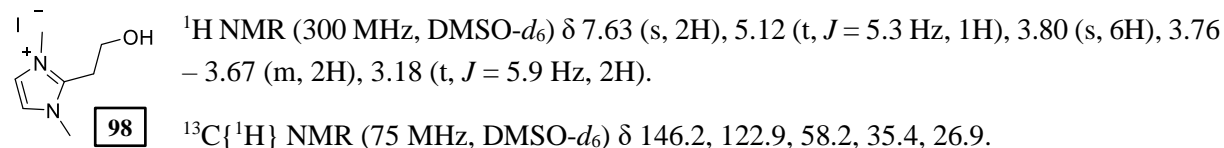
Commercially available substrates were used as received unless stated otherwise. 1,3-dibromopropane (**46**) and **Ru-9** were commercially available. **46** was freeze/pump/thaw degassed and stored under Ar over activated 4 Å molecular sieves for at least 12 h prior to use. Compounds **40**,^[240] **41**,^[194] **Rh-1**^[241] and **Pd-1**^[242] were synthesized according to literature procedures. K₂CO₃ was dried at 120 °C for at least 12 h prior to use.

5.2.2.2. Attempts to synthesize an NHC-NHO precursor **38**

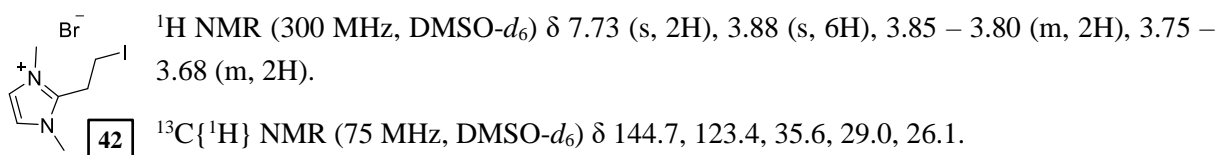
The synthesis refers to Scheme 41A, Chapter 2.3.1.

- Synthesis of compound **42**

In a 20 mL high pressure reactor, substrate **41** (1.448 g, 11.48 mmol, 1 equiv.) was dissolved in 7 mL of DCM and 7 mL of iodomethane (16 g, 113 mmol, 10 equiv.) was added. Everything was mixed for 15 min. at 80 °C, upon which transparent crystals were formed. Next, the solid was filtered off and washed with DCM (4 × 3 mL). The intermediary product **98** was obtained as transparent crystals in 94 % yield (2.904 g, 10.83 mmol).



In a Schlenk flask compound **98** (500 mg, 1.86 mmol, 1 equiv.) and CBr₄ (680 mg, 2.05 mmol, 1.1 equiv.) were placed. After exchanging the atmosphere for nitrogen, 20 mL of dry DMF was added. Reactants were solubilized at 80 °C and upon cooling down to room temperature the solution remained homogeneous. PPh₃ (538 mg, 2.05 mmol, 1.1 equiv.) was added at ambient temperature and the solution was stirred for 2 h. Next, the solvent was removed *in vacuo* and a crude product was taken up with 12 mL of distilled water. The aqueous solution was washed with DCM (4 × 10 mL). Water was removed *in vacuo* and the crude product was crystallized from 50 mL of hot (80 °C) MeCN by cooling down the solution to –22 °C. The product **42** was obtained as transparent crystal needles (273.5 mg, 0.826 mmol). A second crystallization gave 125 mg (0.378 mmol) of **42**. Yield of the second step – 65 %.

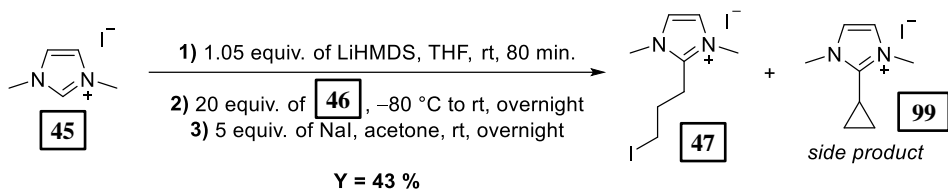


- **Attempts to synthesize 38 and characterization of elimination product 43**

Compound **42** was dried over P₂O₅ under the reduced pressure of an oil pump for overnight, after which it was handled inside a glovebox due to its hygroscopicity. *N*-mesityl imidazoline (**40**) (60 mg, 0.317 mmol, 1.05 equiv.) and **42** (100 mg, 0.302 mmol, 1 equiv.) were mixed in a Schlenk flask and 10 mL of anhydrous MeCN was added. The content of the flask was stirred at 90 °C for overnight. After solvent removal *in vacuo*, the elimination product **43** was characterized in a crude reaction mixture.

5.2.2.3. Synthesis of the NHC-NHO precursor **48**

- **Synthesis of compound 47**

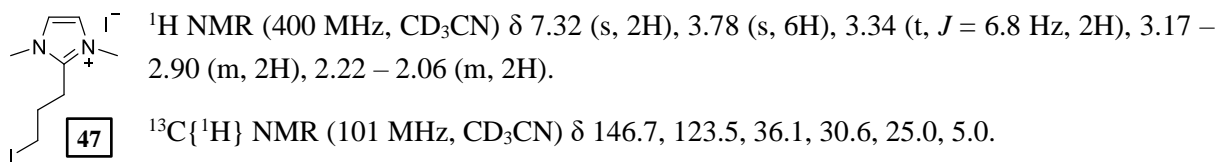


Scheme 62 Synthesis of compound **47**.

Dimethylimidazolium iodide (**45**) was dried over P₂O₅ under the reduced pressure of an oil pump for overnight, after which it was handled inside a glovebox due to its hygroscopicity. In a 250 mL Schlenk flask equipped with a magnetic stir bar, LiHMDS (1.96 g, 11.72 mmol, 1.05 equiv.) was placed along with **45** (2.50 g, 11.16 mmol, 1 equiv.) and dry THF (200 mL) was added. The reaction mixture was stirred for 80 min. at ambient temperature. The imidazolium salt has almost completely solubilized giving a yellow, hazy solution.

In a second Schlenk flask, 1,3-dibromopropane (**46**) (23 mL, 45.8 g, 0.227 mol, 20 equiv.) was mixed with 40 mL of dry THF. The Schlenk with dibromopropane solution was cooled down to –80 °C. Into the dibromopropane solution, the carbene solution was slowly added with a cannula with a paper filter. The content of the Schlenk flask was mixed allowing it to warm up to room temperature during overnight. After this time, the product was filtered off using a cannula with a paper filter and the sediment was washed with Et₂O (4 × 24 mL).

The obtained precipitate was dissolved in 400 mL of acetone and 8.36 g of NaI (55.8 mmol, 5 equiv.) was added and everything was stirred at ambient temperature for overnight. The solvent was evaporated *in vacuo* and the product was isolated using CC on a short silica gel column with MeOH in DCM (from 3 % to 10 %) as eluents. After solvent removal, the obtained orange solid was dried under the reduced pressure of an oil pump for several minutes. This protocol gave 2.107 g of a mixture of compound **47** and the side product **99** in a 5.28 to 1 molar ratio (as determined by NMR). This corresponds to 1.9 g (4.85 mmol) of pure **47** and 43 % yield. Such a mixture of **47** and **99** was used for the following synthetic steps. Analytically pure **47** was procured as a slightly yellow solid by washing the mixture with DCM until **99** could not be detected (by NMR).



HRMS (ESI): m/z calcd. for C₈H₁₄IN₂ [M]⁺ 265.0196, found 265.0190.

IR (ATR) ν / cm⁻¹ 3394, 3095, 3049, 1678, 1584, 1534, 1448, 1407, 1292, 1255, 1165, 1135, 795.

Elemental analysis calcd. for C₈H₁₄I₂N₂: C, 24.51; H, 3.60; N, 7.15; I, 64.74. Found C, 24.35; H, 3.65; N, 7.16; I, 64.77.

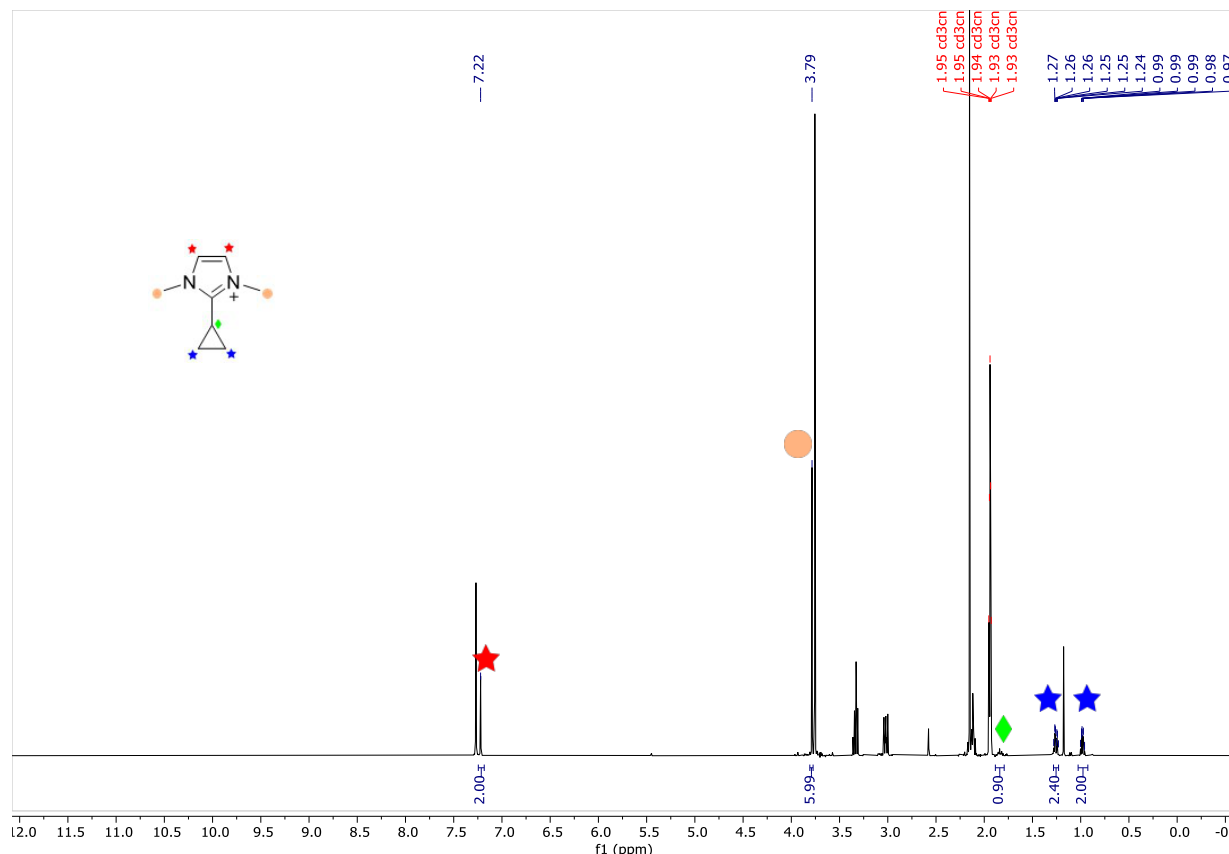


Figure 35 ¹H NMR spectrum of **47** and **99** mixture and signal assignments of the side product **99**. It is not a crude reaction NMR spectrum as the content **99** is increased to facilitate its characterization.

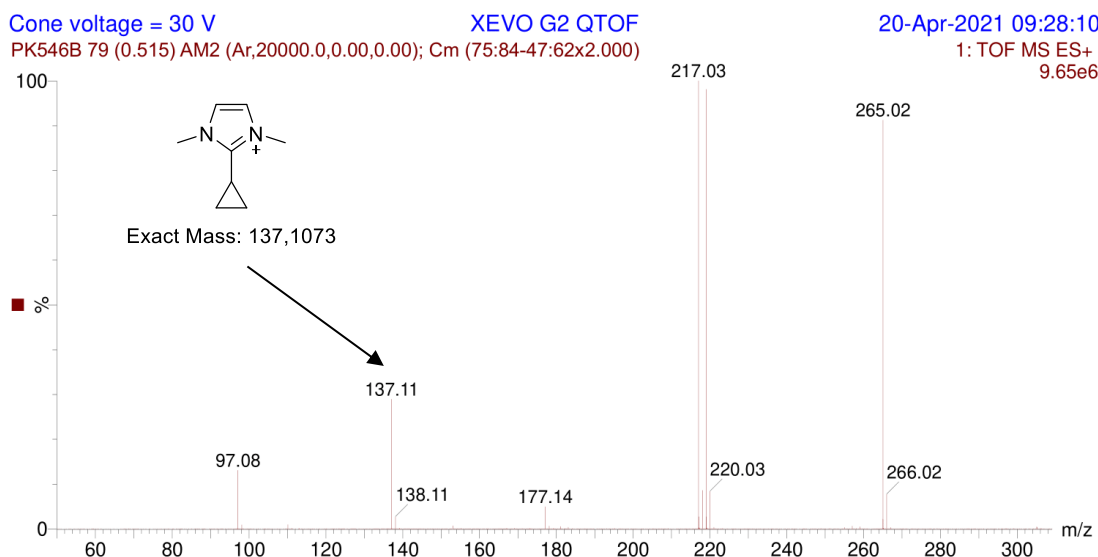
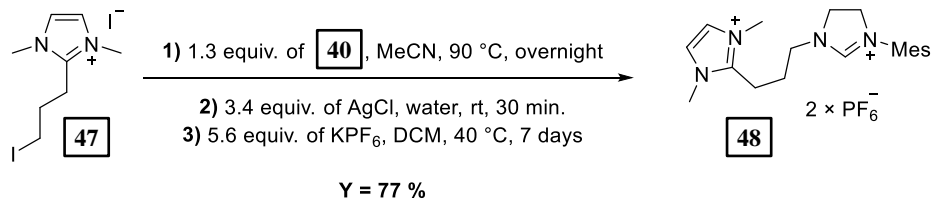


Figure 36 MS (ESI) mass spectrum of a crude reaction mixture (after the second reaction step and before reaction with NaI), m/z calcd. for **99**, $C_8H_{13}N_2 [M]^+$ 137.11, found 137.11.

- **Synthesis of the NHC-NHO precursor **48****

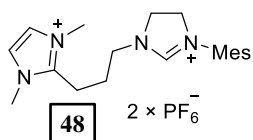


Scheme 63 Synthesis of the NHC-NHO precursor **48**.

1.241 g of the mixture of **47** and **99** (5.28 to 1 molar ratio), which corresponds to 1.1 g (2.81 mmol, 1 equiv.) of pure compound **47**, was placed in a 100 mL Schlenk flask along with *N*-mesitylimidazine (**40**) (707 mg, 3.76 mmol, 1.3 equiv.) were placed in a 100 mL Schlenk flask. Next, dry MeCN (20 mL) was added and the solution was stirred at 90 °C for overnight. The solvent was removed *in vacuo* and the obtained precipitate was washed with THF (20 mL and 4 × 10 mL).

The obtained crude product was dissolved in 30 mL of water and AgCl (1.35 g, 9.41 mmol, 3.4 equiv.) was added. Everything was stirred in light-excluding conditions for 30 min. and silver salts were removed by filtration through a pad of cellite, which was next washed with distilled water (200 mL).

To the water solution, KPF₆ (2.88 g, 15.6 mmol, 5.6 equiv.) was added and the water was removed *in vacuo*. Such obtained precipitate was transferred into a Soxhlet apparatus in which it was washed with refluxing DCM for 1 h. The obtained DCM solution was rejected and a new portion of the solvent was added. Next, the solid was washed in the Soxhlet apparatus with refluxing DCM for 7 days. After that time, DCM was evaporated in *vacuo* the product dried under the reduced pressure of an oil pump at 100 °C for 15 min. Compound **48** was obtained as a white precipitate in 77 % yield (1.335 g, 2.17 mmol). Crystals of **48** suitable for XRD experiments were grown by layering a MeCN compound solution with Et₂O.



¹H NMR (300 MHz, CD₃CN) δ 7.93 (s, 1H), 7.27 (s, 2H), 7.11 – 6.94 (m, 2H), 4.27 – 4.04 (m, 4H), 3.77 (s, 6H), 3.70 – 3.55 (m, 2H), 3.04 – 2.86 (m, 2H), 2.30 (s, 3H), 2.26 (s, 6H), 2.07 – 1.96 (m, 2H).

¹³C{¹H} NMR (75 MHz, CD₃CN) δ 159.3, 146.8, 141.4, 136.8, 131.7, 130.6, 123.7, 51.9, 49.9, 48.1, 36.0, 24.6, 21.0, 20.9, 17.7.

³¹P NMR (121 MHz, CD₃CN) δ -144.62 (hept, *J* = 706.7 Hz).

¹⁹F NMR (282 MHz, CD₃CN) δ -72.84 (d, *J* = 706.6 Hz).

HRMS (ESI): m/z calcd. for C₂₀H₃₀F₆N₄P [M+PF₆]⁺ 471.2112, found 471.2117; C₂₀H₃₀N₄ [M]²⁺ 163.1235, found 163.1232.

IR (ATR) ν / cm⁻¹ 1649, 1537, 1275, 1267, 1195, 823, 765, 750.

Elemental analysis calcd. for C₂₀H₃₀F₁₂N₄P₂: C, 38.97; H, 4.91; N, 9.09. Found C, 38.90; H, 4.15; N, 8.87.

5.2.2.4. Attempts to synthesize ruthenium OM catalyst

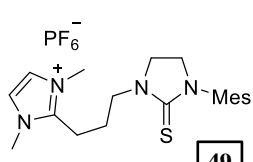
The following procedure refers to Scheme 43, Chapter 2.3.2.

The NHC-NHO ligand precursor **48** (10 mg, 19.7 μmol, 1 equiv.), K₂CO₃ (3.0 mg, 21.7 μmol, 1.1 equiv.) and **Ru-9** (11.9 mg, 19.7 μmol, 1 equiv.) were placed in a 1.5 mL vial equipped with a magnetic stir bar. The vial was transferred into a glovebox in where dry acetone (0.7 mL) was added. The vial was heated at 60 °C for 2 h. TLC and NMR analysis showed no ruthenium NHC complex was formed. Moreover, other reaction conditions were screened (solvents, bases, temperatures and reaction times) with the same outcome.

5.2.2.5. Synthesis of thiourea **49** and characterization of the side product **50**

The synthesis refers to Scheme 45B, Chapter 2.3.2.

Into a 1.5 mL vial the ligand precursor **48** (10 mg, 19.7 μmol, 1 equiv.) was placed along with K₂CO₃ (8.2 mg, 59.2 μmol, 3 equiv.) and sulfur (0.9 mg, 30 μmol, 1.5 equiv.). The vial was transferred into a glovebox in which 0.66 mL of dry acetone was added and the suspension was mixed at 60 °C for overnight. The suspension was filtered through a cellite pad, which was washed with acetone and the solvent was removed *in vacuo*. The product was purified with crystallization from a MeCN/Et₂O mixture. Compound **49** was obtained as slightly yellow oil in 88 % yield (8.7 mg, 17.3 μmol).



¹H NMR (400 MHz, CDCl₃) δ 7.30 (s, 2H), 6.94 – 6.88 (m, 2H), 4.06 – 3.84 (m, 8H), 3.84 – 3.68 (m, 4H), 3.18 – 3.09 (m, 2H), 2.26 (s, 3H), 2.15 (s, 6H), 2.14 – 2.05 (m, 2H).

¹³C{¹H} NMR (101 MHz, CDCl₃) δ 182.3, 146.8, 138.4, 136.6, 134.7, 129.5, 122.8, 47.6, 47.5, 46.7, 35.6, 24.0, 21.2, 20.8, 17.9.

³¹P NMR (162 MHz, CDCl₃) δ -144.54 (hept, *J* = 711.7 Hz).

¹⁹F NMR (376 MHz, CDCl₃) δ -72.59 (d, *J* = 712.3 Hz).

HRMS (ESI): m/z calcd. for C₂₀H₂₉N₄S [M]⁺ 357.2107, found 357.2107.

IR (ATR) ν / cm⁻¹ 1492, 1273, 839, 735.

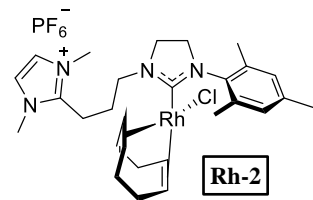
Utilizing solvents other than dry acetone (not dried acetone or dry MeCN) led to a significant formation of the imidazoline ring opened product **50**.

5.2.2.6. Synthesis of rhodium-NHC complexes

The syntheses refer to Scheme 46A, Chapter 2.3.3.

- **Synthesis of the rhodium NHC complex Rh-2**

The NHC-NHO ligand precursor **48** (61.4 mg, 99.6 μ mol, 1 equiv.), K₂CO₃ (15.4 mg, 0.110 mmol, 1.1 equiv.) and rhodium precursor **Rh-1** (23.8 mg, 49.8 μ mol, 0.5 equiv.) were placed in a 4 mL vial equipped with a magnetic stir bar and 3 mL of acetone (HPLC grade, non-dried) was added. Everything was stirred at 60 °C for overnight, after which the solvent was removed *in vacuo*. The product was isolated with CC using MeOH in DCM from 0 to 2 % as eluents. After solvent evaporation, the obtained solid was washed with Et₂O (3 \times 4 mL) and dried under the reduced pressure of an oil pump at 100 °C for 15 min. Complex **Rh-2** was obtained as a yellow solid in 73 % yield (51.9 mg, 72.4 μ mol). Crystals of **Rh-2** suitable for XRD experiments were grown by layering a MeCN complex solution with Et₂O.



¹H NMR (400 MHz, CD₃CN) δ 7.30 (s, 2H), 7.04 – 6.98 (m, 1H), 6.95 (dd, J = 1.4, 0.7 Hz, 1H), 5.09 – 4.80 (m, 1H), 4.62 – 4.49 (m, 1H), 4.49 – 4.36 (m, 1H), 3.86 (s, 6H), 3.83 – 3.70 (m, 3H), 3.68 – 3.55 (m, 2H), 3.49 (t, J = 7.0 Hz, 1H), 3.25 – 2.95 (m, 3H), 2.40 (s, 3H), 2.31 (s, 5H), 2.24 – 1.96 (m, 6H), 1.91 – 1.71 (m, 2H), 1.70 – 1.57 (m, 1H), 1.48 (dt, J = 8.9, 6.0 Hz, 2H).

¹³C{¹H} NMR (101 MHz, CD₃CN) δ 212.0 (d, J = 47.3 Hz), 147.9, 138.8, 138.6, 137.3, 136.5, 130.3, 129.5, 123.5, 98.1 (d, J = 7.0 Hz), 97.7 (d, J = 7.0 Hz), 69.3 (d, J = 13.6 Hz), 68.2 (d, J = 13.9 Hz), 52.5, 50.4, 48.7, 36.2, 34.9, 31.8, 29.8, 28.2, 25.5, 21.3, 21.1, 19.8, 18.2.

³¹P NMR (162 MHz, CD₃CN) δ -144.70 (hept, J = 705.4 Hz).

¹⁹F NMR (377 MHz, CD₃CN) δ -72.90 (d, J = 705.7 Hz).

HRMS (ESI): m/z calcd. for C₂₈H₄₁N₄¹⁰³RhPF₆ [M-Cl+PF₆]⁺ 681.2028, found 681.2043; C₂₉H₄₂N₄O₂¹⁰³RhPF₆ [M-Cl+CO₂H]⁺ 581.2363, found 581.2376; C₂₈H₄₁N₄¹⁰³RhCl [M]⁺ 571.2075, found 571.2089; C₂₈H₄₁N₄¹⁰³Rh [M-Cl]²⁺ 268.1193, found 268.1201.

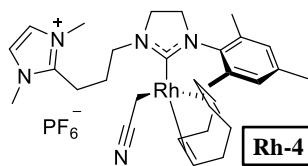
IR (ATR) ν / cm⁻¹ 1539, 1490, 1456, 1384, 1331, 1289, 1265, 1227, 1177, 837.

Elemental analysis calcd. for C₂₈H₄₁ClF₆N₄PRh: C, 46.91; H, 5.76; N, 7.81. Found C, 45.01; H, 5.40; N, 7.33.

- **Synthesis of the rhodium cyanomethyl complex Rh-4**

A 4 mL vial equipped with a magnetic stir bar was charged with the starting rhodium NHC complex **Rh-2** (100 mg, 0.139 mmol, 1 equiv.). The vial was transferred into a glovebox in which KO'Bu (17.2 mg, 0.153 mmol, 1.1 equiv.) was added, followed by dry MeCN (4 mL). Everything was stirred at ambient temperature for 4 h. Next, the obtained suspension was filtered through a syringe filter to a Schlenk flask and the solvents were removed *in vacuo*. The crude product was taken up with a minimal

amount of dry MeCN (2 mL) and dry Et₂O (18 mL) was added which resulted in complex precipitation. The precipitate was filtered off and washed with dry Et₂O (3 × 4 mL). The product **Rh-4** was obtained as a yellow solid in 66 % yield (66 mg, 91.5 µmol). Complex **Rh-4** decomposes in air and slowly degrades in solution, however, in solid form can be stored in a glovebox freezer for a few weeks without change in its composition. Crystals of **Rh-4** suitable for XRD experiments were grown by layering a MeCN complex solution with Et₂O.



¹H NMR (300 MHz, CD₃CN) δ 7.31 (s, 2H), 7.01 (s, 1H), 6.97 (s, 1H), 4.43 (dt, *J* = 13.3, 8.0 Hz, 1H), 4.33 – 4.13 (m, 2H), 4.05 – 3.90 (m, 2H), 3.85 (s, 6H), 3.82 – 3.64 (m, 4H), 3.46 – 3.35 (m, 1H), 3.10 (td, *J* = 7.7, 2.5 Hz, 2H), 2.32 (s, 3H), 2.29 – 2.18 (m, 4H), 2.17 – 2.02 (m, 7H), 1.91 – 1.71 (m, 3H), 1.65 – 1.37 (m, 2H), 0.67 (ddd, *J* = 62.2, 14.0, 3.3 Hz, 2H).

¹³C{¹H} NMR (101 MHz, CD₃CN) δ 219.0 (d, *J* = 5.0 Hz), 147.7, 138.6, 137.8, 137.7, 136.9, 132.5, 130.0, 129.7, 123.6, 91.3 (d, *J* = 8.4 Hz), 90.7 (d, *J* = 8.0 Hz), 78.4 (d, *J* = 9.8 Hz), 77.9 (d, *J* = 9.4 Hz), 53.1, 50.7, 49.1, 36.1, 33.5, 31.3, 30.7, 29.7, 25.9, 21.5, 21.0, 18.7, 18.3, -8.4 (d, *J* = 25.8 Hz).

³¹P NMR (121 MHz, CD₃CN) δ -144.62 (hept, *J* = 706.6 Hz).

¹⁹F NMR (282 MHz, CD₃CN) δ -72.92 (d, *J* = 706.1 Hz).

HRMS (ESI): m/z calcd. for C₃₀H₄₃N₅¹⁰³Rh [M]⁺ 576.2574, found 576.2587.

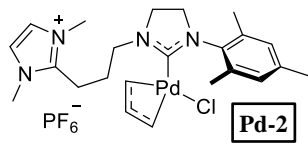
IR (ATR) ν / cm⁻¹ 2924, 2171, 1269, 837.

5.2.2.7. Synthesis of the NHC-NHO palladium complex Pd-3

The syntheses refer to Scheme 49, Chapter 2.3.4.

- **Synthesis of the palladium-NHC complex Pd-2**

The NHC-NHO ligand precursor **48** (300 mg, 0.487 mmol, 1 equiv.), K₂CO₃ (74.0 mg, 0.535 mmol, 1.1 equiv.) and palladium precursor **Pd-1** (89.0 mg, 0.243 mmol, 0.5 equiv.) were placed in a 25 mL round bottom flask and 15 mL of acetone (HPLC grade, non-dried) was added. Everything was stirred at 60 °C for overnight and the solvent was removed *in vacuo*. The product was isolated with CC using MeOH in DCM from 0 to 2 % as eluents. After solvent removal, the product was taken up with a minimal amount of DCM (0.5 mL) and precipitated with Et₂O. The formed precipitate was washed with Et₂O (3 × 4 mL) and dried under the reduced pressure of an oil pump at 100 °C for 15 min. The complex **Pd-2** was obtained as a white powder in 72 % yield (230.2 mg, 0.352 mmol).



¹H NMR (400 MHz, CD₃CN) δ 7.24 (s, 2H), 7.02 – 6.81 (brs, 2H), 5.39 – 4.63 (brs, 1H), 3.89 – 3.76 (m, 12H), 3.69 – 3.17 (brs, 1H), 3.17 – 2.90 (brs, 2H), 2.89 – 2.42 (brs, 1H), 2.39 – 2.16 (m, 9H), 2.13 – 2.00 (brs, 2H).

¹³C{¹H} NMR (101 MHz, CD₃CN) δ 210.2 – 209.1 (brs), 150.3 – 149.8 (brs), 148.3 – 147.3 (brs), 139.7 – 138.3 (brs), 138.1 – 136.8 (brs), 130.0, 123.4, 117.0 – 115.2 (brs), 72.9 – 71.5 (brs), 52.1, 49.9, 49.7, 36.0, 25.6, 21.3, 21.1, 18.8 – 18.4 (brs), 18.4 – 18.0 (brs).

³¹P NMR (162 MHz, CD₃CN) δ -144.62 (hept, *J* = 706.4 Hz).

¹⁹F NMR (376 MHz, CD₃CN) δ -72.91 (d, *J* = 706.2 Hz).

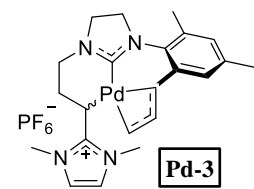
HRMS (ESI): m/z calcd. for $C_{23}H_{34}F_6N_4PPd$ [M-Cl+PF₆]⁺ 617.1469, found 617.1445; $C_{23}H_{34}ClN_4Pd$ [M]⁺ 509.1505, found 509.1489; $C_{23}H_{34}N_4Pd$ [M-Cl]²⁺ 236.0914, found 236.0917.

IR (ATR) ν / cm⁻¹ 1497, 1460, 1271, 837.

Elemental analysis calcd. for $C_{23}H_{34}ClF_6N_4PPd$: C, 42.28; H, 5.25; N, 8.58. Found C, 40.94; H, 4.58; N, 8.07.

• Synthesis of the palladium-NHC-NHO complex Pd-3

A 4 mL vial equipped with a magnetic stir bar was charged with the starting palladium NHC complex **Pd-2** (100 mg, 0.153 mmol, 1 equiv.). The vial was transferred into a glovebox in which KOC(CF₃)₂CH₃ (37.1 mg, 0.168 mmol, 1.1 equiv.) was added, followed by dry THF (4 mL). Everything was stirred at ambient temperature for overnight. Next, solvents were removed *in vacuo* (outside of the glovebox) and the product was isolated with CC using MeOH in DCM from 0 to 1 % as eluents. After solvent removal, the obtained precipitate was washed with Et₂O (3 × 4 mL) and dried under the reduced pressure of an oil pump at 100 °C for 15 min. The complex **Pd-3** was obtained as a white powder in 64 % yield (60.5 mg, 98.1 μmol). Diastereomers of **Pd-3** were formed in dr of 60:40. Crystals of **Pd-3** suitable for XRD experiments were grown by layering a DCM complex solution with heptane.



¹H NMR (400 MHz, CD₃CN) δ 6.94 (d, J = 0.7 Hz, 2H), 6.83 (s, 0.8H), 6.80 (s, 1.2H), 4.79 – 4.52 (m, 1H), 3.94 – 3.74 (m, 4H), 3.61 – 3.31 (m, 8H), 2.90 (dd, J = 9.4, 6.7 Hz, 0.6H), 2.77 (dd, J = 10.5, 6.2 Hz, 0.4H), 2.52 (dd, J = 7.5, 2.4 Hz, 0.6H), 2.47 – 2.39 (m, 0.8H), 2.27 – 2.01 (m, 11.6H), 1.86 (d, J = 14.3 Hz, 0.6H), 1.71 (d, J = 13.1 Hz, 0.4H), 1.51 (d, J = 14.1 Hz, 0.4H), 1.41 (d, J = 14.3 Hz, 0.6H).

¹³C{¹H} NMR (101 MHz, CD₃CN) δ 202.3, 200.8, 164.3, 163.5, 139.3, 139.2, 138.9, 138.9, 137.8, 137.6, 137.5, 137.4, 130.0, 129.9, 129.9, 129.9, 120.5 – 119.4 (brs), 118.9, 118.7, 60.0, 58.9, 53.2, 53.0, 52.5, 52.3, 52.2, 51.9, 51.9, 51.7, 37.5 – 33.9 (brs), 28.0, 27.4, 21.0, 18.4, 18.3, 18.1, 16.4, 16.1.

³¹P NMR (162 MHz, CD₃CN) δ -144.61 (hept, J = 706.7 Hz).

¹⁹F NMR (376 MHz, CD₃CN) δ -72.89 (d, J = 706.6 Hz).

HRMS (ESI): m/z calcd. for $C_{23}H_{33}N_4Pd$ [M]⁺ 471.1749, found 471.1750.

IR (ATR) ν / cm⁻¹ 1510, 1271, 838.

Elemental analysis calcd. for $C_{23}H_{33}F_6N_4PPd$: C, 44.78; H, 5.39; N, 9.08. Found C, 44.76; H, 4.92; N, 8.91.

5.3. Supporting information for Chapter 3

5.3.1. General considerations

Commercially available substrates were used as received unless stated otherwise. Compounds **Ru-9**, **85**, **86**, **90**, **100** and **101** were commercially available. Diphenyliodonium tetrafluoroborate (Ph_2IBF_4)^[243], **Rh-1**^[241] and substrates for olefin metathesis **78a**,^[244] **79a**,^[244] **80a**,^[130] **81a**,^[130] **82a**,^[245] **84a**,^[130] **88**,^[246] **92**^[247] were synthesized according to literature procedures. Olefin metathesis substrates were purified by column chromatography or distillation or crystallization and properly degassed under a dynamic

vacuum. Additionally, substrates were stored over activated neutral Al₂O₃ (except substrate **86**). All OM reactions were quenched using commercially available compound **100**.^[248]

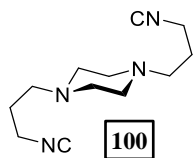
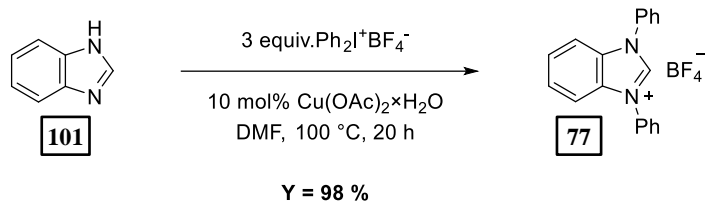


Figure 37 Compound used to quench OM reaction.

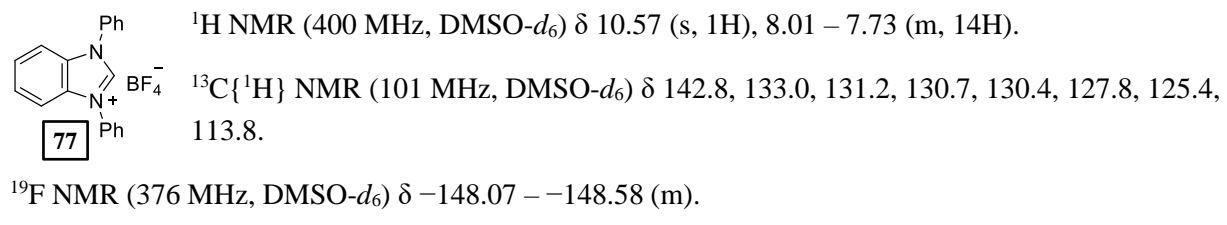
5.3.2. Synthesis of benzimidazolium precursors

5.3.2.1. Synthesis of benzimidazolium salt **77**



Scheme 64 Synthesis of benzimidazolium salt **77**.

Into a 25 mL round bottom flask benzimidazole (**101**) (500 mg, 4.23 mmol, 1 equiv.) was placed along with Ph₂IBF₄ (4.67 g, 12.70 mmol, 3 equiv.), Cu(OAc)₂·H₂O (84.5 mg, 0.423 mmol, 10 mol%) and 17 mL of DMF. The content of the vial was stirred at 100 °C for 20 h. TLC analysis showed complete conversion of the substrate. The solvents were removed *in vacuo* and the crude reaction mixture was taken up with DCM and put on a short silica gel bed. The silica was eluted with DCM and then gradually changing eluent to 1 % MeOH in DCM. After solvent removal *in vacuo*, the product was dried under the reduced pressure of an oil pump at 100 °C for 15 min. The product was obtained as a slightly pinkish light powder in 98 % yield (1.49 g, 4.16 mmol). NMR spectral data match reported previously in the literature.^[249]



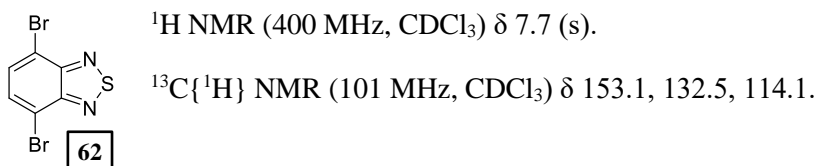
5.3.2.2. Synthesis of the phenyl derived benzimidazolium salt **67**

The syntheses refer to Scheme 53, Chapter 3.2.

- **Synthesis of 4,7-dibromobenzo[c][1,2,5]thiadiazole (62)**

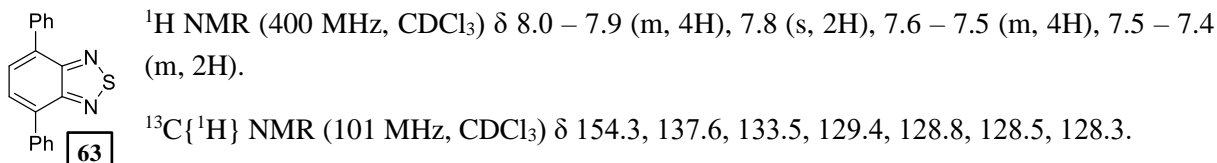
The procedure is based on the previously reported in the literature.^[250] 2,1,3-benzothiadiazole (1 g, 7.34 mmol, 1 equiv.) was put in a 100 mL flask with a dropping funnel, and 15 mL of 48% aqueous HBr solution was added. Then, into the dropping funnel, 10 mL of 48% aqueous HBr solution was added, followed by bromine (1.1 mL, 3.5 g, 22 mmol, 3 equiv.). The bromine solution was slowly added (about one drop per second) into the solution of 2,1,3-benzothiadiazole in HBr_{aq}. After the addition, the dropping funnel was changed to a condenser and the reaction mixture was refluxed overnight (heating set up at 160 °C). After that, the reaction was quenched with a saturated solution of Na₂SO₃ (40 mL). The

aqueous phase was extracted with DCM ($4 \times 50\text{mL}$) and organic phases were collected, dried over MgSO₄ and evaporated to obtain brownish crystals. The product was isolated as a yellow-brownish solid in 98 % yield (2.115 g, 7.19 mmol). NMR spectral data match reported previously in the literature.^[250]



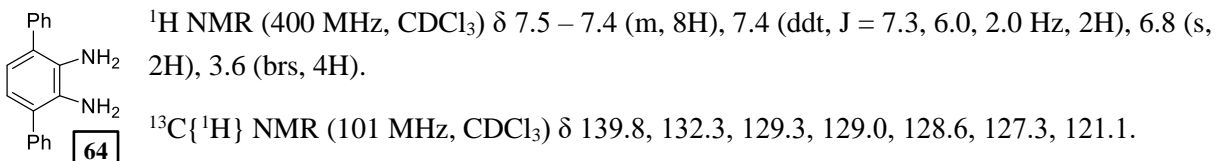
- **Synthesis of 4,7-diphenylbenzo[c][1,2,5]thiadiazole (63)**

The procedure is based on the previously reported in the literature.^[251] A mixture of 4,7-dibromo-benzo[c][1,2,5]thiadiazole (**62**) (10.00 g, 34.0 mmol, 1 equiv.), phenylboronic acid (8.71 g, 71.4 mmol, 2.1 equiv.), potassium carbonate (18.81 g, 136 mmol, 4 equiv.), Pd(PPh₃)₄ (315 mg, 0.272 mmol, 0.8 mol%) was placed in a 250 mL two necked round bottom flask. In a separate 250 mL flask distilled water (68 mL) and toluene (170 mL) were placed and the solvents were degassed by placing the flask in an ultrasound bath and bubbling argon through the solvent mixture for 15 min. The degassed solvents were then transferred to the flask with substrates and a reflux condenser was placed. The flask was heated at 90 °C, at reflux conditions, for 5 h. Next, 170 mL of distilled water was added to the flask and the layers were separated. The aqueous phase was washed with DCM ($3 \times 100\text{ mL}$). The combined organic fractions were dried with anhydrous Na₂SO₄. After the solvent evaporation, the crude product was crystallized by dissolving it in 1.2 L of boiling ethanol and subsequent cooling. The solid was filtered off and washed with EtOH and pentane. The product was obtained as a yellow solid (4.851 g). Two subsequent crystallizations of the supernatant after the first crystallization afforded another 2.296 g of a pure product. Total yield 73 % (7.15 g, 24.8 mmol). NMR spectral data match reported previously in the literature.^[251]



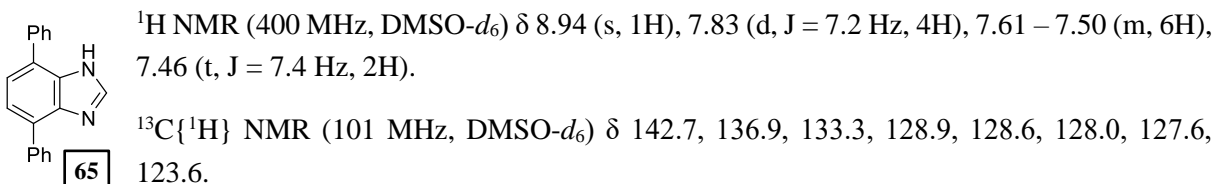
- **Synthesis of 3,6-diphenylbenzene-1,2-diamine (64)**

The procedure is based on the previously reported in the literature.^[252] In a 100 mL round bottom flask 4,7-diphenylbenzo[c][1,2,5]thiadiazole (**63**) (400 mg, 1.39 mmol, 1 equiv.) was dissolved in 12 mL of THF and 38 mL of EtOH was added. To the flask NaBH₄ (472.3 mg, 12.5 mmol, 9 equiv.) was added in portions, followed by CoCl₂×6H₂O (19.8 mg, 83.2 μmol, 6 mol %). The black solid of Co₂B was formed instantly and, in a few minutes, H₂S evolution was noted. The mixture was refluxed for 2 h and cooled to room temperature. The suspension was filtered through a sintered funnel and solvents were evaporated *in vacuo*. Water (50 mL) was added and the organic product was extracted with Et₂O ($3 \times 50\text{ mL}$). The combined organic extracts were dried over Na₂SO₄ and the solvent was removed *in vacuo*. The product was obtained as a slightly pinkish crystalline solid in 99 % yield (356 mg, 1.37 mmol). The product could be stored in an argon atmosphere, at low temperatures (freezer) without notable change in its composition. NMR spectral data match reported previously in the literature.^[252]



- **Synthesis of 4,7-diphenyl-1H-benzo[d]imidazole (65)**

Starting 3,6-diphenylbenzene-1,2-diamine (**64**) (1.00 g, 3.84 mmol, 1 equiv.) was mixed with 26 mL of triethyl orthoformate (excess) and 1.9 mL of HClaq (ca 37 %, 23.1 mmol, 6 equiv.) was added. Everything was stirred in reflux conditions (heating bath temperature – 115 °C) under a slow flow of argon for overnight. After solvent removal *in vacuo*, the crude products were taken up with 25 mL of DCM and washed with 25 mL of Na₂CO₃aq. After separation, the water phase was washed with DCM (3 × 25 mL). The combined organic extracts were dried over anhydrous MgSO₄ and the suspension was filtered. After solvent removal, the obtained precipitate was dried under the reduced pressure of an oil pump at 100 °C for 1 h. The product was obtained as a slightly yellow powder in a quantitative yield (1.05 g, 3.84 mmol).

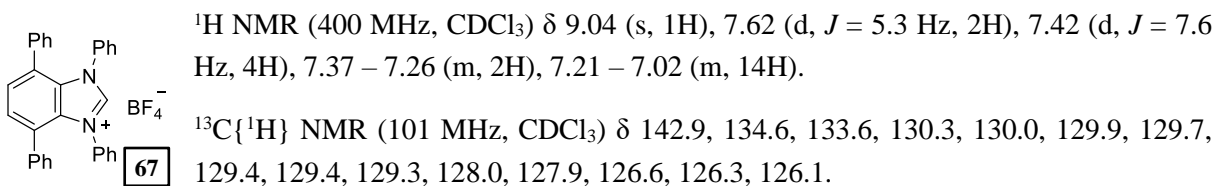


HRMS (ESI): m/z calcd. for C₁₉H₁₅N₂ [M+H]⁺ 271.1230, found 271.1227.

IR (ATR) v / cm⁻¹ 3026, 2953, 2911, 2830, 2745, 2652, 2563, 1621, 1486, 1449, 1355, 1273, 1222, 1028, 900, 830, 750, 692, 618, 593.

- **Synthesis of benzimidazolium salt 67**

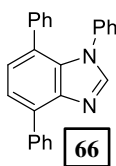
Into a 100 mL round bottom flask 4,7-diphenyl-1H-benzo[d]imidazole (**65**) (1.78 g, 6.57 mmol, 1 equiv.) was placed along with Ph₂IBF₄ (4.83 g, 13.13 mmol, 2 equiv.), Cu(OAc)₂×H₂O (65.6 mg, 0.328 mmol, 5 mol%) and 26 mL of DMF. The content of the vial was stirred at 100 °C for 24 h. After that time another portion of Ph₂IBF₄ (4.83 g, 13.13 mmol, 2 equiv.) and Cu(OAc)₂×H₂O (65.6 mg, 0.328 mmol, 5 mol%) was added and everything was stirred at 100 °C for additional 48 h. The solvents were removed *in vacuo* and a crude reaction mixture was dried under the reduced pressure of an oil pump at 100 °C for 1 h. Products **66** and **67** were separated with column chromatography (eluents from 0 to 2 % MeOH in DCM). Product **67** was isolated in 36 % yield (1.22 g, 2.39 mmol) and **66** was isolated in 58 % yield (1.32 g, 3.81 mmol).



HRMS (ESI): m/z calcd. for C₃₁H₂₃N₂ [M]⁺ 423.1856, found 423.1856.

IR (ATR) v / cm⁻¹ 3165, 3061, 1559, 1482, 1449, 1369, 1325, 1254, 1186, 1058, 1022, 914, 748, 688.

Elemental analysis calcd. for C₃₁H₂₃BF₄N₂: C, 72.96; H, 4.54; N, 5.49. Found C, 72.72; H, 4.32; N, 5.52.



¹H NMR (400 MHz, CDCl₃) δ 8.08 (s, 1H), 8.05 (dt, *J* = 8.1, 1.7 Hz, 2H), 7.61 – 7.52 (m, 3H), 7.45 – 7.39 (m, 1H), 7.35 (d, *J* = 7.7 Hz, 1H), 7.21 – 7.14 (m, 1H), 7.14 – 6.95 (m, 9H).

¹³C{¹H} NMR (101 MHz, CDCl₃) δ 144.6, 142.4, 138.5, 137.8, 136.8, 132.6, 131.9, 129.5, 129.2, 128.7, 128.6, 127.7, 127.6, 127.5, 126.7, 126.6, 126.0, 125.9, 122.3.

HRMS (ESI): m/z calcd. for C₂₅H₁₉N₂ [M]⁺ 347.1543, found 347.1544.

IR (ATR) ν / cm⁻¹ 3116, 3058, 1598, 1499, 1479, 1441, 1393, 1288, 1249, 1210, 1074, 1025, 906, 823, 754, 691.

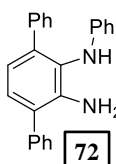
- **Arylation of *N*-phenylbenzimidazole 66 to procure benzimidazolium salt 67**

Into a 20 mL vial, *N*-phenylbenzimidazole **66** (947 mg, 2.73 mmol, 1 equiv.) was placed along with Ph₂IBF₄ (2.01 g, 5.47 mmol, 2 equiv.), Cu(OAc)₂×H₂O (36 mg, 0.18 mmol, 7.5 mol%) and 11 mL of DMF. The content of the vial was stirred at 100 °C for 24 h. The solvents were removed *in vacuo* and a crude reaction mixture was dried under the reduced pressure of an oil pump at 100 °C for 1 h. Benzimidazolium salt **67** was isolated with column chromatography (eluents from 0 to 2 % MeOH in DCM). The product was obtained as an off-white solid in 77 % yield (1.08 g, 2.12 mmol).

5.3.2.3. Synthesis of *N*-phenylbenzimidazole 66 using Buchwald-Hartwig amination

The synthesis refers to Scheme 54A, Chapter 3.2.

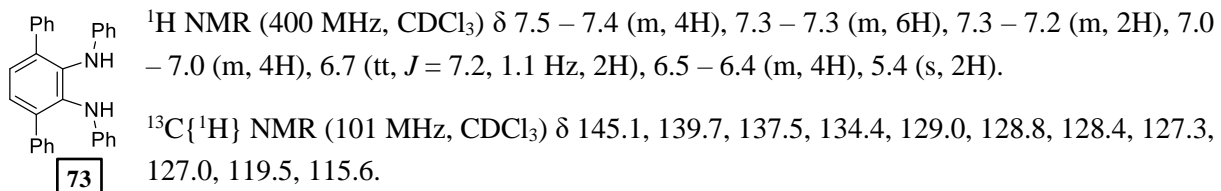
In a glovebox, into a pressure-resistant Schlenk flask 3,6-diphenylbenzene-1,2-diamine (**64**) (1.266 g, 4.86 mmol, 1 equiv.) was placed along with Pd₂(dba)₃ (222.7 mg, 0.243 mmol, 5 mol%) and P'Bu₃ (147.6 mg, 0.729 mmol, 15 mol%). Bromobenzene (25 mL, dried over molecular sieves and degassed with the freeze-pump-thaw method) was also added to the flask. Everything was briefly mixed and KO'Bu (1.09 g, 9.73 mmol, 2 equiv.) was added. The flask was closed, taken out of the glovebox and the content of it was stirred at 160 °C for 3 days. Excess of bromobenzene and all other volatiles were evaporated under the reduced pressure of an oil pump. To the crude reaction mixture, 50 mL of DCM was added, followed by 50 mL of saturated NH₄Cl_{aq}. After the phases were separated, the water phase was washed with DCM (1 × 50 mL and 2 × 25 mL). Combined organic extracts were dried with MgSO₄, filtered and reduced *in vacuo*. The products were separated using column chromatography (eluents from 0 to 5 % EtOAc in hexane). Solvent evaporation gave **72** in the form of yellow powder. It was used as such for the following step. It was possible to isolate traces of **73** using preparative TLC. Utilizing higher loading of palladium catalyst did not yield a satisfactory amount of **73**, as determined by TLC.



¹H NMR (400 MHz, CDCl₃) δ 7.6 – 7.6 (m, 2H), 7.5 – 7.4 (m, 2H), 7.4 – 7.3 (m, 6H), 7.3 – 7.2 (m, 2H), 7.1 (d, *J* = 7.8 Hz, 1H), 6.9 – 6.8 (m, 2H), 6.7 (dd, *J* = 8.6, 1.0 Hz, 2H), 5.2 (s, 1H), 4.1 (s, 2H).

¹³C{¹H} NMR (101 MHz, CDCl₃) δ 145.9, 141.1, 139.7, 139.5, 138.7, 129.5, 129.3, 129.1, 129.0, 128.5, 127.6, 127.6, 127.5, 127.4, 124.7, 119.7, 119.3, 114.8.

HRMS (ESI): m/z calcd. for C₂₄H₂₁N₂ [M+H]⁺ 337.1699, found 337.1699.



HRMS (ESI): m/z calcd. for C₃₀H₂₅N₂ [M+H]⁺ 413.2016, found 413.2012.

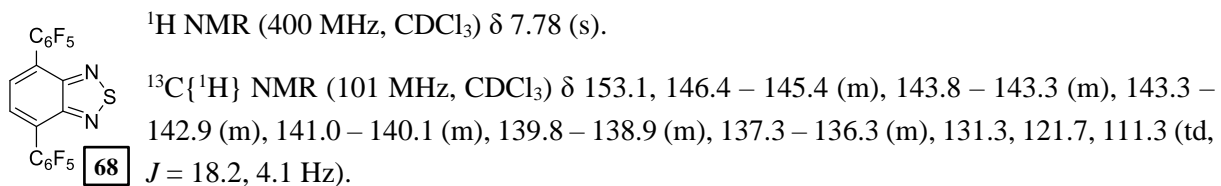
The product of Buchwald-Hartwig amination was mixed with 32 mL of triethyl orthoformate and 1.6 mL of HCl_{aq} (ca 37 %) was added. Everything was stirred in reflux conditions (heating bath temperature – 115 °C) under a slow flow of argon for overnight. After solvent removal *in vacuo*, the crude products were taken up with 50 mL of DCM. 50 mL of saturated Na₂CO₃_{aq} was added and everything was shaken for a while. After phase separation, the water fraction was washed with DCM (3 × 25 mL). The combined organic extracts were dried over anhydrous MgSO₄ and the suspension was filtered. The product was isolated using column chromatography (eluents from 5 to 100 % EtOAc in hexane). The product **66** was isolated as a light-orange solid in 53 % yield (885 mg, 2.55 mmol).

5.3.2.4. Synthesis of the pentafluorophenyl derived benzimidazolium salt **71**

The syntheses refer to Scheme 53, Chapter 3.2.

- **Synthesis of 4,7-bis(pentafluorophenyl)benzo[c][1,2,5]thiadiazole (68)**

Into a two-necked 150 mL round bottom flask magnesium turnings (1.30 g, 53.6 mmol, 3.15 equiv.) were placed. The turnings were dried under the reduced pressure of an oil pump (temperature of a heat gun) for several minutes. After exchanging the atmosphere to argon, dry THF (95.5 mL) was added, followed by a crystal of iodine. The flask was put in a water bath at 40 °C and bromopentafluorobenzene (6.5 mL, 12.60 g, 51.0 mmol, 3 equiv.) was added in portions. The reaction mixture was stirred at 40 °C for 1 h upon which it turned slightly brown. Into a separate Schlenk flask dibromobenzothiadiazole (**62**) (5.00 g, 17.0 mmol, 1 equiv.) was placed along with Pd(PPh₃)₄ (1.97 g, 1.70 mmol, 10 mol%) and dry THF (34 mL). The Grignard reagent solution was filtered through a cannula with a paper filter directly into the Schlenk flask containing a deep red solution of the substrate and Pd catalyst. Everything was stirred at 70 °C for overnight. After that the reaction was quenched with NH₄Cl_{aq} (100 mL of saturated solution) and 100 mL of Et₂O was added. The phases were separated and the water phase was washed with Et₂O (100 mL, then 50 × 3 mL). The combined organic extracts were dried with anhydrous MgSO₄, filtered and evaporated *in vacuo*. The crude reaction mixture was separated using column chromatography (eluents EtOAc in hexane from 0 % to 2 %). After solvent removal, the precipitate was washed with pentane (5 × 5 mL). The product was dried under the reduced pressure of an oil pump at 100 °C for 1 h. The product was obtained as a white precipitate in 76 % yield (6.02 g, 12.9 mmol).



¹⁹F NMR (376 MHz, CDCl₃) δ –138.28 – –139.48 (m, 4F), –152.52 (tt, *J* = 21.0, 1.8 Hz, 2F), –160.75 – –161.51 (m, 4F).

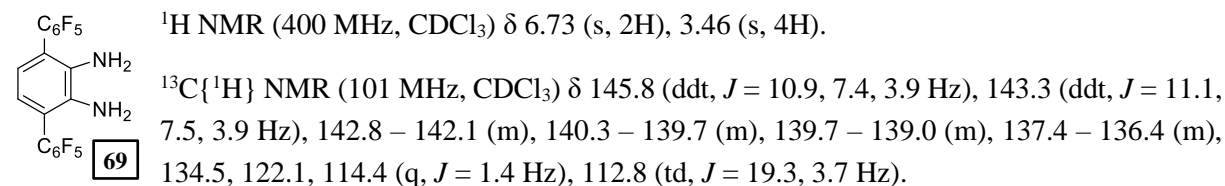
HRMS (ESI): m/z calcd. for C₁₈H₂F₁₀N₂S [M]⁻ 467.9780, found 467.9774.

IR (ATR) ν / cm⁻¹ 1656, 1527, 1490, 1344, 1104, 983, 861, 819.

Elemental analysis calcd. for C₁₈H₂F₁₀N₂S: C, 46.17; H, 0.43. Found C, 47.11; H, 0.60.

• **Synthesis of 3,6-bis(pentafluorophenyl)benzene-1,2-diamine (69)**

Into a 150 mL round bottom flask 4,7-bis(pentafluorophenyl)benzo[c][1,2,5]thiadiazole (**68**) (4.40 g, 9.40 mmol, 1 equiv.) was placed, followed by EtOH (47 mL) and THF (15.5 mL). Next, CoCl₂·6H₂O (156.4 mg, 0.657 mmol, 7 mol%) and NaBH₄ (1.07 mg, 28.2 mmol, 3 equiv.) were added as solid. Immediately formation of a black precipitate was observed. The solution was stirred at 50 °C up to 5 min. The reaction progression was monitored by TLC (15 % EtOAc in hexane) every 30 seconds. It was imperative to stop heating the reaction as soon as the whole substrate was converted, as otherwise unidentified byproducts were formed, which resulted in a substantial decrease in yield. The suspension was filtered on a sintered funnel and the black precipitate was washed with THF. Solvents were evaporated *in vacuo* and brine (100 mL) was added followed by Et₂O (100 mL). The phases were separated and the water fraction was washed with Et₂O (3 × 100 mL). The combined organic extracts were dried with anhydrous MgSO₄ and the drying agent was filtered off. After solvent removal *in vacuo*, the product was isolated using column chromatography (eluents from 5 % to 10 % EtOAc in hexane). The product was obtained as a white solid in 72 % yield (2.96 g, 6.73 mmol).



¹⁹F NMR (376 MHz, CDCl₃) δ –138.39 – –139.38 (m, 4F), –153.88 (ddd, *J* = 20.9, 19.4, 1.3 Hz, 2F), –160.15 – –161.69 (m, 4F).

HRMS (ESI): m/z calcd. for C₁₈H₇F₁₀N₂ [M+H]⁺ 441.0444, found 441.0441.

IR (ATR) ν / cm⁻¹ 3442, 1616, 1525, 1489, 1447, 1426, 1233, 1181, 1069, 975, 816.

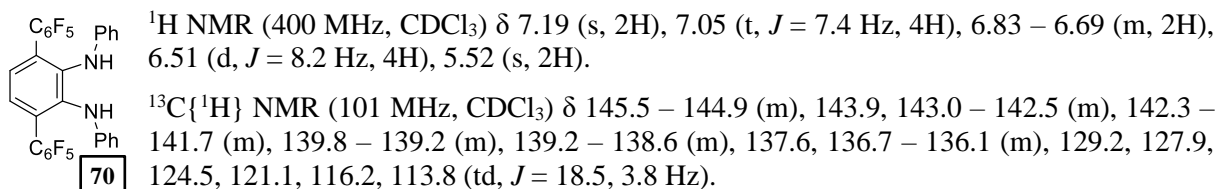
Elemental analysis calcd. for C₁₈H₆F₁₀N₂: C, 49.11; H, 1.37; N, 6.36; F, 43.15. Found C, 49.31; H, 1.35; N, 6.30; F, 43.10.

• **Synthesis of *N*-phenyl-derived aniline 70**

Inside a glovebox, in a 20 mL vial Pd₂dba₃ (294.1 mg, 0.321 mmol, 1 equiv.) was mixed with 16 mL of dry toluene. To the vial, P'Bu₃ (194.9 mg, 0.963 mmol, 3 equiv.) was added and everything was mixed until complete complex dissolution (about 15 min.). Such obtained catalyst stock solution can be kept in a glovebox freezer for several weeks and used in the synthesis of **70** without a decrease in catalytic activity.

Inside a glovebox, in a 4 mL vial equipped with a magnetic stir bar, starting aniline **69** (200 mg, 0.454 mmol, 1 equiv.) was dissolved in bromobenzene (1.70 mL, excess, dried over molecular sieves and degassed with the freeze-pump-thaw method). Pd(dba)P'Bu₃ catalyst stock solution in toluene (0.57 mL of 0.04 M, 0.023 mmol, 5 mol%) was added. Everything was briefly mixed and KHMDS (143.1 mg, 95

% purity, 0.681 mmol, 1.5 equiv.) was added. The vial was closed, taken out of the glovebox and the content of it was stirred at 160 °C for 30 min. To the vial, NaCl_{aq} (2 mL of saturated solution) was added with Et₂O. The phases were separated and the water fraction was washed with Et₂O (3 × 2 mL). Combined organic extracts were dried with MgSO₄ and solvents were removed *in vacuo*. The crude product was dried under the reduced pressure of an oil pump at room temperature for several minutes. The product was isolated using column chromatography on silica gel (eluent 1 % EtOAc in hex). After solvent removal, the product was dried under the reduced pressure of an oil pump at 100 °C for 15 min. The product was obtained as a grey-black powder in 21 % yield (56.5 mg). Product **70** was used without further purification for subsequent synthetic steps. Analytically pure **70** was obtained by washing with a minimal amount of pentane (3 × 1.5 mL) as slightly grey powder.



¹⁹F NMR (376 MHz, CDCl₃) δ –139.41 – –141.31 (m, 4F), –154.62 (t, *J* = 21.0 Hz, 4F), –162.08 (td, *J* = 22.4, 7.4 Hz, 4F).

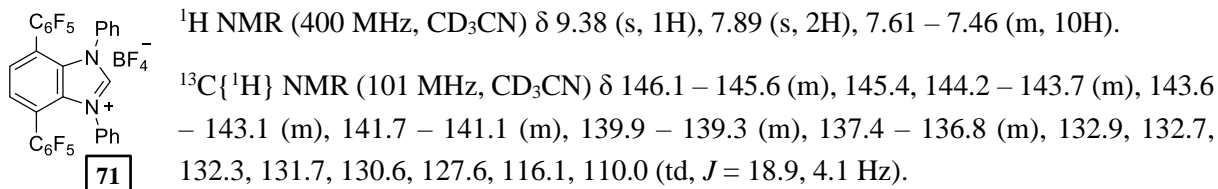
HRMS (ESI): m/z calcd. for C₃₀H₁₅F₁₀N₂ [M+H]⁺ 593.1070, found 593.1070.

IR (ATR) ν / cm^{–1} 3329, 1598, 1526, 1492, 1448, 1380, 1287, 1240, 1078, 982, 831, 749, 696.

Elemental analysis calcd. for C₃₀H₁₄F₁₀N₂: C, 60.82; H, 2.38; N, 4.73. Found C, 60.69; H, 2.38; N, 4.73.

• Synthesis of benzimidazolium salt **71**

Into a 4 mL vial starting aniline **70** (196 mg, 0.33 mmol, 1 equiv.) was placed. Next, 3 mL of HC(OEt)₃ (excess) was added, followed by HBF₄·Et₂O complex (46 µL, 0.33 mmol, 1 equiv.). The vial was closed and the content of it was stirred at 60 °C for 30 min. A red-brown suspension has formed upon heating. After cooling to ambient temperature, the content of the vial was transferred with MeCN into a 25 mL round bottom flask and the solvents were removed *in vacuo*. The product was dried under the reduced pressure of an oil pump (ambient temperature, several minutes). The residue was washed with pentane (6 × 4 mL) and dried under the reduced pressure of an oil pump (100 °C, 1 h) to give a pink solid in a quantitative yield (229 mg, 0.33 mmol). Salt **71** was used without further purification for the formation of NHC complexes. Analytically pure **71** was obtained as a white powder by washing with a minimal amount of DCM (3 × 1.5 mL) and subsequent crystallization from MeCN / Et₂O solution.



¹⁹F NMR (376 MHz, CD₃CN) δ –138.68 – –139.29 (m, 4F), –151.68 – –151.92 (m, 4F), –153.92 (tt, *J* = 20.5, 2.2 Hz, 2F), –162.87 – –164.21 (m, 4F).

HRMS (ESI): m/z calcd. for C₃₁H₁₃F₁₀N₂ [M]⁺ 603.0914, found 603.0912.

IR (ATR) ν / cm^{–1} 3071, 1563, 1494, 1459, 1081, 1061, 984, 845.

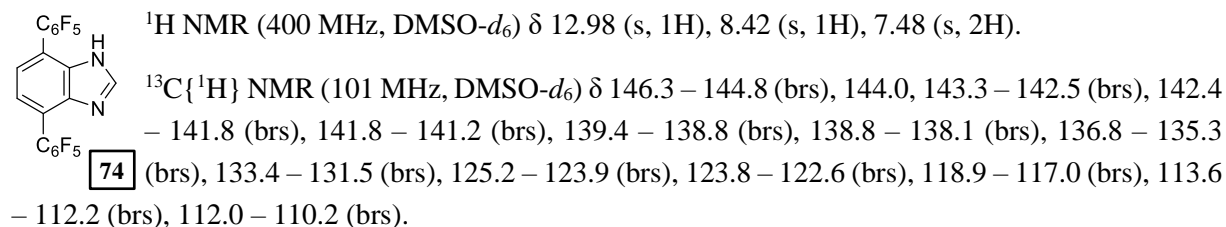
Elemental analysis calcd. for C₃₁H₁₃BF₁₄N₂: C, 53.94; H, 1.90; N, 4.06. Found C, 53.82; H, 1.72; N, 4.04.

5.3.2.5. Resolved synthetic obstacles during the synthesis of 71

The syntheses refer to Scheme 54B, Chapter 3.2.

- **Synthesis of 4,7-bis(perfluorophenyl)-1H-benzo[d]imidazole (74)**

Starting 3,6-bis(pentafluorophenyl)benzene-1,2-diamine (**69**) (206 mg, 0.468 mmol, 1 equiv.) was mixed with 3.1 mL of triethyl orthoformate and 0.25 mL of HCl_{aq} (ca 37 %, 2.81 mmol, 6 equiv.) was added. Everything was stirred in reflux conditions (heating bath temperature – 115 °C) under a slow flow of argon for 1 h. After solvent removal *in vacuo*, the crude product was dried under the reduced pressure of an oil pump at 100 °C for 1 h. The product was obtained as a white powder in an 87 % yield (183 mg, 0.406 mmol).



¹⁹F NMR (376 MHz, DMSO-*d*₆) δ –139.86 (dd, *J* = 24.3, 6.5 Hz, 4F), –153.90 – –157.44 (m, 2F), –159.89 – –166.40 (m, 4F).

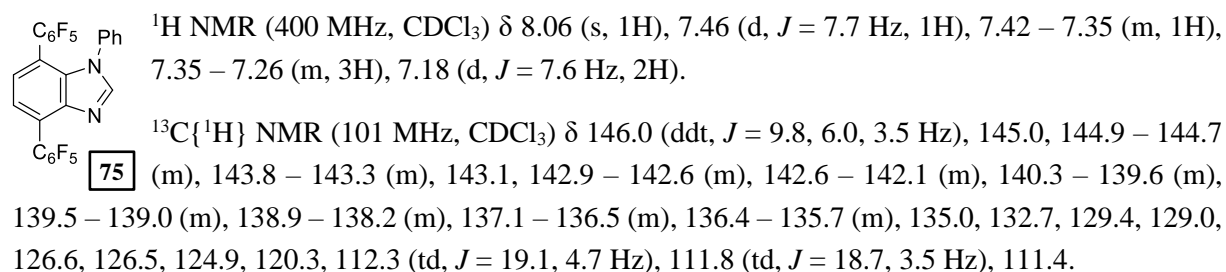
HRMS (ESI): m/z calcd. for C₁₉H₅F₁₀N₂ [M+H]⁺ 451.0288, found 451.0286.

IR (ATR) ν / cm^{–1} 3009, 2817, 1657, 1538, 1496, 1376, 1356, 1328, 1289, 1157, 1092, 977, 937, 837, 821, 781, 633, 524.

Elemental analysis calcd. for C₁₉H₄F₁₀N₂: C, 50.69; H, 0.90; N, 6.22; F, 42.20. Found C, 50.48; H, 0.85; N, 6.15; F, 42.26.

- **Synthesis of 4,7-bis(perfluorophenyl)-1-phenyl-1H-benzo[d]imidazole (75)**

Into a 10 mL tube for microwave reactor benzimidazole **74** (107 mg, 0.238 mmol, 1 equiv.) was placed along with Ph₂IBF₄ (349.8 mg, 0.951 mmol, 4 equiv.), Cu(OAc)₂×H₂O (9.5 mg, 0.048 mmol, 20 mol%) and DMF (0.95 mL). The content of the vial was stirred at 100 °C for 20 h in a microwave reactor. After that solvents were removed *in vacuo* and the crude reaction mixture was dried under the reduced pressure of an oil pump at 100 °C for 15 min. The product was isolated using column chromatography (eluent: 75 % DCM in hexane). The product was obtained as a white solid in 24 % yield (30 mg, 0.057 mmol).



¹⁹F NMR (376 MHz, CDCl₃) δ -138.44 (dd, *J* = 23.3, 8.0 Hz, 2F), -139.20 – -139.68 (m, 2F), -153.99 (t, *J* = 20.8 Hz, 1F), -154.44 (t, *J* = 20.9 Hz, 1F), -161.88 (td, *J* = 22.6, 22.2, 7.5 Hz, 2F), -162.52 (td, *J* = 22.4, 7.7 Hz, 2F).

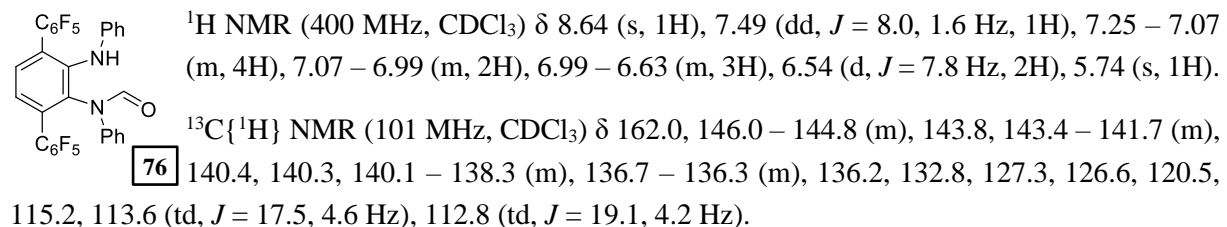
HRMS (ESI): m/z calcd. for C₂₅H₉F₁₀N₂ [M+H]⁺ 527.0601, found 527.0602.

IR (ATR) ν / cm⁻¹ 1537, 1490, 1255, 1230, 1088, 992, 977, 832, 827.

Elemental analysis calcd. for C₂₅H₈F₁₀N₂: C, 57.05; H, 1.53; N, 5.32. Found C, 56.76; H, 1.53; N, 5.26.

• Synthesis of *N*-formylated compound 76

Aniline **69** (436mg, 0.74 mmol, 1 equiv.) was placed in a 25 mL round bottom flask equipped with a magnetic stirrer and 4.9 mL of HC(OEt)₃ (excess) was added followed by 0.4 mL of HCl_{aq} 37%. The content of the vial was heated at 115 °C, at reflux conditions, under a slow flow of argon for overnight. After that, the solvents were removed *in vacuo* and the crude product was dried under the reduced pressure of an oil pump (ambient temperature, several minutes). The product was isolated using column chromatography (eluents from 0 to 10 % EtOAc in hexane). The product was obtained as an off-white solid in 32 % yield (146 mg, 0.24 mmol). Analytically pure **76** was obtained by crystallization from DCM solution using vapor-liquid diffusion of pentane vapors.



¹⁹F NMR (376 MHz, CDCl₃) δ -138.52 (ddt, *J* = 23.4, 8.0, 3.1 Hz, 1F), -139.22 (dd, *J* = 22.7, 8.1 Hz, 1F), -140.72 (dd, *J* = 23.0, 8.3 Hz, 1F), -142.74 (dd, *J* = 23.6, 5.8 Hz, 1F), -153.49 (t, *J* = 20.9 Hz, 1F), -154.35 (t, *J* = 21.0 Hz, 1F), -161.87 (tt, *J* = 22.1, 8.0 Hz, 2F), -162.09 – -162.31 (m, 2F).

HRMS (ESI): m/z calcd. for C₃₁H₁₅F₁₀N₂O [M+H]⁺ 621.1019, found 621.1018.

IR (ATR) ν / cm⁻¹ 3325, 2928, 2855, 1681, 1595, 1526, 1493, 1429, 1273, 1079, 982, 750.

Elemental analysis calcd. for C₃₁H₁₄F₁₀N₂O: C, 60.01; H, 2.27; N, 4.52. Found C, 59.84; H, 2.27; N, 4.55.

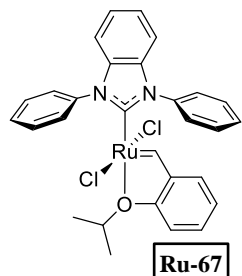
5.3.3. Synthesis of ruthenium catalysts

The syntheses refer to Scheme 55A, Chapter 3.3.

5.3.3.1. Synthesis of Ru-67

The procedure is based on the previously reported in the literature.^[130] In a Schlenk flask benzimidazolium salt **77** (50 mg, 1.40 mmol, 2 equiv.) was placed and dry toluene (28 mL) was added. The Schlenk was transferred into a glovebox and to the suspension, KO(CF₃)₂CH₃ (156.7 mg, 1.40 mmol, 2 equiv.) was added. Upon the addition of the base, the suspension turned a canary color. Everything was stirred at rt for 30 min. Next, Hoveyda-Grubbs 1st generation catalyst (**Ru-9**) (419.3 mg, 0.698 mmol, 1 equiv.) was added and everything was stirred at 60 °C for 1 h. The solution was cooled down to ambient temperature and directly put on a silica gel column packed with dry toluene (SPS grade solvents for column chromatography had to be used). The silica bed was washed with dry toluene, gradually changing to dry

DCM. First, a red-violet band of unreacted **Ru-9** was collected and upon changing eluent to pure DCM a brown band containing the product was washed out. The solvents were removed *in vacuo* and the crude product was taken up with a minimal amount of dry DCM (2 mL) and 6 mL of dry Et₂O was added. After several seconds the product started to crash out and the vial was left in a freezer for overnight to crystallize all of the product. After that, the supernatant was decanted and the crystals were washed with dry Et₂O (3 × 2 mL). In the end, the product was dried under the reduced pressure of an oil pump at 100 °C for 10 min. The product was obtained as green-black crystals in a 19 % yield (80.1 mg, 0.136 mmol). NMR spectral data match reported previously in the literature.^[130]

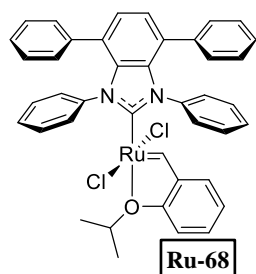


¹H NMR (400 MHz, CD₂Cl₂) δ 16.64 (s, 1H), 8.59 – 8.12 (brs, 2H), 8.11 – 7.82 (brs, 2H), 7.81 – 7.61 (brs, 6H), 7.61 – 7.56 (m, 1H), 7.56 – 7.07 (brs, 4H), 7.06 – 6.87 (m, 3H), 5.11 (hept, *J* = 6.0 Hz, 1H), 1.60 (d, *J* = 6.2 Hz, 6H).

¹³C{¹H} NMR (101 MHz, CD₂Cl₂) δ 293.2, 192.1, 153.6, 143.8, 130.5, 130.4, 123.0, 122.2, 113.6, 109.7, 75.7, 22.3.

5.3.3.2. Synthesis of Ru-68

A Schlenk flask was charged with the starting benzimidazolium salt **67** (200 mg, 0.392 mmol, 1.75 equiv.) and dry benzene (8 mL). The flask was transferred to the glovebox where KOC(CF₃)₂CH₃ (86.3 mg, 0.392 mmol, 1.75 equiv.) was added and the suspension was stirred at ambient temperature for 30 min. After that Hoveyda-Grubbs 1st generation catalyst (**Ru-9**) (134.5 mg, 0.224 mmol, 1 equiv.) was added and the content of the Schlenk flask was stirred at 60 °C for 1 h. After that time, the solvent was removed *in vacuo*, and the crude precipitate was washed with dry hexane (4 × 5 mL). The obtained precipitate was taken up with DCM and the solution was put on a small bed of silica packed with DCM. The silica bed was washed with DCM and the solvent was removed *in vacuo*. The product was further purified by crystallization from THF / pentane mixture and subsequently washed with pentane (9 × 2 mL). Drying under a reduced pressure of an oil pump (100 °C for 15 min.) gave the analytically pure product in a 72 % yield (120 mg, 0.161 mmol).



¹H NMR (400 MHz, CD₂Cl₂) δ 16.20 (s, 1H), 7.94 – 7.70 (m, 2H), 7.54 (ddd, *J* = 8.4, 7.3, 1.7 Hz, 1H), 7.44 (d, *J* = 1.1 Hz, 2H), 7.38 – 7.32 (m, 1H), 7.26 – 6.97 (m, 17H), 6.93 – 6.86 (m, 2H), 6.79 (dd, *J* = 7.6, 1.6 Hz, 1H), 4.97 (hept, *J* = 6.2 Hz, 1H), 1.41 (d, *J* = 6.1 Hz, 6H).

¹³C{¹H} NMR (101 MHz, CD₂Cl₂) δ 296.5, 192.4, 153.2, 144.1, 139.9, 139.5, 137.7, 137.6, 135.1, 133.1, 130.4, 130.3, 130.1, 129.9, 129.6, 129.2, 129.1, 128.9, 127.9, 127.7, 127.0, 126.9, 126.0, 125.8, 125.6, 122.9, 122.2, 113.5, 75.5, 22.2.

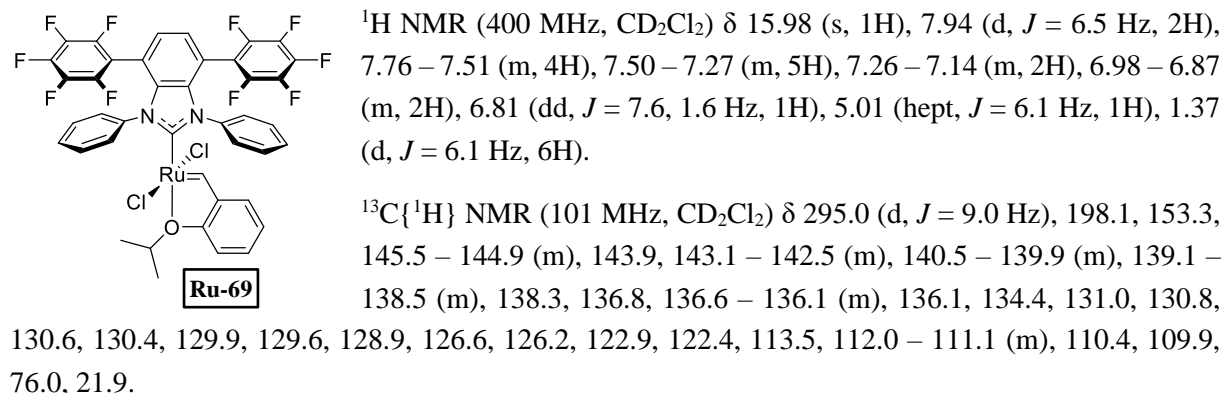
HRMS (ESI): m/z calcd. for C₄₁H₃₄Cl₂N₂ORu [M]⁺ 742.1086, found 742.1082.

IR (ATR) ν / cm⁻¹ 3054, 2961, 2925, 2849, 1588, 1495, 1476, 1452, 1373, 1316, 1294, 1278, 1242, 1213, 1116, 1097, 1026, 940, 754, 699, 692.

Elemental analysis calcd. for C₄₁H₃₄Cl₂N₂ORu: C, 66.30; H, 4.61; N, 3.77. Found C, 66.29; H, 4.65; N, 3.77.

5.3.3.3. Synthesis of Ru-69

A 20 mL vial with a screw cap was charged with 150 mg of benzimidazolium salt **71** (0.217 mmol, 1.75 equiv.) which was then transferred into a glovebox. To the vial dried and degassed benzene (4.4 mL) was added followed by $\text{KOC}(\text{CF}_3)_2\text{CH}_3$ (54.7 mg, 0.248 mmol, 2 equiv.). The suspension was stirred for 15 min. and Hoveyda-Grubbs 1st generation catalyst (**Ru-9**) (74.6 mg, 0.124 mmol, 1 equiv.) was added. The vial was removed from the glovebox and heated for 30 min. at 60 °C. After cooling the reaction mixture to ambient temperature, it was directly put on a silica gel column (packed with hexane). The product was isolated using column chromatography (eluents EtOAc in hexanes from 10 to 20 %). The product was further purified by crystallization from THF / pentane mixture and subsequently washed with pentane (6 × 2 mL). Drying under a reduced pressure of an oil pump (100 °C for 15 min.) afforded the analytically pure product as a brow-orange precipitate in 43 % yield (49.2 mg, 0.053 mmol).



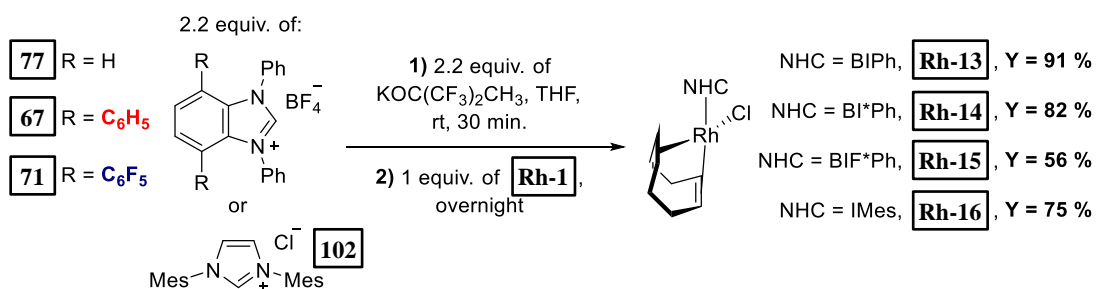
HRMS (ESI): m/z calcd. for $\text{C}_{41}\text{H}_{24}\text{Cl}_2\text{F}_{10}\text{N}_2\text{ORu}$ [M]⁺ 922.0144, found 922.0143.

IR (ATR) ν / cm^{–1} 3071, 1563, 1494, 1459, 1081, 1061, 984, 845.

Elemental analysis calcd. for $\text{C}_{41}\text{H}_{24}\text{Cl}_2\text{F}_{10}\text{N}_2\text{ORu}$: C, 53.38; H, 2.62; N, 3.04. Found C, 53.56; H, 2.43; N, 3.10.

5.3.4. Synthesis of rhodium complexes

5.3.4.1. Synthesis of rhodium-NHC-COD complexes

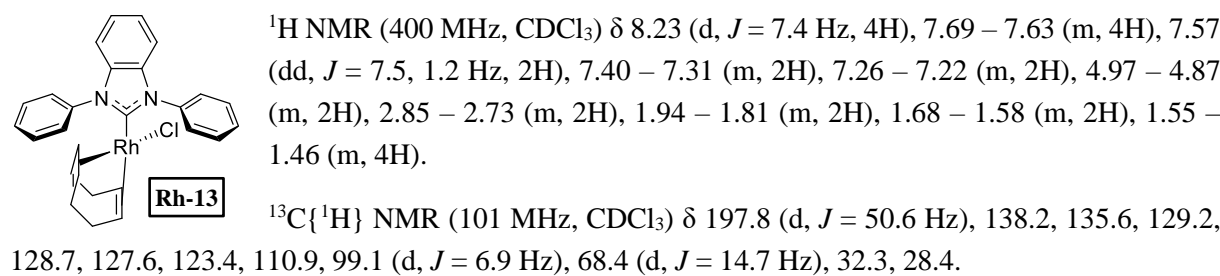


Scheme 65 Synthesis of rhodium-NHC-COD complexes.

- **Synthesis of complex Rh-13**

The following procedure for the synthesis of **Rh-13** is representative of all the other rhodium-NHC-COD complexes.

A 4 mL vial with a screw cap was charged with starting benzimidazolium salt **77** (50 mg, 0.140 mmol, 2.2 equiv.) which was then transferred into a glovebox. To the vial dried and degassed THF (2.8 mL) was added followed by $\text{KOC}(\text{CF}_3)_2\text{CH}_3$ (30.7 mg, 0.140 mmol, 2.2 equiv.). The suspension was stirred for 30 min. and **Rh-1** (31.3 mg, 0.063 mmol, 1 equiv.) was added. The content of the vial was stirred at rt for overnight. Next, the solvents were removed *in vacuo*. The product was isolated using column chromatography (eluents EtOAc in hexanes 10 %). After solvent removal, the crude product was purified by washing with dry pentane (3×2 mL). Drying under a reduced pressure of an oil pump (100°C for 1 h) gave analytically pure product as a yellow precipitate in 91 % yield (59.8 mg, 0.116 mmol).



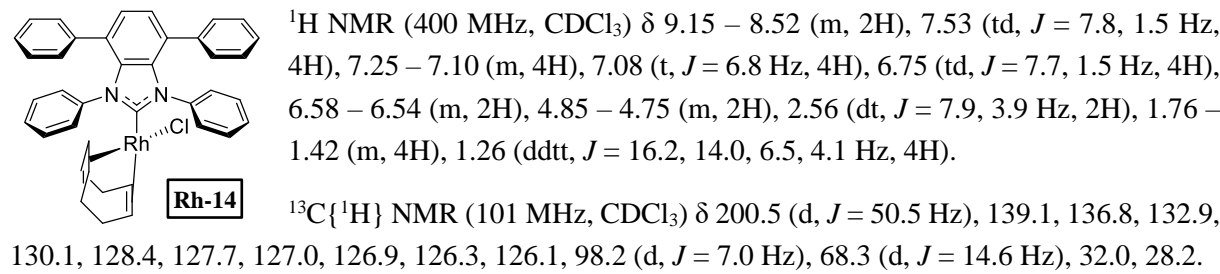
HRMS (ESI): m/z calcd. for $\text{C}_{27}\text{H}_{26}\text{N}_2^{103}\text{Rh} [\text{M}-\text{Cl}]^+$ 481.1151, found 481.1144; $\text{C}_{27}\text{H}_{26}\text{ClN}_2^{103}\text{Rh} [\text{M}]^+$ 516.0834, found 516.0832.

IR (ATR) ν / cm^{-1} 3053, 2982, 2965, 2938, 2907, 2873, 2827, 1592, 1497, 1470, 1376, 1337, 1304, 1283, 1216, 1157, 758, 748, 692.

Elemental analysis calcd. for $\text{C}_{27}\text{H}_{26}\text{ClN}_2\text{Rh}$: C, 62.74; H, 5.07; N, 5.42. Found C, 62.55; H, 5.06; N, 5.47.

- **Synthesis of complex Rh-14**

Obtained according to the procedure for the synthesis of **Rh-13**, from 50 mg of salt **67** (0.098 mmol). Yield – 82 % (48.8 mg, 0.073 mmol); yellow solid.



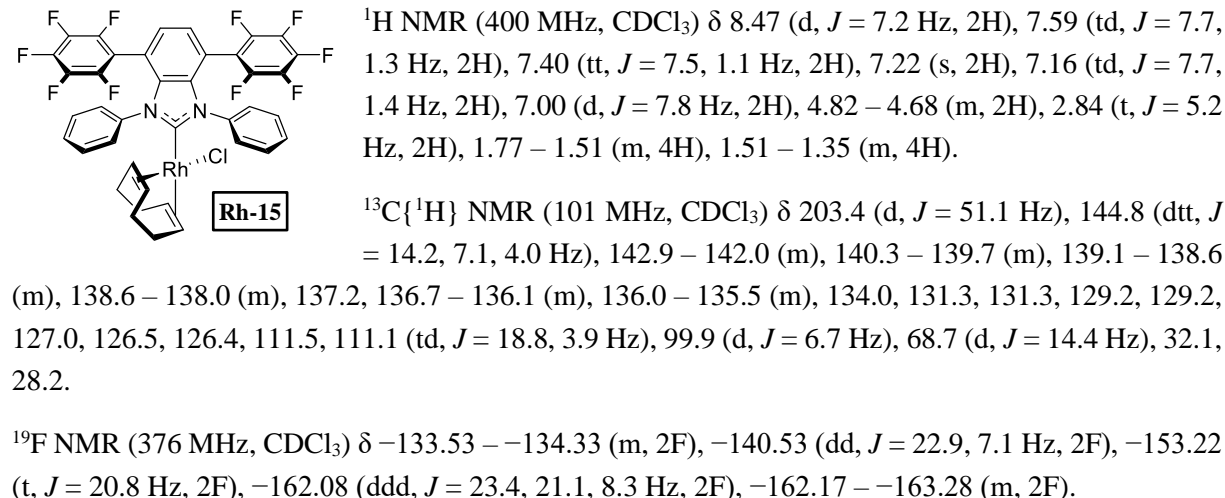
HRMS (ESI): m/z calcd. for $\text{C}_{39}\text{H}_{34}\text{N}_2^{103}\text{Rh} [\text{M}-\text{Cl}]^+$ 633.1777, found 633.1767; $\text{C}_{27}\text{H}_{26}\text{ClN}_2^{103}\text{Rh} [\text{M}]^+$ 668.1460, found 668.1450.

IR (ATR) ν / cm^{-1} 3063, 2991, 2912, 2877, 2828, 2071, 1985, 1595, 1495, 1480, 1376, 1329, 1305, 1287, 1246, 1026, 753, 691.

Elemental analysis calcd. for C₂₇H₂₆ClN₂Rh: C, 70.01; H, 5.12; N, 4.19. Found C, 69.89; H, 5.14; N, 4.30.

• Synthesis of complex Rh-15

Obtained according to the procedure for the synthesis of **Rh-13**, from 50 mg of salt **71** (0.072 mmol) and 2.5 equiv. of KO(CF₃)CH₃ (18.1 mg, 0.082 mmol); the carbene was generated for only 15 min. Yield – 56 % (31.4 mg, 0.037 mmol); yellow solid.



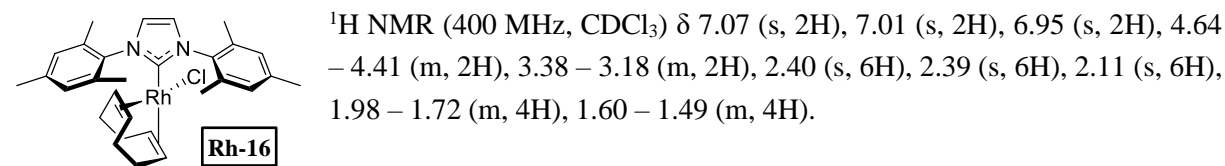
HRMS (ESI): m/z calcd. for C₃₉H₂₄F₁₀N₂¹⁰³Rh [M-Cl]⁺ 813.0835, found 813.0830; C₃₉H₂₄ClF₁₀N₂¹⁰³Rh [M]⁺ 848.0518, found 848.0508.

IR (ATR) ν / cm⁻¹ 2878, 2832, 1534, 1496, 1456, 1423, 1386, 1322, 1308, 1288, 1093, 985, 847.

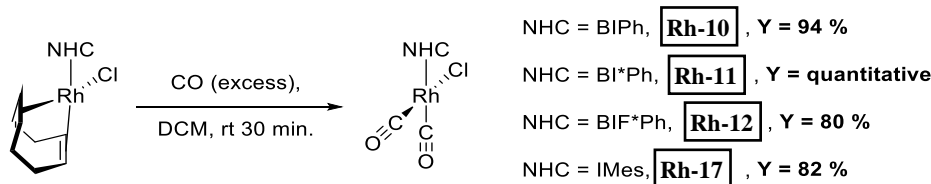
Elemental analysis calcd. for C₃₉H₂₄ClF₁₀N₂Rh: C, 55.18; H, 2.85; N, 3.30. Found C, 55.10; H, 2.86; N, 3.34.

• Synthesis of complex Rh-16

Obtained according to the procedure for the synthesis of **Rh-13**, from 50 mg of dimesitylimidazolium chloride (**102**) (0.147 mmol) using KO'Bu as the base (16.5 mg, 0.147 mmol). Yield – 75 % (54.7 mg, 0.099 mmol); yellow solid. NMR spectral data match reported previously in the literature.^[221]



5.3.4.2. Synthesis of rhodium-NHC-carbonyl complexes

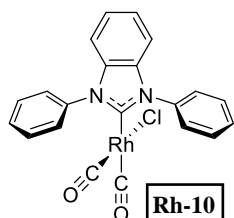


Scheme 66 Synthesis of rhodium-NHC-carbonyl complexes.

- **Synthesis of complex Rh-10**

The following procedure for the synthesis of **Rh-10** is representative of all the other rhodium-NHC-carbonyl complexes.

A 4 mL vial was charged with the starting **Rh-13** complex (45.4 mg, 0.088 mmol) and 2 mL of DCM was added. Through the solution CO gas, freshly prepared from H₂SO₄ and HCOOH, was bubbled for 30 min. The solvent was removed *in vacuo* and the obtained precipitate was washed with pentane (3 × 2 mL). The product was dried under the reduced pressure of an oil pump (100 °C for 1 h). The product was obtained in a 94 % yield (38.4 mg, 0.083 mmol).



¹H NMR (400 MHz, CDCl₃) δ 7.85 – 7.81 (m, 4H), 7.67 – 7.57 (m, 6H), 7.41 – 7.34 (m, 4H).

¹³C{¹H} NMR (101 MHz, CDCl₃) δ 186.6 (d, *J* = 43.4 Hz), 185.4 (d, *J* = 54.7 Hz), 182.4 (d, *J* = 74.7 Hz), 135.4, 129.8, 129.7, 127.8, 124.6, 111.8.

HRMS (ESI): m/z calcd. for C₂₂H₁₇N₃O¹⁰³Rh [M-Cl-CO+CH₃CN]⁺ 442.0421,

found 442.0421.

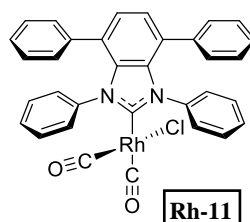
IR (ATR) ν / cm⁻¹ 2089 (v_{CO}), 1994 (v_{CO}), 1960, 1588, 1493, 1470, 1389, 1349, 757, 697.

IR (CH₂Cl₂) ν / cm⁻¹ 2082 (v_{CO}), 2004 (v_{CO}), 1499, 1396, 693.

Elemental analysis calcd. for C₂₁H₁₄ClN₂O₂Rh: C, 54.28; H, 3.04; N, 6.03. Found C, 54.28; H, 3.04; N, 6.02.

- **Synthesis of complex Rh-11**

Obtained according to the procedure for the synthesis of **Rh-10**, from 32.8 mg of complex **Rh-14** (0.049 mmol). Yield – quantitative (30.5 mg, 0.049 mmol); yellow solid.



¹H NMR (400 MHz, CDCl₃) δ 7.77 (d, *J* = 7.9 Hz, 2H), 7.33 (d, *J* = 0.6 Hz, 2H), 7.28 – 7.23 (m, 2H), 7.21 – 7.17 (m, 2H), 7.16 – 6.86 (m, 14H).

¹³C{¹H} NMR (101 MHz, CDCl₃) δ 189.6 (d, *J* = 43.5 Hz), 185.6 (d, *J* = 54.9 Hz), 182.3 (d, *J* = 75.2 Hz), 138.2, 136.3, 132.7, 130.1, 129.3, 128.8, 128.7, 128.1, 127.7, 127.6, 127.3, 127.2, 127.1.

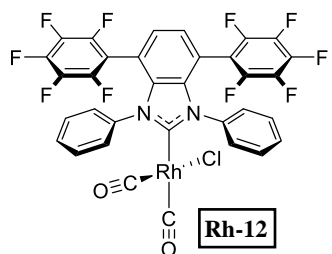
HRMS (ESI): m/z calcd. for C₃₄H₂₅N₃O¹⁰³Rh [M-Cl-CO+CH₃CN]⁺ 594.1047, found 594.1049.

IR (ATR) ν / cm⁻¹ 2078 (v_{CO}), 1986 (v_{CO}), 1496, 1395, 1352, 754, 695.

IR (CH₂Cl₂) ν / cm⁻¹ 2080 (v_{CO}), 2000 (v_{CO}), 1496, 1396, 1352, 692.

- **Synthesis of complex Rh-12**

Obtained according to the procedure for the synthesis of **Rh-10**, from 17.5 mg of complex **Rh-15** (0.021 mmol). Yield – 80 % (13.2 mg, 0.017 mmol); yellow solid.



¹H NMR (400 MHz, CDCl₃) δ 7.68 (brs, 2H), 7.47 – 7.26 (m, 10H).
¹³C{¹H} NMR (101 MHz, CDCl₃) δ 192.4 (d, *J* = 44.0 Hz), 185.0 (d, *J* = 55.0 Hz), 182.2 (d, *J* = 74.1 Hz), 145.2 – 144.5 (m), 143.1 – 142.5 (m), 142.5 – 142.1 (m), 140.6 – 139.8 (m), 138.9 – 138.2 (m), 136.4, 136.3 – 135.7 (m), 133.7, 130.2, 130.1, 129.2, 128.5, 127.8, 127.0, 113.0, 110.3 (td, *J* = 18.8, 3.9 Hz).

¹⁹F NMR (376 MHz, CDCl₃) δ -135.94 – -136.50 (m, 2F), -137.83 – -138.50 (m, 2F), -152.42 (t, *J* = 20.9 Hz, 2F), -161.51 (td, *J* = 22.3, 7.8 Hz, 2F), -161.88 (td, *J* = 22.6, 7.9 Hz, 2F).

HRMS (ESI): m/z calcd. for C₃₆H₁₈F₁₀N₄O¹⁰³Rh [M-Cl-CO+2×CH₃CN]⁺ 815.0371, found 815.0370; C₃₄H₁₅F₁₀N₃O¹⁰³Rh [M-Cl-CO+CH₃CN]⁺ 774.1050, found 774.1050.

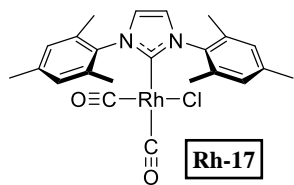
IR (ATR) ν / cm⁻¹ 3060, 2086 (v_{CO}), 1997 (v_{CO}), 1493, 1400, 1351, 1094, 984, 849, 697.

IR (CH₂Cl₂) ν / cm⁻¹ 2085 (v_{CO}), 2005 (v_{CO}), 1501, 991.

Elemental analysis calcd. for C₃₃H₁₂ClF₁₀N₂O₂Rh: C, 49.74; H, 1.52; N, 3.52. Found C, 49.76; H, 1.53; N, 3.61.

• Synthesis of complex Rh-17

Obtained according to the procedure for the synthesis of **Rh-10**, from 54.7 mg of complex **Rh-16** (0.099 mmol). Yield – 92 % (45.4 mg, 0.091 mmol); yellow solid. NMR and IR spectral data match reported previously in the literature.^[221]



¹H NMR (400 MHz, CDCl₃) δ 7.11 (s, 2H), 7.01 (s, 4H), 2.37 (s, 6H), 2.21 (s, 12H).

¹³C{¹H} NMR (101 MHz, CDCl₃) δ 185.0 (d, *J* = 54.0 Hz), 182.9 (d, *J* = 74.5 Hz), 177.7 (d, *J* = 45.0 Hz), 139.5, 135.4, 135.2, 129.4, 123.9, 21.3, 18.6.

IR (ATR) ν / cm⁻¹ 2920, 2067 (v_{CO}), 1985 (v_{CO}), 1487, 1404, 1379, 1331, 1229, 929, 856, 710, 592.

IR (CH₂Cl₂) ν / cm⁻¹ 2079 (v_{CO}), 1996 (v_{CO}).

5.3.5. Synthesis of selenoureas

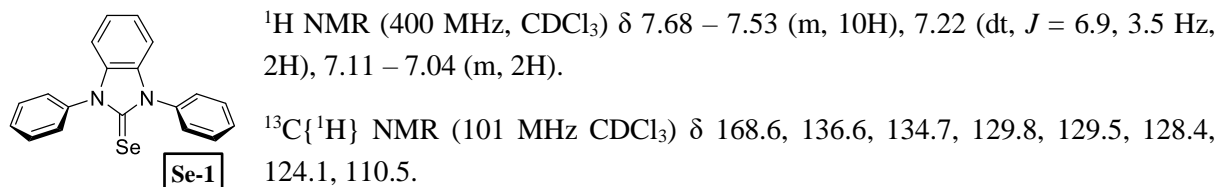
The syntheses refer to Scheme 56, Chapter 3.4.

5.3.5.1. Synthesis of compound Se-1

The following procedure for the synthesis of **Se-1** is representative of all the other selenoureas.

A 4 mL vial with a screw cap was charged with starting benzimidazolium salt **77** (50 mg, 0.140 mmol, 1 equiv.) which was then transferred into a glovebox. To the vial dried and degassed THF (2.8 mL) was added followed by KOC(CF₃)₂CH₃ (30.7 mg, 0.140 mmol, 1 equiv.). The suspension was stirred for 30 min. and Se (22.1 mg, 0.279 mmol, 2 equiv.) was added. The content of the vial was stirred at rt for overnight. Next, the suspension was filtered through a pad of cellite which was then washed with DCM (2 mL). Solvents were removed *in vacuo* and the product was further purified by washing with dry

pentane (3×2 mL). Drying under a reduced pressure of an oil pump (100 °C for 1 h) gave the analytically pure product in 88 % yield (43.1 mg, 0.123 mmol) in the form of white precipitate.



⁷⁷Se NMR (76 MHz, CDCl₃) δ 127.2.

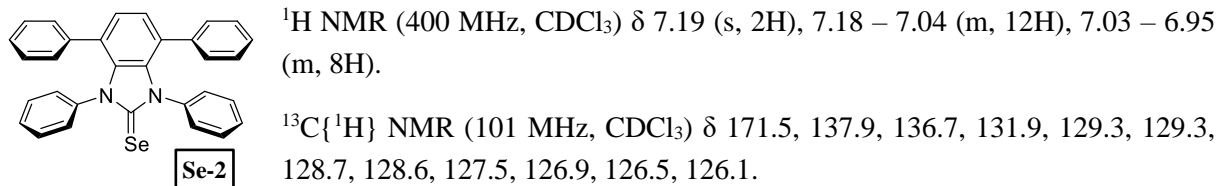
HRMS (ESI): m/z calcd. for C₁₉H₁₅N₂⁸⁰Se [M+H]⁺ 351.0395, found 351.0393.

IR (ATR) ν / cm⁻¹ 3060, 3038, 3012, 1591, 1496, 1471, 1454, 1385, 1316, 1301, 1207, 1151, 739, 689, 606.

Elemental analysis calcd. for C₁₉H₁₄N₂Se: C, 65.33; H, 4.04; N, 8.02. Found C, 65.37; H, 4.08; N, 8.07.

5.3.5.2. Synthesis of compound Se-2

Obtained according to the procedure for the synthesis of **Se-1**, from 30 mg of salt **67** (0.059 mmol). Yield – 76 % (22.3 mg, 0.045 mmol); white solid.



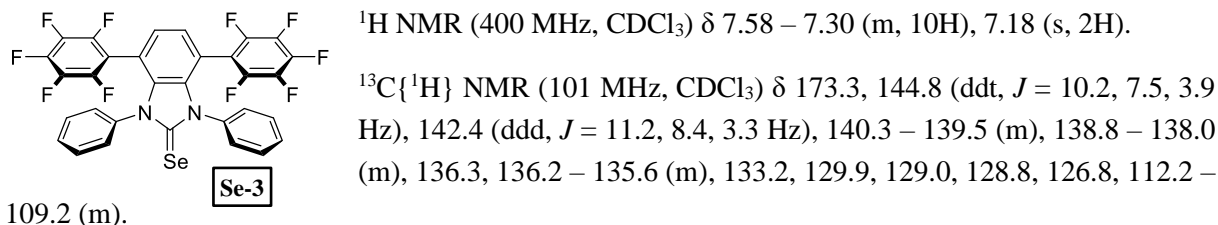
⁷⁷Se NMR (76 MHz, CDCl₃) δ 159.9.

HRMS (ESI): m/z calcd. for C₃₁H₂₃N₂⁸⁰Se [M+H]⁺ 503.1021, found 503.1020.

IR (ATR) ν / cm⁻¹ 3055, 2919, 2850, 1593, 1495, 1380, 1318, 1295, 1282, 1155, 1095, 1025, 907, 810, 746, 722, 698, 687, 610, 519.

5.3.5.3. Synthesis of compound Se-3

Obtained according to the procedure for the synthesis of **Se-1**, from 30 mg of salt **71** (0.043 mmol); the carbene was generated for only 15 min. Yield – 69 % (20.3 mg, 0.030 mmol); white solid.



¹⁹F NMR (376 MHz, CDCl₃) δ -137.36 (dd, *J* = 23.5, 7.9 Hz, 4F), -153.03 (t, *J* = 20.9 Hz, 2F), -160.58 – -163.11 (m, 4F).

⁷⁷Se NMR (76 MHz, CDCl₃) δ 197.8.

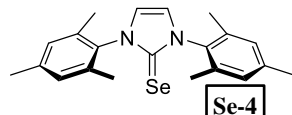
HRMS (ESI): m/z calcd. for C₃₁H₂₃N₂⁸⁰Se [M+H]⁺ 815.0371, found 815.0370.

IR (ATR) ν / cm⁻¹ 1532, 1494, 1419, 1383, 1295, 1282, 1226, 1092, 984, 849, 823, 754, 695, 641.

Elemental analysis calcd. for C₃₁H₁₂F₁₀N₂Se: C, 54.64; H, 1.78; N, 4.11. Found C, 54.42; H, 1.72; N, 4.17.

5.3.5.4. Synthesis of compound Se-4

Obtained according to the procedure for the synthesis of **Se-1**, from 50 mg of dimesitylimidazolium chloride (**102**) (0.147 mmol) using KO'Bu as the base (16.5 mg, 0.147 mmol). Yield – 78 % (44.1 mg, 0.115 mmol); off-white solid. NMR spectral data match reported previously in the literature.^[222]



¹H NMR (400 MHz, CDCl₃) δ 7.02 (s, 4H), 6.97 (s, 2H), 2.35 (s, 6H), 2.14 (s, 12H).

¹³C{¹H} NMR (101 MHz, CDCl₃) δ 157.6, 139.4, 135.4, 134.3, 129.4, 120.3, 21.3, 18.1.

⁷⁷Se NMR (76 MHz, CDCl₃) δ 27.0.

5.3.6. Stability tests of ruthenium complexes

The procedures and results refer to Figure 26A and B, Chapter 3.5.

5.3.6.1. CD₂Cl₂ at ambient temperature

An NMR tube with a screw cap was charged with ruthenium complex (4.5 μmol, ca. 3 – 4 mg) and trimethoxybenzene (0.3 mg, 1.5 μmol). 0.45 mL of dry and degassed CD₂Cl₂ was added and NMR spectra were recorded. The survival rate was calculated according to equation 6.

$$Surv.\ rate = \frac{\int_{Ru_t}/\int_{TMB_t}}{\int_{Ru_t_0}/\int_{TMB_t_0}} \quad (6)$$

Where ∫ - an integral of the corresponding signal; Ru – from alkylidene signal; TMB – from the signal of trimethoxybenzene (at 6.07 ppm).

• Ru-67

Table 9 Stability of complex **Ru-67** in CD₂Cl₂ at rt.

Time (days)	Survival rate
0.0	100 %
0.9	98 %
3.8	93 %
5.0	94 %
8.9	82 %
11.0	79 %
13.0	68 %
15.0	64 %
18.0	54 %
19.0	48 %

- **Ru-68**

Table 10 Stability of complex **Ru-68** in CD₂Cl₂ at rt.

Time (days)	Survival rate
0.0	100 %
1.3	100 %
2.3	101 %
5.1	102 %
6.9	103 %
9.2	102 %
12.1	100 %
17.2	97 %
19.3	100 %

- **Ru-69**

Table 11 Stability of complex **Ru-69** in CD₂Cl₂ at rt.

Time (days)	Survival rate
0.0	100 %
0.6	100 %
1.0	100 %
1.6	98 %
3.2	100 %
3.6	99 %
6.1	99 %
6.7	101 %
7.7	100 %
9.7	99 %
10.7	98 %
14.0	99 %
15.7	99 %
18.0	100 %

5.3.6.2. C₆D₆ at 80 °C

An NMR tube with a screw cap was charged with ruthenium complex (4.5 µmol, ca. 3 – 4 mg) and trimethoxybenzene (0.3 mg, 1.5 µmol). 0.45 mL of dry and degassed C₆D₆ was added and an initial NMR spectrum was recorded. The sample was heated at 80 °C and the spectra were recorded. The survival rate was calculated according to the following equation 7.

$$Surv.\ rate = \frac{\int_{Ru,t} / \int_{TMB,t}}{\int_{Ru,t_0} / \int_{TMB,t_0}} \quad (7)$$

Where \int - an integral of the corresponding signal; Ru – from alkylidene signal; TMB – from the signal of trimethoxybenzene (at 6.26 ppm).

- **Ru-67**

Table 12 Stability of complex **Ru-67** in C₆D₆ at 80 °C.

Time (hours)	Survival rate
0	100 %
1.08	96 %
4.78	79 %
18.83	33 %
27.40	2 %
41.45	1 %

- **Ru-68**

Table 13 Stability of complex **Ru-68** in C₆D₆ at 80 °C.

Time (hours)	Survival rate
0	100 %
2.58	92 %
7.27	87 %
22.57	73 %
29.58	71 %
45.05	56 %
53.15	49 %
68.42	43 %
76.00	42 %
91.82	36 %
101.18	33 %

- **Ru-69**

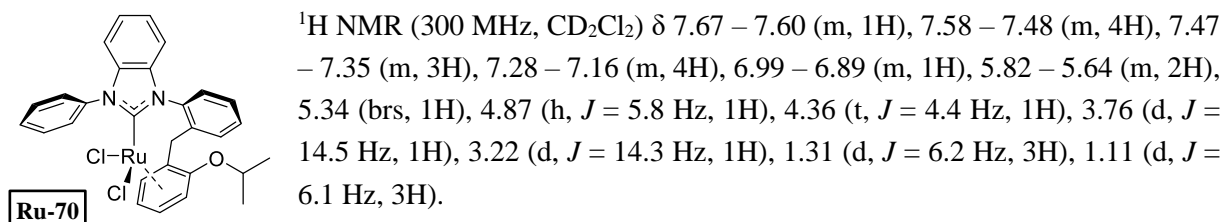
Table 14 Stability of complex **Ru-68** in C₆D₆ at 80 °C.

Time (hours)	Survival rate
0	100 %
2.20	94 %
5.63	92 %
21.45	85 %
29.32	79 %
45.23	73 %
52.78	70 %
60.82	64 %
76.40	60 %
84.25	57 %
99.88	54 %

5.3.7. Isolation of the decomposition product Ru-70

The synthesis refers to Figure 26C, Chapter 3.5.

In a Schlenk flask, catalyst **Ru-67** (25.4 mg, 0.043 mmol) was dissolved in 2 mL of dried and degassed DCM. The solution was stirred at 40 °C for 7 days. After this time, the solution was directly put on a short silica bed packed with dry DCM, which was next washed with dry DCM to remove the unreacted starting complex. Next, a dark red-violet band was washed out from the silica gel by washing with 2 % MeOH in DCM (dry solvents). After solvent removal *in vacuo*, the product was placed in a 4 mL vial and dissolved in 0.5 mL of dry DCM. The product was crystallized by pentane vapors diffusion into DCM solution. After this, the product red crystals were removed from the vial. Red crystals were washed with dry pentane (3 × 4 mL) and dried under the reduced pressure of an oil pump at 100 °C for 15 min. The product was obtained as deep red crystals in 29 % yield (7.4 mg, 0.013 mmol). Crystals suitable for XRD experiments were obtained by layering a DCM complex solution with pentane.



¹³C{¹H} NMR (101 MHz, CD₂Cl₂) δ 190.4, 138.0, 137.6, 136.6, 135.0, 134.7, 133.7, 132.0, 130.6, 129.5, 129.0, 128.5, 128.0, 127.5, 127.1, 124.1, 123.8, 111.7, 111.2, 101.2, 89.9, 76.3, 74.6, 74.0, 72.5, 35.5, 23.5, 21.3.

HRMS (ESI): m/z calcd. for C₂₉H₂₆ClN₂ORu [M-Cl]⁺ 555.0782, found 555.0791.

IR (ATR) ν / cm⁻¹ 3443, 2926, 2854, 1495, 1472, 1455, 1375, 1317, 1307, 1273, 1107, 2938, 843, 753, 698.

5.3.8. Catalysis

The procedures refer to Chapter 3.7.

5.3.8.1. GC analysis

GC analysis was conducted using an internal standard method. Substrates stock solutions containing trimethoxybenzene (ca 0.1 equiv. with respect to substrate) as reference were prepared. Conversions were calculated from the following formula:

$$Conv. = 1 - \frac{A_{Sub_t}/A_{TMB_t}}{A_{Sub_t0}/A_{TMB_t0}} \quad (8)$$

A – signal area; Sub – from a substrate; TMB – from trimethoxybenzene.

Exemplary GC are reported therein:

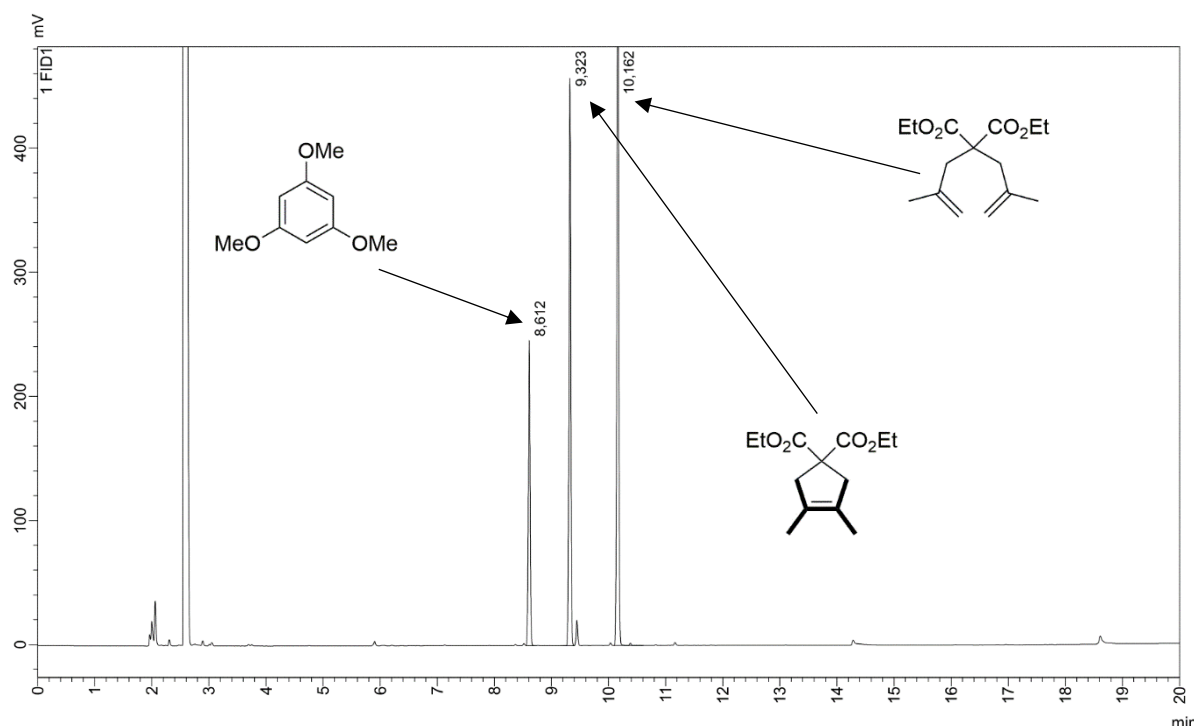
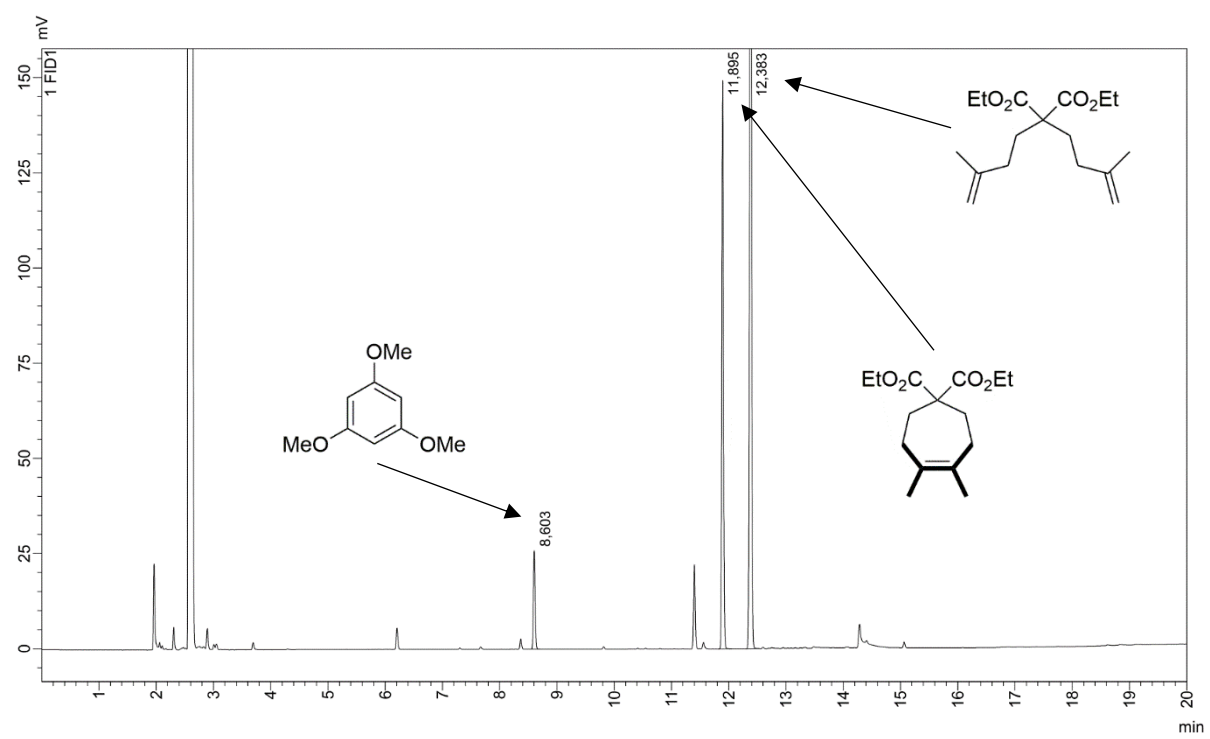
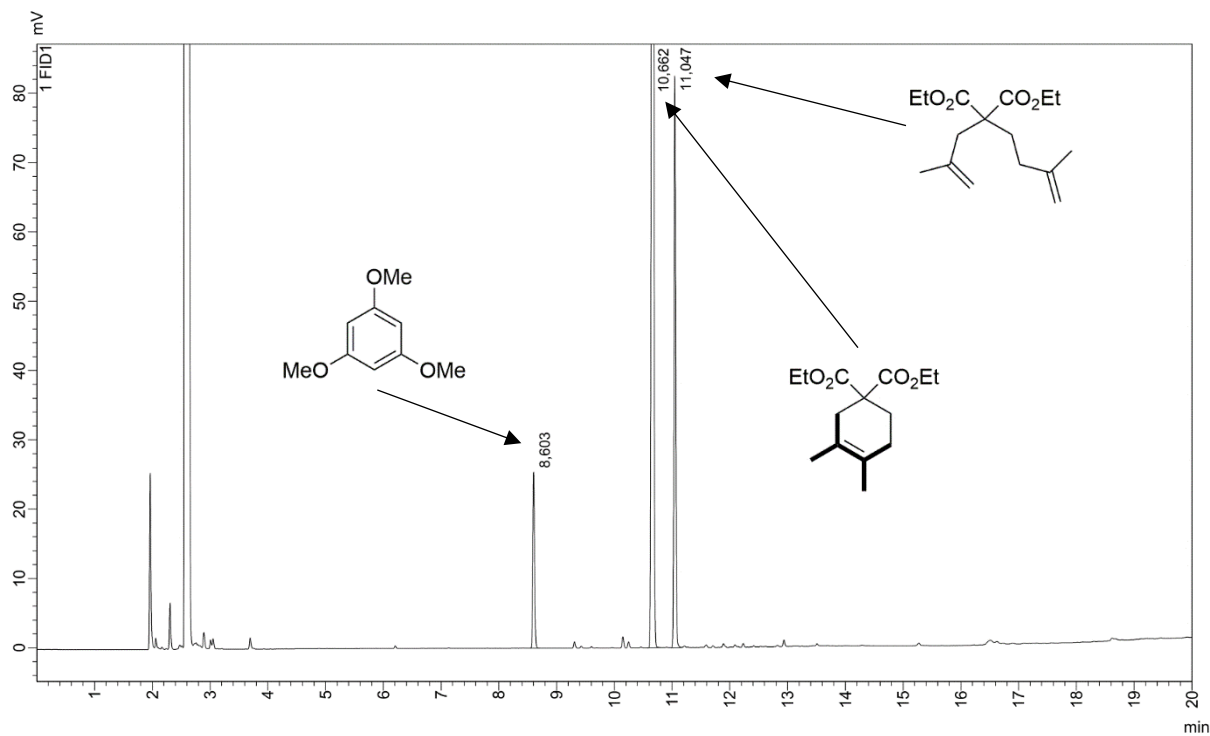


Figure 38 Gas chromatogram of an exemplary reaction mixture from RCM of **78a**. Oven temperature program – 120 °C for 1 min.; then 10 °C/min. to 300 °C for 1 min.



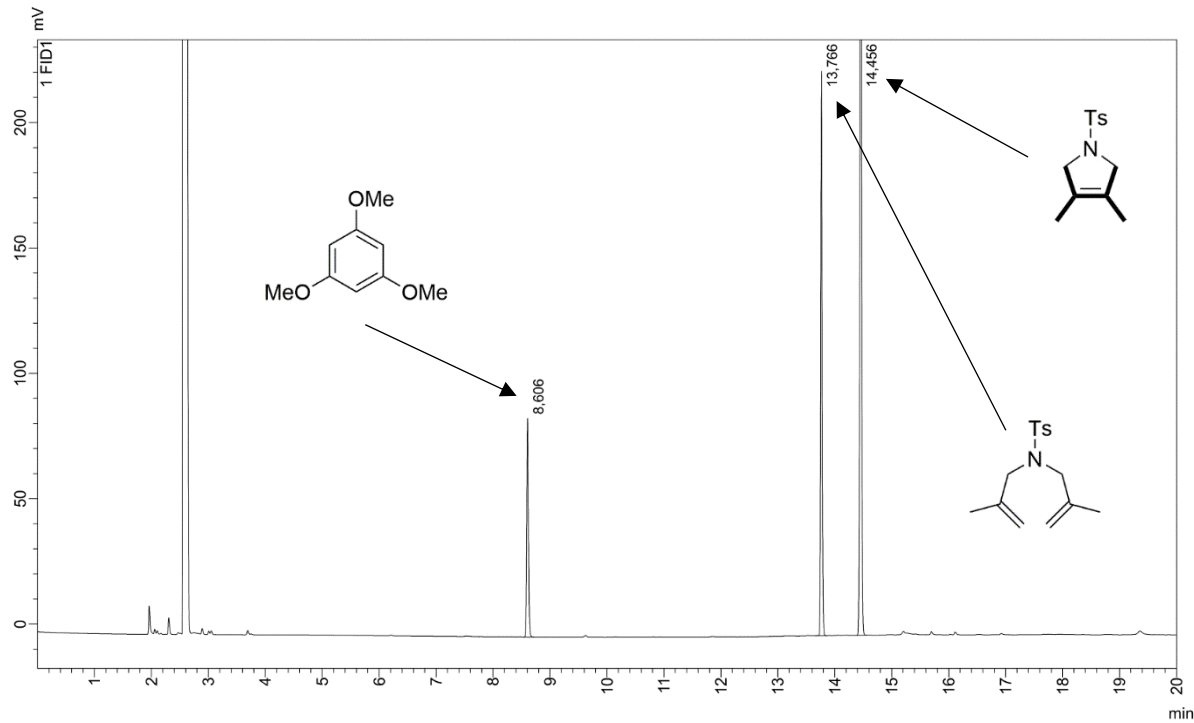


Figure 41 Gas chromatogram of an exemplary reaction mixture from RCM of **81a**. Oven temperature program – 120 °C; then 20 °C/min. to 270 °C; then 30 °C/min. to 300 °C for 6.5 min.

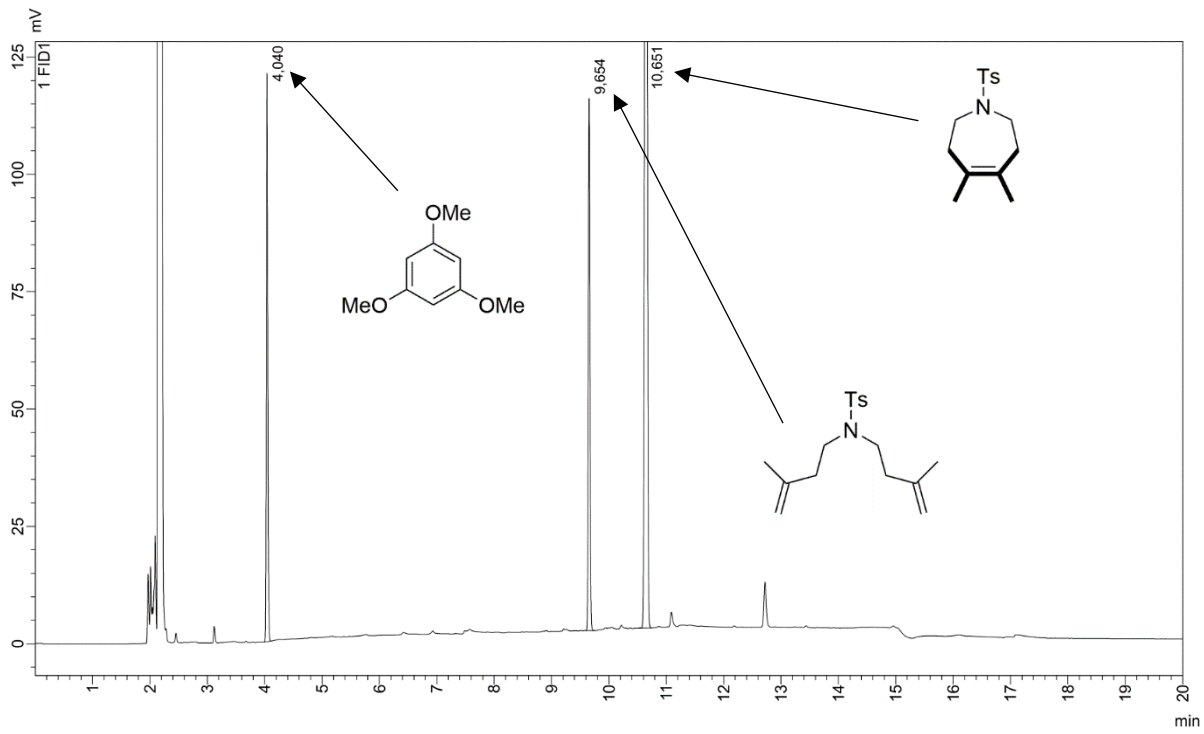


Figure 42 Gas chromatogram of an exemplary reaction mixture from RCM of **82a**. Oven temperature program – 170 °C; then 13 °C/min. to 300 °C for 10 min.

5.3.8.2. RCM of 78a – time-conversion plots

Into a 4 mL vial catalyst stock solution (ca 10 mg/mL) in DCE (dried and degassed) was added (volume measured with Hamilton syringe corresponding to 0.40 μ mol, 0.2 mol%). The solvent was removed *in*

vacuo and the vial was transferred into a glovebox. Substrate **78a** stock solution (1.00 mL of 0.2 M solution in dry toluene, 0.2 mmol, 1 equiv., trimethoxybenzene added as reference) was added and the vial was closed with a screw cap with a septum. The content of the vial was stirred at 80 °C. At specific time intervals, small samples (ca 0.05 mL) were removed from the vial and quenched with 0.10 mL of **100** stock solution in toluene (5 mg/mL).

- **Ru-67**

Table 15 Time-conversion relation in RCM of **78a** with complex **Ru-67**.

Time	Conversion
30 sec	1 %
1 min	0 %
2 min	1 %
5 min	13 %
10 min	33 %
15 min	40 %
30 min	52 %
1 h	61 %
2 h	67 %
5 h	72 %

- **Ru-68**

Table 16 Time-conversion relation in RCM of **78a** with complex **Ru-68**.

Time	Conversion
30 sec	0 %
1 min	1 %
2 min	4 %
5 min 20 sec	52 %
10 min	67 %
15 min	73 %
30 min	82 %
1 h	87 %
2 h	90 %
5 h	91 %

- **Ru-69**

Table 17 Time-conversion relation in RCM of **78a** with complex **Ru-69**.

Time	Conversion
30 sec	0 %
1 min	0 %
2 min	2 %
5 min	29 %
10 min	54 %
15 min	65 %
30 min	78 %
1 h	87 %
2 h 5 min	93 %
5 h 4 min	96 %

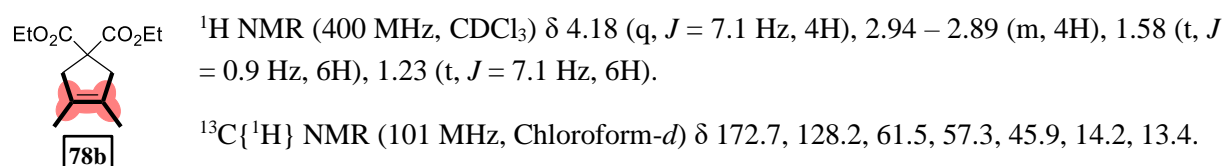
5.3.8.3. Substrate scope – RCM

- **General procedure**

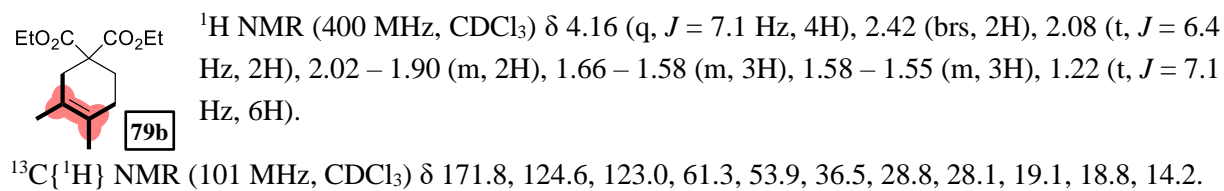
Into a 4 mL vial catalyst stock solution (ca 10 mg/mL) in DCE (dried and degassed) was added (the volume was measured with a Hamilton syringe). The amount of the catalyst depended on the loading. The solvent was removed *in vacuo* and the vial was transferred into a glovebox. Substrate stock solution (0.50 mL of 0.2 M solution in dry toluene, 0.1 mmol, 1 equiv., trimethoxybenzene added as reference) was added and the content of the vial was stirred at 80 °C for 20 h. After that time, the vial was cooled to ambient temperature and **100** was added (from a stock solution in toluene, 4.4 equiv. with respect to catalyst). GC was measured from such obtained crude reaction mixture.

- **Compounds characterization data**

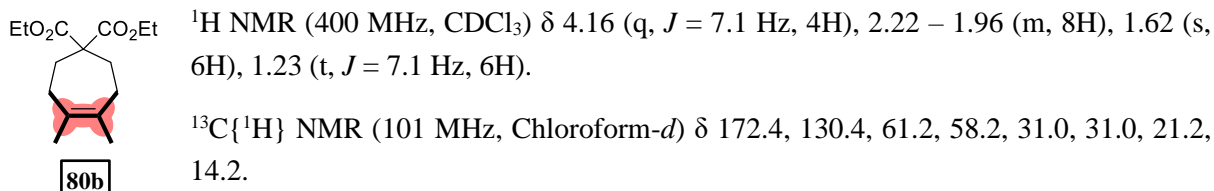
To confirm their structure, products were isolated using column chromatography.



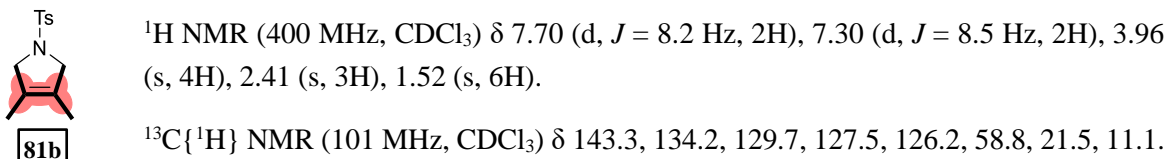
NMR spectral data match reported previously in the literature.^[253]



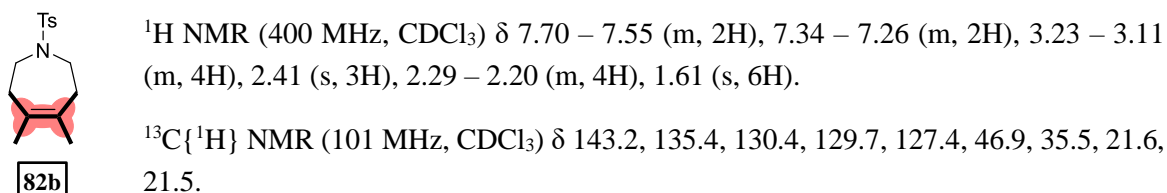
NMR spectral data match reported previously in the literature.^[253]



NMR spectral data match reported previously in the literature.^[254]



NMR spectral data match reported previously in the literature.^[255]



NMR spectral data match reported previously in the literature.^[246]

5.3.8.4. RCM of **84a**

- **Reaction profiles – general procedure**

Into a 4 mL vial catalyst stock solution (ca 10 mg/mL) in DCE (dried and degassed) was added (volume measured with Hamilton syringe corresponding to 4 µmol, 2 mol%). The solvent was removed *in vacuo* and the vial was transferred into a glovebox. Substrate **84a** stock solution (1.00 mL of 0.2 M solution in dry toluene, 0.2 mmol, 1 equiv., trimethoxybenzene added as reference) was added and the vial was closed with a screw cap with a septum. The content of the vial was stirred at 80 °C. At a specific time, intervals small samples (ca 0.05 mL) were removed from the vial and quenched with 0.10 mL of **100** stock solution in toluene (5 mg/mL).

- **Reaction profiles – GC analysis**

Analogically to previous examples, GC analysis was conducted using an internal standard method. Molar fractions (x_{84x}) of each reactant at a given time were calculated from the numbers of moles. Numbers of moles were calculated according to the following formulas:

$$n_{84a}(t) = n_{84a}(t_0) \cdot \frac{A_{84a}(t)/A_{TMB}(t)}{A_{84a}(t_0)/A_{TMB}(t_0)} \quad (9)$$

$$n_{84a'}(t) = n_{84a}(t_0) \cdot \frac{A_{84a'}(t)/A_{TMB}(t)}{A_{84a}(t_0)/A_{TMB}(t_0)} \quad (10)$$

$$n_{84b}(t) = n_{84a}(t_0) \cdot f_{(84b/84a)} \cdot \frac{A_{84b}(t)/A_{TMB}(t)}{A_{84a}(t_0)/A_{TMB}(t_0)} \quad (11)$$

Where: A – signal area; **84a** – from substrate **84a**; **84a'** – from product **84a'**; **84b** – from product **84b**; TMB – from trimethoxybenzene; (t) – at a given time t; (t0) – at the start of the reaction; $n_{84a}(t_0) = 0.2$ mmol; $f_{(84b/84a)} = 1.394$.

Table 18 Molar fractions of **84a**, **84b** and **84a'** and relative **83** release.

Catalyst	Time	n _{84a} (mmol)	n _{84b} (mmol)	n _{84a'} (mmol)	x _{84a·100}	x _{84b·100}	x _{84a'·100}	A _{83/ATMB}	83 release
Ru-67	8 h	0.191	0.003	0.005	96	1.4	2.7	-	-
	30 sec	0.199	0.002	0.000	99	0.8	0.0	0.014	5 %
	1 min.	0.194	0.007	0.000	97	3.3	0.0	0.027	9 %
	2 min.	0.173	0.027	0.000	87	13	0.1	0.048	17 %
	5 min.	0.130	0.069	0.001	65	34	0.3	0.081	29 %
	10 min.	0.104	0.095	0.001	52	48	0.4	0.127	45 %
Ru-68	30 min.	0.071	0.128	0.000	36	64	0.2	0.207	73 %
	1 h	0.055	0.140	0.001	28	71	0.3	0.236	84 %
	2 h	0.047	0.145	0.001	24	75	0.6	0.276	98 %
	4 h 4 min.	0.044	0.146	0.002	23	76	0.8	0.283	100 %
	8 h	0.041	0.126	0.002	24	75	0.9	0.282	100 %
	30 sec	0.202	0.000	0.000	100	0.0	0.0	0.005	2 %
Ru-69	1 min.	0.200	0.000	0.000	100	0.2	0.0	0.011	5 %
	2 min.	0.199	0.003	0.000	99	1.3	0.0	0.023	9 %
	5 min.	0.187	0.014	0.000	93	6.7	0.2	0.041	17 %
	10 min.	0.170	0.030	0.001	85	15	0.4	0.056	23 %
	42 min.	0.132	0.063	0.001	67	32	0.6	0.136	55 %
	1 h	0.125	0.071	0.002	63	36	0.8	0.164	66 %
Ru-69	2 h 1 min.	0.107	0.078	0.004	56	41	2.3	0.213	86 %
	4 h	0.096	0.083	0.009	51	44	4.8	0.246	100 %
	8 h	0.089	0.077	0.009	51	44	5.4	0.247	100 %

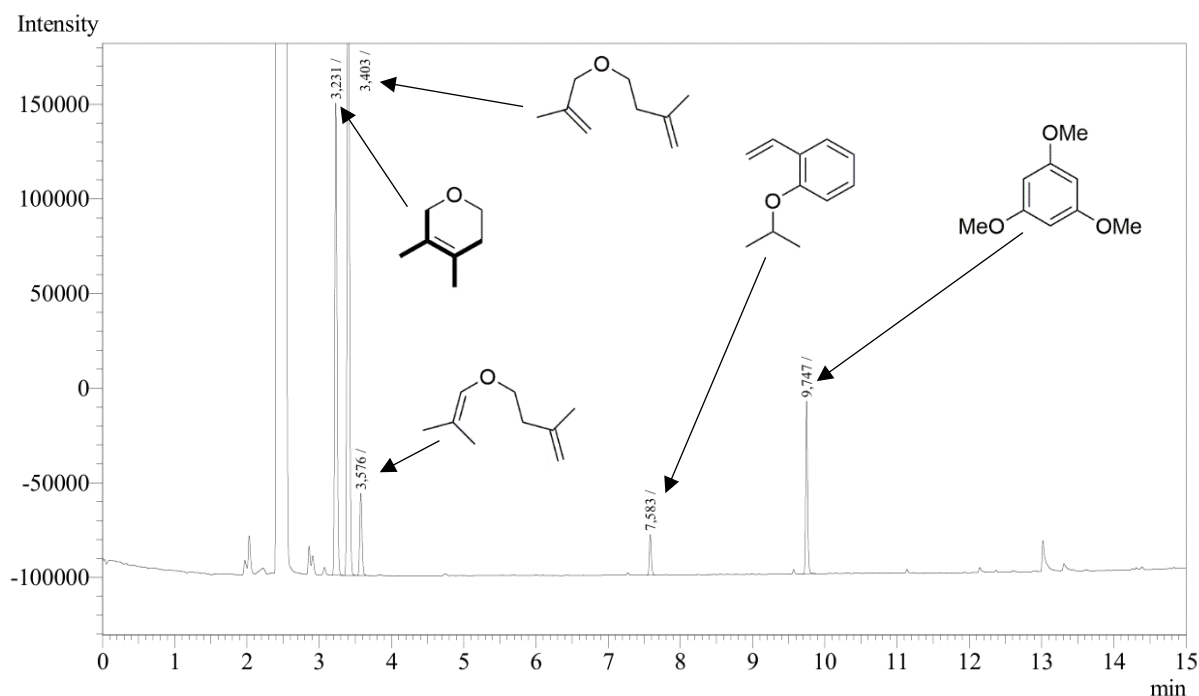
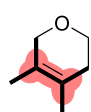


Figure 43 Gas chromatogram of an exemplary reaction mixture from RCM of **84a**. Oven temperature program – 100 °C for 5 min.; then 20 °C/min. to 300 °C.

Experimental section

- **Compound 84b characterization data**



¹H NMR (400 MHz, CDCl₃) δ 3.95 – 3.87 (m, 2H), 3.75 (t, *J* = 5.6 Hz, 2H), 2.07 – 1.87 (m, 2H), 1.67 – 1.63 (m, 3H), 1.55 – 1.49 (m, 3H).

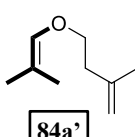
84b

¹³C{¹H} NMR (101 MHz, CDCl₃) δ 124.7, 123.8, 69.4, 65.0, 30.9, 18.5, 14.2.

Full NMR spectral data for this compound have never been reported in the literature about its synthesis.^[130,133,256]

- **Compound 84a' characterization data**

Inside a glowbox, into a 4 mL vial equipped with a magnetic stir bar RuCl₂(PPh₃)₃ (1.9 mg, 2 μmol, 1 mol%) and LiAlH₄ (0.4 mg, 10 μmol, 5 mol%) were placed. Substrate **84a** stock solution in dry C₆D₆ (1 mL of 0.2 M, 0.2 mmol, 1 equiv.) was added and the vial was closed with a screw cap. The content of the vial was stirred at 80 °C for overnight. After this time, additional portions of RuCl₂(PPh₃)₃ and LiAlH₄ were added and again the content of the vial was stirred at 80 °C for overnight. A crude solution of **84a'** was distilled (bulb-to-bulb) and such C₆D₆ solution was used for compound characterization.



¹H NMR (300 MHz, C₆D₆) δ 5.71 (h, *J* = 1.4 Hz, 1H), 4.80 – 4.71 (m, 2H), 3.56 (t, *J* = 6.8 Hz, 2H), 2.19 (t, *J* = 6.5 Hz, 2H), 1.75 (s, 3H), 1.60 (s, 3H), 1.52 (s, 3H).

84a'

¹³C{¹H} NMR (75 MHz, C₆D₆) δ 140.8, 112.0, 70.3, 38.2, 22.8, 19.7, 15.4.

GC-MS (EI): m/z (%): 140.1 (23.1) [M]⁺.

IR (ATR) ν / cm⁻¹ 2920, 2349, 1692, 1650, 1453, 1376, 1215, 1166, 1148, 1054, 891.

5.3.8.5. Substrate scope – CM

- **General procedure**

Into a 4 mL vial catalyst stock solution (ca 10 mg/mL) in DCE (dried and degassed) was added (the volume was measured with a Hamilton syringe). The amount of the catalyst depended on the loading. The solvent was removed *in vacuo* and the vial was transferred into a glovebox. Substrate stock solution (0.33 mL of 0.3 M solution in dry toluene, 0.1 mmol, 1 equiv., trimethoxybenzene added as reference) was added, followed with dry toluene (0.11 mL) and Z-diacetoxybutene (64 μL, 69 mg, 0.4 mmol, 4 equiv.) and the content of the vial was stirred at 80 °C for 20 h. After that time, the vial was cooled to ambient temperature and **100** was added (from a stock solution in toluene, 4.4 equiv. with respect to catalyst). GC was measured from such obtained crude reaction mixture and substrate conversion was calculated according to equation 8.

Exemplary GC are reported therein:

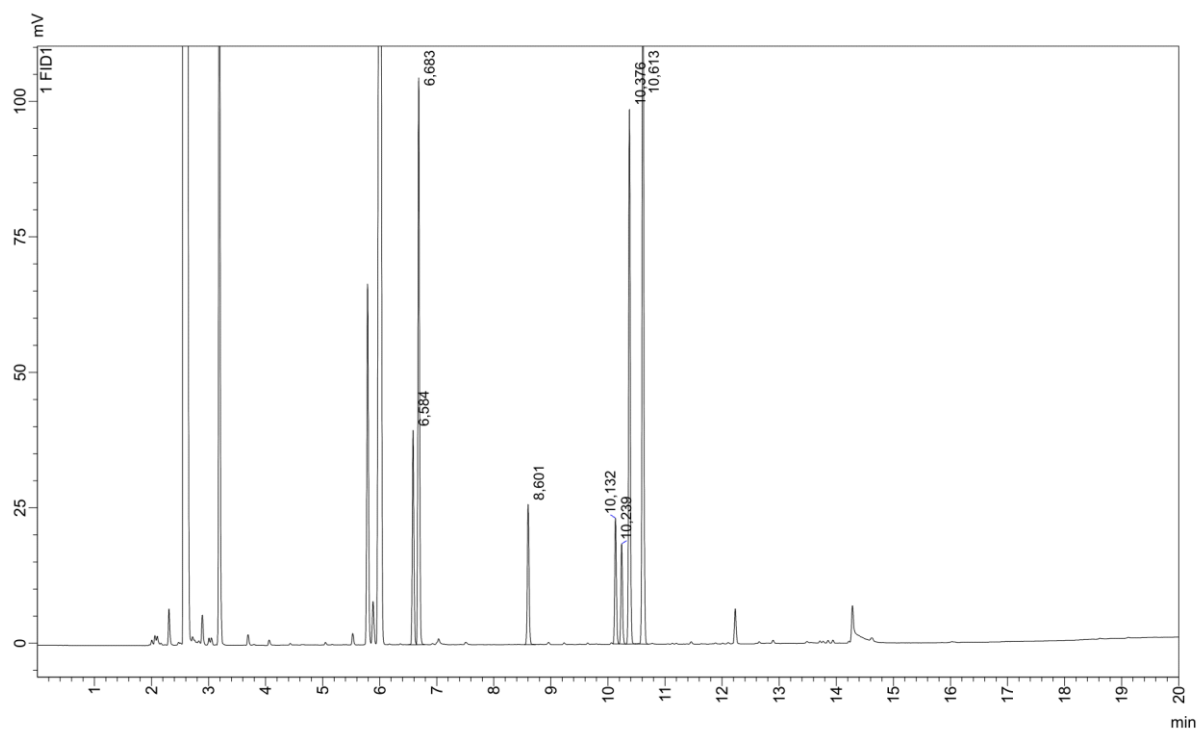


Figure 44 Gas chromatogram of an exemplary reaction mixture from CM of **88** with **86**. Oven temperature program – 120 °C for 1 min.; then 10 °C/min. to 300 °C for 1 min.

Table 19 Structures of compounds with their retention time (CM of **88** with **86**).

Structure	Retention time [min.]
<chem>CC(=O)C/C=C\COAc</chem>	5.8 (<i>Z</i>), 6.0 (<i>E</i>)
<chem>CC(C)(C)C1(C)C=C(C)C[C@H]1C(=O)OCC</chem>	6.584 (<i>trans</i>), 6.683 (<i>cis</i>)
<chem>Oc1ccc(O)c(O)c1</chem>	8.601
<chem>CC(C)(C)C1(C)C=C(C)C[C@H]1C(=O)OCC</chem>	10.132 (<i>trans/Z</i>), 10.239 (<i>cis/Z</i>), 10.376 (<i>cis/E</i>), 10.613 (<i>trans/E</i>)

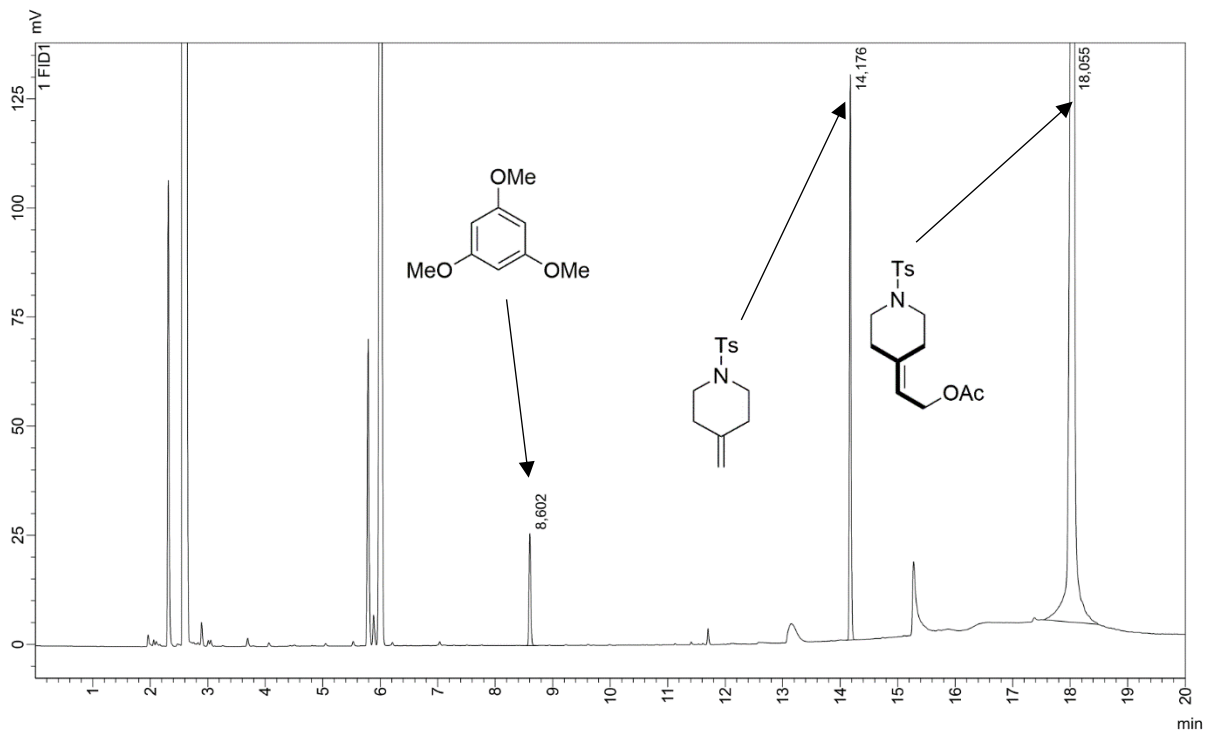


Figure 45 Gas chromatogram of an exemplary reaction mixture from CM of **88** with **86**. Oven temperature program – 120 °C for 1 min.; then 10 °C/min. to 300 °C for 1 min.

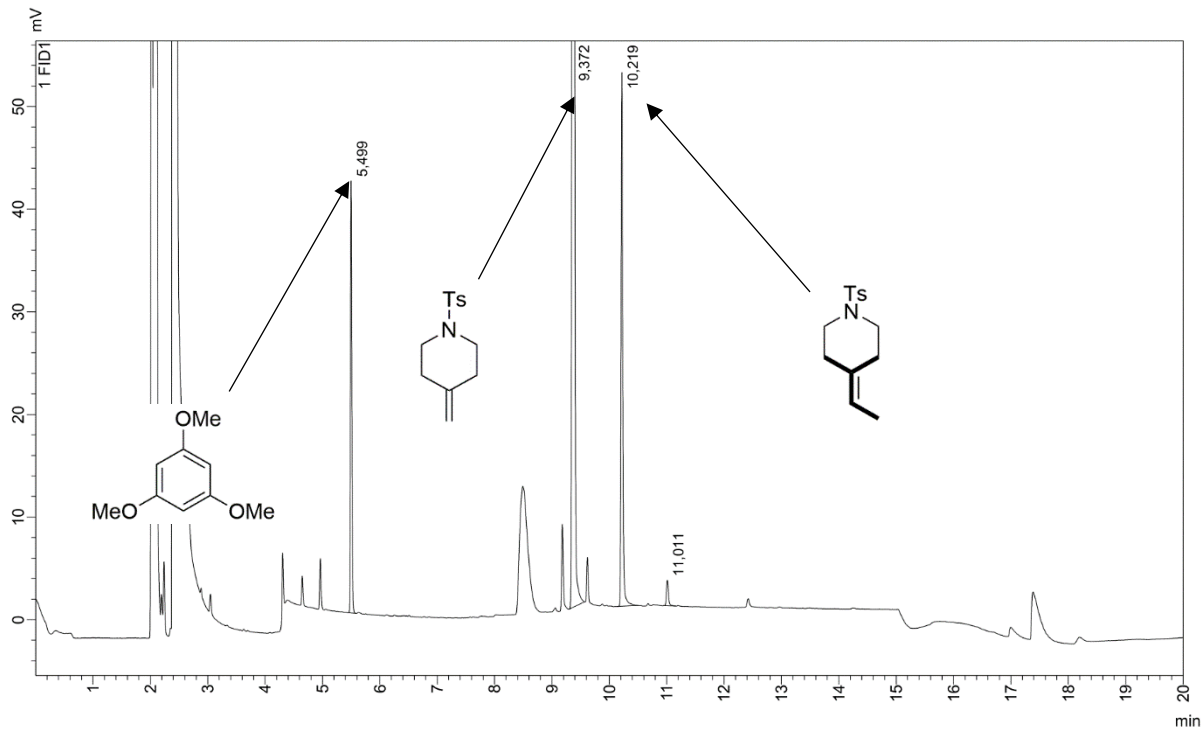
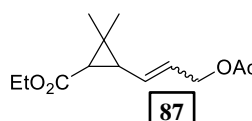


Figure 46 Gas chromatogram of an exemplary reaction mixture from CM of **88** with amylenne (**90**). Oven temperature program – 150 °C; then 10 °C/min. to 300 °C for 5 min.

- Compounds characterization data

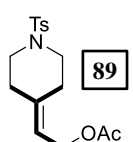
To confirm its structure, the products were isolated using column chromatography.



¹H NMR (400 MHz, CDCl₃) δ 6.13 (ddt, *J* = 15.4, 9.7, 1.2 Hz, 0.33H, *cis/E*), 5.96 (ddt, *J* = 10.9, 9.5, 1.4 Hz, 0.04H, *cis/Z*), 5.79 – 5.70 (m, 0.90H, *cis* and *trans/E*), 5.70 – 5.61 (m, 0.10H, *cis* and *trans/Z*), 5.52 (ddt, *J* = 15.3, 8.7, 1.1 Hz, 0.57H, *trans/E*), 5.34 (ddt, *J* = 10.7, 9.3, 1.4 Hz, 0.07H, *trans/Z*), 4.75 – 4.66 (m, 0.27H, *cis* and *trans/Z*), 4.55 (dd, *J* = 6.6, 1.2 Hz, 0.66H, *cis/E*), 4.52 (dd, *J* = 6.5, 1.1 Hz, 1.11H, *trans/E*), 4.19 – 4.04 (m, 2H), 2.06 (s, 3H), 1.88 – 1.63 (m, 1H), 1.61 – 1.51 (m, 1H), 1.29 – 1.23 (m, 6H), 1.18 (d, *J* = 10.8 Hz, 3H).

¹³C{¹H} NMR (101 MHz, CDCl₃) δ 171.8, 171.1, 171.0, 171.0, 170.9, 133.3, 131.9, 131.2, 129.3, 126.1, 126.0, 125.9, 65.4, 65.0, 60.9, 60.8, 60.6, 60.6, 60.2, 35.6, 35.5, 35.4, 34.3, 31.3, 30.8, 29.8, 28.9, 28.7, 27.3, 22.3, 22.1, 21.2, 21.2, 20.4, 20.4, 14.8, 14.7, 14.5, 14.5.

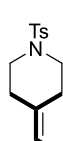
NMR spectral data match reported previously in the literature.^[142]



¹H NMR (400 MHz, CDCl₃) δ 7.75 – 7.50 (m, 2H), 7.35 – 7.26 (m, 2H), 5.33 (t, *J* = 7.2 Hz, 1H), 4.49 (d, *J* = 7.2 Hz, 2H), 3.03 (dt, *J* = 8.6, 5.8 Hz, 4H), 2.39 (d, *J* = 8.1 Hz, 5H), 2.29 (t, *J* = 5.6 Hz, 2H), 1.99 (s, 3H).

¹³C{¹H} NMR (101 MHz, CDCl₃) δ 170.9, 143.7, 139.9, 133.3, 129.8, 127.7, 118.8, 60.0, 47.5, 47.0, 35.1, 28.0, 21.6, 21.1.

NMR spectral data match reported previously in the literature.^[142]



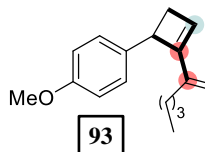
¹H NMR (400 MHz, CDCl₃) δ 7.65 – 7.60 (m, 2H), 7.32 – 7.28 (m, 2H), 5.21 (qt, *J* = 6.7, 1.3 Hz, 1H), 2.99 (td, *J* = 5.6, 3.5 Hz, 4H), 2.41 (s, 3H), 2.31 (t, *J* = 6.0 Hz, 2H), 2.26 – 2.20 (m, 2H), 1.51 (d, *J* = 6.7 Hz, 2H).

¹³C{¹H} NMR (101 MHz, CDCl₃) δ 143.5, 133.7, 133.4, 129.7, 127.8, 118.9, 48.1, 47.2, 35.3, 27.3, 21.6, 12.7.

NMR spectral data match reported previously in the literature.^[257]

5.3.8.6. Substrate scope – enyne metathesis

Into a tube for microwave reactor catalyst stock solution (ca 10 mg/mL) in DCE (dried and degassed) was added. The volume of stock solution (measured with a Hamilton syringe) corresponded to 3.75 μmol, 10 mol% of the catalyst. The tube was transferred into a glovebox in which substrate stock solution (1 mL of 37.5 mM solution in dry toluene or C₆F₅CF₃, trimethoxybenzene added as reference). The content of the vial was stirred at 70 °C for 35 min. After that, the reaction was cooled and SnatchCat (3.6 mg, 16.6 μmol, 44 mol%) was added and the solvent was removed *in vacuo* (for reactions made in C₆F₅CF₃ the solvent was not evaporated). Such crude sample was submitted for NMR analysis, from which yield was calculated. To confirm its structure, the product was isolated using column chromatography (hexane as eluent).



¹H NMR (400 MHz, CDCl₃) δ 7.16 – 7.12 (m, 2H), 6.85 – 6.81 (m, 2H), 6.13 (s, 1H), 4.77 (s, 1H), 4.64 (s, 1H), 3.99 (dd, *J* = 4.8, 1.8 Hz, 1H), 3.79 (s, 3H), 2.89 (ddd, *J* = 14.1, 4.8, 1.1 Hz, 1H), 2.24 – 2.11 (m, 3H), 1.54 – 1.46 (m, 2H), 1.39 – 1.30 (m, 2H), 0.92 (t, *J* = 7.3 Hz, 3H).

¹³C{¹H} NMR (101 MHz, CDCl₃) δ 158.1, 150.4, 142.1, 135.2, 128.1, 127.8, 113.9, 112.2, 55.4, 46.1, 37.5, 31.9, 31.0, 22.7, 14.1.

NMR spectral data match reported previously in the literature.^[235]

Crude samples from reactions in toluene were dissolved in CDCl₃ and NMR spectra were recorded. Samples from reactions in C₆F₅CF₃ were directly submitted for NMR analysis (sample locked and shimmed with a capillary insert containing C₆D₆). Yield was calculated according to the following equation:

$$Yield = \frac{\int_{prod_t}/\int_{TMB_t}}{\int_{sub_to}/\int_{TMB_to}} \quad (12)$$

Where: ∫ - integral of the corresponding signal; sub – from CH_{olefinic} substrate peak [in CDCl₃ - 5.84 ppm (ddt), in C₆F₅CF₃ with C₆D₆ capillary - 5.62 ppm (ddt)]; prod – from CH_{olefinic} product peak (in CDCl₃ – 6.13 ppm, in C₆F₅CF₃ with C₆D₆ capillary - 5.89 ppm); TMB – from CH_{aromatic} peak of trimethoxybenzene (in CDCl₃ – 6.09 ppm, in C₆F₅CF₃ with C₆D₆ capillary - 5.34 ppm).

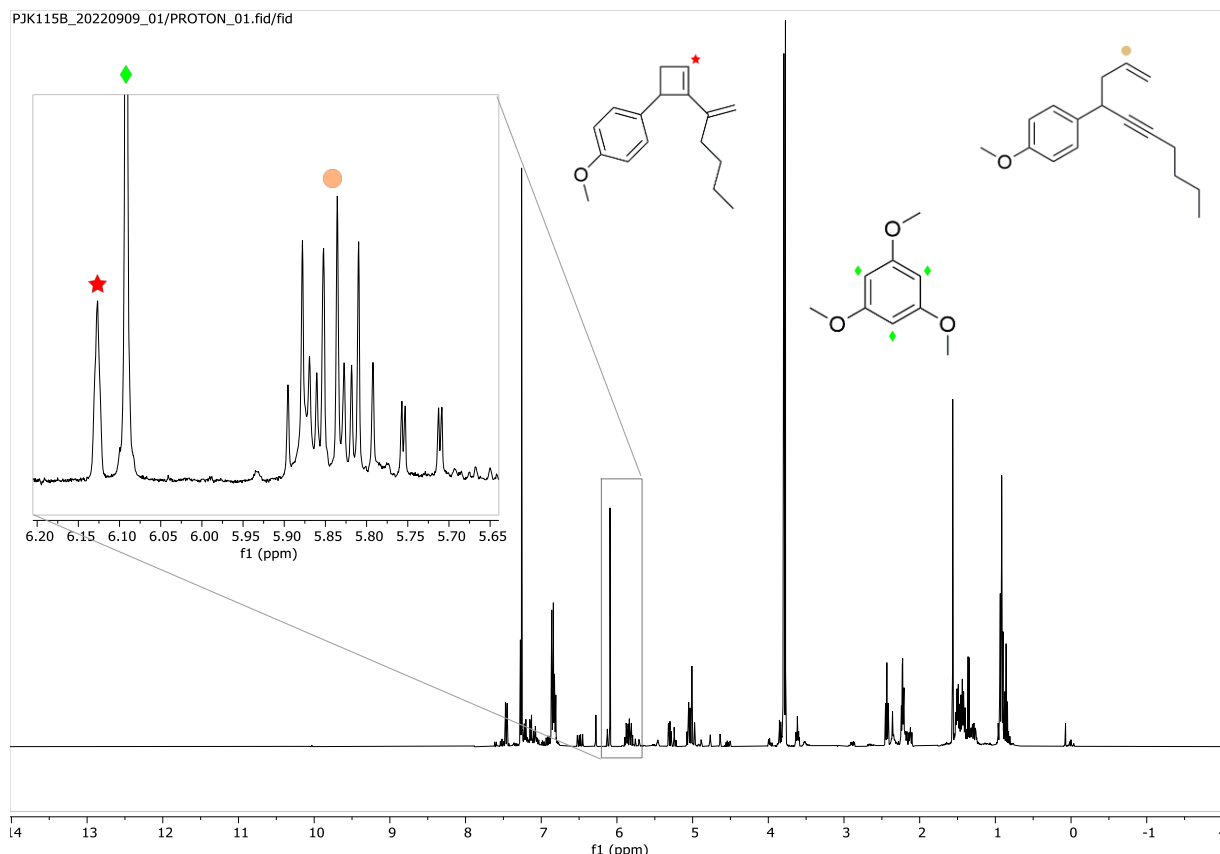


Figure 47 ¹H NMR spectrum of an exemplary reaction mixture from cycloisomerization reaction of **92**.

5.4. Supporting information for Chapter 4

5.4.1. General considerations

Commercially available catalysts **Ru-10**, **Ru-18**, **Ru-17**, **Ru-71**, **100**, Ti(OⁿBu)₄, 1,8-diaminoctane and diols were used as received. Catalyst **Ru-68** and **Ru-69** were prepared according to the procedure from Chapter 5.3.3. Technical methyl oleate was distillation from activated neutral Al₂O₃ at 1 mbar pressure two times consecutively and stored under nitrogen protective atmosphere over activated Al₂O₃.

5.4.2. Self-CM of methyl oleate

5.4.2.1. Catalysts screening – general procedure

20 mL vial, equipped with a magnetic stir bar, was charged with catalyst stock solution in dichloroethane (approximately 10 mg/mL). The amount of catalyst solution was adjusted to the catalyst loading. The solvent was removed in the flow of nitrogen and methyl oleate was added (1.73 g, 2 mL, 5.84 mmol). The vial was purged with nitrogen and closed with a screw cap. The reaction was stirred at 50 °C for 3 h. After that hexadecane stock solution (1.00 mL of 170 mg/mL) was added, followed by **100** (to quench the catalysis). The sample was analyzed by GC.

5.4.2.2. GC analysis

GC was performed using the following instrument setup:

Injector – split mode; temperature: 300 °C; split ratio 70:1.

Oven – 100 °C for 7 min.; then 10 °C/min. to 200 °C for 5 min.; then 15 °C/min to 240 °C for 5 min. and 15 °C/min. to 250 °C for 4.67 min.

Mobile phase – helium

Injection volume – 1 µL.

Flame ionization detector – temperature: 300 °C.

- **Calculation of 28(Z) and 94 conversion**

Three t0 samples were prepared (without the addition of the catalyst). 1.73 g of the distilled methyl oleate was mixed with 1 mL of 170 mg/mL hexadecane stock solution in toluene and a gas chromatogram was measured. The average area ratio of signals of methyl oleate **28(Z)** and methyl linoleate **94** to hexadecane was determined as 8.562. Conversion was calculated according to the following formula:

$$Conv. = 1 - \frac{A_{28(Z)+94}/A_{hexadecane}}{8.562} \quad (13)$$

Where: A_[28(Z)+94] – signal area of methyl oleate **28(Z)** and methyl linoleate **94**; A_{hexadecane} – the signal area of hexadecane.

- **Calculation of 29 yield**

Three samples were prepared by mixing octadec-9-enedioate **29** (88.8 mg, 190.4 mg and 366.4 mg) with 1 mL of 170 mg/mL hexadecane stock solution in toluene and gas chromatograms were measured.

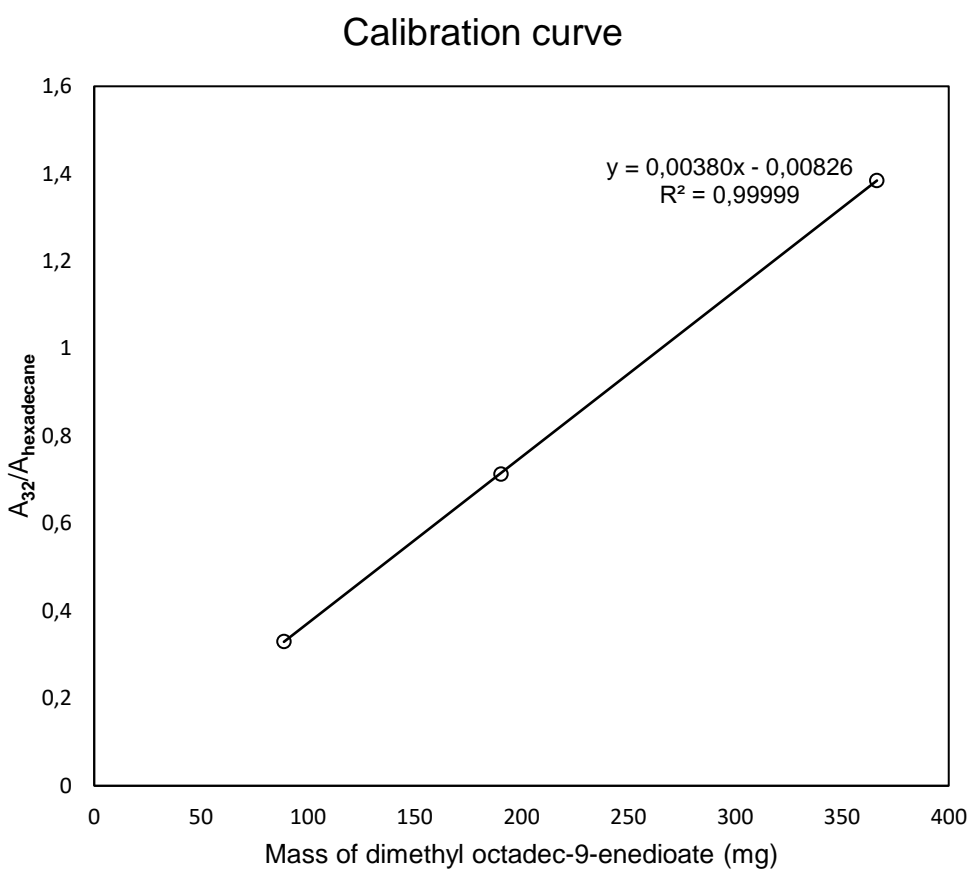


Figure 48 Calibration curve for dimethyl octadec-9-enedioate (32).

Yield was calculated according to the following formula:

$$\text{Yield} = \frac{m_{32(\text{in sample})}}{m_{32(\text{theoretical})}} = \frac{\left(\frac{A_{32}}{A_{\text{hexadecane}}} + 0.00826 \right) / 0.00380}{994.54} \quad (14)$$

Where: A_{32} – the signal area of octadec-9-enedioate (32); $A_{\text{hexadecane}}$ – the signal area of hexadecane.

- **Exemplary gas chromatogram**

Table 20 Structures of compounds with their retention time.

Structure	Retention time [min.]
	97 14.565
Hexadecane	16.176
	30 18.587
	96 19.031
	103 21.108
	28 24.355 (Z), 24.450 (E)
	104 24.691
	95 28.908
	29 29.533 (Z), 29.694 (E)

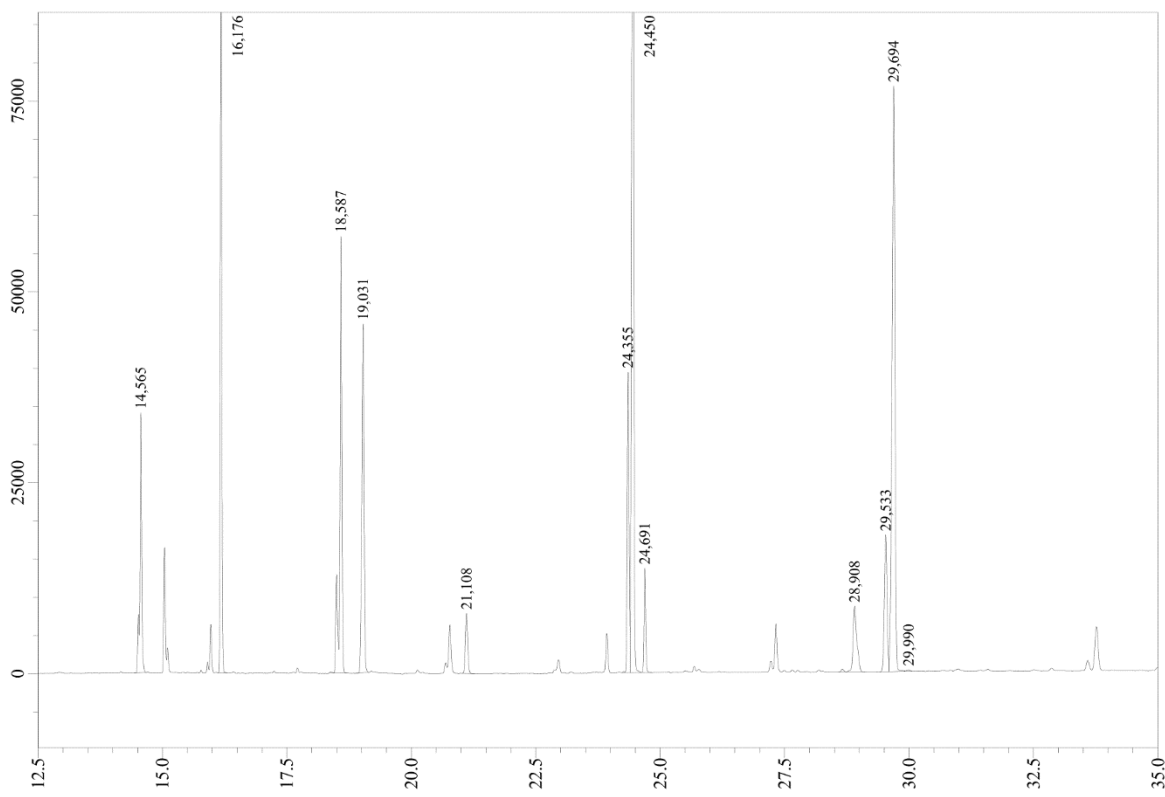
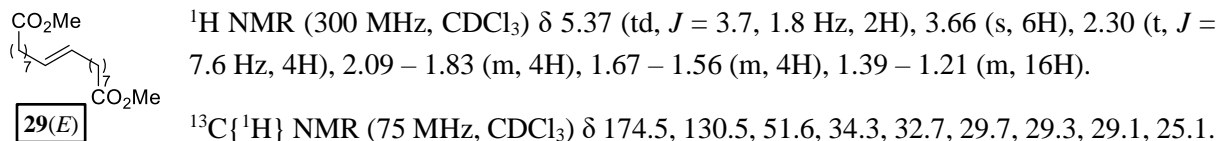


Figure 49 Gas chromatogram of exemplary crude reaction mixture.

5.4.2.3. Synthesis of dimethyl *E*-octadec-9-enedioate

500 mL one necked flask, equipped with a magnetic stir bar, was charged with ca. 300 mL (249.58 g, 0.842 mol) of methyl oleate. Catalyst **Ru-10** (52.8 mg, 84.2 µmol, 100 ppm) was added in a solid form and the atmosphere in the flask was exchanged for nitrogen using the Schlenk technique. The content of the flask was stirred at 50 °C for 3 h. After that time, **100** (81.6 mg, 370.4 µmol, 440 ppm) was added in solid form and everything was stirred for 30 min. 1.7 g of SiO₂ (gel for column chromatography) was added and everything was stirred for overnight. SiO₂ was filtered off and washed with hexane. The product was isolated using fractional distillation. At 1 mbar pressure, the fraction containing the product was collected at 172–192 °C. The diester was further purified by crystallization from methanol at -30 °C and washed with ice-cold methanol to afford 34.32 g of product as a transparent solid of 96.6 % purity. Further product crystallization from the supernatant gave 2nd crystallization crop – 21.57 g of 85.1 % purity. The amount of pure diester product in both crystallization crops corresponds to 51.51 g, 0.151 mol, the total yield of 36 %. Analytical data match the previously reported for this compound.^[258]



5.4.3. Polycondensation reactions

5.4.3.1. General procedure

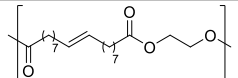
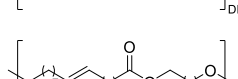
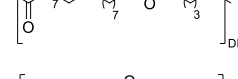
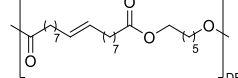
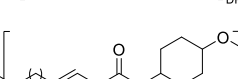
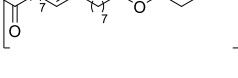
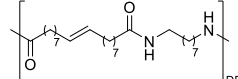
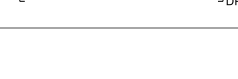
Into a 50 mL, round bottom flask Ti(O*t*Bu)₄ (10 mg, 29.4 µmol, 1 mol%), diester **29** (1.00 g, 2.94 mmol, 1 equiv.) and comonomer (number of equivalents varied, see Table 21) were placed. The content of the

flask was stirred using a magnetic stir bar and the temperature was elevated (oil bath heating) using the following temperature program: 150 °C for 20 min.; then 160 °C for 20 min.; then 170 °C for 20 min.; then 180 °C for 20 min.; then 190 °C for 20 min.; then 200 °C for 20 min.; then 200 °C, N₂ purge for 20 min.; then 200 °C, vacuum (1 mbar, time varied, see Table 21). Stirring stopped after 2 h of the vacuum step. Reaction workup differed when oligomers and polymers were synthesized.

Work up for oligomers. The material was solubilized chloroform (10 mL) and precipitated with MeOH (100 mL). The brown material was washed with MeOH (3 x 100 mL) and dried under a vacuum to give oligomers.

Work up for polymers. To the reaction flask 30 mL of chloroform was added and the flask was closed with a plastic stopper. The content of the flask was stirred at 80 °C for 15 min. After this procedure, the polymer was soaked with solvent and detached more easily from the flask walls. The content of the flask was stirred for an additional 15 min. at 80 °C. The product was filtered off on a sintered funnel and washed with 30 mL of chloroform. Drying the product under the reduced pressure of an oil pump (100 °C for 30 min.) afforded a brown-orange jelly solid.

Table 21 Yields and conditions of synthesis of oligo- and polymers.

Entry	Polymer	Equivalents of comonomer	Vacuum time	Yield
1		4	30 min.	51 %
2		4	19 h	52 %
3		1.5	225 min.	76 %
4		1.5	21 h	81 %
5		1.2	180 min.	74 %
6		1.2	21 h	88 %
7		1.2	19 h	24 %
9		1.2	19 h	51 %

5.4.3.2. End group analysis

One method for determining a polymer's average molecular weight is end group analysis. The chemical environment for the end group in an NMR study differs from the environment for the repeat unit in the center of the oligomer chain. The acetyl group, which carries a methyl group with a chemical shift of roughly 3.7 ppm, will serve as the end groups. Each repeat unit of the chain has four aliphatic hydrogens that resonate between 2.2 and 2.4 ppm.

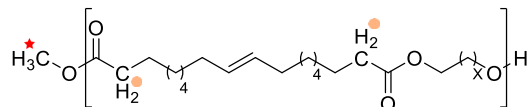


Figure 50 Proton groups used for end group analysis of obtained oligomers.

The number of repeat units (DP) in the oligomer chain may be determined using the following equation, which involves measuring the integration of the methyl group hydrogens I_{end} by ^1H NMR and that of the methylene hydrogens (I_n) present in each repeat unit (RU).

$$DP = \frac{I_{end}}{I_n} \cdot \frac{3}{4} \quad (15)$$

$$M_n = RU \cdot DP \quad (16)$$

6. References

- [1] *Handbook of Heterogeneous Catalysis*, 2nd revised ed. (Eds.: G. Ertl, H. Knözinger, F. Schüth, J. Weitkamp), John Wiley & Sons, **2008**.
- [2] *Applied Homogeneous Catalysis with Organometallic Compounds*, 3d revised ed. (Eds.: B. Cornils, W. Herrmann A., M. Beller, R. Paciello), John Wiley & Sons, **2017**.
- [3] R. Poli, *Comments on Inorg. Chem.* **2009**, *30*, 177–228.
- [4] S. Kozuch, J. M. L. Martin, *ACS Catal.* **2012**, *2*, 2787–2794.
- [5] D. Bourissou, O. Guerret, F. P. Gabbaï, G. Bertrand, *Chem. Rev.* **2000**, *100*, 39–92.
- [6] H. W. Wanzlick, *Angew. Chem. Int. Ed. Engl.* **1962**, *1*, 75–80.
- [7] H.-W. Wanzlick, H.-J. Schönher, *Angew. Chem. Int. Ed. Engl.* **1968**, *7*, 141–142.
- [8] K. Öfele, *J. Organomet. Chem.* **1968**, *12*, 42–43.
- [9] A. Igau, H. Grutzmacher, A. Baceiredo, G. Bertrand, *J. Am. Chem. Soc.* **1988**, *110*, 6463–6466.
- [10] A. J. I. Arduengo, R. L. Harlow, M. Kline, *J. Am. Chem. Soc.* **1991**, *113*, 361–363.
- [11] M. N. Hopkinson, C. Richter, M. Schedler, F. Glorius, *Nature* **2014**, *510*, 485–496.
- [12] H. V. Huynh, *Chem. Rev.* **2018**, *118*, 9457–9492.
- [13] Y. Liu, P. E. Lindner, D. M. Lemal, *J. Am. Chem. Soc.* **1999**, *121*, 10626–10627.
- [14] F. E. Hahn, L. Wittenbecher, D. Le Van, R. Fröhlich, *Angew. Chem. Int. Ed.* **2000**, *39*, 541–544.
- [15] C. M. Weinstein, C. D. Martin, L. L. Liu, G. Bertrand, *Angew. Chem. Int. Ed.* **2014**, *53*, 6550–6553.
- [16] D. Enders, K. Breuer, G. Raabe, J. Rumsink, J. H. Teles, J.-P. Melder, K. Ebel, S. Brode, *Angew. Chem. Int. Ed. Engl.* **1995**, *34*, 1021–1023.
- [17] G. W. Nyce, S. Csihony, R. M. Waymouth, J. L. Hedrick, *Chem. Eur. J.* **2004**, *10*, 4073–4079.
- [18] N. Kuhn, T. Kratz, *Synthesis* **1993**, *1993*, 561–562.
- [19] L. Benhamou, E. Chardon, G. Lavigne, S. Bellemin-Laponnaz, V. César, *Chem. Rev.* **2011**, *111*, 2705–2733.
- [20] A. J. Arduengo, R. Krafczyk, R. Schmutzler, H. A. Craig, J. R. Goerlich, W. J. Marshall, M. Unverzagt, *Tetrahedron* **1999**, *55*, 14523–14534.
- [21] C. A. Tolman, *J. Am. Chem. Soc.* **1970**, *12*, 2953–2956.
- [22] T. Dröge, F. Glorius, *Angew. Chem. Int. Ed.* **2010**, *49*, 6940–6952.
- [23] O. Back, M. Henry-Ellinger, C. D. Martin, D. Martin, G. Bertrand, *Angew. Chem. Int. Ed.* **2013**, *52*, 2939–2943.
- [24] A. Liske, K. Verlinden, H. Buhl, K. Schaper, C. Ganter, *Organometallics* **2013**, *32*, 5269–5272.
- [25] H. V. Huynh, Y. Han, R. Jothibasu, J. A. Yang, *Organometallics* **2009**, *28*, 5395–5404.
- [26] Q. Teng, H. Vinh Huynh, *Dalton Trans.* **2017**, *46*, 614–627.
- [27] K. Verlinden, H. Buhl, W. Frank, C. Ganter, *Eur. J. Inorg. Chem.* **2015**, *2015*, 2416–2425.
- [28] G. Meng, L. Kakalis, S. P. Nolan, M. Szostak, *Tetrahedron Lett.* **2019**, *60*, 378–381.
- [29] A. B. P. Lever, *Inorg. Chem.* **1990**, *29*, 1271–1285.
- [30] C. A. Tolman, *J. Am. Chem. Soc.* **1977**, *77*, 313–348.
- [31] A. C. Hillier, W. J. Sommer, B. S. Yong, J. L. Petersen, L. Cavallo, S. P. Nolan, *Organometallics* **2003**, *22*, 4322–4326.
- [32] A. Poater, B. Cosenza, A. Correa, S. Giudice, F. Ragone, V. Scarano, L. Cavallo, *Eur. J. Inorg. Chem.* **2009**, *2009*, 1759–1766.
- [33] L. Falivene, R. Credendino, A. Poater, A. Petta, L. Serra, R. Oliva, V. Scarano, L. Cavallo, *Organometallics* **2016**, *35*, 2286–2293.
- [34] L. Falivene, Z. Cao, A. Petta, L. Serra, A. Poater, R. Oliva, V. Scarano, L. Cavallo, *Nat. Chem.* **2019**, *11*, 872–879.
- [35] H. Clavier, S. P. Nolan, *Chem. Commun.* **2010**, *46*, 841–861.
- [36] *SambVca 2.1* can be found under <https://www.molnac.unisa.it/OMtools/sambvca2.1/index.html>, accessed 28 August 2023.
- [37] A. A. William, M. N. George, *Polymeric Bicyclo-(2, 2, 1)-2-Heptene*, **1955**, US2721189A.
- [38] P. J.-L. Hérisson, Y. Chauvin, *Makromol. Chem.* **1971**, *141*, 161–176.
- [39] C. P. Casey, T. J. Burkhardt, *J. Am. Chem. Soc.* **1974**, *96*, 7808–7809.
- [40] T. R. Howard, J. B. Lee, R. H. Grubbs, *J. Am. Chem. Soc.* **1980**, *102*, 6876–6878.

- [41] C. P. C. Bradshaw, E. J. Howman, L. Turner, *J. Catal.* **1967**, *7*, 269–276.
- [42] N. Calderon, E. A. Ofstead, J. P. Ward, W. A. Judy, K. W. Scott, *J. Am. Chem. Soc.* **1968**, *90*, 4133–4140.
- [43] G. S. Lewandos, R. Pettit, *J. Am. Chem. Soc.* **1971**, *93*, 7087–7088.
- [44] R. H. Grubbs, T. K. Brunck, *J. Am. Chem. Soc.* **1972**, *94*, 2538–2540.
- [45] C. G. Biefeld, H. A. Eick, R. H. Grubbs, *Inorg. Chem.* **1973**, *12*, 2166–2170.
- [46] I. C. Stewart, B. K. Keitz, K. M. Kuhn, R. M. Thomas, R. H. Grubbs, *J. Am. Chem. Soc.* **2010**, *132*, 8534–8535.
- [47] J. H. Wengrovius, R. R. Schrock, M. R. Churchill, J. R. Missett, W. J. Youngs, *J. Am. Chem. Soc.* **1980**, *102*, 4515–4516.
- [48] G. C. Bazan, J. H. Oskam, H. N. Cho, L. Y. Park, R. R. Schrock, *J. Am. Chem. Soc.* **1991**, *113*, 6899–6907.
- [49] S. T. Nguyen, L. K. Johnson, R. H. Grubbs, J. W. Ziller, *J. Am. Chem. Soc.* **1992**, *114*, 3974–3975.
- [50] M. S. Sanford, J. A. Love, R. H. Grubbs, *J. Am. Chem. Soc.* **2001**, *123*, 6543–6554.
- [51] T. E. Wilhelm, T. R. Belderrain, S. N. Brown, R. H. Grubbs, *Organometallics* **1997**, *16*, 3867–3869.
- [52] S. M. Hansen, F. Rominger, M. Metz, P. Hofmann, *Chem. Eur. J.* **1999**, *5*, 557–566.
- [53] P. Schwab, M. B. France, J. W. Ziller, R. H. Grubbs, *Angew. Chem. Int. Ed. Engl.* **1995**, *34*, 2039–2041.
- [54] K. J. Harlow, A. F. Hill, J. D. E. T. Wilton-Ely, *J. Chem. Soc., Dalton Trans.* **1999**, *0*, 285–292.
- [55] H.-J. Schanz, L. Jafarpour, E. D. Stevens, S. P. Nolan, *Organometallics* **1999**, *18*, 5187–5190.
- [56] J. P. Selegue, *Organometallics* **1982**, *1*, 217–218.
- [57] A. Wolinska, D. Touchard, P. H. Dixneuf, A. Romero, *J. Organomet. Chem.* **1991**, *420*, 217–226.
- [58] D. Touchard, S. Guesmi, M. Bouchaib, P. Haquette, A. Daridor, P. H. Dixneuf, *Organometallics* **1996**, *15*, 2579–2581.
- [59] H. Katayama, F. Ozawa, *Organometallics* **1998**, *17*, 5190–5196.
- [60] J. S. Kingsbury, J. P. A. Harrity, P. J. Bonitatebus, A. H. Hoveyda, *J. Am. Chem. Soc.* **1999**, *121*, 791–799.
- [61] S. Gessler, S. Randl, S. Blechert, *Tetrahedron Lett.* **2000**, *41*, 9973–9976.
- [62] M. S. Sanford, M. Ulman, R. H. Grubbs, *J. Am. Chem. Soc.* **2001**, *123*, 749–750.
- [63] E. L. Dias, S. T. Nguyen, R. H. Grubbs, *J. Am. Chem. Soc.* **1997**, *119*, 3887–3897.
- [64] C. A. Urbina-Blanco, A. Poater, T. Lebl, S. Manzini, A. M. Z. Slawin, L. Cavallo, S. P. Nolan, *J. Am. Chem. Soc.* **2013**, *135*, 7073–7079.
- [65] G. C. Vougioukalakis, R. H. Grubbs, *Chem. Eur. J.* **2008**, *14*, 7545–7556.
- [66] T. Vorfalt, K.-J. Wannowius, H. Plenio, *Angew. Chem. Int. Ed. Engl.* **2010**, *49*, 5533–5536.
- [67] I. W. Ashworth, I. H. Hillier, D. J. Nelson, J. M. Percy, M. A. Vincent, *Chem. Commun.* **2011**, *47*, 5428–5430.
- [68] V. Thiel, M. Hendann, K.-J. Wannowius, H. Plenio, *J. Am. Chem. Soc.* **2012**, *134*, 1104–1114.
- [69] F. Nuñez-Zarur, X. Solans-Monfort, L. Rodríguez-Santiago, M. Sodupe, *Organometallics* **2012**, *31*, 4203–4215.
- [70] T. Vorfalt, K. J. Wannowius, V. Thiel, H. Plenio, *Chem. Eur. J.* **2010**, *16*, 12312–12315.
- [71] J. S. Kingsbury, A. H. Hoveyda, *J. Am. Chem. Soc.* **2005**, *127*, 4510–4517.
- [72] M. Bieniek, A. Michrowska, D. L. Usanov, K. Grela, *Chem. Eur. J.* **2008**, *14*, 806–818.
- [73] J. M. Bates, J. A. M. Lummiss, G. A. Bailey, D. E. Fogg, *ACS Catal.* **2014**, *4*, 2387–2394.
- [74] A. Chołuj, W. Nogaś, M. Patrzałek, P. Krzesiński, M. J. Chmielewski, A. Kajetanowicz, K. Grela, *Catalysts* **2020**, *10*, 438.
- [75] D. J. Nelson, S. Manzini, C. A. Urbina-Blanco, S. P. Nolan, *Chem. Commun.* **2014**, *50*, 10355–10375.
- [76] M. Scholl, T. M. Trnka, J. P. Morgan, R. H. Grubbs, *Tetrahedron Lett.* **1999**, *40*, 2247–2250.
- [77] J. Huang, E. D. Stevens, S. P. Nolan, J. L. Petersen, *J. Am. Chem. Soc.* **1999**, *121*, 2674–2678.
- [78] C. Adlhart, P. Chen, *J. Am. Chem. Soc.* **2004**, *126*, 3496–3510.
- [79] S. Torker, D. Merki, P. Chen, *J. Am. Chem. Soc.* **2008**, *130*, 4808–4814.

References

- [80] H.-C. Yang, Y.-C. Huang, Y.-K. Lan, T.-Y. Luh, Y. Zhao, D. G. Truhlar, *Organometallics* **2011**, *30*, 4196–4200.
- [81] K. Getty, M. U. Delgado-Jaime, P. Kennepohl, *J. Am. Chem. Soc.* **2007**, *129*, 15774–15776.
- [82] J. A. M. Lummiss, C. S. Higman, D. L. Fyson, R. McDonald, D. E. Fogg, *Chem. Sci.* **2015**, *6*, 6739–6746.
- [83] R. Dorta, E. D. Stevens, N. M. Scott, C. Costabile, L. Cavallo, C. D. Hoff, S. P. Nolan, *J. Am. Chem. Soc.* **2005**, *127*, 2485–2495.
- [84] F. C. Courchay, J. C. Sworen, K. B. Wagener, *Macromolecules* **2003**, *36*, 8231–8239.
- [85] T. Ritter, A. Hejl, A. G. Wenzel, T. W. Funk, R. H. Grubbs, *Organometallics* **2006**, *25*, 5740–5745.
- [86] J. A. Love, J. P. Morgan, T. M. Trnka, R. H. Grubbs, *Angew. Chem. Int. Ed.* **2002**, *41*, 4035–4037.
- [87] S. Leuthäußer, V. Schmidts, C. M. Thiele, H. Plenio, *Chem. Eur. J.* **2008**, *14*, 5465–5481.
- [88] E. Merino, E. Poli, U. Díaz, D. Brunel, *Dalton Trans.* **2012**, *41*, 10913–10918.
- [89] D. J. Nelson, P. Queval, M. Rouen, M. Magrez, F. Caijo, E. Borré, I. Laurent, C. Crévisy, O. Baslé, M. Mauduit, J. M. Percy, *ACS Catal.* **2013**, *3*, 259–264.
- [90] H. Wakamatsu, S. Blechert, *Angew. Chem. Int. Ed.* **2002**, *41*, 794–796.
- [91] H. Wakamatsu, S. Blechert, *Angew. Chem. Int. Ed.* **2002**, *41*, 2403–2405.
- [92] K. Grela, S. Harutyunyan, A. Michrowska, *Angew. Chem. Int. Ed.* **2002**, *41*, 4038–4040.
- [93] P. E. Romero, W. E. Piers, *J. Am. Chem. Soc.* **2005**, *127*, 5032–5033.
- [94] A. G. Wenzel, R. H. Grubbs, *J. Am. Chem. Soc.* **2006**, *128*, 16048–16049.
- [95] C. E. Webster, *J. Am. Chem. Soc.* **2007**, *129*, 7490–7491.
- [96] C. Luján, S. P. Nolan, *J. Organomet. Chem.* **2011**, *696*, 3935–3938.
- [97] C. Luján, S. P. Nolan, *Catal. Sci. Technol.* **2012**, *2*, 1027–1032.
- [98] G. Occhipinti, F. R. Hansen, K. W. Törnroos, V. R. Jensen, *J. Am. Chem. Soc.* **2013**, *135*, 3331–3334.
- [99] W. Smit, V. Koudriavtsev, G. Occhipinti, K. W. Törnroos, V. R. Jensen, *Organometallics* **2016**, *35*, 1825–1837.
- [100] G. Occhipinti, K. W. Törnroos, V. R. Jensen, *Organometallics* **2017**, *36*, 3284–3292.
- [101] W. Smit, J. B. Ekeli, G. Occhipinti, B. Woźniak, K. W. Törnroos, V. R. Jensen, *Organometallics* **2020**, *39*, 397–407.
- [102] K. Endo, R. H. Grubbs, *J. Am. Chem. Soc.* **2011**, *133*, 8525–8527.
- [103] P. Liu, X. Xu, X. Dong, B. K. Keitz, M. B. Herbert, R. H. Grubbs, K. N. Houk, *J. Am. Chem. Soc.* **2012**, *134*, 1464–1467.
- [104] B. K. Keitz, K. Endo, M. B. Herbert, R. H. Grubbs, *J. Am. Chem. Soc.* **2011**, *133*, 9686–9688.
- [105] J. Hartung, R. H. Grubbs, *J. Am. Chem. Soc.* **2013**, *135*, 10183–10185.
- [106] V. M. Marx, M. B. Herbert, B. K. Keitz, R. H. Grubbs, *J. Am. Chem. Soc.* **2013**, *135*, 94–97.
- [107] M. B. Herbert, V. M. Marx, R. L. Pederson, R. H. Grubbs, *Angew. Chem. Int. Ed.* **2013**, *52*, 310–314.
- [108] H. Miyazaki, M. B. Herbert, P. Liu, X. Dong, X. Xu, B. K. Keitz, T. Ung, G. Mkrtumyan, K. N. Houk, R. H. Grubbs, *J. Am. Chem. Soc.* **2013**, *135*, 5848–5858.
- [109] *Hoveyda-Grubbs Catalyst M2001 Umicore (1352916-84-7)* can be found under:
<https://www.sigmadralich.com/FR/en/product/aldrich/771082>, accessed 28 August 2023.
- [110] B. K. Keitz, K. Endo, P. R. Patel, M. B. Herbert, R. H. Grubbs, *J. Am. Chem. Soc.* **2012**, *134*, 693–699.
- [111] S. M. Bronner, M. B. Herbert, P. R. Patel, V. M. Marx, R. H. Grubbs, *Chem. Sci.* **2014**, *5*, 4091–4098.
- [112] A. Dumas, R. Tarrieu, T. Vives, T. Roisnel, V. Dorcet, O. Baslé, M. Mauduit, *ACS Catal.* **2018**, *8*, 3257–3262.
- [113] M. B. Herbert, B. A. Suslick, P. Liu, L. Zou, P. K. Dornan, K. N. Houk, R. H. Grubbs, *Organometallics* **2015**, *34*, 2858–2869.
- [114] L. E. Rosebrugh, M. B. Herbert, V. M. Marx, B. K. Keitz, R. H. Grubbs, *J. Am. Chem. Soc.* **2013**, *135*, 1276–1279.
- [115] L. E. Rosebrugh, V. M. Marx, B. K. Keitz, R. H. Grubbs, *J. Am. Chem. Soc.* **2013**, *135*, 10032–10035.

- [116] K. Endo, M. B. Herbert, R. H. Grubbs, *Organometallics* **2013**, *32*, 5128–5135.
- [117] K. Gajda, A. Sytniczuk, L. Vendier, B. Trzaskowski, N. Lughan, A. Kajetanowicz, S. Bastin, K. Grela, V. César, *Eur. J. Inorg. Chem.* **2023**, *26*, e202300169.
- [118] M. B. Herbert, Y. Lan, B. K. Keitz, P. Liu, K. Endo, M. W. Day, K. N. Houk, R. H. Grubbs, *J. Am. Chem. Soc.* **2012**, *134*, 7861–7866.
- [119] J. Sun, C. Ou, C. Wang, M. Uchiyama, L. Deng, *Organometallics* **2015**, *34*, 1546–1551.
- [120] P. Ríos, H. Fouilloux, J. Díez, P. Vidossich, A. Lledós, S. Conejero, *Chem. Eur. J.* **2019**, *25*, 11346–11355.
- [121] D. Paul, B. Beiring, M. Plois, N. Ortega, S. Kock, D. Schlüns, J. Neugebauer, R. Wolf, F. Glorius, *Organometallics* **2016**, *35*, 3641–3646.
- [122] M. J. Koh, R. K. M. Khan, S. Torker, M. Yu, M. S. Mikus, A. H. Hoveyda, *Nature* **2015**, *517*, 181–186.
- [123] R. K. M. Khan, S. Torker, A. H. Hoveyda, *J. Am. Chem. Soc.* **2013**, *135*, 10258–10261.
- [124] A. M. Johns, T. S. Ahmed, B. W. Jackson, R. H. Grubbs, R. L. Pederson, *Org. Lett.* **2016**, *18*, 772–775.
- [125] M. J. Koh, R. K. M. Khan, S. Torker, A. H. Hoveyda, *Angew. Chem. Int. Ed.* **2014**, *53*, 1968–1972.
- [126] J. M. Grandner, H. Shao, R. H. Grubbs, P. Liu, K. N. Houk, *J. Org. Chem.* **2017**, *82*, 10595–10600.
- [127] I. Reim, G. Occhipinti, K. W. Törnroos, D. E. Fogg, V. R. Jensen, *Top Catal.* **2022**, *65*, 448–461.
- [128] T. S. Ahmed, R. H. Grubbs, *J. Am. Chem. Soc.* **2017**, *139*, 1532–1537.
- [129] E.-J. Y. Boisvert, H. C. Max, D. E. Fogg, *ACS Catal.* **2023**, *13*, 2885–2891.
- [130] J. M. Berlin, K. Campbell, T. Ritter, T. W. Funk, A. Chlenov, R. H. Grubbs, *Org. Lett.* **2007**, *9*, 1339–1342.
- [131] F. Ragone, A. Poater, L. Cavallo, *J. Am. Chem. Soc.* **2010**, *132*, 4249–4258.
- [132] *Hoveyda-Grubbs Catalyst M720 Umicore (301224-40-8)* can be found under: <https://www.sig-maaldrich.com/FR/en/product/aldrich/569755>, accessed 28 August 2023.
- [133] I. C. Stewart, T. Ung, A. A. Pletnev, J. M. Berlin, R. H. Grubbs, Y. Schrödi, *Org. Lett.* **2007**, *9*, 1589–1592.
- [134] K. M. Kuhn, J.-B. Bourg, C. K. Chung, S. C. Virgil, R. H. Grubbs, *J. Am. Chem. Soc.* **2009**, *131*, 5313–5320.
- [135] I. C. Stewart, C. J. Douglas, R. H. Grubbs, *Org. Lett.* **2008**, *10*, 441–444.
- [136] Y. Liang, R. Raju, T. Le, C. D. Taylor, A. R. Howell, *Tetrahedron Lett.* **2009**, *50*, 1020–1022.
- [137] K. Albitz, D. Csókás, Z. Dobi, I. Pápai, T. Soós, *Angew. Chem. Int. Ed.* **2023**, *62*, e202216879.
- [138] S. H. Hong, A. Chlenov, M. W. Day, R. H. Grubbs, *Angew. Chem. Int. Ed.* **2007**, *46*, 5148–5151.
- [139] J. Mathew, N. Koga, C. H. Suresh, *Organometallics* **2008**, *27*, 4666–4670.
- [140] A. Poater, L. Cavallo, *J. Mol. Catal. A Chem.* **2010**, *324*, 75–79.
- [141] K. Vehlow, S. Gessler, S. Blechert, *Angew. Chem. Int. Ed.* **2007**, *46*, 8082–8085.
- [142] S. Planer, P. Małecki, B. Trzaskowski, A. Kajetanowicz, K. Grela, *ACS Catal.* **2020**, *10*, 11394–11404.
- [143] E. Ivry, A. Frenklah, Y. Ginzburg, E. Levin, I. Goldberg, S. Kozuch, N. G. Lemcoff, E. Tzur, *Organometallics* **2018**, *37*, 176–181.
- [144] X. Bantreil, T. E. Schmid, R. A. M. Randall, A. M. Z. Slawin, C. S. J. Cazin, *Chem. Commun.* **2010**, *46*, 7115–7117.
- [145] T. Vorfalt, S. Leuthäußer, H. Plenio, *Angew. Chem. Int. Ed.* **2009**, *48*, 5191–5194.
- [146] C. K. Chung, R. H. Grubbs, *Org. Lett.* **2008**, *10*, 2693–2696.
- [147] W. Kośnik, D. Lichosyt, M. Śnieżek, A. Janaszkiewicz, K. Woźniak, M. Malińska, B. Trzaskowski, A. Kajetanowicz, K. Grela, *Angew. Chem. Int. Ed.* **2022**, *61*, e202201472.
- [148] F. Rodriguez, C. Cohen, C. K. Ober, L. Archer, *Principles of Polymer Systems*, CRC Press, **2014**.
- [149] M. A. R. Meier, J. O. Metzger, U. S. Schubert, *Chem. Soc. Rev.* **2007**, *36*, 1788–1802.
- [150] H. Mutlu, M. A. R. Meier, *Eur. J. Lipid Sci. Technol.* **2010**, *112*, 10–30.
- [151] Y. Xia, R. C. Larock, *Green Chem.* **2010**, *12*, 1893–1909.

References

- [152] U. Biermann, U. Bornscheuer, M. A. R. Meier, J. O. Metzger, H. J. Schäfer, *Angew. Chem. Int. Ed.* **2011**, *50*, 3854–3871.
- [153] F. D. Gunstone, *Eur. J. Lipid Sci. Technol.* **2001**, *103*, 307–314.
- [154] Y.-M. Choo, K.-E. Ooi, I.-H. Ooi, D. D. H. Tan, *J. Am. Oil Chem. Soc.* **1996**, *73*, 333–336.
- [155] J. C. Mol, *Green Chem.* **2002**, *4*, 5–13.
- [156] J. C. Mol, *Top Catal.* **2004**, *27*, 97–104.
- [157] Technology can be found under <https://elevance.com/technology/>, accessed 9 January 2023.
- [158] J. Spekreijse, J. P. M. Sanders, J. H. Bitter, E. L. Scott, *ChemSusChem* **2017**, *10*, 470–482.
- [159] Press Release: Verbio Vereinigte BioEnergie can be found under: <https://www.marketscreener.com/quote/stock/VERBIO-VEREINIGTE-BIOENER-516720/news/PRESS-RELEASE-VERBIO-Vereinigte-BioEnergie-AG-2-36482898/>, accessed 29 January 2023.
- [160] H. L. Ngo, T. A. Foglia, *J. Am. Oil Chem. Soc.* **2007**, *84*, 777–784.
- [161] G. S. Forman, R. M. Bellabarba, R. P. Tooze, A. M. Z. Slawin, R. Karch, R. Winde, *J. Organomet. Chem.* **2006**, *691*, 5513–5516.
- [162] M. K. Elmkadem, P. de Caro, S. Thiébaud-Roux, Z. Moulongui, E. Vedrenne, *OC&L* **2016**, *23*, D507.
- [163] R. Kadyrov, C. Azap, S. Weidlich, D. Wolf, *Top Catal.* **2012**, *55*, 538–542.
- [164] J. Allard, I. Curbet, G. Chollet, F. Tripoteau, S. Sambou, F. Caijo, Y. Raoul, C. Crévisy, O. Baslé, M. Mauduit, *Chem. Eur. J.* **2017**, *23*, 12729–12734.
- [165] Methyl oleate 99% can be found under: <https://www.sigmaaldrich.com/FR/en/product/aldrich/311111>, accessed 28 August 2023.
- [166] G. D. Lawrence, APPENDIX B.: FATTY ACID COMPOSITION OF DIETARY FATS AND OILS, In *The Fats of Life: Essential Fatty Acids in Health and Disease*, Rutgers University Press, **2010**, pp. 219–221.
- [167] A. Behr, N. Döring, S. Durowicz-Heil, B. Ellenberg, C. Kozik, Ch. Lohr, H. Schmidke, *Fett/Lipid* **1993**, *95*, 2–12.
- [168] S. Nogales-Delgado, J. M. Encinar, Á. González Cortés, *Ind. Crops Prod.* **2021**, *170*, 113701.
- [169] M. Qaim, Genetically Modified Crops, In *Encyclopedia of Food Security and Sustainability* (Eds.: P. Ferranti, E.M. Berry, J.R. Anderson), Elsevier, Oxford, **2019**, pp. 159–164.
- [170] I. Benaissa, K. Gajda, L. Vendier, N. Lugan, A. Kajetanowicz, K. Grela, V. Michelet, V. César, S. Bastin, *Organometallics* **2021**, *40*, 3223–3234.
- [171] O. Esposito, D. E. Roberts, F. G. N. Cloke, S. Caddick, J. C. Green, N. Hazari, P. B. Hitchcock, *Eur. J. Inorg. Chem.* **2009**, *2009*, 1844–1850.
- [172] I. C. Watson, Y. Zhou, M. J. Ferguson, E. Rivard, *Z. Anorg. Allg. Chem.* **2022**, *648*, e20220.
- [173] S. Ando, A. Ohara, T. Ohwada, T. Ishizuka, *Organometallics* **2021**, *40*, 3668–3677.
- [174] I. C. Watson, A. Schumann, H. Yu, E. C. Davy, R. McDonald, M. J. Ferguson, C. Hering-Junghans, E. Rivard, *Chem. Eur. J.* **2019**, *25*, 9678–9690.
- [175] K. Powers, C. Hering-Junghans, R. McDonald, M. J. Ferguson, E. Rivard, *Polyhedron* **2016**, *108*, 8–14.
- [176] D. A. Imbrich, W. Frey, S. Naumann, M. R. Buchmeiser, *Chem. Commun.* **2016**, *52*, 6099–6102.
- [177] M. Iglesias, A. Iturmendi, P. J. S. Miguel, V. Polo, J. J. Pérez-Torrente, L. A. Oro, *Chem. Commun.* **2015**, *51*, 12431–12434.
- [178] A. Fürstner, M. Alcarazo, R. Goddard, C. W. Lehmann, *Angew. Chem. Int. Ed.* **2008**, *47*, 3210–3214.
- [179] N. Kuhn, H. Bohnen, D. Bläser, R. Boese, *Chem. Ber.* **1994**, *127*, 1405–1407.
- [180] Z. Li, P. Ji, J.-P. Cheng, *J. Org. Chem.* **2021**, *86*, 2974–2985.
- [181] Z. Wang, Q.-H. Niu, X.-S. Xue, P. Ji, *J. Org. Chem.* **2020**, *85*, 13204–13210.
- [182] R. Schuldt, J. Kästner, S. Naumann, *J. Org. Chem.* **2019**, *84*, 2209–2218.
- [183] S. Naumann, *Chem. Commun.* **2019**, *55*, 11658–11670.
- [184] A. Doddi, M. Peters, M. Tamm, *Chem. Rev.* **2019**, *119*, 6994–7112.
- [185] M. M. D. Roy, E. Rivard, *Acc. Chem. Res.* **2017**, *50*, 2017–2025.
- [186] K. Gajda, PhD thesis, University of Warsaw (PL), in preparation.
- [187] C. S. Day, D. E. Fogg, *Organometallics* **2018**, *37*, 4551–4555.
- [188] L. Jafarpour, J. Huang, E. D. Stevens, S. P. Nolan, *Organometallics* **1999**, *18*, 3760–3763.

- [189] C. H. Leung, C. D. Incarvito, R. H. Crabtree, *Organometallics* **2006**, *25*, 6099–6107.
- [190] D. S. Müller, Y. Raoul, J. Le Nôtre, O. Baslé, M. Mauduit, *ACS Catal.* **2019**, *9*, 3511–3518.
- [191] M. O. Albers, D. J. A. D. Waal, D. C. Liles, D. J. Robinson, E. Singleton, M. B. Wiege, *J. Chem. Soc., Chem. Commun.* **1986**, *0*, 1680–1682.
- [192] C. Ernst, O. Walter, E. Dinjus, S. Arzberger, H. Görls, *J. Prakt. Chem.* **1999**, *341*, 801–804.
- [193] C. Ernst, O. Walter, E. Dinjus, *J. Organomet. Chem.* **2001**, *627*, 249–254.
- [194] D. Q. Nguyen, H. W. Bae, E. H. Jeon, J. S. Lee, M. Cheong, H. Kim, H. S. Kim, H. Lee, *J. Power Sources* **2008**, *183*, 303–309.
- [195] N. Touj, J. J. Taping, N. Tumanov, J. Wouters, L. Delaude, *Chem. Eur. J.* **2023**, e202302402.
- [196] D. R. Burfield, R. H. Smithers, *J. Org. Chem.* **1978**, *43*, 3966–3968.
- [197] I. Benissa, R. Taakili, N. Lugan, Y. Canac, *Dalton Trans.* **2017**, *46*, 12293–12305.
- [198] W. Reeve, C. M. Erikson, P. F. Aluotto, *Can. J. Chem.* **1979**, *57*, 2747–2754.
- [199] J. P. Richard, G. Williams, J. Gao, *J. Am. Chem. Soc.* **1999**, *121*, 715–726.
- [200] D. Emeljanenko, A. Peters, V. Vitske, E. Kaifer, H.-J. Himmel, *Eur. J. Inorg. Chem.* **2010**, *2010*, 4783–4789.
- [201] K. Tomomatsu, Y. Yamada, Y. Koga, K. Matsubara, *Chem. Lett.* **2022**, *51*, 836–839.
- [202] A. M. Oertel, V. Ritleng, M. J. Chetcuti, L. F. Veiros, *J. Am. Chem. Soc.* **2010**, *132*, 13588–13589.
- [203] R. McCrindle, G. Ferguson, A. J. McAlees, M. Parvez, P. J. Roberts, *J. Chem. Soc., Dalton Trans.* **1982**, *0*, 1699–1708.
- [204] K. Suzuki, H. Yamamoto, S. Kanie, *J. Organomet. Chem.* **1974**, *73*, 131–136.
- [205] R. Ros, R. A. Michelin, R. Bataillard, R. Roulet, *J. Organomet. Chem.* **1977**, *139*, 355–359.
- [206] A. D. English, T. Herskovitz, *J. Am. Chem. Soc.* **1977**, *99*, 1648–1649.
- [207] M. G. Crestani, A. Steffen, A. M. Kenwright, A. S. Batsanov, J. A. K. Howard, T. B. Marder, *Organometallics* **2009**, *28*, 2904–2914.
- [208] V. G. Albano, L. Busetto, F. Marchetti, M. Monari, V. Zanotti, *J. Organomet. Chem.* **2002**, *649*, 64–69.
- [209] G. L. Crocco, K. E. Lee, J. A. Gladysz, *Organometallics* **1990**, *9*, 2819–2831.
- [210] T. Tsuda, T. Nakatsuka, T. Hirayama, T. Saegusa, *J. Chem. Soc., Chem. Commun.* **1974**, 557–558.
- [211] Y. Canac, C. Lepetit, M. Abdalilah, C. Duhayon, R. Chauvin, *J. Am. Chem. Soc.* **2008**, *130*, 8406–8413.
- [212] Y. Ding, R. Goddard, K.-R. Pörschke, *Organometallics* **2005**, *24*, 439–445.
- [213] M. S. Viciu, O. Navarro, R. F. Germaneau, R. A. Kelly, W. Sommer, N. Marion, E. D. Stevens, L. Cavallo, S. P. Nolan, *Organometallics* **2004**, *23*, 1629–1635.
- [214] P. I. Jolly, A. Marczyk, P. Małecki, O. Ablijahimov, D. Trzybiński, K. Woźniak, S. Osella, B. Trzaskowski, K. Grela, *Chem. Eur. J.* **2018**, *24*, 4785–4789.
- [215] P. I. Jolly, A. Marczyk, P. Małecki, D. Trzybiński, K. Woźniak, A. Kajetanowicz, K. Grela, *Catalysts* **2020**, *10*, 599.
- [216] Y. Borguet, G. Zaragoza, A. Demonceau, L. Delaude, *Dalton Trans.* **2015**, *44*, 9744–9755.
- [217] Y. Borguet, G. Zaragoza, A. Demonceau, L. Delaude, *Dalton Trans.* **2013**, *42*, 7287–7296.
- [218] T. Lv, Z. Wang, J. You, J. Lan, G. Gao, *J. Org. Chem.* **2013**, *78*, 5723–5730.
- [219] S.-K. Kang, S.-H. Lee, D. Lee, *Synlett* **2000**, *2000*, 1022–1024.
- [220] M. Iglesias, D. J. Beetstra, B. Kariuki, K. J. Cavell, A. Dervisi, I. A. Fallis, *Eur. J. Inorg. Chem.* **2009**, *2009*, 1913–1919.
- [221] S. Wolf, H. Plenio, *J. Organomet. Chem.* **2009**, *694*, 1487–1492.
- [222] S. V. C. Vummasetti, D. J. Nelson, A. Poater, A. Gómez-Suárez, D. B. Cordes, A. M. Z. Slawin, S. P. Nolan, L. Cavallo, *Chem. Sci.* **2015**, *6*, 1895–1904.
- [223] Y. Zhang, G. Lavigne, N. Lugan, V. César, *Chem. Eur. J.* **2017**, *23*, 13792–13801.
- [224] S. B. Garber, J. S. Kingsbury, B. L. Gray, A. H. Hoveyda, *J. Am. Chem. Soc.* **2000**, *122*, 8168–8179.
- [225] A. W. Addison, T. N. Rao, J. Reedijk, J. van Rijn, G. C. Verschoor, *J. Chem. Soc., Dalton Trans.* **1984**, 1349–1356.
- [226] B. J. Coe, S. J. Glenwright, *Coord. Chem. Rev.* **2000**, *203*, 5–80.

References

- [227] V. César, Y. Zhang, W. Kośnik, A. Zieliński, A. A. Rajkiewicz, M. Ruamps, S. Bastin, N. Lugan, G. Lavigne, K. Grela, *Chem. Eur. J.* **2017**, *23*, 1950–1955.
- [228] C. A. Hunter, J. K. M. Sanders, *J. Am. Chem. Soc.* **1990**, *112*, 5525–5534.
- [229] R. Zhao, R.-Q. Zhang, *Phys. Chem. Chem. Phys.* **2016**, *18*, 25452–25457.
- [230] N. Mukherjee, S. Planer, K. Grela, *Org. Chem. Front.* **2018**, *5*, 494–516.
- [231] C. Lecourt, S. Dhambri, L. Allievi, Y. Sanogo, N. Zeghbib, R. B. Othman, M.-I. Lannou, G. Sorin, J. Ardisson, *Nat. Prod. Rep.* **2018**, *35*, 105–124.
- [232] C. S. Higman, L. Plais, D. E. Fogg, *ChemCatChem* **2013**, *5*, 3548–3551.
- [233] S. Krompiec, N. Kuźnik, M. Krompiec, R. Penczek, J. Mrzigod, A. Tórz, *J. Mol. Catal. A Chem.* **2006**, *253*, 132–146.
- [234] B. Schmidt, *Eur. J. Org. Chem.* **2004**, *2004*, 1865–1880.
- [235] O. Debleds, J.-M. Campagne, *J. Am. Chem. Soc.* **2008**, *130*, 1562–1563.
- [236] S. Warwel, F. Brüse, C. Demes, M. Kunz, M. R. gen Klaas, *Chemosphere* **2001**, *43*, 39–48.
- [237] Y. Tang, I. Benaissa, M. Huynh, L. Vendier, N. Lugan, S. Bastin, P. Belmont, V. César, V. Michélet, *Angew. Chem. Int. Ed.* **2019**, *58*, 7977–7981.
- [238] S. Bouzbouz, L. Boulard, J. Cossy, *Org. Lett.* **2007**, *9*, 3765–3768.
- [239] J. Tönnemann, J. Rissee, Z. Grote, R. Scopelliti, K. Severin, *Eur. J. Inorg. Chem.* **2013**, *2013*, 4558–4562.
- [240] M. Bessel, F. Rominger, B. F. Straub, *Synthesis* **2010**, *2010*, 1459–1466.
- [241] G. C. R. H. Giordano, R. M. Heinz, D. Forster, D. E. Morris, Di- μ -chloro-bis-(η^4 -1,5-cyclooctadiene)-dirhodium(I), In *Inorganic Syntheses: Reagents for Transition Metal Complex and Organometallic Syntheses* (Ed.: R.J. Angelici), John Wiley & Sons, **1990**, p. 88.
- [242] Y. Tatsuno, T. Yoshida, S. Otsuka, (η^3 -Allyl)palladium(II) complexes, In *Inorganic Syntheses: Reagents for Transition Metal Complex and Organometallic Syntheses* (Ed.: R.J. Angelici), John Wiley & Sons, **1990**, pp. 342–343.
- [243] E. Jürgens, K. N. Buys, A.-T. Schmidt, S. K. Furfari, M. L. Cole, M. Moser, F. Rominger, D. Kunz, *New J. Chem.* **2016**, *40*, 9160–9169.
- [244] T. A. Kirkland, R. H. Grubbs, *J. Org. Chem.* **1997**, *62*, 7310–7318.
- [245] Q. Yao, Y. Zhang, *J. Am. Chem. Soc.* **2004**, *126*, 74–75.
- [246] F. Romanov-Michailidis, K. F. Sedillo, J. M. Neely, T. Rovis, *J. Am. Chem. Soc.* **2015**, *137*, 8892–8895.
- [247] M. N. Pennell, P. G. Turner, T. D. Sheppard, *Chem. Eur. J.* **2012**, *18*, 4748–4758.
- [248] G. Szczepaniak, K. Urbaniak, C. Wierzbicka, K. Kosiński, K. Skowerski, K. Grela, *ChemSusChem* **2015**, *8*, 4139–4148.
- [249] W. Huang, J. Guo, Y. Xiao, M. Zhu, G. Zou, J. Tang, *Tetrahedron* **2005**, *61*, 9783–9790.
- [250] F. S. Mancilha, B. A. DaSilveira Neto, A. S. Lopes, P. F. Moreira Jr., F. H. Quina, R. S. Gonçalves, J. Dupont, *Eur. J. Org. Chem.* **2006**, *2006*, 4924–4933.
- [251] J. Liu, L. Bu, J. Dong, Q. Zhou, Y. Geng, D. Ma, L. Wang, X. Jing, F. Wang, *J. Mater. Chem.* **2007**, *17*, 2832–2838.
- [252] N. Noujeim, K. Zhu, V. N. Vukotic, S. J. Loeb, *Org. Lett.* **2012**, *14*, 2484–2487.
- [253] J. Heppekausen, A. Fürstner, *Angew. Chem. Int. Ed.* **2011**, *50*, 7829–7832.
- [254] A. Fürstner, O. R. Thiel, L. Ackermann, H.-J. Schanz, S. P. Nolan, *J. Org. Chem.* **2000**, *65*, 2204–2207.
- [255] R. Gawin, A. Kozakiewicz, P. A. Guńka, P. Dąbrowski, K. Skowerski, *Angew. Chem. Int. Ed.* **2017**, *56*, 981–986.
- [256] B. Stenne, J. Timperio, J. Savoie, T. Dudding, S. K. Collins, *Org. Lett.* **2010**, *12*, 2032–2035.
- [257] S. Nagasawa, Y. Sasano, Y. Iwabuchi, *Chem. Eur. J.* **2017**, *23*, 10276–10279.
- [258] T. Witt, M. Häußler, S. Kulpa, S. Mecking, *Angew. Chem. Int. Ed.* **2017**, *56*, 7589–7594.

Titre : Catalyseurs de métathèse des oléfines au ruthénium à stabilité et efficacité accrues par conception de nouveaux ligands carbènes N-hétérocycliques

Mots clés : complexes organométalliques, carbène N-hétérocycliques, catalyse homogène, ruthénium, chimie de coordination, sélectivité Z

Résumé : La catalyse est l'un des outils synthétiques clés de l'industrie chimique, en permettant d'obtenir une myriade de molécules parfois inaccessibles autrement. Les ligands auxiliaires jouent un rôle important dans le contrôle de l'activité, de la sélectivité et de la stabilité des catalyseurs organométalliques résultants. À cet égard, les ligands carbènes N-hétérocycliques (NHCs) se sont révélés extrêmement efficaces pour stabiliser les intermédiaires catalytiques. L'impact le plus important des NHCs se situe sans doute dans le domaine de la métathèse des oléfines (OM), une réaction qui s'est révélée d'une importance capitale en synthèse organique. Les travaux décrits ici visent à concevoir des ligands NHCs afin d'obtenir des catalyseurs OM plus stables, durables et donc plus efficaces. Deux stratégies ont été étudiées pour optimiser des catalyseurs NHC de MO correspondants. La première stratégie visait à développer des catalyseurs Z-sélectifs robustes, en introduisant des ligands bidentes NHC de type LX, où le ligand X serait un ligand carboné plus stable qu'un ligand alkyle. Pour cela, deux axes ont été étudiés : La synthèse de catalyseurs de MO portant des ligands NHCs bidentes comprenant un hétérocycle barbiturique (axe A), ou un fragment oléfine N-hétérocyclique (NHO) (axe B). Plusieurs complexes de ruthénium(II) portant le ligand NHC-barbiturique cible ont été synthétisés avec succès. Cependant, le catalyseur de MO correspondant n'a pas pu être obtenu et un mécanisme a été proposé pour expliquer la réactivité observée. Dans la partie suivante, la synthèse d'un catalyseur NHC-NHO de MO a été tentée. Cependant, la formation du complexe ruthénium-NHC correspondant a été empêchée en raison d'une ouverture inattendue du cycle de l'hétérocycle imidazolinylidène formé. La réactivité du nouveau ligand NHC-NHO a été explorée avec des centres métalliques du rhodium (I) et du palladium (II), conduisant finalement à la synthèse du premier complexe NHC-NHO basé sur une plateforme de palladium. La deuxième stratégie concerne le développement de catalyseurs de MO plus efficaces et stables pour la formation de doubles liaisons carbone-carbone tétrasubstituées. Considérant que la voie de désactivation délétère du catalyseur nécessite la rotation du bras N-aryle du ligand NHC, un deuxième niveau de groupes aromatiques dans les ligands N-phényl NHC à base de benzimidazolylidène a été introduit. Cela a conduit à des catalyseurs de MO au ruthénium robustes et très efficaces dans les réactions de métathèse difficiles de formation des oléfines tri- et tétrasubstituées. L'effet bénéfique de ce deuxième pont de cycles aromatiques sur la stabilité et l'activité des complexes de ruthénium est rationalisé grâce à la détermination expérimentale des propriétés stéréoélectroniques des ligands NHCs, complétée par des calculs DFT sur la nature des interactions dans l'espace entre les aromatiques et sur la voie de décomposition des précatalystes. Enfin, les systèmes catalytiques obtenus ont été testés dans la synthèse de polyesters et polyamides biosourcés. Pour démontrer l'applicabilité de cette étude, un oléate de méthyle de qualité technique a été utilisé pour l'étape de métathèse d'auto-croisement. Un tel matériau dérive d'huile de tournesol ou de colza largement disponible et contient une quantité substantielle (20 % en poids) de linoléate de méthyle. L'octadéc-9-énedioate de diméthyle obtenu a été utilisé dans une polycondensation ultérieure avec un co-monomère (diol ou diamine), ce qui a abouti à la formation de matériaux polymères.

Title: N-heterocyclic carbene ligands designed for improved stability and efficiency of ruthenium-based olefin metathesis catalysts

Key words: ruthenium, organometallic complexes, olefin metathesis, N-heterocyclic carbene, coordination chemistry, homogeneous catalysis

Abstract: No doubt catalysis is one of the most relevant tools used in the chemical industry, allowing to obtain a myriad of sometimes otherwise inaccessible molecules. Catalyst's auxiliary ligands play a significant role in defining the activity, selectivity and stability of the resulting catalysts. In this respect, N-heterocyclic carbene (NHC) ligands have shown a broad utility as spectator ligands that can stabilize catalytic intermediates. The most important impact of NHCs is arguably in the field of olefin metathesis (OM), a reaction that has already become a device of prominent importance in organic synthesis. The work described here aimed at NHC ligand design to achieve more stable, durable and thus more efficient OM catalysts. Two strategies were investigated to enhance the stability of corresponding NHC OM catalysts. The thesis is divided into six chapters. The first chapter of the thesis describes relevant state-of-the-art. In the second chapter, a strategy for a robust Z-selective OM catalyst was investigated, followed by chapter three reporting catalysts designed for an efficient tetrasubstituted carbon-carbon double bond formation. The last part of the work describes in chapter four a potential application of the obtained catalytic systems. The thesis concludes with an experimental section and references in chapters five and six respectively. Within the first strategy for a more efficient catalyst, attempts to obtain a robust Z-selective catalyst bearing a chelating LX-type NHC ligand were explored by altering the X-type carbon-based ligand. The research objectives were diversified into two axes, where a synthesis of OM catalysts bearing bidentate NHC ligands comprising either a barbituric heterocycle (axis A) or N-heterocyclic olefin (NHO) moiety (axis B) were attempted. Several ruthenium(II) complexes bearing the targeted NHC-barbiturate ligand were successfully synthesized. However, the corresponding OM catalyst could not be obtained and a mechanism was proposed to explain the observed reactivity. In the next part, the synthesis of an NHC-NHO OM catalyst was attempted. However, the formation of the corresponding ruthenium-NHC complex was precluded due to an unexpected ring opening of the formed imidazolinylidene heterocycle. The reactivity of the novel class NHC-NHO ligand was explored in the coordination chemistry of rhodium(I) and palladium(II) metal centers, ultimately leading to the synthesis of the first NHC-NHO complex based on a palladium platform. The third chapter is based on a second strategy for a more efficient catalyst, presenting advancements in the formation of tetrasubstituted carbon-carbon double bonds using OM. Considering that the anticipated, deleterious catalyst deactivation pathway requires the rotation of the N-aryl arm of the NHC ligand, a second decker of aromatic groups in benzimidazolylidene-based N-phenyl NHC ligands was introduced. This led to robust and highly efficient ruthenium OM catalysts in challenging metathesis reactions of tri- and tetra-substituted olefins. The beneficial effect of these upper aromatic "wings" on the stability and activity of ruthenium complexes is rationalized through the experimental determination of the stereoelectronic properties of the NHC ligands, complemented by DFT calculations on the nature of the through-space interactions between the aromatics and on the decomposition pathway of precatalysts. At last, the obtained catalytic systems were tested in the synthesis of bio-based polyesters and polyamides. To demonstrate the applicability of this study, a technical grade methyl oleate was used for the self-cross metathesis step. Such material derives from broadly available sunflower or rapeseed oil and contains a substantial amount (20 wt%) of methyl linoleate. The obtained dimethyl octadec-9-énedioate was used in a subsequent polycondensation with a co-monomer (diol or diamine), which resulted in the formation of polymeric materials.